



UNIVERSITAT DE
BARCELONA

North Atlantic Oscillation imprints in the Central Iberian Peninsula for the last two millennia: from ordination analyses to the Bayesian approach

Guionmar Sánchez López

ADVERTIMENT. La consulta d'aquesta tesi queda condicionada a l'acceptació de les següents condicions d'ús: La difusió d'aquesta tesi per mitjà del servei TDX (www.tdx.cat) i a través del Dipòsit Digital de la UB (deposit.ub.edu) ha estat autoritzada pels titulars dels drets de propietat intel·lectual únicament per a usos privats emmarcats en activitats d'investigació i docència. No s'autoritza la seva reproducció amb finalitats de lucre ni la seva difusió i posada a disposició des d'un lloc aliè al servei TDX ni al Dipòsit Digital de la UB. No s'autoritza la presentació del seu contingut en una finestra o marc aliè a TDX o al Dipòsit Digital de la UB (framing). Aquesta reserva de drets afecta tant al resum de presentació de la tesi com als seus continguts. En la utilització o cita de parts de la tesi és obligat indicar el nom de la persona autora.

ADVERTENCIA. La consulta de esta tesis queda condicionada a la aceptación de las siguientes condiciones de uso: La difusión de esta tesis por medio del servicio TDR (www.tdx.cat) y a través del Repositorio Digital de la UB (deposit.ub.edu) ha sido autorizada por los titulares de los derechos de propiedad intelectual únicamente para usos privados enmarcados en actividades de investigación y docencia. No se autoriza su reproducción con finalidades de lucro ni su difusión y puesta a disposición desde un sitio ajeno al servicio TDR o al Repositorio Digital de la UB. No se autoriza la presentación de su contenido en una ventana o marco ajeno a TDR o al Repositorio Digital de la UB (framing). Esta reserva de derechos afecta tanto al resumen de presentación de la tesis como a sus contenidos. En la utilización o cita de partes de la tesis es obligado indicar el nombre de la persona autora.

WARNING. On having consulted this thesis you're accepting the following use conditions: Spreading this thesis by the TDX (www.tdx.cat) service and by the UB Digital Repository (deposit.ub.edu) has been authorized by the titular of the intellectual property rights only for private uses placed in investigation and teaching activities. Reproduction with lucrative aims is not authorized nor its spreading and availability from a site foreign to the TDX service or to the UB Digital Repository. Introducing its content in a window or frame foreign to the TDX service or to the UB Digital Repository is not authorized (framing). Those rights affect to the presentation summary of the thesis as well as to its contents. In the using or citation of parts of the thesis it's obliged to indicate the name of the author.

**NORTH ATLANTIC OSCILLATION IMPRINTS IN THE CENTRAL IBERIAN
PENINSULA FOR THE LAST TWO MILLENNIA: FROM ORDINATION
ANALYSES TO THE BAYESIAN APPROACH**

Memoria presentada por Guiomar Sánchez López para optar al grado de doctora dentro del Programa de Doctorado de Ciències de la Terra de la Universitat de Barcelona. Esta memoria ha sido realizada bajo la dirección del Dr. Santiago Giralt Romeu (ICTJA-CSIC) y el Dr. Armand Hernández Hernández (IDL-Universidade de Lisboa), y bajo la tutela del Dr. Lluís Cabrera Pérez (Universitat de Barcelona).

Guiomar Sánchez López

En Barcelona, Julio del 2016

Dr. Santiago Giralt Romeu

Dr. Armand Hernández Hernández

Dr. Lluís Cabrera Pérez

*“Daría todo lo que sé,
por la mitad de lo que ignoro”*

René Descartes

A mi madre

A Chema

CONTENTS

Agradecimientos/Acknowledgements	x
Abstract	xiii
Resumen	xv
Glossary	xxv
CHAPTER 1: INTRODUCTION	1
CLIMATE	1
1.1 Global circulation model (GCM) of climate	2
1.1.1 The Intertropical Convergence Zone (ITCZ)	7
1.1.2 Climate modes	8
1.2 Climate variability in the North Atlantic region	8
1.2.1 The North Atlantic Oscillation (NAO)	10
1.2.2 Other climate modes in the North Atlantic: the East Atlantic (EA), Scandinavian (SCAND) and Atlantic Multidecadal Oscillation (AMO)	15
1.3 The climate variability in the Iberian Peninsula	20
1.3.1 Regional climate	20
1.3.2 Influence of the main climate modes on the present-day climate of the Iberian Peninsula	20
1.3.3 African dust episodes in the Iberian Peninsula	22
1.4 Climate reconstructions	25
1.4.1 Quantitative reconstructions	28
1.4.2 The Bayesian method	31
1.4.3 NAO reconstructions	33
1.4.4 Reconstructions in the Iberian Peninsula	35
LAKES	37
1.5 Alpine lakes	38

1.6 Lacustrine sediments	42
AIMS	44
THESIS STRUCTURE	44
CHAPTER 2: STUDY SITES	46
2.1 The Iberian Central Range	46
2.1.1 Peñalara Lake	47
2.1.2 Cimera Lake	50
CHAPTER 3: DATA, MATERIALS AND METHODOLOGY	53
3.1 Instrumental data	53
3.1.1 Climate index	53
3.1.2 Climatic data	53
3.1.3 Limnological data	55
- Lake water column temperatures	55
- Ice phenology	57
3.2 Lake coring campaigns	60
3.3 Core selection, image acquisition and sediment characterization	61
3.4 Radiometric dating	63
3.4.1 ^{210}Pb and ^{137}Cs dating	63
3.4.2 AMS ^{14}C radiocarbon dating	67
3.4.3 Chronological models	67
3.5 Geochemical analyses	68
3.5.1 X-Ray Fluorescence (XRF) core scanning	68
3.5.2 Bulk X-Ray Diffraction (XRD)	68
3.5.3 Clay X-Ray Diffraction (XRD)	69
3.5.4 Bulk elemental (TC, TN) and stable isotope ($\delta^{13}\text{C}$, $\delta^{15}\text{N}$) organic chemistry	70
3.5.5 Elemental chemical analyses ($[\text{NO}_3^-]$, $[\text{SO}_4^{2-}]$, $[\text{TP}]$)	72
3.6 Statistical treatment of data	73

3.6.1 Pearson product-moment correlation coefficients	73
3.6.2 Redundancy Data Analyses (RDAs)	73
3.6.3 Principal Component Analyses (PCAs)	75
3.6.4 The Bayesian model: random walk-modularised model	75
CHAPTER 4: RESULTS	81
4.1 Relationships between climate index, climatic and limnological data	81
4.1.1 Peñalara Lake	81
4.1.2 Cimera Lake	81
4.2 Facies description	86
4.2.1 Peñalara Lake	86
4.2.2 Cimera Lake	86
4.3 Chronological models	89
4.3.1 Peñalara Lake	89
4.3.2 Cimera Lake	91
4.4 Geochemical and mineralogical characterization of the lake sediments	93
4.4.1 Peñalara Lake	93
4.4.2 Cimera Lake	93
4.5 Geochemical and mineralogical characterization of an aeolian dust sample	96
4.6 Redundancy Data Analyses (RDAs)	96
4.6.1 Peñalara Lake	96
4.6.2 Cimera Lake	97
4.7 Principal Component Analyses (PCAs)	97
4.7.1 Peñalara Lake	97
4.7.2 Cimera Lake	99
4.8 Bayesian model: random walk-modularised	100
DISCUSSION	
CHAPTER 5: THE PRESENT-DAY NAO EFFECTS ON	106

THE ICE PHENOLOGY OF IBERIAN ALPINE LAKES	
5.1 Conceptual lake model	106
5.2 Differences in winter NAO effects	111
5.2.1 Morphometric factors	111
5.2.2 The altitude effect	112
5.2.3 The latitude effect	112
CHAPTER 6: THE EA PATTERN AND NAO INTERPLAY OVER THE IBERIAN PENINSULA FOR THE LAST TWO MILLENNIA	114
6.1 Sedimentology and interpretation of statistical analyses (RDAs and PCAs)	114
6.2 Climatic and environmental changes in the Iberian Central Range and the Iberian Peninsula over the last two millennia	119
6.2.1 The Roman Period (RP; ca. 250 BC – 500 AD)	120
6.2.2 The Early Middle Ages (EMA; 500 – 900 AD)	122
6.2.3 The Medieval Climate Anomaly (MCA; 900 – 1300 AD)	123
6.2.4 The Little Ice Age (LIA; 1300 – 1850 AD)	124
6.2.5 The Industrial Era (1850 – 2012 AD)	125
6.3 Climate-forcing mechanisms driving climate variability in the Iberian Peninsula over the last two millennia	125
CHAPTER 7: THE NAO IMPRINTS ON THE IBERIAN CENTRAL RANGE FOR THE LAST TWO MILLENNIA RECONSTRUCTED USING A BAYESIAN APPROACH	130
7.1 The NAO impact on the Iberian Central Range	130
7.2 Global aspects of the NAO impact on the Iberian Central Range	131
CHAPTER 8: CONCLUSIONS AND FUTURE WORKS	135
8.1 Concluding remarks	135
8.1.1 Methodological conclusions	135
8.1.2 Limnological conclusions	135
8.1.3 Climatic conclusions	136
8.2 Perspectives and future works	136

REFERENCES	138
APPENDICES	178
Theoretical R session (Appendix A)	178
Chemical and mineralogical data (Appendix B)	183

Agradecimientos/Acknowledgements

Después de un largo camino por fin ha llegado el momento más dulce, el de agradecer a todas las aquellas personas que me han ayudado a llegar hasta aquí y sin las cuales no habría sido posible esta tesis. Espero no dejarme alguna en el tintero porque han sido tantas...

Santi y Armand, gracias por guiarme y alumbrarme durante el recorrido que ha supuesto esta tesis. Os agradezco enormemente vuestra ayuda, apoyo, infinita paciencia, sí infinita creedme, gran conocimiento, pasión por la ciencia, rigor científico, esfuerzo y enseñanzas, y por supuesto, vuestra calidad humana y vuestro cariño... porque sin todo eso no hubiese sido posible llegar hasta aquí. Algunas veces el camino no ha sido fácil, pero sabía que siempre ibais a estar ahí para apoyarme en mis tropiezos y para continuar guiándome, simplemente ¡¡gracias!!

Chusa y Olga, por ser unas excelentes compañeras durante esta travesía. Habéis hecho que este largo viaje haya sido más ameno, divertido y mucho más llevadero. Olga, no te puedes imaginar la de veces que me he acordado de tus consejos y de tus frases cargadas de experiencia, han sido de gran ayuda. Chusa, gracias por tu vitalidad y alegría que han llenado el despacho de energía positiva durante toda la tesis y por estar siempre dispuesta a echar una mano y colaborar.

Alberto, Juan José y Roberto, por formar parte de lo que considero mi familia científica y por tratarme siempre con tanto cariño, ayudarme en todo lo que he necesitado y transmitirme vuestro enorme conocimiento.

Kiko y Manolo, gracias a vuestra dedicación, esfuerzo y pasión por los lagos, que ha permitido llevar a cabo las campañas de campo de esta tesis y obtener valiosos datos para el desarrollo de la misma. Habéis realizado y realizáis un gran trabajo que, sin ninguna duda, va mucho más allá de vuestras obligaciones profesionales. Igualmente os agradezco el conocimiento que me habéis transmitido sobre ambientes lacustres durante estos años y que ha sido fundamental para alcanzar la meta final.

Al hilo de las campañas de campo, agradecer al personal del centro de visitantes Peñalara, por su ayuda y atención durante la campaña de campo en la Laguna de Peñalara, aportaron su grano de arena para poder obtener los sedimentos que forman parte de esta tesis.

Vitor y Pedro, gracias por hacer tan llevadera la campaña de Azores y por facilitarnos las cosas y por supuesto por trabajar tan duro en ella, y aunque no forme parte directamente de esta tesis fue mi primera campaña de campo y siempre la recordaré con mucho cariño, ¡disfruté muchísimo en ella y en mi memoria quedarán para siempre grandes momentos vividos!

Sergi, porque sin tus “temidas” correcciones no hubiese salido adelante un gran trabajo, y aunque me han dado más de un dolor de cabeza e incluso me han hecho sudar un poco tinta a veces, han sido inmensamente beneficiosas y enriquecedoras, ¡¡gracias Sergi!!

Javier Sigró y Ricardo Trigo gracias por enseñarme tanto sobre clima, aunque me quede tantísimo por aprender aún, por ayudarme durante la tesis y por transmitirme

grandes ideas.

Marta Rejas, gracias por preguntarme e interesarte por mí cuando nos encontramos por el instituto, los empujoncitos de ánimo siempre son de gran ayuda en esta andadura que es la tesis. Sole, Jordi y Josep, gracias por resolverme cualquier duda de difracción y facilitarme siempre con una sonrisa cualquier cosa que os he pedido o he necesitado. Joan Manel Bruach, gracias por enseñarme y ser tan atento durante los días que estuvimos preparando algunas muestras para las dataciones de plomo y por pasarme las fotos de los aparatos que he necesitado. Laia Comas, muchas gracias por resolverme dudas y facilitarme con tanta rapidez las figuras necesarias.

Me gustaría dar las gracias a María José Ortiz y al grupo de Física del Clima de la Universidad de Alcalá por darme la oportunidad de comenzar mi formación científica en ese campo.

También me gustaría agradecer el apoyo económico recibido y sin el cual no hubiese sido posible la realización de esta tesis doctoral. Por eso cito a los proyectos PaleoNAO (CGL2010-15767; subprograma BTE) y RapidNAO (CGL2013-40608-R) así como a la beca de doctorado JAE PreDOC (JAEPRE2011-01171, BOE 20/06/2011) que me han permitido el desarrollo de todas las actividades científicas y estancias en el extranjero.

I would like to thank for my first short stay abroad to all the hospitable people from Québec and from the research centre Eau Terre Environnement of the Institut National de la Recherche Scientifique, especially to Pierre and François. I also feel grateful to Patricia, María and Kamil from the University of Lisbon for helping and inspiring me about Bayesian reconstructions. I would like to thank to Andrew and Niamh for helping to conduct the last part of this thesis, and to John, Thinh, Sarah and Nancy for allowing me to have nice meals with them during the three months that I was in Dublin. Derek and Jane, thank you for allowing me to stay in your lovely and comfortable home during these three months and for playing lovely music during this period.

A Helena, Mari, Chusa, Encarni, Laura, Clara y Pili. No tiene precio vuestra compañía y apoyo durante todo este tiempo. Sin duda, vuestra amistad y cariño es una de las mejores cosas de esta etapa. Los buenos momentos y las risas (y alguna que otra lagrimita) que hemos compartido son de las mejores cosas que me ha dado la tesis. La risoterapia ha sido de gran ayuda para el estrés y en los momentos difíciles. Todo ello me ha ayudado a seguir hacia delante y me ha hecho tan agradable y divertida la existencia durante este periodo. ¡¡No puedo evitar esbozar una enorme sonrisa cuando me acuerdo de todas vosotras!! :) y estoy segura de que nos quedan muchas más alegrías y risas por compartir!! ¡¡Muuuchas gracias chicas!! Y a las que todavía seguís remando para alcanzar la orilla deciros que no os rindáis nunca, que un día, casi sin daros cuenta, estaréis pisando tierra firme.

Mamá, una tesis es mucho más que el fruto de unos pocos años, y sin tu enorme sacrificio y lucha para sacar a tus hijas adelante no habría sido posible que yo llegara hasta aquí. Muchas veces me pregunto si yo hubiese sido capaz de hacer todo lo que tú has hecho, de haber salido adelante y de no haberme rendido jamás. Sin dudarlo has sido y eres un ejemplo de lucha, de tesón y de positivismo y en esta etapa de mi vida he

sido más consciente que nunca de ello. Has sido y serás mi gran ejemplo a seguir siempre. Todos mis logros te los debo a ti, y a la gran madre que eres, y aunque a cualquier persona su madre le parecerá la mejor, yo estoy convencida que la mía tiene algo especial, te quiero mamá.

Abuela, aunque no estés aquí para poder sentirte orgullosa de mí, siempre has sido y serás otro gran ejemplo de lucha en esta vida. Mientras formaste parte de ella nos ayudaste en todo lo que pudiste y nos diste tu cariño, amor y cuidados. Siempre estarás presente en mis recuerdos. Te echo tanto de menos y añoro tanto tus comidas.

Natalia, por ser la mejor hermana del mundo mundial, por tu cariño y por preocuparte por mí y apoyarme en todo lo que puedes ahora y siempre, te quiero hermana.

Iván y Eva, por hacerme partícipe de vuestra vida y de la de Simón y Marco. Gracias por cultivar el cariño que recibo de ellos, que no es fácil con la distancia que nos separa, y aunque no puedo disfrutar de vosotros todo lo que me gustaría, siempre que tengo la ocasión hacéis que sea entrañable y divertido, os quiero familia.

Merce y Jose, por tratarme con tanto cariño y amor durante todos estos años, y por preocuparos y ayudarnos en todo lo que podéis en la otra gran aventura, la de emanciparse. Os quiero familia.

Chema, sin tu amor, tu cariño, tu apoyo, tu paciencia, tus consejos y tu fuerza no habría podido llegar hasta aquí. Por creer en mí, muchas veces incluso más que yo misma. Porque en muchas ocasiones me has dado el aliento necesario para tirar para delante cuando estaba agotada y creía que no podía más. Por aguantarme, sé que a veces no ha sido nada fácil. Por haber sacrificado muchas cosas para que yo consiguiese alcanzar esta meta. Por recibirme al llegar a casa con una enorme sonrisa y un mimo después de un día duro. Por ser el mejor compañero durante todos estos años y los que vendrán. Y por todo lo que me aportas y que no soy capaz de expresar con palabras, pero que tú y yo sabemos. Sencillamente, te quiero Chema.

Y como ya he dicho al principio, gracias a todas aquellas personas que me dejó en el tintero y que no por ello son menos importantes, todas han contribuido a que finalizase esta tesis.

Abstract

The climate variability of the Iberian Peninsula (IP) can be explained in terms of relatively few large-scale atmospheric modes of climate variability, such as the North Atlantic Oscillation (NAO), the East Atlantic (EA) and the Scandinavian (SCAND) patterns. Many studies on the present-day IP climatology clearly show that the NAO is the most prominent mode, especially in winter. However, the most recent investigations have highlighted that, in spite of this importance, other climate modes seem to play a key role in both modulating the NAO-climate relationship and controlling certain meteorological parameters, such as the precipitation and/or temperature during a given season of the year. These complex present-day climate dynamics have begun to be well characterized from the meteorological perspective, but little is known about the past evolution of these climate interactions. Furthermore, there is a reasonable understanding of the past NAO evolution in the northern and the southern latitudes of the IP, but almost no information is available on the evolution of this climate mode in the Central IP. This knowledge is crucial to accurately characterizing the past climate evolution of the entire IP.

Within this framework, the main aim of this PhD thesis is to characterize the impacts of the NAO on the Central IP over the last 2,000 years. For that, three steps have been followed: 1) the establishment of a conceptual model to depict the NAO influence on the ice phenology of the Peñalara and Cimera alpine lakes (Iberian Central Range, ICR); 2) to characterize the main climate changes in the ICR using Peñalara and Cimera sediments and the spatio-temporal evolution of the NAO, as well as its relationships with other climate modes, over the last two millennia; and 3) to perform a quantitative regional NAO reconstruction using the geochemical composition of the Cimera Lake sediments and a random walk-modularised Bayesian model.

The conceptual lake model formulated to understand the present-day influence of the NAO on the limnological evolution of Peñalara (2016 m asl) and Cimera (2140 m asl) lakes was established using Pearson's correlation coefficients between seasonal time-scale series of the NAO index, climatic data (i.e., air temperature and precipitation data) and ice phenology records from both lakes. The results suggest that the effects of the NAO are only reflected in the thawing process via the air temperature and the insulating effect of snow accumulation on the ice cover. An altitude component is evident in our survey because the effects of the NAO on Peñalara Lake are restricted to winter, whereas for higher Iberian alpine lakes (i.e., Redon Lake, Pyrenees), the effects extend into spring. A latitudinal component is also clear: in northern Europe, the NAO signal is primarily reflected in lake ice phenology via the air temperature, whereas our results confirm that in southern Europe, the strong dependence of both precipitation and temperature on the NAO determines the importance of these climatic variables for lake ice cover.

The past NAO impacts on the Central IP were determined by the multi-proxy characterization of the sediments of Peñalara and Cimera lakes using ordination statistical analyses. This approach was used to reconstruct the intense runoff events, the lake productivity and the soil erosion in the Cimera Lake catchment and to interpret these factors in terms of temperature and precipitation variability in the ICR for the last

two millennia. The spatio-temporal integration of this reconstruction with other Iberian reconstructions was employed to identify the main climate drivers over this region. During the Roman Period (RP; 200 BC – 500 AD) and the Early Middle Ages (EMA; 500 – 900 AD), N–S and E–W humidity gradients, respectively, were dominant in the IP, whereas during the Medieval Climate Anomaly (MCA; 900 – 1300 AD) and Little Ice Age (LIA; 1300 – 1850 AD), these gradients were not evident. These differences could be ascribed to the interactions between the NAO and EA climate modes. During the RP, the generally warm conditions and the E–W humidity gradient in the IP indicate a dominant interaction between a negative NAO phase and a positive EA phase (NAO^- – EA^+), whereas the opposite conditions during the EMA indicate a NAO^+ – EA^- interaction. The dominantly warm and arid conditions during the MCA and the opposite conditions during the LIA in the IP indicate the interaction of the NAO^+ – EA^+ and NAO^- – EA^- , respectively. Furthermore, the higher solar irradiance and fewer tropical volcanic eruptions during the RP and MCA may support the predominance of the EA^+ phase, whereas the opposite conditions during the EMA and LIA may support the predominance of the EA^- phase, which would favour the occurrence of frequent and persistent blocking events in the Atlantic region. In addition, evidence of African dust inputs in these lakes could denote a coupled displacement between the Intertropical Convergence Zone and the NAO during the study period.

Finally, a Bayesian random walk-modularised model was formulated to quantitatively reconstruct the evolution of the NAO impacts in the ICR (NAO_{ICR}) for the last two millennia using the raw chemical element profiles obtained from the Cimera Lake sediments using an X-Ray-Fluorescence Avaatech® core scanner. The obtained quantitative values of the NAO_{ICR} were in accordance with previously reconstructed precipitation and temperature conditions. In addition, the comparison of the NAO_{ICR} with other NAO approaches show that the local impact of the NAO can also display global aspects of this climate mode and that this impact reconstruction could therefore be considered an approximately regional index for the entire IP.

Resumen

Introducción (capítulo 1)

El clima incluye el análisis del comportamiento de diferentes componentes como la atmósfera, la hidrosfera, la criosfera, la pedosfera y la biosfera, así como de sus procesos, sus interacciones y el intercambio de flujos de energía y materia entre ellos. Por tanto, la circulación climática global comprende las interacciones entre las circulaciones atmosférica y oceánica y es la responsable de la distribución de energía desde el ecuador hasta los polos. Como consecuencia de estas interacciones, variables climáticas globales y regionales como la temperatura, la precipitación o la presión atmosférica fluctúan de manera regular y forman patrones climáticos. Muchas de estas fluctuaciones son conocidas como modos u oscilaciones climáticas, que poseen características identificables y efectos regionales específicos. El estado de estos modos climáticos se monitoriza mediante valores escalares llamados índices climáticos.

En el sector del Atlántico Norte operan diferentes modos climáticos pero, la Oscilación del Atlántico Norte (siglas en inglés, NAO), ha sido reconocida desde hace casi un siglo como el principal modo atmosférico de variabilidad climática a gran escala en esta región, sobre todo durante el invierno. La NAO tiene dos centros de acción: el sistema de altas presiones centrado en Azores y el de bajas presiones situado en Islandia. Durante la fase positiva (negativa) de la NAO ambos centros de acción son reforzados (debilitados), asociándose dicha fase con vientos fuertes (débiles) del oeste que provocan condiciones cálidas y húmedas (frías y secas) en el norte de Europa y las contrarias en el sur.

El patrón del Atlántico Este (siglas en inglés, EA), así como el Escandinavo (siglas en inglés, SCAND), son otros dos modos atmosféricos a gran escala que también contribuyen a la variabilidad climática de la región del Atlántico Norte. Uno de sus impactos más destacados es su influencia en la posición geográfica e intensidad de los dos centros de acción del dipolo de la NAO y, por tanto, de la relación NAO-clima en el sector europeo del Atlántico Norte.

La Oscilación Multidecadal Atlántica (siglas en inglés, AMO) es otro patrón que actúa en la región Atlántica. La AMO ha sido identificada como un patrón de oscilaciones de baja frecuencia (ciclos de 65-80 años) de las temperaturas de la superficie del mar del Atlántico y regula variables climáticas sobre diferentes regiones del hemisferio Norte.

Mucha de la variabilidad climática en la Península Ibérica (siglas en inglés IP) puede ser explicada por un reducido número de modos atmosféricos a gran escala que operan en el sector noratlántico, aunque la NAO es el principal modo regulador de la climatología de esta región. Los efectos de la NAO de invierno en el clima de la IP son más evidentes en los registros de precipitación que en los de temperatura. Por su parte, el EA y el SCAND también influyen en el clima de esta región. El EA gobierna las temperaturas de invierno y de verano, mientras que los efectos del SCAND en el clima ibérico son más variables y muestran patrones espacio-temporales menos claros, aunque mayoritariamente este modo climático muestra relaciones significativas con la

precipitación durante el invierno y con la temperatura durante el verano.

Los ecosistemas lacustres de alta montaña son uno de los indicadores más sensibles de la variabilidad climática regulada por estos patrones climáticos. En particular, los efectos de la NAO de invierno se suelen ver reflejados en la fenología del hielo de los lagos a través de la temperatura del aire, especialmente en la fecha del inicio del deshielo. Sin embargo, estos efectos no han sido muy estudiados en áreas meridionales del Atlántico Norte debido a que las series de datos existentes sobre la fenología del hielo de los lagos de esta región suelen ser escasas y cortas. Además, los efectos de la señal de la NAO a través de otras variables climáticas como la nieve acumulada sobre la cubierta de hielo tampoco han sido bien determinados hasta ahora.

Por otra parte, las evidencias de estos cambios climáticos durante largos períodos de tiempo son comúnmente conservadas en archivos naturales como, por ejemplo, el hielo, los sedimentos marinos, los espeleotemas, los anillos de los árboles y/o corales, aunque uno de los archivos más extensamente utilizados en ecosistemas continentales son los sedimentos lacustres. En la IP los estudios más frecuentes sobre registros lacustres son de áreas de altitud media o baja, lo cual conlleva muchas veces a que estas reconstrucciones tengan que enfrentarse con el reto adicional de distinguir entre las señales ambientales o climáticas y las antrópicas.

Antes de los años 70 muchas reconstrucciones ambientales o climáticas se restringían a interpretaciones cualitativas como “frío”, “temperado”, “húmedo”, “seco”, etc. Sin embargo, los problemas derivados del calentamiento global y de los impactos antrópicos provocaron una respuesta rápida de las paleodisciplinas para enfrentarse a estos problemas, transformando su enfoque descriptivo y académico en uno cuantitativo y aplicado. Los parámetros biológicos y los llamados métodos clásicos han sido los más usados para llevar a cabo estas reconstrucciones cuantitativas aunque, en las últimas décadas, la estadística bayesiana ha ganado en popularidad. Esta estadística forma parte de las llamadas “estadísticas de aprendizaje”, cuya metodología está basa en “aprender” de los datos, presentando así una mayor ventaja en su coherencia y manejo de las incertidumbres comparada con la estadística clásica. No obstante, la mayoría de las aproximaciones bayesianas también utilizan parámetros biológicos, mientras que el uso de parámetros alternativos, los cuales implican menores costes de tiempo, muestreo y análisis como, como por ejemplo datos geoquímicos de sedimentos lacustres, no han sido aún bien explorado en este tipo de estadística.

Objetivos

El objetivo de esta Tesis Doctoral es caracterizar los impactos de la NAO en la zona central de la IP para los últimos 2000 años. Para ello se han seguido tres pasos: 1) establecer un modelo conceptual que represente la influencia actual de la NAO en la fenología del hielo de las lagunas alpinas de Peñalara y Cimera, localizadas en Sistema Central Ibérico (en adelante ICR, siglas en inglés); 2) caracterizar los principales cambios climáticos en el ICR utilizando los sedimentos lacustres de las lagunas anteriormente mencionadas así como la evolución espacio-temporal de la NAO y su relación con otros modos climáticos para los últimos dos mil años; y 3) obtener una reconstrucción cuantitativa regional de la NAO usando la composición geoquímica de

los sedimentos de la laguna de Cimera y un modelo bayesiano de camino aleatorio-modularizado.

Lugares de estudio: Laguna de Peñalara y Laguna Cimera (capítulo 2)

La laguna de Peñalara ($40^{\circ}50'N$ – $3^{\circ}57'O$) es una pequeña (0,6 ha, 115 m de largo, y 71,5 m de ancho) y somera (4,8 m de profundidad máxima) laguna alpina (2016 m snm) localizada en el flanco sureste del macizo de Peñalara en la Sierra de Guadarrama en el ICR. Esta laguna se asienta en una depresión de un circo glaciar y el área de su cuenca (149 ha) está compuesta de rocas metamórficas (gneiss) y pequeñas zonas de arbustos, pastos y turberas. La laguna está cubierta de hielo desde noviembre-diciembre hasta marzo-abril, es monomictica con estratificación térmica de sus aguas bajo la cubierta de hielo durante el periodo invernal aunque el resto del año la columna de agua suele permanecer homogénea.

La laguna Cimera ($40^{\circ}15'N$ – $5^{\circ}18'O$) es la más alta (2140 m snm) de una serie de cinco lagunas alpinas localizadas en un circo glaciar del Macizo Central de la Sierra de Gredos en el ICR. Cimera es una laguna somera (9,4 m de profundidad máxima) con una superficie pequeña (5 ha, 384 m de largo y 177 m de ancho) y una cuenca pequeña (75,6 ha) principalmente compuesta de roca plutónica (granitos) y con suelos escasamente desarrollados y pequeñas praderas. Cimera es una laguna polimictica discontinua que normalmente se hiela entre noviembre-diciembre y está totalmente libre de hielo en mayo-junio.

El clima del ICR es de tipo alpino inmerso en un clima mediterráneo continentalizado. La llegada frecuente de depresiones atlánticas desde el suroeste suele ocurrir en otoño, en invierno y en primavera; sin embargo en verano el anticiclón de las Azores es persistente evitando el transporte de humedad desde el oeste. Como consecuencia de estas situaciones, el clima del ICR se caracteriza por abundantes precipitaciones en estado sólido y bajas temperaturas durante el invierno y por condiciones secas y cálidas durante el verano. Las temperaturas máximas y mínimas estimadas para el periodo 1951–1999 AD varían entre 0 y 2°C y entre 20 y 22°C, respectivamente. La precipitación líquida total anual estimada para el periodo 1951–1999 AD es aproximadamente de 1400 mm.

Datos, materiales y metodología (capítulo 3)

Para determinar los efectos actuales de la NAO en la fenología del hielo de las lagunas de Peñalara y Cimera se han empleado tres conjuntos de datos: un índice climático, datos limnológicos y climáticos.

El índice climático utilizado está basado en datos mensuales del índice de la NAO durante el periodo 1825–2013 AD. Estos datos se obtuvieron del Climatic Research Unit (CRU) de la Universidad East Anglia (UK). Para la región de Peñalara se utilizaron datos mensuales de precipitación total, temperatura media del aire y días de nieve para el periodo 1950–2011 AD, siendo obtenidos todos estos datos de la estación meteorológica del puerto de Navacerrada ($40^{\circ}46'N$ – $4^{\circ}19'O$; 1860 m snm). Para la región de Cimera, se emplearon datos de anomalías regionales mensuales de

precipitación y de temperaturas máximas y mínimas del aire de 16 estaciones meteorológicas localizadas en sus alrededores para el periodo 1950–2011 AD. Los datos de espesor de nieve para el periodo 2010–2013 AD se obtuvieron del nivómetro Puerto Peones ($40^{\circ}15'N$ – $5^{\circ}26'O$; 2165 m snm), localizado aproximadamente a 10 km al oeste de la laguna. En la laguna de Peñalara, la temperatura de su agua fue medida a 0.5, 1, 2, 3 y 4 m de profundidad a intervalos de diez minutos, dos y cuatro horas durante el periodo 1950–2011 AD mediante diferentes cadenas de termistores HOBO Water Temp Pro V1 & V2. En la laguna de Cimera, la temperatura de su agua se midió cada hora a 0.5, 3, 6 y 9 m de profundidad para el periodo 2006–2013 AD mediante el mismo modelo de cadenas de termistores. Los datos diarios medios de estas temperaturas se calcularon a partir de estas medidas. Los datos de fenología del hielo incluyen las fechas de formación y desaparición de la cubierta de hielo así como de su duración. Para la laguna de Peñalara estos datos se obtuvieron a partir de observaciones diarias de la laguna y comprenden el periodo 1993–2013 AD, mientras que para Cimera fueron deducidos de las medidas de temperatura de su agua, siendo este método validado mediante la comparación de medidas de la temperatura del agua de Peñalara y sus datos de fenología del hielo. Este último conjunto de datos de Cimera abarca el periodo 2006–2013 AD.

Se emplearon análisis de correlaciones de Pearson a 1%, 5% y 10% niveles de significación para obtener los coeficientes de correlación y sus respectivos p-valores entre series mensuales y entre series estacionales de invierno (enero–marzo) y primavera (marzo–mayo) de los diferentes conjuntos de datos instrumentales.

De todos los sondeos de sedimento obtenidos en ambas lagunas, un sondeo de cada laguna fue seleccionado y empleado para reconstruir las condiciones climáticas de los últimos dos milenios en el ICR. Ambos sondeos fueron abiertos longitudinalmente y fotografiados en color mediante una cámara situada en el escáner de fluorescencia de rayos-X para sondeos de la Universidad de Barcelona (España). Estas imágenes junto con 30 frotis en Peñalara y 41 en Cimera, preparados cada 5 cm y en las capas sedimentarias más relevantes, sirvieron para identificar y cuantificar cualitativamente los principales componentes de los sedimentos y sus evoluciones temporales.

Los perfiles de concentración de ^{210}Pb y las dataciones radiocarbónicas se obtuvieron en ambos sondeos. El modelo de edad del testigo de Peñalara se construyó mediante interpolación lineal, mientras que para el sondeo de Cimera se utilizó el paquete 'clam' del programa estadístico R.

Ambos sondeos fueron muestrados para determinar el carbono orgánico total (siglas en inglés TOC), el nitrógeno total (siglas en inglés TN) y sus respectivos isótopos estables ($\delta^{13}\text{C}$, $\delta^{15}\text{N}$). Estos análisis se realizaron mediante un espectrómetro de masas Finnigan DELTAplus[®] TC/EA-CF-IRMS situado en los Centros Científicos y Tecnológicos de la Universidad de Barcelona (CCiT-UB, Barcelona, España). La composición química de los sedimentos de ambos sondeos fue obtenida mediante el escáner Avaatech[®] de fluorescencia de rayos X (de aquí en adelante XRF, siglas en inglés). Se midieron un total de treinta elementos aunque sólo diez ligeros (Al, Si, K, Ca, Ti, V, Cr, Mn, Fe and Zn) y tres pesados (Rb, Sr and Zr) tuvieron suficiente intensidad (cuentas por segundo) como para ser considerados estadísticamente consistentes. Las mismas muestras empleadas para medir el contenido de materia

orgánica fueron utilizadas para determinar su composición mineralógica mediante difracción de rayos X (siglas en inglés XRD). Este análisis fue realizado mediante el difractómetro de rayos X automático SIEMENS®-D500 situado en el instituto de Ciencias de la Tierra Jaume Almera (ICTJA-CSIC; Barcelona, España). Una selección de estas muestras también fue utilizada para identificar su composición arcillosa mediante XRD. La composición arcillosa y las concentraciones de nitratos (NO_3^-), fósforo total y sulfatos (SO_4^{2-}) también fueron determinados en una muestra de polvo recogida en la cuenca de Cimera en junio del 2014. Los nitratos y sulfatos fueron determinados mediante cromatografía iónica y el fósforo mediante espectrometría de masas por inducción de plasma (siglas en inglés ICP-MS) en los CCiT-UB.

Con el fin de establecer el origen de los parámetros geoquímicos y sus relaciones con las fases minerales asociadas, se aplicaron los análisis estadísticos de redundancias (siglas en inglés RDAs) en el conjunto de datos geoquímicos (XRF, TOC, TN, $\delta^{13}\text{C}$ y $\delta^{15}\text{N}$), como variable respuesta, y en los datos mineralógicos obtenidos mediante los análisis de XRD, como variable explicativa, de cada sondeo. El análisis de componentes principales (siglas en inglés PCAs) se aplicó a los datos geoquímicos normalizados para determinar los principales procesos ambientales que controlan la entrada, distribución y depósito de los sedimentos en ambos lagos.

El modelo bayesiano de camino aleatorio-modularizado se formuló para reconstruir la evolución de los impactos de la NAO en el ICR (de aquí en adelante NAO_{ICR}) durante los últimos dos milenios a partir de los datos de composición química de los sedimentos de la laguna de Cimera obtenidos mediante XRF. Este modelo es de camino-aleatorio porque la reconstrucción de la NAO_{ICR} depende del tiempo actual y es modularizado porque se divide en tres pasos diferentes; aunque también incluye un cuarto paso que corresponde a la validación del modelo. Estos cuatro pasos consisten brevemente en:

I) Calibración inicial en que el que se realiza una estimación del nexo causal entre el clima (NAO) y el parámetro utilizado (datos de XRF) durante el periodo de solapamiento instrumental seleccionado que, en este caso, ha sido de 1930–2012 AD.

II) Obtención de las distribuciones de probabilidad a posteriori de la NAO utilizando sólo la información de cada capa del sondeo. Estas distribuciones son conocidas como las distribuciones marginales de la NAO.

III) Ajuste del modelo donde se crean las distribuciones posteriores de la NAO_{ICR} utilizando las distribuciones marginales obtenidas en el paso anterior.

IV) Validación del modelo mediante validación cruzada.

Resultados (capítulo 4)

Los principales resultados obtenidos están integrados en los siguientes capítulos (capítulos 5, 6 y 7) que constituyen la discusión de la tesis con el fin de facilitar la compresión de las ideas discutidas en cada uno.

Los efectos actuales de la NAO en la fenología del hielo de lagos alpinos ibéricos (capítulo 5)

El modelo conceptual del lago obtenido a partir los coeficientes de correlación de Pearson entre las series estacionales (invierno y primavera) del índice de la NAO, datos climáticos (precipitación, temperatura del aire y nieve) y las variables limnológicas (registros de fenología del hielo) de la laguna de Peñalara permitió determinar los efectos de la NAO en la cubierta de hielo de los lagos alpinos del ICR.

Los resultados sugieren que los datos climáticos correspondientes al área de Peñalara están altamente influenciados por la NAO de invierno. En inviernos con prevalencia de fases negativas de la NAO existe un efecto bien definido en la temperatura del aire (más fría) y en la precipitación (más abundante), lo que conlleva a una mayor abundancia de días de nieve en la zona. Estas condiciones climáticas controlan los procesos de fenología del hielo (congelación y derretimiento) a diferentes escalas temporales dado que el proceso de formación de hielo ocurre más rápido que el deshielo debido a las diferentes propiedades físicas del agua y del hielo. La fecha de formación de la cubierta de hielo no presenta relación estadísticamente significativa ni con las variables climáticas en invierno ni en primavera; esta variable sólo presenta relación con la temperatura media mensual del aire en noviembre. El proceso de formación de la cubierta de hielo está principalmente controlado por las propiedades particulares de cada lago, las cuales determinan la pérdida de calor antes de la formación del hielo y por tanto, este proceso no suele verse reflejado a escala estacional. Por el contrario, los resultados muestran que la duración de la cubierta de hielo y la fecha de deshielo están correlacionadas negativamente con la temperatura del aire en invierno y positivamente con los días de nieve en invierno. El proceso de deshielo de la cubierta es más lento que el de formación y depende primordialmente de la radiación solar y de las condiciones climáticas estacionales. Éste comienza cuando la temperatura empieza a elevarse a finales del invierno o principios de la primavera. Sin embargo, la nieve que se ha ido acumulando durante el invierno sobre la cubierta de hielo reduce el calor absorbido por la misma debido a su baja conductividad térmica. Por tanto, la temperatura del aire en invierno acoplada con el efecto aislante de la cubierta de nieve controlan la duración de la cubierta de hielo y la subsiguiente fecha de deshielo.

Además, otros factores no climáticos, como la morfometría del lago, la altitud o la latitud pueden controlar parcialmente la fenología del hielo y, por tanto, los efectos de la NAO sobre esta variable.

Interacción entre el patrón del Atlántico Este (EA) y la NAO en la Península Ibérica durante los dos últimos milenios (capítulo 6)

Los modelos de edad, la caracterización multiparamétrica de los sedimentos de las lagunas de Peñalara y Cimera, y las interpretaciones de los análisis de PCA y RDA han indicado que la deposición sedimentaria de ambas lagunas está principalmente gobernada por cambios en la intensidad de la escorrentía superficial y la productividad de las lagunas, así como, en el caso de Cimera, por la erosión del suelo en la cuenca.

Estos procesos fueron principalmente controlados por los eventos lluvia-sobre-nieve y por la duración de la cubierta de hielo, respectivamente. A su vez, dichos procesos se desencadenaron por variaciones de precipitación y temperatura durante los últimos dos mil años.

Estos resultados han permitido caracterizar las condiciones climáticas y ambientales en el ICR para los últimos dos milenios: el comienzo del Periodo romano (de aquí en adelante RP; 200 ac – 500 AD) se caracterizó por una alternancia entre períodos fríos y cálidos indicado por oscilaciones en la intensidad de la escorrentía superficial y la erosión del suelo, aunque condiciones cálidas dominaron durante el final de este periodo y el comienzo de la Alta edad media (de aquí en adelante EMA; 500 – 900 AD). Un descenso notable en eventos de intensa escorrentía y la reducción progresiva de la erosión del suelo al final de la EMA indican un cambio hacia condiciones de temperatura más frías. En términos de precipitación, tanto el RP como la EMA presentan una transición de condiciones áridas hacia más húmedas que condujeron a la disminución de la productividad de los lagos por una mayor duración de sus cubiertas de hielo. La Anomalía Cálida Medieval (de aquí en adelante MCA; 900 – 1300 AD) se caracterizó por condiciones cálidas y secas con frecuentes episodios de intensa escorrentía superficial y un incremento de la productividad de los lagos y de la erosión del suelo en Cimera, mientras que la Pequeña edad del hielo (de aquí en adelante LIA; 1300 – 1850 AD) presentó condiciones climáticas opuestas. Finalmente, el periodo industrial (1850 – 2012 AD) muestra un aumento de la productividad de los lagos probablemente relacionado con el calentamiento global.

La integración espacio temporal de la reconstrucción en el ICR con otras reconstrucciones llevadas a cabo en diferentes partes de la IP ha permitido identificar los principales mecanismos climáticos que actuaron en esta región durante estos dos últimos milenios. El RP y la EMA se caracterizaron por el predominio de gradientes de humedad N–S y E–W mientras que en la LIA y la MCA dichos gradientes no fueron evidentes. Estas diferencias climáticas pueden deberse a interacciones entre el EA y la NAO. De este modo, durante el RP, las condiciones cálidas generalizadas y el gradiente de humedad E–W indican un predominio en la interacción entre la fase negativa de la NAO y la positiva del EA (NAO^-EA^+), mientras que las condiciones opuestas durante la EMA señalan una interacción NAO^+EA^- . Las condiciones cálidas predominantes durante la MCA y las frías durante la LIA muestran las interacciones NAO^+EA^+ y NAO^-EA^- respectivamente.

Así mismo, las variaciones en la llegada de polvo Africano a la IP durante los últimos dos mil años podría ser el resultado del movimiento acoplado entre la Zona de Convergencia Intertropical (siglas en inglés ITCZ) y la NAO. De este modo, un predominio de NAO^+ provocaría una reducción de las precipitaciones en el sur de Europa y en el norte de África y una posición más septentrional de la ITCZ favorecería las emisiones de polvo desde el norte de África (oeste y norte de la región desértica del Sahara) facilitando intensas emisiones de polvo y su transporte hacia la IP. Por el contrario, una fase NAO^- acoplada a una posición más meridional de la ITCZ derivaría en el escenario opuesto. Por consiguiente, la evidencia de la llegada de polvo Africano a la laguna de Cimera durante períodos secos como la EMA y la MCA quizás sugiera un predominio de NAO^+ acoplado con una posición más septentrional del ITCZ. A su vez,

estas condiciones podrían derivar en un predominio de veranos más secos en la IP durante ambos periodos. Sin embargo, las menores evidencias de estas llegadas a la laguna de Cimera durante períodos más húmedos como el RP o la LIA apuntarían al escenario opuesto, apoyando la hipótesis de un predominio de la fase NAO⁻ acoplada con una posición más meridional del ITCZ durante ambos períodos. Esta situación también podría evidenciar, por tanto, el aumento de la frecuencia de veranos más húmedos en la IP durante el RP y la LIA.

Huellas de la NAO en el Sistema Central Ibérico para los dos últimos milenios reconstruidas utilizando una aproximación bayesiana (capítulo 7)

La NAO reconstruida mediante el modelo bayesiano de camino aleatorio-modularizado muestra el impacto de la NAO en el ICR (NAO_{ICR}) para los dos últimos milenios. La comparación de esta NAO con el índice multidecadal de la NAO obtenido del CRU para el periodo 1930–1825 AD evidencia que ambas curvas muestran variaciones multidecadales similares. Además, la NAO_{ICR} debería estar en concordancia con las condiciones climáticas del ICR derivadas de la aproximación multiparamétrica. Por ello, se comparó este impacto de la NAO en el ICR con las condiciones térmicas (frío/cálido) y de humedad (árido/húmedo) de esta región deducidas de los análisis de PCAs y RDAs. La NAO_{ICR} durante el RP muestra variaciones multidecadales entre fases de impactos positivos y negativos aunque presenta un predominio de valores negativos, los cuales estarían en concordancia con un escenario dominado por condiciones húmedas. Las condiciones térmicas durante este periodo presentan cambios entre períodos cálidos y fríos. El comienzo de la EMA se caracteriza por un impacto positivo de la NAO coincidiendo con condiciones cálidas en el ICR, aunque el impacto contrario prevalece durante el resto del periodo simultáneamente con un cambio de condiciones secas a más húmedas. Un impacto positivo de la NAO prevalece durante la MCA junto con el predominio de condiciones cálidas y áridas mientras que, por el contrario, una tendencia hacia una fase negativa del impacto de este modo climático caracterizaría la LIA así como un escenario generalizado de condiciones húmedas. Este impacto predomina hasta el comienzo de la era industrial coincidiendo con un marcado periodo húmedo. Por lo tanto, las condiciones de humedad y de temperatura obtenidas a partir de los registros lacustres de Peñalara y Cimera parecen ser consistentes con las posibles condiciones climáticas asociadas a la NAO_{ICR} .

Finalmente, la comparación de la NAO_{ICR} con otras tres reconstrucciones de este índice (dos más simples realizadas por Trouet et al. (2009) y Olsen et al. (2012) y otra mucho más robusta llevada a cabo por Ortega et al. (2015)) muestra que una sencilla aproximación de la NAO podría reflejar aspectos regionales o globales de este índice climático y por lo tanto, la NAO_{ICR} podría llegar a considerarse un índice regional de este modo climático para la IP. Sin embargo, hay dos inconvenientes que deben tenerse en cuenta cuando se lleve a cabo una reconstrucción simplista de la NAO: 1) La precisión de la baja resolución temporal de la reconstrucción, que principalmente depende de la resolución del parámetro empleado; y 2) el papel de otros modos de variabilidad climática en la evolución del clima así como sus interacciones con la NAO durante los últimos milenios. Este papel no ha sido todavía bien abordado a pesar de la

gran relevancia que ha mostrado en los datos meteorológicos instrumentales.

Conclusiones (capítulo 8)

El estudio de los impactos de la NAO y su integración con otras reconstrucciones en la IP han dado lugar a las siguientes conclusiones metodológicas, limnológicas y climáticas:

Conclusiones metodológicas:

- El impacto climático de la NAO en los lagos alpinos de la IP ha sido caracterizado mediante un modelo conceptual, el cual ha contribuido a entender la transmisión de la señal de la NAO a los sedimentos de los lagos alpinos.

- Los datos geoquímicos procedentes del análisis por XRF mediante escáner y el modelo bayesiano de camino aleatorio-modularizado pueden considerarse una herramienta precisa para llevar a cabo una reconstrucción climática con bajos costes en términos de tiempo, muestreo y análisis.

- Una reconstrucción local de los impactos de la NAO puede mostrar aspectos globales de este modo climático y puede ser utilizada como un índice aproximado para la IP. A su vez, este índice regional puede integrarse en una reconstrucción más robusta de dicho índice.

- La interacción entre la NAO y los otros modos climáticos puede ser un factor clave en la relación causal entre el parámetro y los datos climáticos y debe de ser tenida en cuenta cuando se reconstruye el primer modo climático.

Conclusiones limnológicas:

- El proceso de deshielo de la cubierta de los lagos alpinos ibéricos está fuertemente afectado por la NAO, mientras que el de formación de la misma depende de condiciones sinópticas a corto plazo y de factores no climáticos como la morfometría del lago.

- La fecha de deshielo y la duración de la cubierta de los lagos alpinos de la IP refleja los efectos de la NAO a través de la temperatura del aire y de la nieve acumulada sobre dicha cubierta.

- La sedimentación en las lagunas de Peñalara y Cimera está dominada por la escorrentía, la productividad del lago así como, en el caso de Cimera, por la erosión del suelo. Estos procesos están principalmente controlados por los eventos lluvia-sobre-nieve y por la duración de la cubierta de hielo, respectivamente.

Conclusiones climáticas:

- A menor altitud, la señal de la NAO se manifiesta vía el efecto acoplado de la temperatura del aire y la precipitación (nieve acumulada en la cubierta) durante el invierno. A mayor altitud, los efectos de la NAO sobre la cubierta de hielo se transmiten mediante estas variables desacopladas, a través de la temperatura de primavera y la nieve acumulada durante el invierno.

- En el norte de Europa, los efectos de la NAO en la cubierta de los lagos alpinos están principalmente relacionados con la temperatura del aire, mientras que en el sur es a través de esta variable climática y la precipitación en forma de nieve.

- Las condiciones cálidas y los gradientes de humedad registrados en la IP durante el RP sugieren un predominio de las fases NAO⁻–EA⁺, mientras que las condiciones opuestas durante la EMA sugieren una preponderancia de las fases NAO⁺–EA⁻ en esta región. Por el contrario, la homogeneidad espacial de condiciones cálidas y áridas durante la MCA y las contrarias durante la LIA indican interacciones de NAO⁺–EA⁺ y NAO⁻–EA⁻, respectivamente.

- La evidencia de la llegada de polvo africano a la laguna de Cimera durante períodos áridos como la EMA y la MCA, sugieren un predominio de la fase NAO⁺ acoplada con una posición más septentrional del ITCZ, así como un particular predominio de veranos más áridos durante ambos períodos. Por el contrario, la menor evidencia de esta llegada durante el RP y la LIA sugieren el escenario climático contrario.

- Se ha reconstruido la evolución y el impacto de la NAO en el centro de la IP para los últimos dos mil años, los cuales presentan concordancia con otras reconstrucciones de la NAO con diferentes grados de robustez metodológica y resoluciones temporales.

Glossary

Acronyms and abbreviations

AABW	Antarctic Bottom Water
AD	Anno Dómini
AMO	Atlantic Multidecadal Oscillation
AMOC	Atlantic Meridional Overturning Circulation
AMS	Accelerator Mass Spectrometry
ANN	Artificial Neural Networks
AO	Arctic Oscillation
BP	Before present
CCD	Charged Coupled Device
CCiT-UB	Centres Científics i Tecnològics of the Universitat de Barcelona
CF:CS	Constant Flux: Constant Sedimentation model
Chl-a	chlorophyll a
CRU	Climatic Research Unit of the University of East Anglia (United Kingdom)
CSIC	Consejo Superior de Investigaciones Científicas
E	East
EA	East Atlantic
EA ⁻	negative phase of East Atlantic
EA ⁺	positive phase of East Atlantic
EAi	East Atlantic index
EMA	Early Middle Ages
ENSO	El Niño–Southern Oscillation
EOF	Empirical Orthogonal Function
EU1	Eurasian Type 1
GCM	Global Circulation Model
GLR-ML	Gaussian logit regression and maximum-likelihood calibration
ICP-MS	Inductively Coupled Plasma Mass Spectrometry
ICR	Iberian Central Range

ICTJA	Instituto de Ciencias de la Tierra Jaume Almera
IGME	Instituto Geológico y Minero de España
IP	Iberian Peninsula
ITCZ	Intertropical Convergence Zone
JFM	January to March
LaRAM	Laboratori de Radioactivitat Ambiental of the Institut de Ciència i
ICTA-UAB	Tecnologia Ambientals at the Universitat Autònoma de Barcelona
LIA	Little Ice Age
LOI	Loss On Ignition
MAM	March to May
MAT	Modern Analogue Technique
MCA	Medieval Climate Anomaly
MDP	Marginal Data Posterior
MJO	Madden-Julian Oscillation
N	North
NADW	North Atlantic Deep Water
NAM	Northern Annular Mode
NAO	North Atlantic Oscillation
NAO ⁻	negative phase of North Atlantic Oscillation
NAO ⁺	positive phase of North Atlantic Oscillation
NAO _i	North Atlantic Oscillation index
NAO _{ICR}	ancient NAO impact in the ICR
NAO _{Ols}	NAO approach by Olsen et al. (2012)
NAO _{Ort}	NAO approach by Ortega et al. (2015)
NAO _{Tro}	NAO approach by Trouet et al. (2009)
NAO _{Vinther}	NAO approach by Vinther et al. (2003a)
NOAA	National Oceanic and Atmospheric Administration of the U.S.
P or Precip	precipitation
PC	Principal Component
PC1 _{cim}	first eigenvector of Cimera Lake record
PC1 _{pe}	first eigenvector of Peñalara Lake record

PC2 _{cim}	second eigenvector of Cimera Lake record
PC2 _{pe}	second eigenvector of Peñalara Lake record
PC3 _{cim}	third eigenvector of Cimera Lake record
PCA	Principal Component Analysis
PCR	Principal components regression
PDO	Pacific Decadal Oscillation
PhD	Doctor of Philosophy
RDA	Redundancy Data Analysis
RMSE	Root Mean Squared Error
RMSEP	Root Mean Squared Error of Prediction
RP	Roman Period
RSD	Relative Standard Deviation
S	South
SCAND	Scandinavian
SCAND ⁻	negative phase of Scandinavian
SCAND ⁺	positive phase of Scandinavian
SCANDi	Scandinavian index
SLP	Sea Level Pressure
SR	Sedimentation Rate
SST	Sea Surface Temperature
T or Temp	temperature
TC	Total Carbon
TN	Total Nitrogen
TOC	Total Organic Carbon
TP	Total Phosphorous
UK	United Kingdom
US	United States
W	West
WA	Weighted-Averaging regression
WA-PLS	Weighted-Averaging Partial Least Squares regression
XRD	X-Ray Diffraction

XRF X-Ray Fluorescence

Alb Albite
Clc Clinochlore
Kln Kaolinite
Mc Microcline
Ms Muscovite
Pkg Palygorskite
Qtz Quartz
Sap Saponite

asl about sea level
ca circa
cal calibrated
kyr thousand years
n number of samples
r Pearson's correlation coefficient
s second
sp species
spp plural species
subsp subspecies
yr year

Elements, isotopes and chemical formulas

Al Aluminium
Ca Calcium
Cr Chromium
Cu Copper
Fe Iron
K Potassium

Mn Manganese

Rb Rubidium

Si Silicon

Sn Tin

Sr Strontium

Ti Titanium

V Vanadium

Zn Zinc

Zr Zirconium

^{137}Cs isotope caesium-137

^{210}Pb isotope lead-210

$^{210}\text{Pb}_{\text{ex}}$ excess of isotope
lead-210

^{226}Ra isotope radium-226

CO_2 Carbon dioxide

HCl Hydrochloric acid

HF Hydrofluoric acid

NO_3^- Nitrate

SO_4^{2-} Sulphate

Symbols

$\delta^{13}\text{C}$ Stable carbon isotopes; the ratio of ^{13}C to ^{12}C in a sample relative to a standard

$\delta^{15}\text{N}$ Stable nitrogen isotopes; the ratio of ^{15}N to ^{14}N in a sample relative to a standard

$\delta^{18}\text{O}$ Stable oxygen isotopes; the ratio of ^{18}O to ^{16}O in a sample relative to a standard

σ standard deviation

\emptyset empty set

$f()$ response function

X_m	matrix of modern data predictors
Y_m	matrix of modern data responses
$p()$	probability distribution

Units

ppm	parts per million
%o	per mil; one part per thousand
%	percentage
wt%	weight percentage
°	degree
°C	degree Celsius
K	degree Kelvin
cps	counts per second
s	second
μm	micrometre
mm	millimetre
cm	centimetre
m	metre
km	kilometre
ha	hectare
μg	microgram
mg	milligram
g	gram
μg Chl-a l ⁻¹	microgram of chlorophyll-a per litre
μg P-PO4 l ⁻¹	microgram of phosphates per litre
Tg yr ⁻¹	teragram per year
ml	millilitre
cc	cubic centimetre
mm yr ⁻¹	millimetre per year
mb	milibar

$\mu\text{S}/\text{cm}$	microsiemens per centimetre
mA	milliampere
kV	kilovolt
Bq/kg	becquerel per kilogram

Notation used in the mathematical derivations of the random-walk modularised Bayesian model (section 3.6.4)

m, f	superscripts denote modern and fossil elements, respectively
i, j	subscripts correspond to the number of the core layers (i.e., depths) and chemical elements from XRF proxy, respectively
t	age of all depths in the sediment core
t_i^m	modern ages of the overlapping period in AD years
t_i^f	fossil ages not included in the overlapping period in AD and BC years
XRF_{ij}	represents the chemical element j measured at the depth i of CIM12-04A core expressed as count per second
XRF_{ij}^m	XRF $_{ij}$ modern data in the overlapping period
XRF_{ij}^f	XRF $_{ij}$ modern data in the overlapping period
NAO_i^m	modern annual index data for each t_m of the overlapping period
NAO^{grid}	grid of NAO values of length k
MDP	Marginal Data Posterior
θ	set of parameters ($\beta_0, \beta_1, \beta_2, \mu, \sigma$) governing the relationship between NAO and XRF in the overlapping period.
μ	mean
σ	standard deviation
NAO^f	is the fossil impact of NAO estimated by the model
$\varepsilon_{\max}, \varepsilon_{\min}$	maximum and minimum uncertainties, respectively
prec	precision
$\text{Ga}()$	Gamma distribution
$\text{N}()$	Normal distribution

1. INTRODUCTION

CLIMATE

Climate in a narrow sense is usually defined as the statistical description of weather in terms of the mean and variability of relevant surface variables, such as the temperature, precipitation, wind, pressure, cloudiness, and humidity, among others, over a period of time (Le Treut et al., 2007). The classical period for averaging these variables is 30 years, as defined by the World Meteorological Organization, although other periods can be used depending on the purpose. For instance, when climatologists analyse the distant past, such as the Last Glacial Maximum between 21,000 and 18,000 years ago, depending on whether marine or continental records are employed, they are often interested in variables characteristic of longer time intervals (Goosse et al., 2010). Climate differs from weather in that the latter only describes the short-term conditions of the meteorological variables in a given region (Gutro, 2005).

Climate in a wider sense is the state, including a statistical description, of the climate system (Le Treut et al., 2007). Consequently, this definition includes the analysis of the behaviour of the five major components of the climate system: the atmosphere (the gaseous envelope surrounding the Earth), the hydrosphere (liquid water, i.e., oceans, lakes, underground water, etc.), the cryosphere (solid water, i.e., sea ice, glaciers, ice sheets, etc.), the pedosphere (land surface and soil) and the biosphere (all living organisms), as well as their processes, the interactions and the exchange fluxes of energy and matter between them (Goosse et al., 2010; Siedler, et al., 2013) (Fig. 1.1). In addition, the climate system evolves over time under the influence of its own internal dynamics and external forcings, such as volcanic eruptions, solar variations and anthropogenic impacts (Le Treut et al., 2007). Therefore, the lithosphere, which comprises the solid Earth, which supplies minerals through processes such as volcanism and weathering, and the anthroposphere (i.e., human activities) are two additional components that also form part of the climate system (Siedler, et al., 2013) (Fig. 1.1).

The importance of climate is so basic that sometimes it is overlooked. If the climate were not more or less as it is, life and civilization on this planet would not have developed in the same ways (Huntington, 1922; Fagan, 2009). Climate affects human lives in many ways; for example, climate influences the type of clothing and housing that people have developed. In the modern world, with the great technological advances of the last century, one might think that climate no longer constitutes a force capable of changing the course of human history. However, this is an apparent illusion since we are as sensitive now as we have ever been to climate fluctuations and climate changes (Hartmann, 2015). Hence, the understanding of the past and present climate and the prediction of future climate scenarios are necessary for human development and the preservation of natural environments.

The surface climate of Earth is varied, ranging from the heat of the tropics to the cold of the polar regions and from the drought of a desert to the moisture of a rain forest. This variety is due to the differences in the distribution of energy on Earth. The global climate circulation determines the distribution of energy and water near the surface and consists primarily of the interactions between the atmosphere, the oceans and the land surface (Hartmann, 2015).

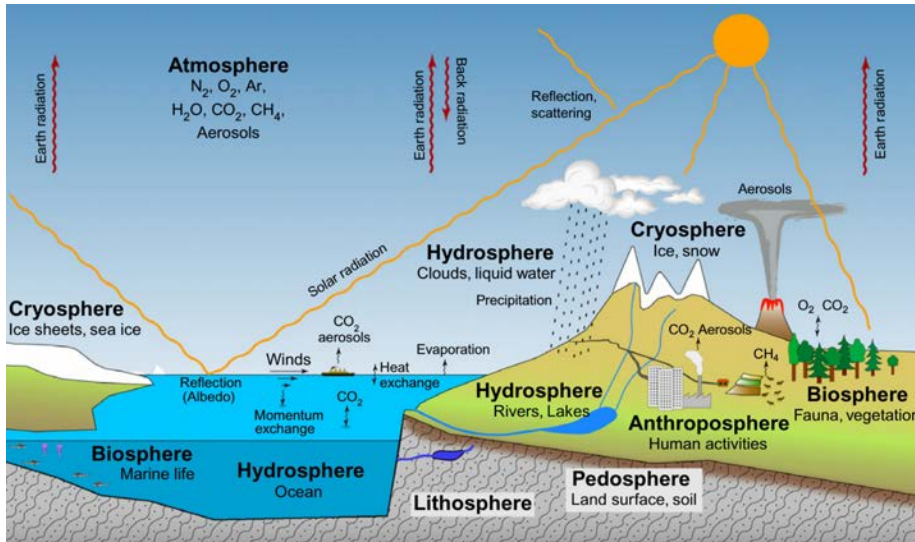


Figure 1.1. Schematic view of the components of the climate system, their processes, exchange fluxes of energy and matter, and interactions. The image was obtained from Siedler et al. (2013).

1.1 Global circulation model (GCM) of climate

The amount of solar radiation absorbed by the Earth decreases with latitude from the equator to the polar circles due to the tilt of the Earth's axis of rotation. To compensate for this surplus and deficit of radiation in the different regions of the globe, atmospheric and oceanic transport processes distribute the energy around the Earth. This transport is accomplished by both atmospheric (winds) and ocean (currents) circulations as the two systems are coupled (Goosse et al., 2010; Marshall and Plumb, 2013).

The peak of total poleward transport in each hemisphere occurs at 35° latitude, where atmospheric transport accounts for 78% of the total in the Northern Hemisphere and 92% in the Southern Hemisphere (Trenberth and Caron, 2001). This atmospheric transport of energy is accomplished in each hemisphere by three major convection cells known, from the equator to the poles, as Hadley, Ferrel, and Polar circulation cells (Fig. 1.2) (Marshall and Plumb, 2013).

In the Northern Hemisphere, the Hadley cell begins when the intense incoming solar radiation in the equatorial region creates hot moist rising air. The rising air cools,

moisture condenses and intense precipitation results, releasing latent heat. Once the air has risen, it flows northwards at high levels, cools, and eventually sinks at approximately 30°N (Trenberth and Stepaniak, 2003) (Fig. 1.2). The descending air is very dry, having lost most of its moisture in the tropics, and when it is warmed, its capacity to take up moisture is further increased. The resulting hot dry air causes intense evaporation at the Earth's surface, and this gives rise to the subtropical belt of deserts centred between 15° and 30°N (Wallace and Hobbs, 2006; Berner and Berner, 2012) (Fig. 1.2). After reaching the Earth's surface, the air flows southwards, picking up moisture as it flows over the oceans and being deflected to the right by the Coriolis force due to the rotation of the Earth. This surface flow is known as the northeast trade winds (Wallace and Hobbs, 2006; Berner and Berner, 2012) (Fig. 1.2). Upon reaching the equator, the dry northeast trades converge with the humid southeast trades from the Southern Hemisphere and form a band of increased convection, cloudiness, and heavy precipitation called the Intertropical Convergence Zone (ITCZ). Finally, the air rises at the equator to complete the low-latitude cycle forming the convection cell (Fig. 1.2) (Trenberth and Stepaniak, 2003).

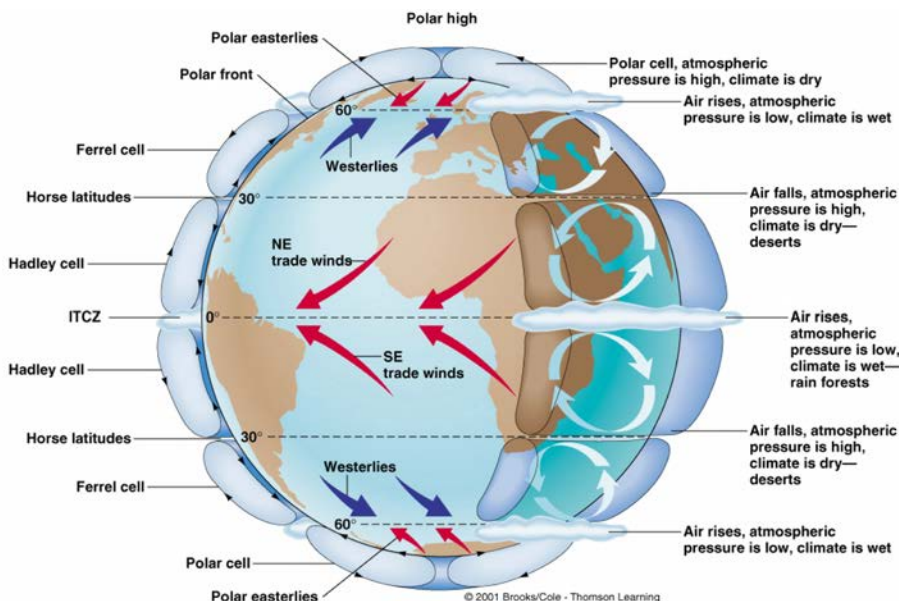


Figure 1.2. Schematic representation of the global atmospheric circulation on the Earth (© 2001 Brooks/Cole-Thomson Learning). The figure shows the three convection cells (Hadley, Ferrel and Polar cells) and air circulation patterns.

At approximately 30°N, additional air descends and then flows north along the surface rather than south. This is the beginning of the Ferrel cell (Trenberth and Stepaniak, 2003) (Fig. 1.2). The northward-flowing air is deflected to the right, forming the prevailing westerlies, which flow from southwest to northeast in the Northern Hemisphere. The westerlies continue until they encounter a cold mass of air moving south from the North Pole at approximately 50°N. This zone where the air masses meet is known as the polar front, and it is a region of unstable air, storm activity, and

abundant precipitation (Fig. 1.2). The polar jet stream (a very fast air stream) occurs at this boundary (Wallace and Hobbs, 2006; Berner and Berner, 2012). The warmer air from the south rises over the polar air and then turns south at high altitude to complete the Ferrel cell (Fig. 1.2). Meanwhile, the southward-flowing polar air (polar easterlies) is warmed by condensation at the polar front and by contact with the southern air. As a result, it too rises and then flows northward at high altitude to the pole, where it sinks, thus completing the polar cell (Wallace and Hobbs, 2006; Berner and Berner, 2012) (Fig. 1.2).

Global oceanic circulation also plays an essential role in distributing the heat around the Earth (Marshall and Plumb, 2013; Siedler, et al., 2013). The surface ocean circulation is mainly driven by the prevailing winds. At mid-latitudes, the atmospheric westerlies induce eastward currents in the ocean while the trade winds are responsible for westward currents in the tropics (Talley et al., 2011) (Fig. 1.3). Because of the presence of continental barriers, those currents form loops called subtropical gyres (i.e., the Pacific, Atlantic, and Indian Ocean gyres; Fig. 1.3). The surface currents in these gyres are intensified along the western boundaries of the oceans (the east coasts of continents), thereby inducing well-known strong currents, such as the Gulf Stream off the east coast of the USA and the Kuroshio of Japan (Marshall and Plumb, 2013; Siedler, et al., 2013) (Fig. 1.3). At higher latitudes in the Northern Hemisphere, the easterlies aid in the formation of weaker subpolar gyres. In the Southern Ocean, because of the absence of continental barriers, a current that connects all the ocean basins can be maintained: the Antarctic Circumpolar Current (Marshall and Plumb, 2013; Siedler, et al., 2013) (Fig. 1.3). All these currents run basically parallel to the surface winds. In contrast, the equatorial counter-currents, which are present at or just below the surface in all the ocean basins, run in the direction opposite to the trade winds (Talley et al., 2011; Talley, 2013; Siedler, et al., 2013) (Fig. 1.3).

The deep ocean circulation is driven by density variations arising from differences in temperature and salinity, giving rise to the term thermohaline circulation (Berner and Berner, 2012) (Fig. 1.4). At high latitudes, because of its low temperature and relatively high salinity, surface water can be dense enough to sink to great depths. This process, often referred to as deep oceanic convection, is only possible in a few places worldwide, and it occurs mainly in the North Atlantic and in the Southern Ocean (Siedler, et al., 2013; Marshall and Plumb, 2013) (Fig. 1.4). In the North Atlantic, the Labrador and Greenland-Norwegian Seas are the main sources of the North Atlantic Deep Water (NADW), which flows southward along the western boundary of the Atlantic towards the Southern Ocean (Fig. 1.4). There, it is transported to the other oceanic basins after some mixing with ambient water masses. This deep water then slowly upwells towards the surface in the other oceanic basins, forming upward fluxes in the North Indian and North Pacific Oceans (Talley et al., 2011; Talley, 2013) (Fig. 1.4). Although sinking occurs within very small regions, upwelling is broadly distributed throughout the ocean. The return flow to the sinking regions is achieved through surface and intermediate-depth circulation (Talley et al., 2011; Talley, 2013) (Fig. 1.4). In the Southern Ocean, Antarctic Bottom Water (AABW) is mainly produced in the Weddell and Ross Seas. This water mass is colder and denser than NADW and thus flows below it (Talley et al., 2011; Talley, 2013) (Fig. 1.4).

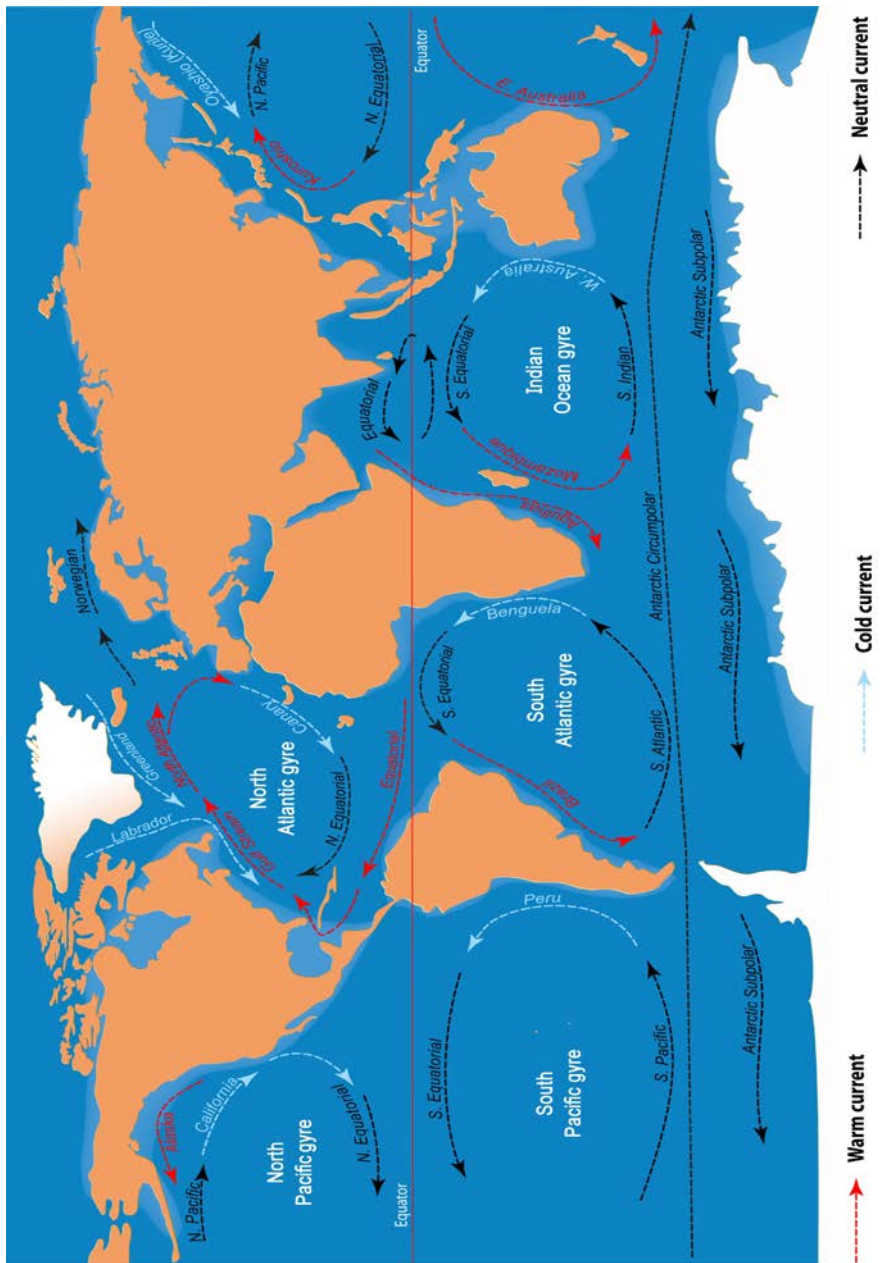


Figure 1.3. Illustration of the global surface oceanic currents and oceanic gyres (Talley et al., 2011).

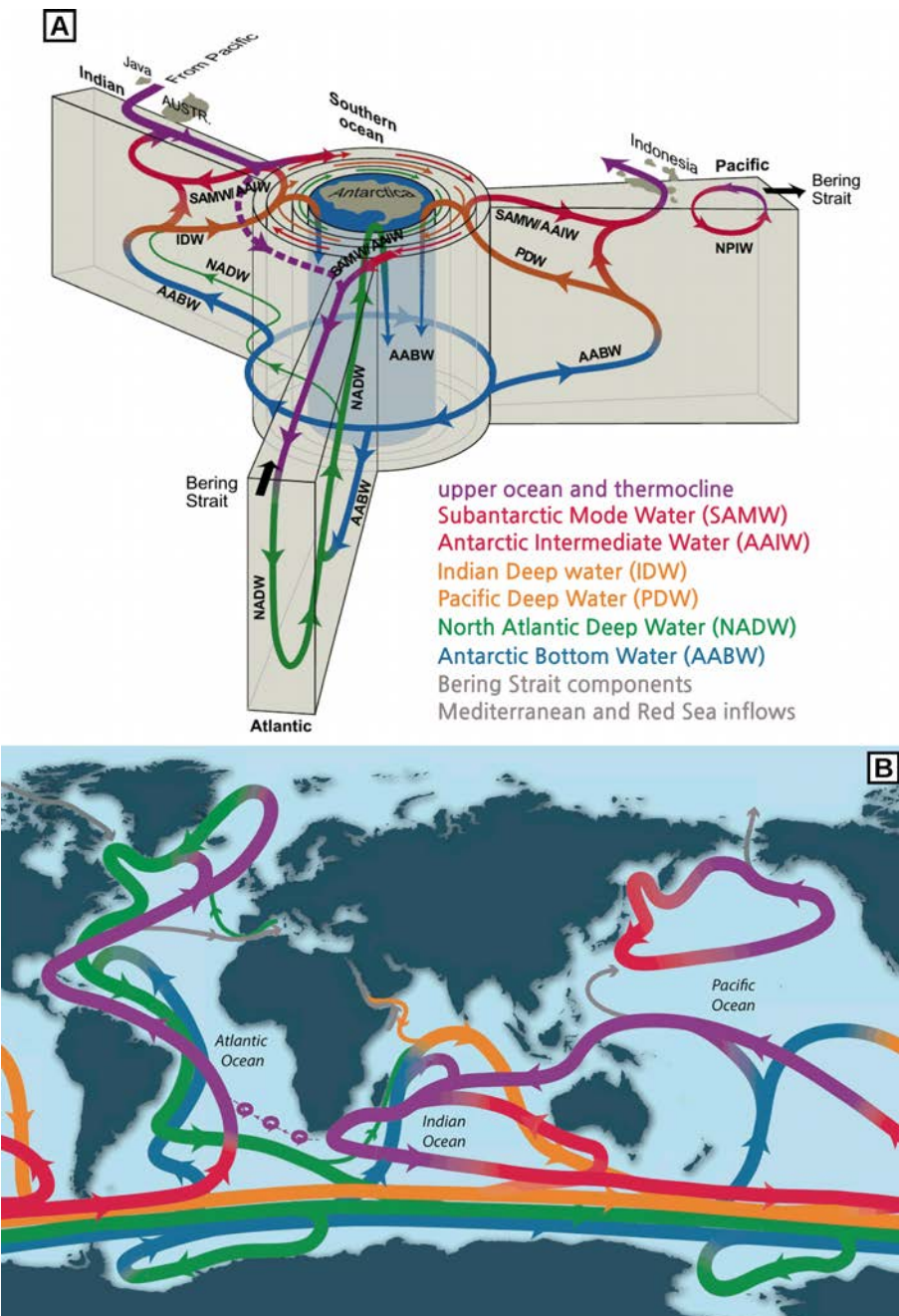


Figure 1.4. A) A three-dimensional schematic representation of the global oceanic circulation from a Southern Ocean perspective. The figure shows the connection between the three major ocean basins and the various water masses involved in this flow. B) A global map with a two-dimensional schematic representation of the deep oceanic circulation shown in A. Both figures have a common legend and were obtained from Talley (2013).

1.1.1 The Intertropical Convergence Zone (ITCZ)

The ITCZ is one of the most noticeable aspects of the global circulation. As stated before, the ITCZ is the zone of low pressure that encircles the Earth near the equator, from approximately 5° north to 5° south, where the trade winds converge and where the tropical rain forests are found (Figs. 1.2 and 1.5). The ITCZ moves north and south following the sun during the year and presents a seasonal pattern, moving north starting in February, reaching its most northern position in June/August at approximately 20°N (Hastenrath, 1991) and retreating southwards until December (Fig. 1.5B). This seasonal pattern in the atmospheric general circulation is responsible for the rainy season (monsoon) in many equatorial regions of South America, Africa and Indonesia. An important impact of these seasonal changes in the positions of the ITCZ and associated rainfall distributions is that they partially explain the annual cycle of African dust emissions (Engelstaedter et al., 2006).

On longer time scales, palaeorecords indicate that the migration of the ITCZ exhibits a seasonal-like pattern following differently warming between hemispheres (Haug et al., 2001; Wanner et al., 2008). For example, clear evidence for these ITCZ migrations come from the Cariaco basin records (Haug et al., 2001; Schneider et al., 2014). The ITCZ appeared to shift to a more southerly position as the Northern Hemisphere cooled from the Holocene thermal maximum at approximately 8 kyr BP to the beginning of the Little Ice Age at ca. 1450 (Haug et al., 2001). Simultaneously, the Afro-Asian summer monsoon rainfall systems were less active, and the corresponding continental areas were exposed to increasing aridity (Wanner and Brönnimann, 2012; Schneider et al., 2014). These ITCZ variations in the Holocene mostly arose because summer insolation in the Northern Hemisphere weakened with the precession of the Earth's perihelion from the Northern Hemisphere to the Southern Hemisphere summer (Schneider et al., 2014).

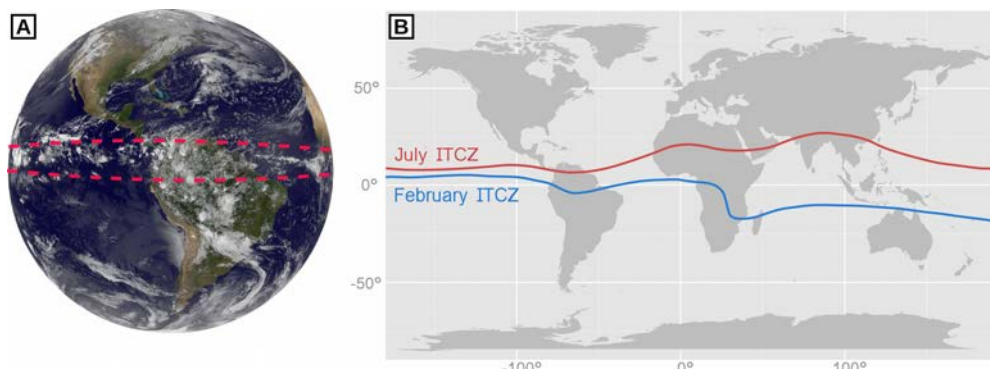


Figure 1.5. A) View of the Americas from space as captured by NOAA's GOES-East satellite on 22nd April, 2014, at 11:45 UTC/7:45 a.m. EDT (<http://www.nasa.gov>). Near the equator, GOES imagery shows a line (region between dashed red lines) of pop-up thunderstorms associated with the Intertropical Convergence Zone (ITCZ). B) Mean seasonal position of the ICTZ in July (boreal summer; red line) and February (austral summer; blue line) (<http://www.weatherwise.org>).

1.1.2 Climate modes

The Earth's atmosphere, oceans, cryosphere, and continental hydrology exchange mass and energy on all time scales. Consequently, global- or regional-scale climate variables, such as the temperature, rainfall, surface pressure, or wind speed, fluctuate more or less regularly and form climate patterns (e.g., Ropelewski and Halpert, 1987; Hurrell and van Loon, 1997; Viron et al., 2013). Many of these fluctuations are known as modes or oscillations with identifiable characteristics and specific regional effects, and their states are monitored by using scalar values of the so-called climate indices (e.g., Ropelewski and Jones, 1987; Hurrell, 1995; Thompson and Wallace, 2000; Enfield et al., 2001; Deser et al., 2010; Christensen et al., 2013). Some of the best-known oscillations extend over large areas of the globe, such as the El Niño–Southern Oscillation (ENSO), the North Atlantic Oscillation (NAO), the Pacific Decadal Oscillation (PDO), and the Madden-Julian Oscillation (MJO) (e.g., Philander 1983; Hurrell, 1995; Zhang et al., 1997; Zang, 2005). Furthermore, many teleconnections between these indices are also known to exist (e.g., Wallace and Gutzler, 1981; Alexander et al., 2002; Liu and Alexander, 2007), whereas certain oscillations are more localized and are thus associated with the climate of smaller regions.

Barnston and Livezey (1987) identified 12 different climate modes in the Northern Hemisphere. Currently, more than 25 different climate modes have been identified for recent decades at the global scale (Viron et al., 2013; Table. 1.1).

1.2 Climate variability in the North Atlantic region

The complexity of the climate variability in the North Atlantic region and its numerous impacts have attracted the attention of a wide variety of scientific communities, most of them focussed on disentangling the processes that control these variations (e.g., Marshall et al., 2001; Vicente-Serrano and Trigo, 2011). The climate variability in this region is highly influenced by a number of different climate modes that operate in the North Atlantic sector, such as the Atlantic Multidecadal Oscillation (AMO), the Arctic Oscillation (AO) and the NAO (e.g., Sutton and Hodson, 2005; Hurrell et al., 2006; Hurrell, 2015). These modes induce significant changes in surface air temperature, precipitation, ocean surface temperature and heat content, ocean currents, ocean current-related heat transport from the equator to the North Pole, and sea ice cover in the Arctic and sub-Arctic regions (Hurrell et al., 2006; Hurrell, 2015). Such climatic fluctuations affect agricultural harvests, water management, energy supply and demand, primary activities over land and sea, etc., thereby affecting the human welfare of millions of people and the equilibrium of numerous environmental cycles in the North Atlantic region (e.g., Hurrell et al., 2003; Vicente-Serrano and Trigo, 2011).

Over the middle and high latitudes of the Northern Hemisphere, the NAO is the most prominent and recurrent pattern of atmospheric variability and explains a large proportion of the climate variability of the North Atlantic Ocean, North America, the Arctic, Eurasia and the Mediterranean areas (Hurrell and van Loon, 1997; Jones et al., 2003; Hurrell et al., 2003).

Abbreviation	Index Name
AAO	Antarctic Oscillation
AMMSST	Atlantic Meridional Mode
AMO	Atlantic Multidecadal Oscillation
AO	Arctic Oscillation
ATLTRI	Atlantic Tripole SST EOF
BRAZILRAIN	Northeast Brazil Rainfall Anomaly
CAR	Caribbean SST
EA	East Atlantic
EOFPAC	Tropical Pacific SST EOF
EPO	East/North Pacific Oscillation
GMSST	Global Mean Land/Ocean Temperature
INDIAMON	Central Indian Precipitation
MJO	Madden-Julian Oscillation
NAO	North Atlantic Oscillation
NOI	Northern Oscillation
NP	North Pacific Pattern
PACWARM	Pacific Warmpool
PDO	Pacific Decadal Oscillation
PNA	Pacific North American
SAHELRAIN	Sahel Standardized Rainfall
SCAND	Scandinavian
SOI	Southern Oscillation
SWMONSOON	SW Monsoon Region Rainfall
TNA	Tropical Northern Atlantic
TSA	Tropical Southern Atlantic
WHWP	Western Hemisphere Warm pool
WP	Western Pacific Index

Table 1.1. List of the most relevant worldwide indices of large-scale modes of climate variability (Viron et al., 2013).

1.2.1 The North Atlantic Oscillation (NAO)

The NAO has been recognized for almost a century as the leading large-scale mode of climate variability in the North Atlantic region, especially during winter (Hurrell et al., 2003). The NAO is related to the redistribution of atmospheric mass between the Arctic and the subtropical Atlantic and is manifested as a meridional dipole anomaly in sea-level pressure (SLP), with the two centres of action located approximately over Iceland and the Azores (Hurrell, 1995; Hurrell et al., 2003) (Fig. 1.6A).

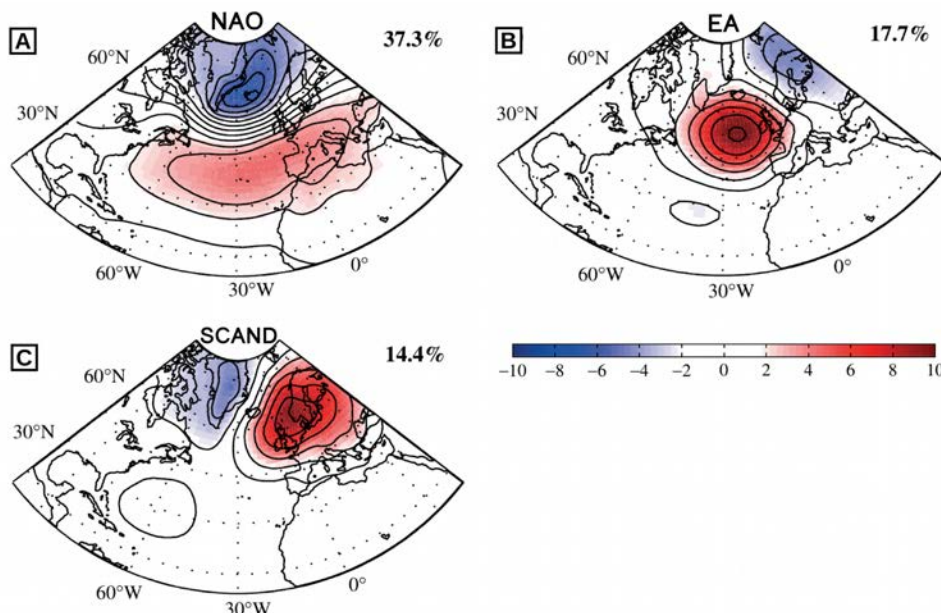


Figure 1.6. Spatial display of the first three eigenvectors of the gridded winter (December–February) monthly sea-level pressure anomalies (in mb) for the North Atlantic domain (1872–2009 AD) calculated using the 20CRv2 global dataset (Compo et al., 2011): A) North Atlantic Oscillation (NAO), B) East Atlantic pattern (EA) and C) Scandinavian pattern (SCAND). The empirical orthogonal function was performed using the cross-correlation matrix. Values adjacent to each map are the percentage of the total variance explained by each eigenvector. All the figures were obtained from Comas-Bru and McDermott (2014).

The first descriptions of phenomena associated with the NAO were given by Scandinavian seafarers, who realized that winter temperatures in Greenland and Scandinavia varied in opposite phase (Wanner et al., 2001; Stephenson et al., 2003; Luterbacher et al., 2008; Hense and Glowienka-Hense, 2010). The colonization of Greenland began in 985 AD, and until 1300 AD, ships frequently sailed between Scandinavia and Greenland, enabling a detailed understanding of the weather, climate, and remote links (Haine, 2008). The first published work dates back to the mid-18th century and focused on the description of thermal and hydrological conditions in Greenland versus Scandinavia (Egede, 1745; Crantz, 1765). In 1811 AD, Gronau

described the links between the weather conditions in Greenland and Germany (Gronau, 1811). Later studies confirmed these relationships by analysing early temperature time series (Dove, 1839). However, the concept of the NAO with two pressure centres appeared with the availability of pressure data over Europe and North Atlantic and with the development of correlation analysis in the late 19th and early 20th centuries (Teisserenc, 1883; Defant, 1924; Walker, 1924).

The NAO has two phases, and the swings from one phase to another produce large changes in the mean wind speed and direction over the Atlantic, in the heat and moisture transport between the Atlantic and the neighbouring continents, especially Europe, and in the intensity, paths and number of storms (Hurrell and van Loon 1997; Hurrell et al., 2003). The positive NAO phase (NAO^+) is characterized by an intensified Azores high and deeper Iceland low, which leads to a stronger meridional pressure gradient over the North Atlantic, a more zonal flow regime and stronger westerlies, in particular in the central and eastern North Atlantic, as well as a more northerly track of stronger storms crossing the Atlantic (Fig. 1.7A). Consequently, NAO^+ is associated with warmer and wetter conditions over Northern and Central Europe as a result of the succession of low-pressure centres embedded in the northwesterly flow and with dry conditions over southern Europe (Fig. 1.7A). The effects on the ocean of the NAO^+ involve a tripole pattern in the sea surface temperatures (SSTs), with negative SST anomalies from the Greenland and Irminger Seas to Newfoundland, positive SST anomalies in the central North Atlantic and negative SST anomalies further south along the western coast of Africa (Pinto and Raible, 2012) (Fig. 1.7A). During a negative NAO (NAO^-) phase, the Azores high is weaker and the Iceland low is shallower. This atmospheric circulation pattern leads to a reduced meridional pressure gradient and produces weaker westerlies over the North Atlantic and Western Europe and a more southerly track of storms crossing the Atlantic (Fig. 1.7B). Over Southern Europe, the NAO^- leads to unsteady weather conditions that are typically wetter than normal, while over Northern Europe, dryer and colder conditions are found, usually associated with a blocking (stationary high) situation extending from Urals/Eastern Europe to Western/Central Europe. Such a blocking high may remain in place for several weeks, leading to stable weather conditions over Central Europe (Pinto and Raible, 2012) (Fig. 1.7B). The SST anomalies during NAO^- are opposite in sign to those during NAO^+ (Fig. 1.7).

The NAO has also been related to the frequency of atmospheric blocking episodes in the North Atlantic region. An atmospheric blocking is a large-scale mid-latitude phenomenon often associated with a split in the zonal jet as well as with persistent quasi-stationary synoptic-scale high-pressure systems (e.g., Diao et al., 2006). This phenomenon causes large-scale circulation anomalies and exerts a strong impact upon the weather patterns (Sillmann and Croci-Maspoli, 2009; Sillmann et al., 2011; Pfahl and Wernli, 2012). Thus, the NAO^+ leads to a ‘cold ocean/warm land’ pattern (Fig. 1.7A), which is unfavourable for the development and persistence of blocking events, whereas the NAO^- phase leads to a ‘warm ocean/cold land’ pattern (Fig. 1.7B), which promotes the formation and persistence of blocking events (Shabbar et al., 2001; Barriopedro et al., 2006). Furthermore, these blocking events have also been related to variations in the zonal position of the NAO; thus, the frequency of Euro-Atlantic

blocking events is distributed along the northwest-southeast (southwest-northeast) direction for NAO⁺ (NAO⁻). One blocking action centre over south Europe is observed during NAO⁺ while two blocking action centres in Greenland and European continent are observed during NAO⁻ (Yao and Luo, 2014) (Fig. 1.7). Over longer periods, these blocking events have also been associated with solar irradiance variations. The development of frequent and persistent atmospheric blocking events in the eastern North Atlantic is promoted when low solar irradiance conditions predominate (e.g., Moffa-Sánchez et al., 2014).

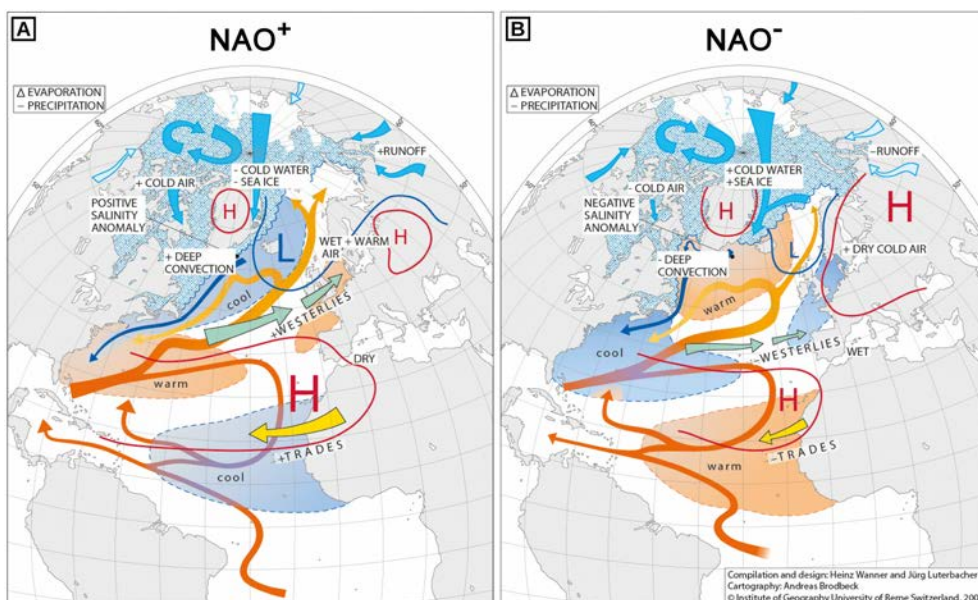


Figure 1.7. A schematic overview of the two phases of the NAO: A) the positive phase (NAO⁺) and B) the negative phase (NAO⁻). Shading indicates SSTs (bordered by dashed contours) and sea-ice extent. Arrows show the flow systems in the ocean (light red and blue), atmosphere (green and yellow arrows represent the westerly and trade winds, respectively) and rivers. Solid blue and red contours indicate SLPs (H=high, L=Low), and white rectangles describe either characteristic climate conditions or important processes. Modified from Wanner et al. (2001).

The measure for the temporal state of the NAO, i.e., the variability in the strength of the SLP gradient, is traditionally expressed as the North Atlantic Oscillation index (NAO_i). The first index of the NAO was constructed by Walker and Bliss (1932) using a linear combination of surface pressure and temperature measurements from weather stations on both sides of the Atlantic basin. However, and since there is no unique way to define the spatial structure of the NAO, there is no universally accepted index to assess the temporal evolution of this mode (Hurrell et al., 2003). Most modern indices of NAO are derived either from 1) the simple difference in SLP anomalies between various northern and southern locations or 2) the Principal Component (PC) time series of the leading Empirical Orthogonal Function (EOF) of regional gridded SLP data. The first indices were usually based on instrumental records from individual stations near

the NAO centres of action, such as the indices that Hurrell et al. (1995) and Jones et al. (1997) obtained from SLP data from Stykkisholmur (Iceland) and Lisbon (Portugal) and from Stykkisholmur (Iceland) and Gibraltar (UK), respectively. Furthermore, the indices are also sometimes obtained from gridded SLP analyses (e.g., Portis et al., 2001; Luterbacher et al., 2002). The major advantage of most of these indices is their extension back to the mid-19th century or earlier (Jones et al., 2003). Nevertheless, the disadvantage of these station-based indices is that, on one hand, they can only adequately capture NAO variability for parts of the year because they are fixed in space and the NAO centres of action vary spatially through the annual cycle, and, on the other hand, they contain noisy signals from small-scale meteorological phenomena not related to the NAO that affect individual station pressures. The second indices (Wang et al., 2012; Moore et al., 2013; Comas-Bru and McDermott, 2014), based on the PC time series, are more optimal representations of the full NAO spatial pattern as they are based on gridded SLP data; however, they can only be computed for the 20th century due to the lack of reliable gridded instrumental data further back in time (Hurrell et al., 2003).

These definitions led to slightly different NAO indices and also to different characteristic spatial patterns. However, the different NAO indices are strongly correlated ($r = 0.71\text{--}0.97$; Leckebusch et al., 2008) with each other on interannual and longer time scales, although the choice of the southern station makes some difference. In contrast, the specific location of the northern node (among stations in Iceland) is not critical since the temporal variability over this region is much greater than the spatial variability (Jones et al., 2003).

The NAO, as stated previously, is typically a winter mode, although it also varies on shorter time scales, such as the daily scale (Pinto et al., 2009; Blessing et al., 2005), and its index is usually determined for each month of the year (e.g., Barnston and Livezey, 1987; Jones et al., 1997; Comas-Bru and McDermott, 2014). Nonetheless, the effects of the NAO are not restricted to winter, and several recent studies have characterized the dynamics of the summer NAO (e.g., Folland et al. 2009) and its corresponding impact on European climate (e.g., Chronis et al. 2011; Bladé et al. 2012). The variability in the NAO has also been investigated and reconstructed (see section 1.4.3 for further details) for longer time scales, such as decadal and centennial time scales, mostly to assess its potential long-term predictability. It seems that the NAO does not vary on any preferred time scale (Hurrell et al., 2003). Nevertheless, there are periods in which NAO patterns persist over consecutive years or decades. For instance, Hurrell (1995) provided evidence that the NAO has shifted phase over the last 130 years (Figure 1.8): the NAO shifted from a predominantly more negative phase before 1910 AD to a more positive phase in the 1920s, followed by a negative trend enduring until the late 1960s. Afterwards, a strong positive trend developed and persisted until the mid-1990s. In the past 15 years (1995–2010), a negative trend in the NAO indices has been observed (Cattiaux et al., 2010; Jung et al., 2011). Conversely, the winter index has shown a clear positive trend during the last four years (Figure 1.8).

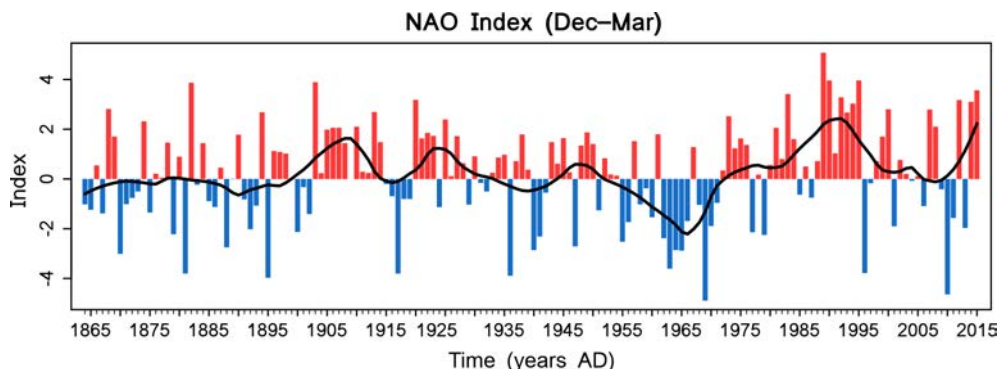


Figure 1.8. Winter (December to March) station-based NAO index (Hurrell, 1995) for the period 1846–2015 AD (updated data from <https://climatedataguide.ucar.edu/climate-data/hurrell-north-atlantic-oscillation-nao-index>). The red and blue bars represent unfiltered data from year to year; the black line represents the smoothed data obtained after applying the Loess function and a span degree of 0.15 to illustrate the low-frequency behaviour.

The low-frequency NAO variability (decadal and longer) and its importance for the winter atmospheric circulation over the North Atlantic and Europe have motivated the assessment of the possible underlying physical mechanisms behind them (e.g., Wanner et al., 2001; Marshall et al., 2001; Hurrell et al., 2003). In fact, the origin of the low-frequency variability has led to debate in the scientific community during the last decades. Several authors suggested that external parameters, such as volcanoes (Marshall et al., 2001; Fischer et al., 2007), solar activity (Spangehl et al., 2010; Schindell, 2001) or stratospheric–tropospheric coupling (Perlitz et al., 2000; Scaife et al., 2005), are the major drivers of the low-frequency variability, while other authors suggested that internal variability in the atmosphere, i.e., wave–wave interaction, is the leading factor (James and James, 1989; Franzke et al., 2000; Feldstein, 2000; Woollings et al., 2008). In addition, other factors such as the coupling between the ocean and the atmosphere (Bjerknes, 1964; Lau, 1997; Wanner et al., 2001), feedback processes associated with the oceanic Atlantic Meridional Overturning Circulation (AMOC), the branch of the thermohaline circulation in the Atlantic Ocean (Timmermann et al., 1998) (Figs. 1.4 and 1.7) and links to tropical SSTs, either over the Indian Ocean (Hoerling et al., 2001) or the Pacific Ocean (Trenberth et al., 1998; Müller, 2008), may also be of great importance for the decadal and longer time scales of NAO variability.

Another main aspect of NAO is its importance and evolution in future climate scenarios. The relevance of NAO in future climate changes mostly depends on the region, although there is high confidence that the NAO index will increase in response to anthropogenic forcing (Visbeck et al., 2001; Christensen et al., 2013). For example, by mid-21st century, the anthropogenic warming signal in North America will very likely be large compared to natural variability, such as that stemming from the NAO (Christensen et al., 2013). In Europe, the model simulations show that NAO changes contribute to the uncertainty of predictions in the near-term projections, whereas NAO trends do not account for a large fraction of the long-term future changes in mean temperature or precipitation (Stephenson et al., 2006; Kjellström et al., 2013). In the Arctic region, the NAO is assigned high relevance in temperature and precipitation

variability (Christensen et al., 2013).

Therefore, the marked importance of NAO in many different climatic aspects that affect large areas of the Northern Hemisphere and their ascribed impacts have led to many of the studies referred to in this section. However, a number of interesting questions and aspects about this phenomenon remain unanswered or unexplored, including the climatic processes that govern NAO variability, how the phenomenon has varied in the past or will vary in the future, and whether it is at all predictable (Hurrell et al., 2003).

1.2.2 Other climate modes in the North Atlantic: the East Atlantic (EA), Scandinavian (SCAND) and Atlantic Multidecadal Oscillation (AMO)

The NAO exerts a major influence on the climate of the North Atlantic region; however, there are other large-scale modes that may also contribute significantly to the climate variability of the North Atlantic sector (Fig. 1.6).

The East Atlantic (EA) mode is the second mode of climate variability in this region (Fig. 1.6B). The EA was first described by Wallace and Gutzler (1981) as anomalously high 500 mb height anomalies over the subtropical North Atlantic and Eastern Europe when it is in positive mode. This atmospheric pattern is structurally similar to the NAO and consists of a north-south dipole of anomalous SLP centres spanning the North Atlantic from east to west (Barnston and Livezey, 1987) (Fig. 1.6B). As a climate mode, its temporal variability is measured using an index, the EA index (EAI) (Fig. 1.9). Moore and Renfrew (2012) derived the EAI in 1870 AD based on SLP data from Valentia Island (Ireland), although this index has also been defined in the literature as the second leading EOF of regional gridded SLP (Moore et al., 2013). The EA is also more prominent during winter (Barnston and Livezey, 1987) and may have a role in positioning the primary North Atlantic storm track (Seierstad et al., 2007; Woollings et al., 2010). Its two phases are currently associated with variations in temperatures and precipitation in Scandinavia, Europe and North America (e.g., Rodríguez-Puebla et al., 1998; Krichak and Alpert, 2005; Comas-Bru and McDermott, 2014). This mode has also exhibited very strong multidecadal variability during recent decades.

The Scandinavian pattern (SCAND) is the third leading mode of winter SLP variability in the North Atlantic region. The SCAND was originally identified by Barnston and Livezey (1987) through an orthogonally rotated principal component analysis applied to monthly-mean 700 mb height anomalies over the extratropical Northern Hemisphere, and they referred to this climate mode as Eurasian Type 1 (EU1). The SCAND has a primary centre of action around the Scandinavian Peninsula, with two other centres of action with the opposite sign, one over Western Europe and the other over eastern Russia–western Mongolia (Fig. 1.6C). The SCAND index (SCANDi) defined by Barnston and Livezey (1987) has been updated by the Climate Prediction Center of the United States National Oceanic and Atmospheric Administration (NOAA) (Fig. 1.9). Its positive phase is characterized by prominent anticyclonic anomalies near

the Scandinavian Peninsula that give rise in winter to below-normal temperatures across central Russia and western Europe, above-normal precipitation across southern Europe, and dry conditions over the Scandinavian region. Additionally, this mode also appears to influence the East Asian climate (Bueh and Nakamura, 2007).

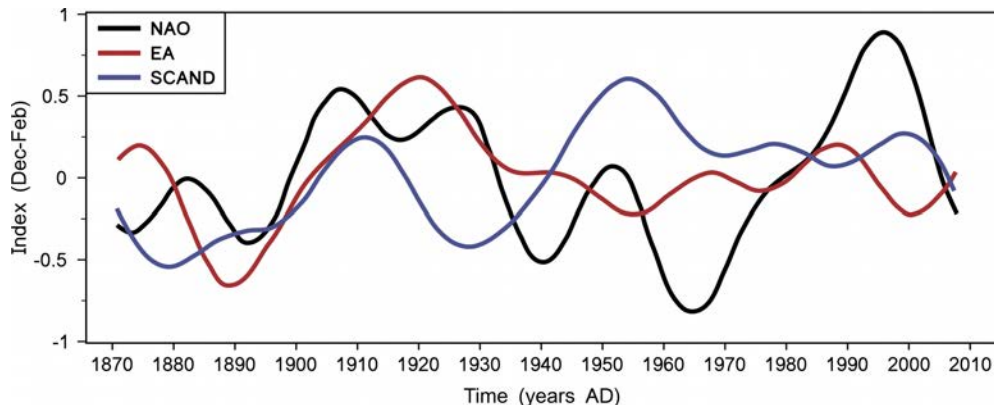


Figure 1.9. Time series of the winter mean (December to February) indices of the NAO (black curve), EA (red curve), and SCAND (blue curve) for the period 1871–2008 AD. The indices are derived from the principal components of the EOF decomposition of the monthly mean winter (December to February) SLP field from the 20CR reanalysis dataset. A low-pass filter with a cut-off of 21 years was used. Modified from Moore et al. (2013).

Hence, in addition to the NAO, these two last climate modes also modulate the climate variability over the Atlantic region and influence the geographical position and strength of the two centres of action of the NAO dipole, modifying the NAO-climate relationship in the European North Atlantic sector (Comas-Bru et al., 2014). The EA and SCAND were described almost three decades ago, but studies focusing on this subject have emerged in the last few years. Moore et al. (2011) proposed for the first time that the phase of the EA plays a role in modulating the location and strength of the NAO dipole. This work was expanded and completed by Moore and Renfrew (2012). Subsequently, Moore et al. (2013) investigated the effects of both the EA and SCAND modes on the variability of the NAO centres of action by selecting winters characterized by different combinations of the NAO–EA and NAO–SCAND phases. These authors described the movement of the NAO structure along a northeast-southwest axis depending on the state of the EA and a clockwise/anticlockwise movement associated with the state of the SCAND. More recently, Comas-Bru and McDermott (2014), following the approach of Moore et al. (2013), also found important modulating influences of the EA and the SCAND on the geographical positions of the NAO dipole. When the NAO and the EA are of the same sign, the NAO centres of action migrate northeastwards, whereas during phases of opposite sign, they move towards the southwest. When the NAO and the SCAND show the same sign, the centres of action of the first climate mode move anticlockwise, while when their phases are of opposite sign, they follow a clockwise rotation (Fig. 1.10). However, the most relevant contribution of these authors is that they have demonstrated for the first time that much of the multidecadal climate variability during the twentieth century in the North

Atlantic–European sector can be linked to specific combinations of NAOi–EAi and NAOi–SCANDi signs (Comas-Bru and McDermott, 2014) (Fig. 1.11). Another important contribution of this study is that these excursions of the NAO dipole modulated by EA and SCAND can result in spatial and temporal non-stationarity of the NAO-climate relationship. This situation could have important implications for reconstructions of the NAOi in the past using climate-sensitive proxies (e.g., tree rings, speleothems, lake sediments, and corals) as some regions may exhibit temporal non-stationarities in the proxy-NAOi relationship, which is a key factor of a reconstruction (Comas-Bru and McDermott, 2014; Comas-Bru et al., 2016).

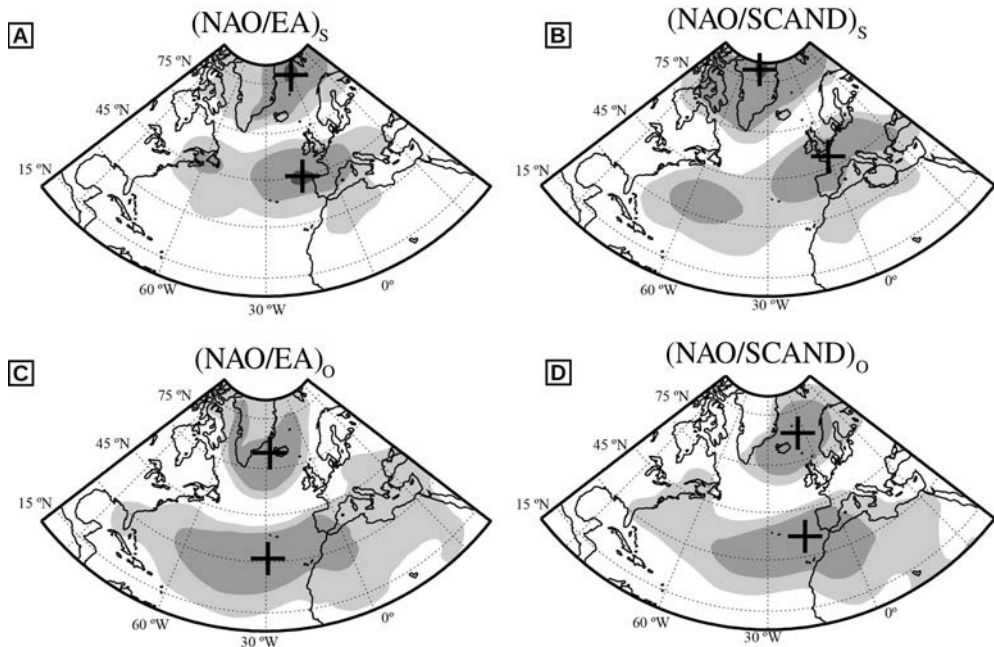


Figure 1.10. Teleconnectivity matrix of the winter (December to February) monthly sea-level pressure field in the North Atlantic region ($10\text{--}80^\circ\text{N}$, $100^\circ\text{W}\text{--}40^\circ\text{E}$) for the period 1872–2009 AD for different linear combinations of NAO–EA (left) and NAO–SCAND (right). In A) and B), both patterns exhibit the same sign, i.e., $(\text{NAO–EA})_S$ and $(\text{NAO–SCAND})_S$, whereas in C) and D), they exhibit opposite signs, i.e., $(\text{NAO–EA})_O$ and $(\text{NAO–SCAND})_O$. Light, medium and dark grey shadings represent areas with correlations of 0.5, 0.6 and 0.7, respectively. Black crosses indicate the location of the grid cells with the highest correlation. This figure was obtained from Comas-Bru and McDermott (2014).

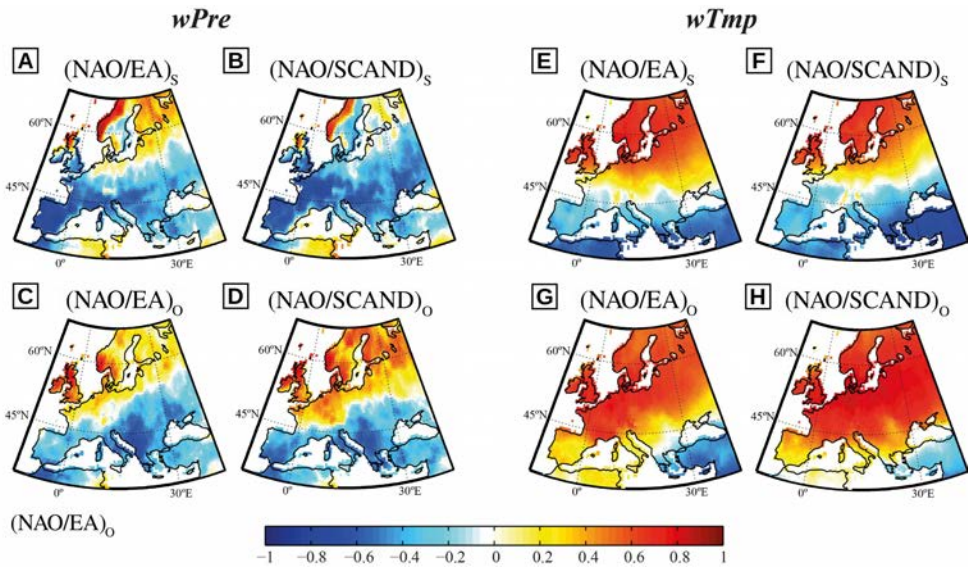


Figure 1.11. Correlation distribution maps that show the spatial coherence of the NAO–climate relationship with the CRU-TS3.1 dataset and our EOF-based indices for different combinations of signs: A) and E) (NAO–EA)_S, n = 57; C) and G) (NAO–EA)_O, n = 51; B) and F) (NAO–SCAND)_S, n = 56; D) and H) (NAO–SCAND)_O, n = 52. This figure was obtained from Comas-Bru and McDermott (2014).

In contrast, the Atlantic Multidecadal Oscillation (AMO) has been identified as a coherent pattern of low-frequency oscillations (65–80 yr cycle) of North Atlantic SSTs. Early studies only identified the multidecadal SST variations (e.g., Kushnir, 1994; Schlesinger and Ramankutty, 1994). Nevertheless, since the work of Kerr (2000), the pattern has been commonly referred to as the AMO. Although this is still a point of controversy (Clement et al., 2015), the AMO is generally suggested to be induced by Atlantic thermohaline circulation variations and associated ocean heat transport fluctuations (e.g., Folland et al., 1986; Gray et al., 1997; Delworth and Mann, 2000; Knight et al., 2005; McCarthy et al., 2015).

Indices of the AMO have traditionally been based on average annual SST anomalies in the North Atlantic region (Kaplan, 1998), whereas the modern AMO index is obtained after removing any linear trend in order to account for the influence of the recent global warming. Therefore, this revised index is defined by subtracting the global mean SST anomalies from the North Atlantic SST anomalies (Fig. 1.12) (Trenberth and Shea, 2006; Parker et al., 2007). However, because the instrumental SST records only span ca. 150 years, it remains a matter of debate whether the observed SST variability merely reflects a transient feature on a ‘red noise’ background or a truly oscillatory phenomenon (Delworth and Mann, 2000; Knudsen et al., 2011).

Several studies have linked climate changes to AMO variability, but the coupling between the AMO and the precipitation anomalies is spatially complex. The AMO drives climate and precipitation patterns over North America (Enfield et al., 2001; Sutton and Hodson, 2005; Hu and Feng, 2008), droughts in the Sahel region of Africa

(Folland, 1986), variability in Northeast Brazilian rainfall (Folland, 2001), and tropical hurricane frequency and intensity (Goldenberg, 2001). The positive AMO phase is associated with a pattern of horseshoe-shaped SST anomalies in the North Atlantic with pronounced warming in the tropical and parts of the eastern subtropical North Atlantic, an anomalously cool area off the US East Coast, and warm anomalies surrounding the southern tip of Greenland. The negative AMO phase is associated with the opposite conditions (Fig. 1.12) (Bjerknes, 1964; Kushnir, 1994). Cool AMO phases occurred in the 1900s – 1920s and 1960s – 1980s, while a warm phase occurred in the 1930s – 1950s and since the beginning of the mid-1990s (Fig. 1.12)

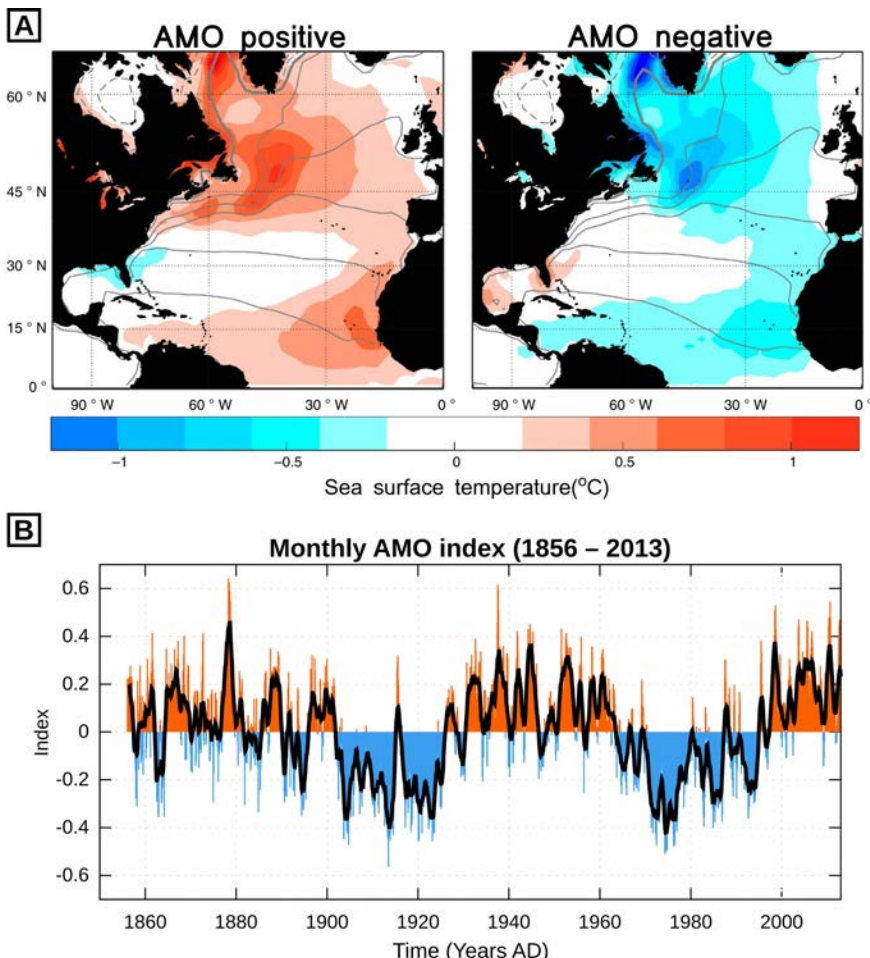


Figure 1.12. A) Composite maps of the SST field showing the spatial pattern of the AMO index for the period 1940–2011 AD. The thick grey contour line denotes 0 °C, whereas thin (dashed) lines denote positive (negative) SST at intervals of 5 °C (Yamamoto and Palter, 2016). B) AMO index computed as the linearly detrended North Atlantic SST anomalies for the period 1856–2013 AD. The data were obtained from <http://www.esrl.noaa.gov/psd/data/timeseries/AMO/>.

1.3 The climate variability in the Iberian Peninsula

1.3.1 Regional climate

The precipitation and temperature regimes in the Iberian Peninsula (IP) are characterized by spatial and temporal variability. Both regimes exhibit a strong seasonal and interannual variability, and east–west and north–south gradients due to the distribution of orography and the Atlantic origin of many synoptic disturbances (Serrano et al., 1999). Annual precipitation values over the IP range from ca. 300 mm yr⁻¹ in the southeastern coastal semidesert regions (Romero et al., 1998; Rodriguez-Puebla et al., 1998) to more than ca. 1200 mm yr⁻¹ in the northwestern provinces (Rodriguez-Puebla et al., 1998; Esteban-Parra et al., 2003), whereas the annual mean temperatures range from ca. 17 °C in southern Iberia to ca. 11 °C in northern Iberia (Brunet et al., 2001, 2007; Rodríguez-Puebla et al., 2001; Esteban-Parra et al., 2003) (Fig. 1.13). The spatial and seasonal variability of the climatic variables can be partly explained by the global circulation (e.g., seasonal movements of the Azores high-pressure system) and the regional geography (e.g., latitude, orography, and oceanic and continental influences) (Trigo and Paulotikof, 2001). However, the interannual variability, i.e., the large range of values for precipitation and temperature observed from year to year, is mainly controlled by the main large-scale atmospheric circulation modes and related blocking conditions that affect the IP (von Storch et al., 1993; Rodríguez-Puebla et al., 1998; Trigo et al. 2004; Sousa et al. 2015).

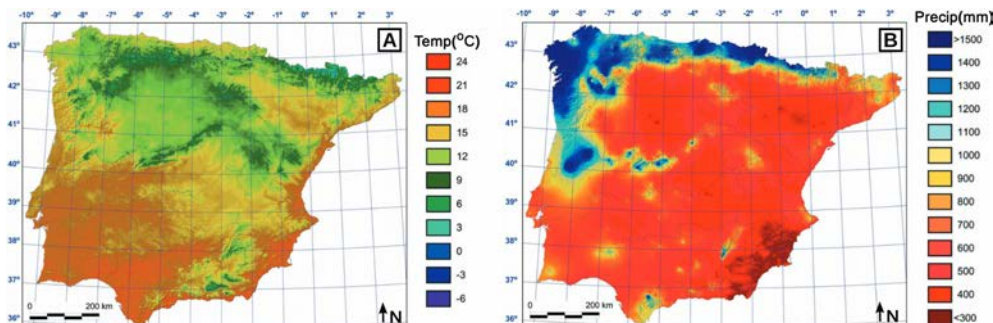


Figure 1.13. Maps of mean annual A) temperature (°C) and B) precipitation (mm) for the Iberian Peninsula obtained from Ninyerola et al. (2005).

1.3.2 Influence of the main climate modes on the present-day climate of the Iberian Peninsula

Most of the climatic variability over the IP can be explained in terms of relatively few large-scale atmospheric modes that mainly operate in the North Atlantic-European sector and, to a lesser extent, in the Mediterranean region (El Kenawy et al., 2012). The NAO is the most prominent mode, especially in winter (Jerez and Trigo, 2013). The effects of the winter NAO on the IP climate are more evident in the precipitation records than in the air temperature measurements (Castro-Díez et al. 2002; Trigo et al.,

2002; Comas-Bru and McDermott, 2014). These effects are also observed in the mountainous regions of Spain, such as the Central Range and the Pyrenees. In these regions, the winter NAO primarily causes deviations between wet and dry climatic conditions rather than between cold and warm conditions (López-Moreno et al. 2011; Durán et al. 2014). Other modes may have received less attention, although their impacts have also been reported. In particular, the EA and the SCAND modes have demonstrated their influence on the Iberian climate (Paredes et al., 2006; Trigo et al., 2008; Martín et al., 2010; Ramos et al., 2010; Hernández et al 2015). The EA governs winter and summer temperatures, whereas SCAND impacts on Iberian climate are more variable and display a less clear pattern, although it shows the most significant relationships with precipitation during winter and with temperatures during summer (Comas-Bru and McDermott, 2014; Hernández et al., 2015) (Fig. 1.14).

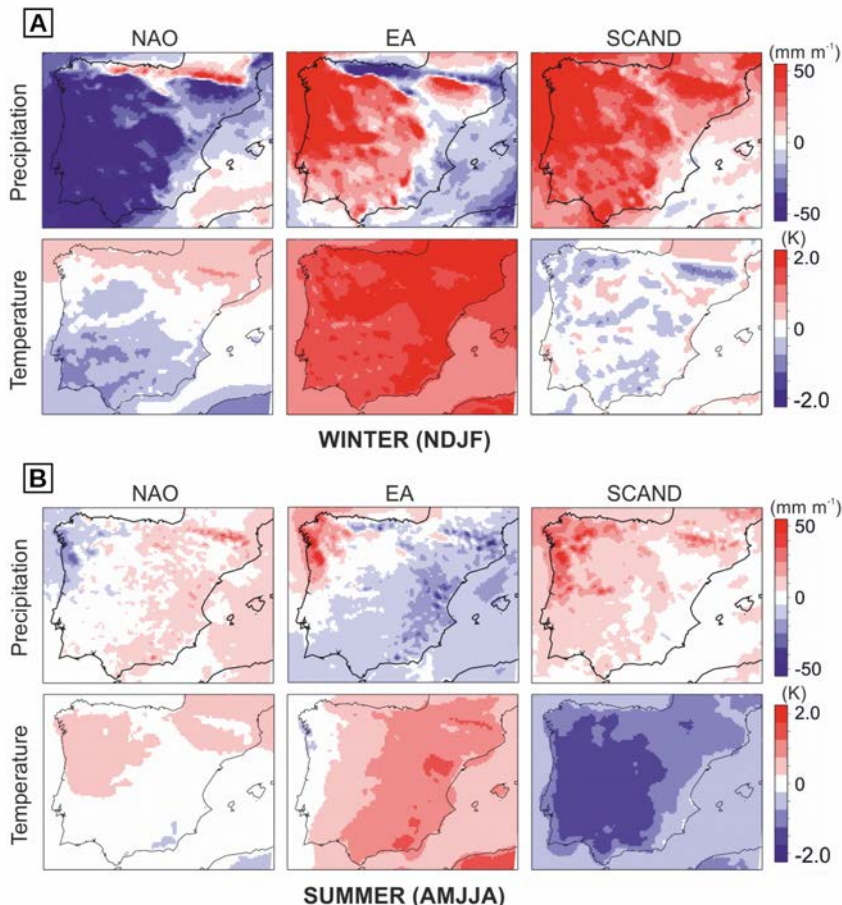


Figure 1.14. Composites showing the impact of the NAO (1st column), EA (2nd column) and SCAND modes (3rd column) on the mean precipitation (1st row) and temperature (2nd row) for A) winter (November to February average, NDJF) and B) summer (April to August average, AMJJA). Units are as follows: mm month^{-1} for precipitation and K for temperature. The time period was 1959–2007 AD. Data source: MM5 simulation. The image was modified from Hernández et al. (2015).

1.3.3 African dust episodes in the Iberian Peninsula

North Africa is widely regarded as the Earth's largest source of dust (e.g., Prospero et al., 2002; Washington et al., 2003; Ginoux et al., 2004, 2012). The amount of dust emitted annually from this region is estimated to be approximately 1400 Tg yr^{-1} , which represents 65% of the global dust emissions (Ginoux et al., 2004). This airborne plume of dust from arid and semi-arid regions, such as the Sahara and the Sahel, is transported yearly over the Atlantic Ocean, the Caribbean, Mediterranean sea and Europe (Prospero et al., 1981; Coudé -Gaussien, 1982).

Annual westward Atlantic transport occurs under the influence of trade winds and presents a marked seasonality modulated by the migration of the ITCZ (Prospero et al., 1981; Pye, 1987; Torres-Padrón et al., 2002; Engelstaedter et al., 2006). In the boreal winter, sources located in the southern Sahara and the Sahel ($< 20^\circ \text{ N}$) are especially active and are linked to dry northeasterly trade winds that prompt dust export across the North African tropical coast ($< 15^\circ \text{ N}$) (Engelstaedter and Washington, 2007; Menut et al., 2009; Marticorena et al., 2010; Fig. 1.15). During the boreal summer the northeasterly trade winds and the ITCZ shift northward, enhancing emissions from Saharan sources and increasing dust export at subtropical latitudes ($20\text{--}30^\circ \text{ N}$). Concurrently the northward shift in the monsoon rain band to the southern Sahel tends to decrease Sahelian dust emissions (Engelstaedter and Washington, 2007; Knippertz and Todd, 2010; Ashpole and Washington, 2013) (Fig. 1.15).

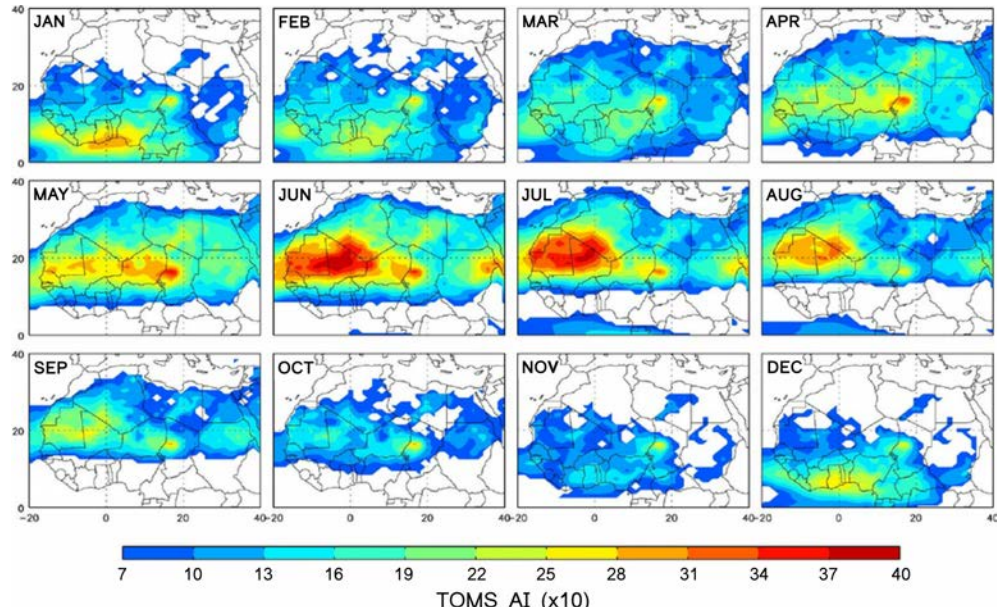


Figure 1.15. Monthly mean data from the Total Ozone Mapping Spectrometer absorbing Aerosol Index (TOMS AI) ($\times 10$) for the period 1980–1992 AD (Engelstaedter et al., 2006). These satellite data show the marked seasonality in dust emissions from the North African region.

The annual northwards dust transport leads to the occurrence of dust episodes over the Mediterranean and the IP (Fig. 1.16). This transport towards higher latitudes is related to cyclonic activity inside and around the Mediterranean basin (Alpert and Ziv, 1989; Bergametti et al., 1989) and is driven by more complex wind fields than in the case of the Atlantic transport. The wind trajectories depend on the relative position of both high- and low-pressure systems over the Atlantic Ocean and the Mediterranean Sea and on the westerly wind regime over Europe (Coudé-Gaussen et al., 1982; Bergametti et al., 1989; Moulin et al., 1997; Rodríguez et al., 2001). Such meridional transport occurs when the westerly regime is weak, disrupted or displaced northward, and this type of transport is more frequent during the summer (Coudé-Gaussen et al., 1982; Guerzoni et al., 1997; Rodríguez et al., 2001; Torres-Padrón et al., 2002; Ginoux et al., 2004). Three main atmospheric configurations (Fig. 1.17) favour the transport of dust from North Africa towards the Mediterranean and the IP (Coudé-Gaussen, 1982; Coudé-Gaussen et al., 1987; Bergametti et al., 1989; Rodríguez et al., 2001): 1) a SW–NE transport towards the northern part of the Mediterranean occurs mostly in winter when a large depression system develops between the Canary Islands and the IP (Fig. 1.17A); 2) between seasons, a SE–NW transport is initiated by the simultaneous occurrence of a strong central European anticyclone and a depression off Portugal (Fig. 1.17B); and 3) summer dust transport mainly results from the westwards shift in the North African anticyclone associated with the remoteness of the Azores high (Fig. 1.17C), which provides a SW–NE depression trench along the African coast towards the IP and the western part of the Mediterranean (Coudé-Gaussen, 1982; Rodríguez et al., 2001; Bout-Roumazeilles et al., 2007).



Figure 1.16. A) Natural-colour image of dust sweeping over the Iberian Peninsula acquired by the Moderate Resolution Imaging Spectroradiometer (MODIS) on NASA's Aqua satellite at 2 p.m. local time (14:00 UTC) on 21st February, 2016 (<http://earthobservatory.nasa.gov/IOTD/view.php?id=87566&src=eo4-iota>). B) African dust plume detected by the Ozone Monitoring Profile Suite (OMPS) on the Suomi NPP satellite. The image also shows the OMPS Aerosol Index over VIIRS RGB (<http://ozoneaq.gsfc.nasa.gov/omps/blog/2016/02/saharan-dust-over-spain>).

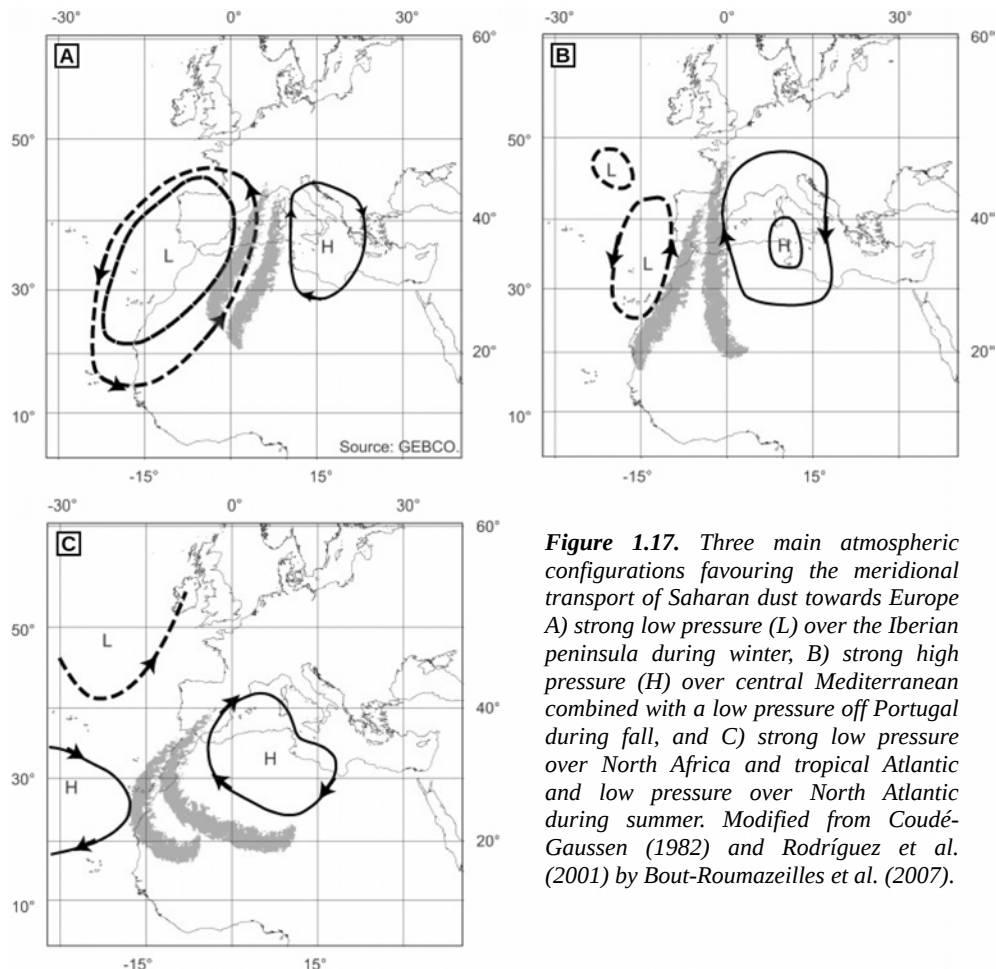


Figure 1.17. Three main atmospheric configurations favouring the meridional transport of Saharan dust towards Europe A) strong low pressure (L) over the Iberian peninsula during winter, B) strong high pressure (H) over central Mediterranean combined with a low pressure off Portugal during fall, and C) strong low pressure over North Africa and tropical Atlantic and low pressure over North Atlantic during summer. Modified from Coudé-Gaussen (1982) and Rodríguez et al. (2001) by Bout-Roumazeilles et al. (2007).

In addition, interannual and multiannual variations in North Africa dust emissions have been extensively related to variability in atmospheric modes, such as the NAO and the ENSO (e.g., Prospero and Nees, 1986; Moulin et al., 1997; Chiapello and Moulin, 2002; Rodríguez et al., 2015). As stated previously, the meridional transport of African dust implies weak, disrupted and/or displaced northward westerlies. Such synoptic situations are very similar to the positive phase of the NAO (Hurrell, 1995). During NAO⁺ years, precipitation is most likely to be lower over the Mediterranean and large areas of North Africa, favouring the intensity of both dust uptake and meridional transport, whereas during NAO⁻ years, the opposite conditions prevail (Moulin et al., 1997).

1.4 Climate reconstructions

The climate on Earth varies on all time scales, from years to millions of years. Different mechanisms and factors, some external to the climate system (e.g., solar activity, Earth orbital parameters, volcanism) and others internal to the system (e.g., Earth system feedbacks), are responsible for this climate variability (Jones and Mann, 2004; Mann, 2007).

Any improvements in our ability to predict future climate changes are most likely to result from a better understanding of the workings of the climate system as a whole (Bradley, 2015). Such improvements in understanding can, in turn, be achieved through a better ability to document and explain, from a fundamental dynamical point of view, observed past variations (Bradley and Eddy, 1991; Alverson et al., 1999, 2003; Bradley, 2008). Instrumental meteorological records only span a tiny fraction ($< 10^{-7}$) of the Earth's climatic history (Bradley, 2015), and they can only assess large-scale (hemispheric and global) climate changes over roughly the past 100 – 150 years, while more regionally limited data (e.g., in Europe) are available as far back as the early 18th century (Jones and Mann, 2004). Consequently, these records cannot provide a totally adequate perspective on climatic variations and the evolution of the present-day climate (Bradley, 2015). Thus, improved knowledge of past large-scale climate changes are essential to place recent, potentially anomalous, climate changes in a longer-term context, such as multicentury time scales (Jones and Mann, 2004).

Evidence of past climatic conditions is commonly preserved in natural archives, such as ice, marine and lacustrine sediments, cave deposits (speleothems), tree rings and corals, among others. Therefore, the records retrieved from these natural archives provide materials that contain climatic signals and are thus indirect indicators, or proxies, of past climatic conditions (Juggins and Birks, 2012; Bradley, 2015) (Table 1.2). Ice cores provide a unique record for reconstructing precipitation, temperature, atmospheric composition, atmospheric circulation, wind speed, the occurrence of explosive volcanic eruptions, and even past variations in solar activity, principally via the study of stable isotopes (e.g., Dansgaard et al., 1993; Grootes and Stuiver, 1997; Jouzel et al., 2007). The remains of calcareous and siliceous organisms (e.g., diatoms and foraminifera) preserved in marine sediment records are an excellent tool with which to determine temperature and sea level variations and past atmospheric compositions (i.e., past CO₂ concentration levels) via oxygen isotopic compositions (e.g., Mix, 1987; Ravelo and Hillaire-Marcel, 2007), quantitative interpretations of species assemblages, spatial variations through time (e.g., Imbrie and Kipp, 1971; Molfino et al., 1982; Guiot and de Vernal, 2007), and Mg/Ca ratios (e.g., Rosenthal, 2007). Lacustrine records are one of the most widely used archives to conduct different palaeoclimate inferences due to the large number of proxies available, including lithostratigraphic proxies, such as varve thickness (e.g., Ojala and Alenius, 2005; Besonen et al., 2008; Ortega et al., 2015); geochemical proxies, such as chemical elements obtained by scanning X-ray fluorescence analysis (e.g., Bakke et al. 2010); organic geochemical biomarkers, such as lipids, which act as palaeothermometers (e.g., Tierney et al., 2008, 2010; Powers et al., 2010, 2011); physical proxies, such as sediment magnetic properties, optical properties, and stable isotope ratios (Yancheva et al., 2007); and extensively used biological proxies,

such as pollen, diatoms, chironomids, cladocerans, and chrysophytes (Birks, 2003), although these latter proxies commonly involve high costs in terms of time, sample collection and analyses (Juggins and Birks, 2012). The high temporal resolution of speleothems (i.e., yearly) provide records of rapid environmental changes in the form of stable isotopes of oxygen and carbon and are usually employed for reconstructing the temperature or precipitation history of a given site (e.g., Martín-Chivelet et al., 2011; Medina-Elizalde et al., 2010). Variations in tree-ring widths from one year to the next are also a high temporal resolution source of climatic information; thus, temperatures, droughts and even climate modes have been reconstructed using them (Cook et al., 2002, 2007; Büntgen et al., 2008; McGregor et al. 2010). Coral growth rates, isotopes, and trace elements in the coral structure provide information about temperature, rainfall, river runoff, ocean circulation, and modes of ocean-atmospheric circulation, such as ENSO or the Indian Ocean Dipole (e.g., Swart et al., 1996; Felis et al., 2000; Asami et al., 2005; Goodkin et al., 2012). Although many of these works are limited to the last few centuries or to short windows of time to reduce analytical costs, corals dating back to the last interglacial, or even earlier, are often found on raised marine terraces throughout the tropics, making it possible to reconstruct SSTs for much longer periods (e.g., Gagan et al., 1998).

Before the 1970s, many of the reconstructions were typically restricted to qualitative interpretations, and they were presented as 'acid', 'mildly basic', 'cool', 'temperate', 'moist', or 'dry' (Battarbee et al., 1986; Smol et al., 2012). Early palaeolimnological studies usually only considered academic questions, such as lake ontogeny, changes in lake productivity, processes and rates of lake infilling, the balance between internal (autochthonous) and external (allochthonous) organic sources, and the time and impact of catchment disturbances on lake development (e.g., Deevey 1955; Livingstone, 1957; Wright 1966; Pennington et al. 1972; Likens and Davis 1975; Oldfield, 1977; Likens 1985). However, the increasing realization of the major environmental problems facing society, such as the eutrophication of inland water bodies, atmospheric contamination by heavy metals and persistent organic pollutants in the late 1970s and early 1980s and global warming in the early 1990s, provoked disciplines such as palaeoecology, palaeoclimatology, and palaeoceanography to quickly respond to the challenges posed by these environmental problems and transformed their fields from primarily descriptive and academic disciplines into quantitative and strongly applied disciplines (Birks, 2012).

Geologic	Terrestrial	Biological
Marine (ocean sediment cores)	Speleothems (stable isotope and trace element composition)	Tree rings (width, density, and stable isotope composition)
Biogenic sediments (planktonic and benthic fossils)	Glacial deposits and features of glacial erosion	Pollen (type, relative abundance, and/or absolute concentration)
Oxygen isotopic composition	Lacustrine sediments and erosional features (shorelines)	Diatoms, ostracods, and other biota in lake sediments (assemblages, abundance, and geochemistry, including organic biomarkers)
Faunal and floral abundance	Aeolian deposits (mainly loess; also relict sand dunes)	Insects (assemblage characteristics)
Trace elements (e.g., Mg/Ca)	Periglacial features	Corals (geochemistry, fluorescence, and growth rates)
Organic biomarkers (e.g., alkenones and Tex86)	Shorelines (eustatic and glacioeustatic features)	Plant macrofossils (age and distribution)
Inorganic sediments	Pedological features (relict soils)	Modern population distribution (refugia and relict populations of plants and animals)
Terrestrial (Aeolian) dust and ice-rafted debris; grain size	Glaciological (ice cores)	
Elemental ratios (e.g., Pa/Th)	Geochemistry (major ions; isotopes of oxygen and hydrogen) Gas composition and air pressure in air bubbles Microparticle concentration and elemental composition	

Table 1.2. Different sources of proxy data used in environmental and/or climatic reconstructions (Bradley, 2015).

1.4.1 Quantitative reconstructions

The appearance of the concept of calibration, namely 'transfer functions', in the early 1970s revolutionised Quaternary palaeoecology. Imbrie and Kipp (1971) presented, for the first time, a procedure for the quantitative reconstruction of past environmental variables (i.e., SSTs) based on biostratigraphical fossil assemblages (i.e., planktonic foraminifer assemblages) involving so-called transfer functions. A transfer function is a mathematical equation for reconstructing past environmental conditions from the abundance of multiple species. Hence, this term refers not to a single numerical method but to a range of regression-based techniques. The equation is empirically derived from a training or calibration dataset of modern samples and associated environmental measurements. A mathematical representation of the transfer function concept can be written as follows:

$$Y_m = f(X_m) + \text{error} \quad (\text{Eq. 1.1})$$

where Y_m is a matrix of modern data responses (i.e., taxon abundances), X_m is a matrix of contemporary physico-chemical environmental 'predictors', and $f()$ is a set of ecological response functions (i.e., transfer functions).

Since the pioneering work of Imbrie and Kipp (1971), the general approach of quantitative palaeoenvironmental reconstruction has been adopted in many palaeodisciplines and multiple methods have been proposed that attempt to account for, either explicitly or implicitly, the particular numerical properties of different palaeorecords. In any case, a quantitative reconstruction usually involves three separate steps (Juggins and Birks, 2012): 1) the development of the modern training set, 2) the development of the numerical model to solve the mathematical equation that relates the palaeorecord data and the environment in the present, and 3) the application of the model to the fossil stratigraphic record and the evaluation of the resulting reconstruction. Each of these steps involves a number of decisions concerning training-set selection; data transformation and screening; choice of numerical method; model selection, testing, and evaluation; and assessment of the final reconstruction (Figure 1.18).

Different methods exist to conduct quantitative reconstructions, although most of them are applied to biostratigraphical proxies with different ecological or statistical bases (Figure 1.19). There is a major conceptual distinction between inverse and classical methodological approaches and between methods that assume a linear response of the proxy to a given environmental gradient and methods that assume a non-linear relationship (ter Braak, 1995; Birks, 1995, 2003; Guiot and de Vernal, 2007; Birks et al., 2010). The classical approaches estimate the response function $f()$ of Eq. 1.1 using a regression of Y_m on X_m (Birks, 2012). The regression can be linear, non-linear, or multivariate. An example of the classical method approach is the Gaussian logit regression and maximum-likelihood calibration (GLR-ML) (Figure 1.19). In contrast, inverse approaches estimate the inverse of $f()$ directly from the training set using an inverse regression of X_m on Y_m (Birks, 2012). The Weighted-Averaging regression (WA), Weighted-Averaging Partial Least Squares Regression (WA-PLS), Modern Analogue Technique (MAT), Principal Components Regression (PCR) or Artificial Neural Networks (ANN) are examples of inverse methods (Figure 1.19) (Juggins and Birks, 2012).

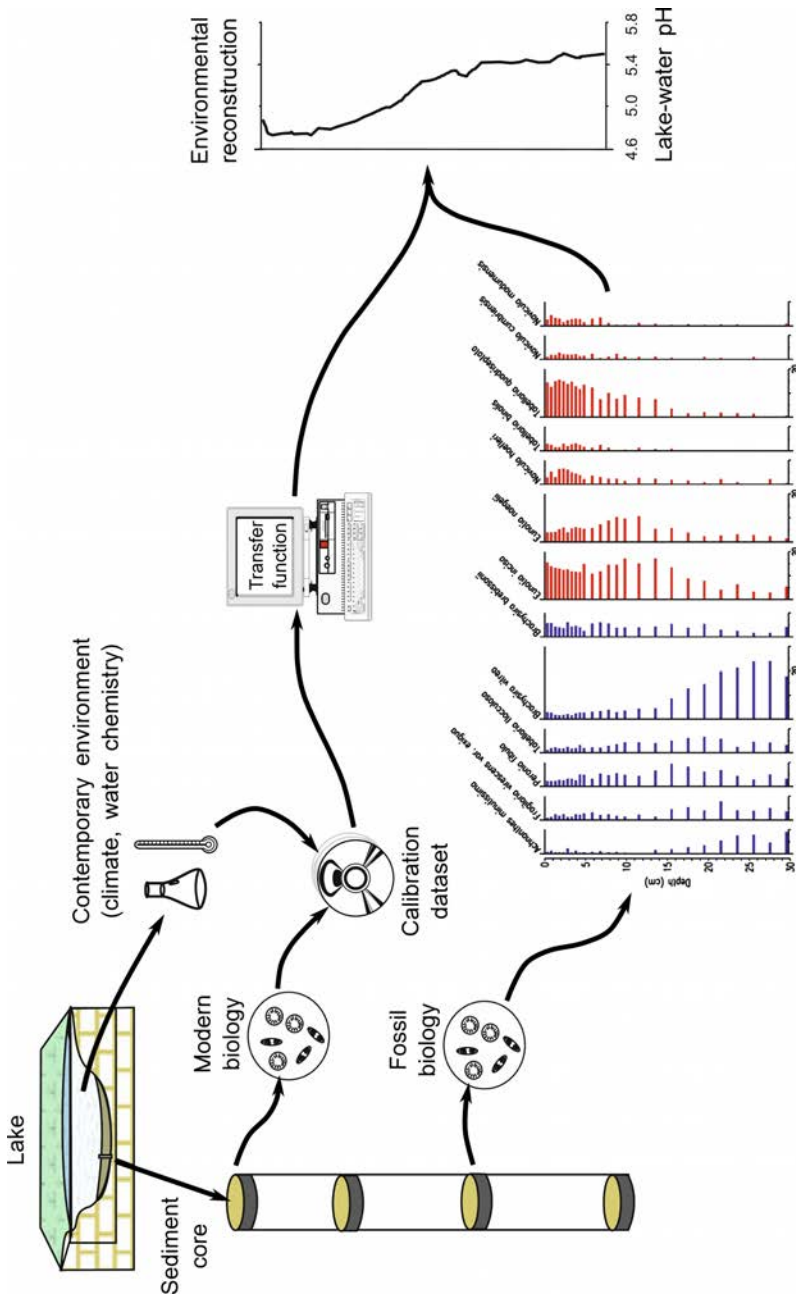


Figure 1.18. Schematic diagram showing the steps involved in a quantitative reconstruction from biostrigraphical palaeolimnological data using a modern training or calibration dataset.

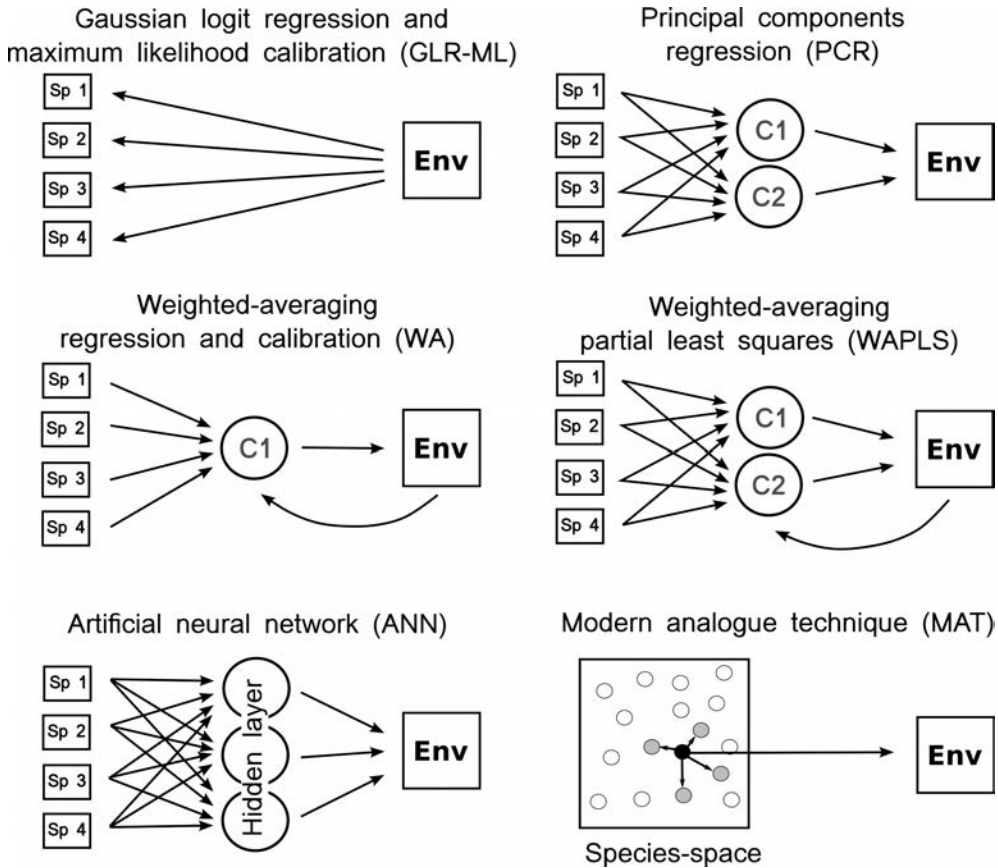


Figure 1.19. Conceptual diagram illustrating the different approaches to multivariate calibration using a biological proxy. Sp represents biological taxa in the modern training set and Env is the environmental variable of interest in the modern data. C represents components. The figure was obtained from Juggins and Birks (2012).

A basic requirement for a reconstruction model is that it should be statistically significant, accurate, precise, and reliable, and it should make sense from the ecological and palaeoecological points of view (Birks et al., 2010; Juggins and Birks, 2012). If a model is statistically significant, the obtained results are not likely to occur randomly and are likely attributable to a specific cause, such as climate. Statistical significance can be strong or weak and does not always indicate practical significance (Harris, 1998). Model accuracy and precision are measured by the prediction error, which is usually calculated as the root mean squared error (RMSE). Some form of cross-validation provides a more realistic estimate of the prediction error when the model is applied to new data (Juggins and Birks, 2012). Ideally, this would involve testing the model using an independent test dataset, a so-called external cross-validation (Birks, 2012). However, we rarely have the luxury of an additional test dataset – these samples are usually employed more profitably in the training set (Lotter et al., 1999). Instead, an internal cross-validation of the training set simulating the likely errors is used when the

model is applied to new data. There are three main types of internal cross-validation available: k-fold leave-out, leave-one-out, and bootstrapping (Juggins and Birks, 2012). In the k-fold leave-out method, the order of the samples is randomized and a fixed proportion (e.g., 20%) is left out of the training set (giving, in this case, a five-fold leave-out). The calibration function based on the remaining samples is then applied to the left-out samples, which act as the test set, and the squared errors accumulate to form the RMSE of the prediction (RMSEP). Note that the RMSEP is distinguished from the so-called apparent RMSE calculated solely from the training set. The leave-one-out method is a special case of k-fold leave-out in which each sample is left out to form a single sample test set (Manly, 1997). Larger training sets usually include some inherent replication; thus, as the training-set size increases, leave-one-out RMSEP becomes a less reliable estimate of true prediction errors (Næs et al., 2002). The k-fold leave-out method provides a more rigorous test but can be overly pessimistic because the training sets in each step are of a correspondingly smaller size (Webb, 2002). This problem is addressed in bootstrap cross-validation by selecting samples from the original training set (of size n) with replacement to give a new bootstrap training set also of size n (Stine, 1990; Mooney and Duval 1993; Manly 1997). Since samples are selected with replacement, some will be included more than once and, on average, approximately one third will remain unselected. These become the bootstrap test dataset. This procedure is repeated a large number of times (typically 1000) and the squared errors for the test samples accumulate across all bootstrap cycles to form the bootstrap RMSEP (Birks et al. 1990; Simpson and Birks, 2012).

In any case, there is no single ‘best’ or ‘optimal’ method that can be recommended: differences in training-set size, taxonomic diversity in biological proxies, and form and complexity of the proxy–environment relationship make some numerical techniques more useful than others for particular datasets. Model selection thus becomes a crucial step in any quantitative reconstruction (Xu et al., 2010). For instance, Juggins and Birks (2012) using diatom data and most of the methods show in Figure 1.19 illustrate the issues of model selection and reconstruction evaluation by reconstructing the recent acidification history of The Round Loch of Glenhead, a small soft-water lake in Galloway located in southwestern Scotland.

1.4.2 The Bayesian method

Bayesian statistics is based on Bayes’ theorem. This theorem was discovered by the Reverend Thomas Bayes but was published posthumously two years after his death, in 1763 AD. Laplace and other statisticians used this method in the 19th century, but it had largely fallen from favour by the early 20th century. However, by the middle of the 20th century, interest in Bayesian methods was renewed by different statisticians, such as De Finetti, Jeffreys, Savage, and Lindley. They developed a complete method of statistical inference based on Bayes’ theorem (Bolstad, 2007). Bayesian statistics belongs to the so-called ‘statistical learning’ methods because it learns from the data (Hastie et al., 2011), and it is considered to be an inverse method.

The mathematical equation of the theorem for multiple events is defined as follows:

$$P(B_i|A) = \frac{P(A|B_i) \cdot P(B_i)}{\sum_{j=1}^n P(A|B_j) \cdot P(B_j)} \quad (\text{Eq. 1.2})$$

where B_1, \dots, B_n are n unobservable events with disjoint pair of events, $B_i \cap B_j = \emptyset$ for $i=1, \dots, n$, $j=1, \dots, n$ and $i \neq j$. The equation comes from the definition of conditional probability (Bolstad, 2007). The marginal probability of event A is found by the law of total probability, and each of the joint probabilities is found from the multiplication rule (i.e., denominator of the Eq. 1.2). $P(B_i)$ is the prior probability of event B_i , $P(A|B_i)$ corresponds to the likelihood, and $P(B_i|A)$ is the posterior probability of event B_i .

Furthermore, the equation 1.2 can be simplified and is usually expressed in its proportional form as follows:

$$\text{posterior} \propto \text{prior} \cdot \text{likelihood}$$

The reconstruction methods previously cited in section 1.4.1 (Figure 1.19) have different statistical and ecological motivations but they have one thing in common: they are all so-called frequentist methods and make the assumption that the model parameters (e.g., WA optima and WA-PLS coefficients) are fixed and can be estimated from observations (the measured data) distributed randomly about the fitted values (Holden et al., 2008). Conversely, the Bayesian approach in past reconstructions does not rely on an explicit relationship model between proxy and environmental variables but assumes that the model is unknown and must be estimated from the measured data, which are fixed. Specifically, the Bayesian approach uses measured information to modify some prior belief about the environmental values (Robertson et al., 1999). This additional information is derived from a training set and expressed as a conditional probability density function, namely 'likelihood', which is combined with the prior probability density function to give a posterior density function using the Bayes' theorem (Eq. 1.2). Another advantage of the Bayesian approach is that observations under all conditions are not required, making it possible to reconstruct past situations without analogous proxies in the modern environment (Guiot and de Vernal, 2007).

Bayesian approaches have been applied to several aspects of palaeolimnology, such as the construction of age-depth models (e.g., Buck et al., 1999; Bronk Ramsey, 2007; Blaauw and Christen, 2005; Blaauw et al., 2007; Haslett and Parnell, 2008), although environmental reconstructions, particularly climate reconstructions, are the most popular. For instance, Toivonen et al. (2001) described a Bayesian model with a conditional probability density function based on a unimodal model. Vasko et al. (2000) and Korhola et al. (2002) extended this to include a more realistic multinomial Gaussian response model and applied it to chironomid-based temperature reconstructions. Haslett et al. (2006) further developed these ideas for more generalized modelling of pollen-climate response surfaces, and Holden et al. (2008) described a computationally efficient approach based on probability weighting of species response curves. Li et al. (2010) developed a Bayesian hierarchical model to reconstruct past temperatures that integrates

information from different sources, such as climate proxies with different temporal resolutions. More recently, Parnell et al. (2015) outlined a model (i.e., Bclim) and algorithm to describe the palaeoclimate and its volatility from pollen proxy data. Cahill et al. (2016) developed a Bayesian transfer function to reconstruct relative sea level using foraminifera data. As in the frequentist reconstruction methods, to the best of our knowledge, all of these Bayesian approaches used biological proxies to create the reconstructions.

Although the prediction errors for Bayesian methods are similar to those of conventional approaches, they have a major advantage in their coherent and explicit handling of uncertainty (Birks et al. 2010; Li et al. 2010). However, the lack of available software and the huge computational burden of most existing models (days to weeks for a single reconstruction) currently prevent more widespread use.

1.4.3 NAO reconstructions

The importance of the NAO on the climate variability of the North Atlantic region has promoted different initiatives in recent decades to reconstruct the NAOi at different time scales and temporal resolutions (e.g., Appenzeller et al., 1998; Glueck and Stockton, 2001; Luterbacher et al., 2002; Vinther et al., 2003a, b; Jones and Mann, 2004; Goodkin et al., 2008; Trouet et al., 2009; Küettel et al. 2010; Olsen et al., 2012; Ortega et al., 2015) (Fig. 1.20).

Different proxies can register different aspects of the temporal evolution of the NAO; thus, the NAOi reconstructions are either based on single proxy archives (e.g., ice cores) (Appenzeller et al., 1998), on only pressure-sensitive proxy data distributed across Europe (Casty et al., 2007; Küettel et al., 2010) or on multi-proxy data from different records (e.g., tree rings, speleothems, lake sediments, or documents) that are sensitive to temperature and/or precipitation variations (Luterbacher et al., 2002; Trouet et al., 2009; Ortega et al., 2015). In particular, a common lacustrine sedimentary proxy usually employed in these reconstructions is the varve thickness in varved sediments (e.g., Ortega et al., 2015), although non-varved lacustrine records (e.g., Olsen et al., 2012) and a wide range of other lacustrine proxies have been extensively used to conduct different climate reconstructions (Battarbee, 2000; Smol and Cumming, 2000; Fritz, 2008; Pla-Rabes, 2011). Therefore, non-varved lacustrine sediments and their associated proxies can also constitute a proper alternative when creating an NAOi reconstruction.

As a reconstruction, the NAOi is obtained by estimating an statistical relationship between the employed proxy and climate data or the NAOi during an overlapping instrumental period. Regression techniques are also one of the most extensively types of techniques used to conduct these reconstructions (e.g., Cook et al., 2002; Ortega et al., 2015), although a recent study employed a transfer function and Monte-Carlo-Markov-chain techniques to obtain a NAOi for the past ca. 5000 years (Olsen et al., 2012). NAO reconstructions generally show a good agreement with the instrumental NAOi until ca. 1850 (Fig. 1.20). Farther back in time, considerable discrepancies appear between the reconstructions (Pinto and Raible, 2012). Multiple

factors may be responsible for these disagreements, such as the use of different calibration periods, differences in the response of the proxies to the climate modes and/or the stationarity of the relationship assumed between the proxies and the NAO (Pinto and Raible, 2012; Comas-Bru et al., 2016). Furthermore, chronological uncertainties associated with the dating methods might also contribute to these temporal discrepancies. Therefore, the selection of a statistical method that presents a major advantage in its coherence and explicit handling of uncertainties, such as the Bayesian approach (Juggins and Birks, 2011), could contribute to improving this disagreement. Although Bayesian inference has been extensively used during the last decade for climate and environmental reconstructions using biological proxies (see previous section for further details), neither Bayesian inference nor non-biological proxies have yet been used to conduct a reconstruction of the NAO.

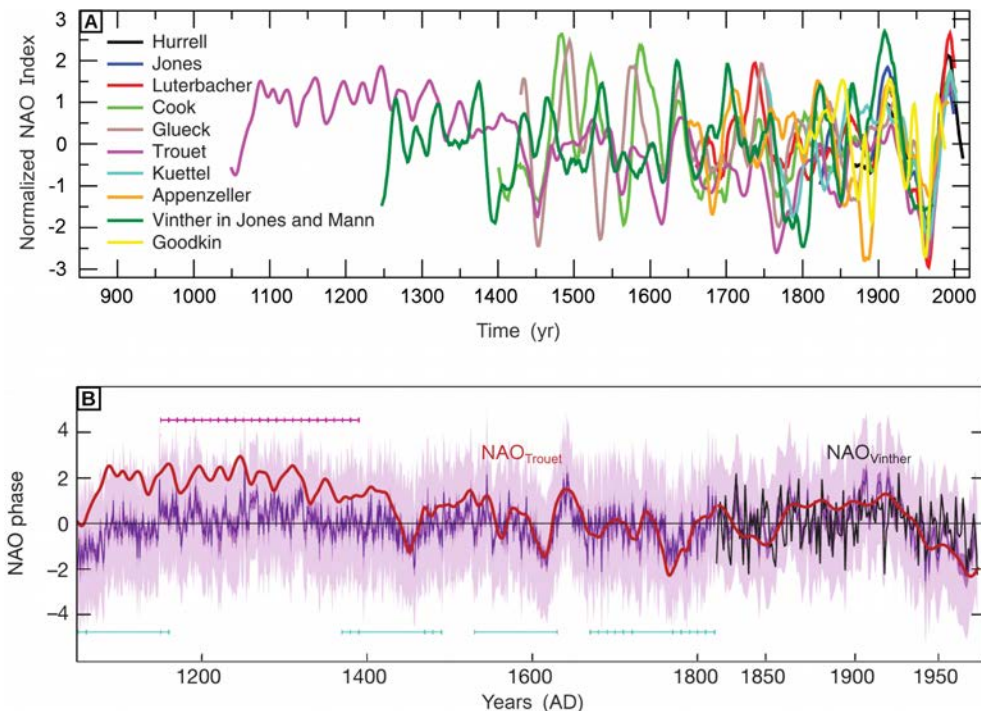


Figure 1.20. A) Low-frequency variability in different NAO reconstructions (Jones et al., 1997; Appenzeller et al., 1998; Glueck and Stockton, 2001; Cook et al., 2002; Luterbacher et al., 2002; Vinther et al., 2003a; Jones, 2004; Goodkin et al., 2008; Trouet et al., 2009; Küttel et al., 2010) for the past millennium and in observations from 1864 to 2009 AD (Hurrell, 1995). The figure was obtained from Pinto and Raible (2012). B) NAO Ensemble reconstruction for 'model-constrained' from Ortega et al. (2015). The intermediate and light purple envelopes represent the total ensemble spread and the regression uncertainties across the ensemble, respectively, whereas the dark purple line shows the ensemble mean. The black and red lines denote NAO_{Vinther} (Vinther et al., 2003b) and NAO_{Trouet} (Trouet et al., 2009), respectively. The horizontal magenta (or cyan) bars enclose centuries (marked by tick marks) with positive (or negative) mean NAO values that are significantly different (p -value < 0.05) than zero.

Another possible solution to reconcile the NAO reconstruction disagreements could be the use of an appropriate concept of the NAO when a reconstruction is attempted. The NAO in a strict sense must be reconstructed using large high temporal resolution multi-proxy datasets from different geographical places, which will provide a much better constrained NAO signal and, consequently, a more accurate NAOi reconstruction (e.g., Ortega et al., 2015). In contrast, a simpler approach, such as the use of one or several proxies from a given region or group of regions will provide the regional NAO effects instead of a more realistic NAO reconstruction (e.g., Trouet et al., 2009; Olsen et al. 2012). Consequently, these different possible concepts of NAO should be taken into account in the NAOi comparisons and in the use of these different reconstructions.

1.4.4 Reconstructions in the Iberian Peninsula

Numerous environmental reconstructions in the IP have been conducted using natural archives, such tree rings (e.g., Büntgen et al., 2008), historical documents (e.g., Benito et al., 2003b), peat bogs (e.g., Martínez-Cortizas et al., 1999), marine sediments (e.g., Nieto-Moreno et al., 2011) and speleothems (e.g., Martín-Chivelet et al., 2011) (Fig. 1.21), and at different temporal scales, from a centennial-resolution climate reconstruction covering the last 50,000 years carried out by Cacho et al. (1999) to annual-resolution climate reconstruction for the last 200 years developed by Campelo et al. (2009).

In spite of the large diversity of natural archives employed in these Iberian reconstructions, lacustrine sedimentary records are one of the most widely used to determine the environmental and climatic history of this region (Fig. 1.21). The most frequently studied lacustrine records are from low- and mid-elevation areas, such as the sedimentary records from Sanabria Lake (1000 m asl; Jambrina-Enríquez et al., 2014) and Enol Lake (1075 m asl; Moreno et al., 2011) in the northern IP; Arreo Lake (655 m asl; Corella et al., 2013), Estanya (670 m asl; Riera et al., 2004; Morellón et al. 2009, 2011) and Montcortès Lake (1027 m asl; Corella et al. 2011) in the Pre-Pyrenees; the Tablas de Daimiel wetland (616 m asl; Gil García et al., 2007) and Taravilla Lake (1100 m asl; Moreno et al., 2008) in the Central IP; and Zoñar Lake (300 m asl; Valero-Garcés et al., 2006; Martín-Puertas et al. 2008, 2010); in the southern IP (Fig. 1.21).

Moreover, climate reconstructions from the main Iberian mountain ranges have increased over the last decade, including reconstructions of the Pyrenees from Redon Lake (2240 m asl; Pla and Catalan, 2005; Pla-Rabes and Catalan, 2011), Marboré Lake (2500 m asl; Salabarnada, 2011) and Basa de la Mora Lake (1914 m asl; Morellón et al., 2012; Moreno et al., 2012; Pérez-Sanz et al., 2013) and the ranges of southern Spain (Sierra Nevada) from Laguna de Rio Seco (3020 m asl; Jiménez-Espejo et al., 2014) (Fig. 1.21). In addition, several environmental reconstructions in the Iberian Central Range (ICR) are based on palynological records from different peatlands (> 1700 m asl; López-Sáez et al., 2014) (Fig. 1.21). However, to the best of our knowledge, only two climate reconstructions have been conducted based on an alpine lake located in this

mountainous region (Cimera Lake, 2140 m asl) (Fig. 1.21), and they cover only the last several centuries (Granados and Toro, 2000; Agustí-Panareda and Thompson, 2002).

The last two millennia are the most reconstructed time interval, and climate reconstructions usually distinguish five main climatic periods: the Roman Period (RP; 650 BC – 500 AD), the Early Middle Ages (EMA; 500 – 900 AD), the Medieval Climate Anomaly (MCA; 900 - 1300 AD), the Little Ice Age (LIA; 1300 - 1850 AD); and the so-called Industrial Era (1850 – present). The studied records provide detailed information on the climatic evolution for specific time windows (e.g., MCA and LIA, Morellón et al., 2012; Moreno et al., 2012), whereas other periods (e.g., EMA and RP, Luterbacher et al., 2016) remain less studied. Furthermore, when comparing the environmental and climate information between the lowlands and highlands, it is clear that the spatial coverage of the latter must be improved.

The influence of the NAO on the IP has also been determined for these historical periods (e.g., Nieto-Moreno et al., 2011; Morellón et al., 2012; Moreno et al. 2012). These climate reconstructions commonly ascribe the warm and arid climate conditions of the MCA to the dominance of the positive phases of the NAO and the humid and cold conditions of the LIA to the dominance of the negative phases of the NAO (Trouet et al., 2009; Ortega et al., 2015). Nevertheless, the role of the other climate modes in the climatic evolution, as well as their interactions with the NAO, over the last millennia has not been well addressed yet.



Figure 1.21. Topographical map of the Iberian Peninsula showing the locations of different records used to conduct environmental reconstructions in the IP. The reader is referred to the figure caption of Fig. 6.4 for references. The record used in this study are underlined.

LAKES

The usual definition of lake is 'an enclosed body of standing water surrounded by land'. Nevertheless, given the great variety of bodies of standing waters, it is not surprising that all lake definitions must be a bit arbitrary (Cohen, 2003; O'Sullivan and Reynolds, 2008).

Lakes comprises a small fraction of the Earth's land surface, approximately 1%, and contain a tiny volume of the Earth's water, less than 0.02% of the hydrosphere's water (Talbot and Allen, 1996; Wetzel, 2001). They can be classified according to different features, such as basin origin (Wetzel, 2001), chemistry (Eugster and Hardie, 1978), mixing period (Lewis, 1983), temperature (Hutchinson and Löffler, 1956), trophic state (Hutchinson, 1969) or the formation of an ice-cover during the winter season, which is the traditional characteristic used to classify a lake as a high mountain or alpine lake (Toro and Granados, 2000).

Physical, chemical and biological lacustrine processes are of interest because they reflect the responses of these water bodies to external forcings, such as climate. In addition, these processes also act as intermediary filters between these external forcing and the palaeolimnological record (Cohen, 2003). For instance, lake-level oscillations are mainly attributed to the difference between water outputs and inputs, which are commonly controlled by climate (Imboden and Wüest, 1995). Lake-level variations can be recorded directly by ancient shoreline elevations or indirectly by salinity indicators and can be used to conduct climate reconstructions (e.g., Corella et al., 2013). The different chemical cycles associated with lakes are also a great focus of attention. For example, CO₂, which plays a key role in photosynthesis and in other processes in the lacustrine carbon cycle, is one of the most important drivers of climate change (Cole et al., 1994, 2007). Thus, variations in CO₂ concentrations will be reflected in lakes, and these effects can be used to study anthropic emissions and their ascribed impacts (Adrian et al., 2009). The biotas of lakes are the most complex components of these natural systems and involve numerous species (e.g., algae, vascular plants, sponges, annelids, crustaceans, insects and molluscs) and various interactions both between the species and with the external environment (Margalef, 1983). The responses of these freshwater organisms to abiotic factors, such as lake water temperature (Granados and Toro, 2000), dissolved oxygen (Dinsmore et al., 1999), pH (Battarbee, 1986), salinity (Bos et al., 1999), and nutrient availability (Leland and Berkas, 1998), have also been extensively used to reconstruct past environmental and climatic conditions and current global change effects.

The highest concentration of lakes is in the boreal and Arctic latitudes (45°–75°N), whereas the abundance of lakes is lower in southern latitudes, where the continental area is also lower (Fig. 1.22A) (Verpoorter et al., 2014). Other distinctive features of these water bodies are that their size distribution decreases dramatically with elevation and that only approximately 10% of lakes are located at elevations higher than 2000 m asl (Fig. 1.22B) (Verpoorter et al., 2014). Alpine lakes, or so-called mountain lakes, form part of this marginal freshwater bodies group. Nevertheless, although this meagre figure suggests alpine lakes play an apparently negligible role in the Earth system, they are particularly suitable ecosystems for studies on certain environmental and

ecological topics (Adrian et al., 2009; Catalan et al., 2013). For this reason, the scientific community has paid far more attention to them than their quantitative relevance would suggest.

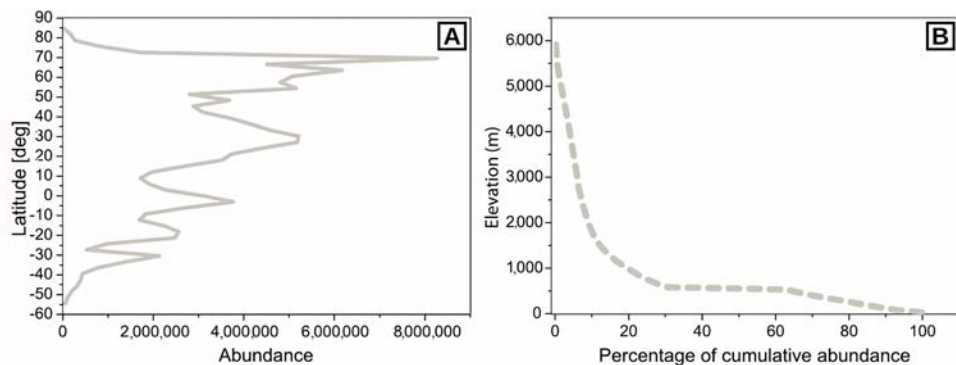


Figure 1.22. A) The latitudinal distribution of lake abundance (grey line) and B) the elevation distribution of lakes by cumulative percentage abundance (dashed grey line). Both data were compiled from a high-resolution satellite imagery database (Global Water Bodies database (GLOWABO)). Both images were modified from Verpoorter et al. (2014).

1.5 Alpine lakes

Alpine lakes are among the most similar ecosystems throughout the world because, as stated previously, they all experience ice cover (Catalan et al., 2006). These lakes are located in most of the large and high ranges around the world (e.g., the Alps, the Pyrenees, Himalayas, Rocky Mountains, Andes, Kilimanjaro), where the low permeability of crystalline bedrock favours their presence (Fig. 1.23). Most alpine lakes originated during the last glaciation due to the interaction of ice and hard bedrock; thus, they are generally young ecosystems (Catalan et al., 2006). Their particular location leads to distinct environmental conditions that define their limnological and biological features. Low rock weathering and limited soil development lead to highly diluted waters in terms of major salt components and nutrients (e.g., Toro et al., 2006). Consequently, lacustrine organisms face challenges, such as oligotrophy, in these extreme habitats. The formation and development of ice and snow covers for several months is the distinctive dynamical feature of these lake ecosystems (Fig. 1.23). This ice cover plays a key role in lake productivity through its influence on the growing season length and summer stratification as well as in the lake overturning strength and timing, which controls the internal lake nutrient cycle (Catalan et al., 2002; Pla-Rabes and Catalan, 2011).

Another common feature of alpine lakes is that they are usually small water bodies in which matter loading from the catchment is fundamental in determining the characteristics and biogeochemical cycles of the lake (Fig. 1.23). Alpine lake catchments are relatively small compared to lowland lakes and are usually poorly vegetated as a result of their positions close to or above the treeline. Consequently, atmospheric loading also tends to be significant in determining the compositional

characteristics of runoff and thus the lake water (Catalan et al., 2006; Adrian et al., 2009; Mladenov et al. 2011). Therefore, atmospheric inputs have a significant influence on the biogeochemistry of alpine lakes and can affect their water chemistry (Reche et al. 2009), which in turn affects their primary productivity (Psenner, 1999) and carbon pool (Psenner, 1999; Mladenov et al. 2011). One of these most important atmospheric loading factors in European alpine lakes is African dust events (e.g., Hervás et al., 2009; Mladenov et al., 2011). European alpine lakes are exposed to these aeolian inputs under certain climatic conditions (Bergametti et al., 1989; Moulin et al. 1997, Ginoux et al., 2004). The African dust includes variable amounts of quartz and clays, such as illite, kaolinite, and smectite, among others components; thus, their arrival leads to the input of limiting nutrients (e.g., phosphorus, nitrogen and iron) to these oligotrophic ecosystems. Different chemical, mineralogical and biological analyses conducted on samples collected from direct atmospheric deposition in lake catchments or at different lake water depths have been employed to assess the arrival and the effects of these African airborne inputs (e.g., Reche et al., 2009; Morales-Baquero et al., 2006). In particular, a fibrous clay called palygorskite has been used to trace the origin of the African dust (Coudé-Gaussen et al., 1982; Molinaroli, 1996). For instance, the western Sahara and southern Morocco are dust sources that are particularly rich in palygorskite (Molinaroli, 1996). In these areas, the formation of palygorskite is favoured by evaporation and chemical concentration (Singer and Galan, 1984) on poorly drained carbonated rocks in the anti-Atlas (El Mouden et al., 2005). These dust sources have been essentially confirmed by back trajectory analysis for dust deposited over northeastern Spain (Middleton and Goudie, 2011). In addition, the chemical and mineral signatures of dust events might be identifiable in the lake sediments (Nieto-Moreno et al. 2013; Jiménez-Espejo et al., 2014), which can also contribute to reconstructions of past climate conditions. In the IP, many different studies support the arrival and biogeochemical effects of African dust in mountain lake ecosystems, particularly in southern Iberian regions (Morales-Baquero et al., 2006; Pulido-Villena et al., 2006, 2008; Mladenov et al., 2011).

In general, mountain lake ecosystems are also sensitive indicators of climatic variability (Thompson et al., 2009). Lakes located in the IP are particularly sensitive to the NAO climate mode due to their geographical position. These freshwater ecosystems respond substantially to changes in air temperature, wind speed or precipitation, among other climatic variables, which are controlled by large-scale climatic fluctuations (Sharma and Magnuson, 2014). These responses are then recorded in lake parameters. Physical lake water parameters, such as water temperature and ice phenology, appear to more rapidly reflect the effects of these climate patterns and exhibit higher sensitivities than other lacustrine parameters, such as chemical or biological ones (Straile et al., 2003; George et al. 2004; Salmaso, 2012). Individual physical lake properties influence freezing processes much more strongly than thawing processes. For instance, the timing of ice-off makes a better direct indicator of climatic changes and thus of NAO effects than the timing of ice-on (Šporka et al. 2006; Adrian et al., 2009). Consequently, the winter NAO effects are typically reflected in the ice phenology via the air temperature, particularly in the ice-off date. In Northern Europe, many studies have found this strong relationship (Yoo and D'Odorico, 2002; Brown and Duguay, 2010). However, relatively

scarce data on ice phenology are available for meridional areas of the Northern Hemisphere (Brown and Duguay, 2010) and for the effects of the NAO signal via other climatic variables, such as snow accumulation (Ghanbari et al., 2009; Ruibo et al., 2012), which can play a key role in the thawing process through its insulating effect (Jensen et al., 2007; Ruibo et al., 2012). In addition, other factors, such as altitude, latitude or lake morphometry, can influence ice phenology and the resulting NAO-ice relationships (Williams and Stefan, 2006; Livingstone and Adrian, 2009). Therefore, ice phenology has become one of the most valuable indicators of the effects of large-scale oscillations on winter lacustrine dynamics throughout the Northern Hemisphere, particularly with respect to the effects of the NAO, which is the main mode of climate variability in the North Atlantic region on the multiannual time scale (Barrie et al., 2006; Ghanbari et al. 2009; Bai et al. 2012). Nevertheless, most of the studies have focussed on determining the influence of the NAO on alpine lakes, whereas to the best of our knowledge, the sensitivity of these water bodies to variations of other climate modes, such as the EA and the SCAND, has not yet been explored either in recent periods or in the past. Some studies have assessed the sensitivity of low-altitude lakes to these modes of climate variability during the instrumental period (Salmaso, 2012; Hernández et al., 2015). However, their impact on alpine lakes remains unknown.

Finally, altitude in alpine lakes also establishes remoteness, which is very relevant for organism colonization and especially for anthropic influence (Catalan et al., 2006). Lakes are ecosystems that have been influenced by humans since remote times (e.g., Corella et al., 2013; Moreno et al. 2009; Park et al., 2010; García-Alix et al., 2013). Thus, reconstructions based on lacustrine sequences from low-altitude lakes usually face the additional challenge of distinguishing between environmental or climatic signals and anthropogenic ones (e.g., Valero-Garcés et al., 2006; Morellón et al., 2011; Barreiro-Lostres et al., 2015). However, alpine lakes have been extensively recognized as sensors of global change and key freshwater reference sites for global-scale processes due to their location outside of direct human influence (Williamson et al., 2009; Mladenov, 2011; Catalan et al., 2013). Consequently, their sediments constitute an excellent archive for conducting environmental reconstructions because they often contain more pristine climatic signals compared with the low-mountain records.



Figure 1.23. Images of alpine lakes. A) Redon Lake (2240 m asl) located in the Pyrenees, B) Cimera Lake (2140 m asl) located in the Iberian Central Range, C) Peñalara Lake (2016 m asl) located in the Iberian Central Range, D) Hagelseewli Lake (2339 m asl) located in the Central Swiss Alps and E) Chasm Lake (3604 m asl) located in the Rocky Mountains.

1.6 Lacustrine sediments

Lakes accumulate sediments from their surrounding environment, and these natural archives provide a continuous and excellent record of environmental changes, resulting in accurate repositories and sources of information about the lake history (Cohen, 2003; Smol, 2008; Nichols, 2009). Sediment accumulation rates in lakes are often high, so lake sediments offer the potential for high-resolution records of recent and past environmental conditions, such as climate variations, providing they can be adequately dated (Birks, 2015). However, no two lakes are identical; thus, the environmental conditions in the lake catchment and the water properties of each lake must be carefully evaluated to make a meaningful interpretation of the sediments (Birks, 2015).

Lake sediments are made up of two basic components: allochthonous material, originating from both outside and within the lake catchment, and autochthonous material, produced within the lake itself (O'Sullivan and Reynolds, 2008; Herschy, 2012) (Fig. 1.24). Allochthonous material is transported to lakes by rivers and streams, overland flow, aeolian activity, and, in some cases, by subsurface drainage. This material is made up of varying amounts of fluvial or aeolian clastic sediment, dissolved salts, terrestrial macrofossils, phytoliths, pollen, charcoal from fires, among other components (O'Sullivan and Reynolds, 2008; Herschy, 2012) (Fig. 1.24). Autochthonous material is either biogenic in origin or may result from inorganic precipitation within the water column (often as a consequence of seasonally varying biological productivity, which can significantly alter the water chemistry) (O'Sullivan and Reynolds, 2008; Herschy, 2012) (Fig. 1.24). Both allochthonous and autochthonous material can be useful for conducting palaeoecological and palaeoclimatic reconstructions (Nichols, 2009; Birks, 2015).

A great deal of basic information about changes in environmental and climatic conditions can be derived from relatively simple measurements of the sedimentary, organic, inorganic and biological compositions of lake sediments (Birks, 2015).

For example, the advance and retreat of glaciers is tracked quite well by changes in loss on ignition (LOI) because the proportion of clastic sediment increases (and/or organic matter production decreases) during times of glacier growth (Nesje et al., 2000). Similarly, magnetic susceptibility also documents changes in the proportion of clastic material in a sediment core, and this also may reflect glacier activity in certain situations (Polissar et al., 2005). Various non-destructive methods are available for sediment analysis, of particular importance is the acquisition of elemental data at very high resolution by scanning X-ray fluorescence (XRF) analysis (Shanahan et al., 2008; Rothwell and Croudace, 2014; Bakke et al. 2010). In many cases, the down-core record of a specific element or elemental ratio can provide valuable insights into past conditions.

Pollen is one of the most widely studied components of lake sediments. It provides a wealth of palaeoenvironmental and palaeoclimatic information (e.g., Rull et al., 2010; Parnell et al., 2015;) and is a staple proxy used in verifying general circulation model simulations (Prentice et al., 1996; Bartlein et al., 1998; Bennett and Willis, 2001). Plant macrofossils (e.g., leaves, seeds, and fruits) are environmental indicators

that are especially helpful in corroborating vegetation reconstructions based on pollen (e.g., Hannon and Gaillard, 1997; Jackson et al., 1997). The analysis of phytoliths, which are morphologically distinctive deposits of opaline silica found in many higher plants, is far less common than the analysis of pollen, but it can provide complementary data to palynological interpretations (e.g., Barboni et al., 1999). Palaeotemperature reconstructions have also been obtained from phytoliths (Fredlund and Tieszen, 1997; Prebble et al., 2002).

The remains of organisms that lived in the water column are another important source of present and past environmental changes. They are particularly indicative of climatic variability because biological productivity in lakes is climatically dependent (Battarbee, 2000). For instance, ostracods are sensitive to a number of variables, including water chemistry, water depth, and, to some extent, temperature (Holmes, 2001; Schwalb, 2003). Therefore, these organisms have been employed to determine water-level changes (e.g., Wirrman and Mourguia, 1995; Holmes, 1998) and palaeotemperatures (e.g., Granados and Toro, 2000). However, one of the most extensively used types of organisms in reconstructions and ecological studies is diatoms. Diatoms are unicellular algae and are sensitive indicators of lake water temperature and water chemistry (pH, dissolved oxygen, salinity, and nutrient content, particularly nitrogen and phosphorus) (e.g., Battarbee et al., 2001; Mackay et al., 2003; Smol and Stoermer, 2010). Certain diatoms are especially diagnostic of changes in salinity (Gasse et al., 1997). Consequently, these algae are commonly used to reconstruct many of these parameters (e.g., Fritz, 1990; Pla-Rabes and Catalan, 2005, 2011; Korhola et al., 2000; Bao et al. 2015).

Isotopic values of oxygen ($\delta^{18}\text{O}$) and carbon ($\delta^{13}\text{C}$), and to a lesser extent nitrogen ($\delta^{15}\text{N}$), also provide valuable insights of present and past environmental and climatic conditions (Leng and Marshall, 2004; Leng, 2006; Leng and Henderson, 2013). $\delta^{18}\text{O}$ values provide insights in variations in humidity (Hodell et al., 1995, 2005; Anderson et al., 2007), temperature (Shemesh and Peteet, 1998) and ocean and atmospheric circulation (von Grafenstein et al., 1999). $\delta^{13}\text{C}$ and $\delta^{15}\text{N}$ values are more difficult to interpret than oxygen isotopic values, but together with other parameters, such as the total carbon to total nitrogen atomic ratio (TC/TN), they can contribute to a more complete understanding of past conditions (Leng, 2006).

Biomarkers, i.e., organic compounds that are produced by specific organisms, also provide a molecular proxy for the climatic or environmental conditions that influenced the life of the organism (Eglinton and Eglinton, 2008; Gaines et al., 2009; Castañeda and Schouten, 2011). For example, an important group of lipids that may be useful palaeotemperature biomarkers in lakes are the isoprenoid glycerol dialkyl glycerol tetraethers (GDGTs–tetraethers with 86 carbon atoms) (e.g., Powers et al., 2010, 2011; Tierney et al., 2010, 2008).

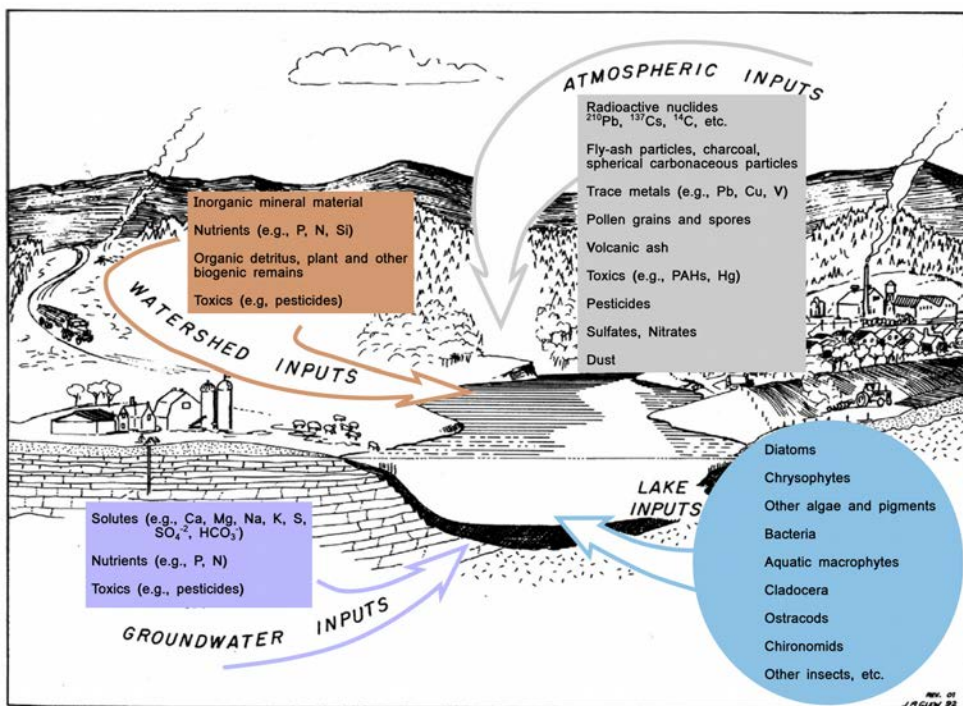


Figure 1.24. Schematic diagram illustrating the transfer of material from the atmosphere, the watershed and the groundwater to sediments in a lake (allochthonous input; rectangles) and from sources within the lake itself (autochthonous input; circle). Modified from Smol et al. (2001).

AIMS

The main aim of this PhD thesis is to characterize the impacts of the NAO on the Central IP for the last 2,000 years. For that, three steps have been followed: 1) establishment of a conceptual model to depict the NAO influence on the ice phenology of the Peñalara and Cimera alpine lakes (ICR) to determine how the NAO signal is transmitted from the atmosphere to their bottom sediments; 2) characterization of the main climate changes in the ICR using Peñalara and Cimera sediments and the spatio-temporal evolution of the NAO and its relationships with other climate modes for the last two millennia; and 3) creation of a regional NAO quantitative reconstruction using the geochemical composition of the Cimera Lake sediments and a Random walk-modularised Bayesian model.

THESIS STRUCTURE

This PhD thesis is composed of eight chapters. Chapter 1 provides a state-of-the-art introduction to climate variability in the European-North Atlantic sector and the IP, climate reconstructions and lakes. The regional setting of Peñalara and Cimera

Lakes, including geographical, geological, vegetation, climatic and limnological features, are presented in Chapter 2. All the methodological procedures employed, including instrumental data, sediment analyses and statistical treatments, are described in Chapter 3. Chapter 4 includes the results of the chemical and statistical analyses performed and the age-depth models of both lake sequences. Discussion is provided in Chapters 5, 6 and 7. Chapter 5 establishes the present-day influence of the NAO on the ice phenology of Iberian alpine lakes by the construction of a conceptual lake model. In Chapter 6, the age-depth models, geochemical compositions and the results from Redundancy Data Analysis and Principal Component Analysis (RDA and PCA) of Peñalara and Cimera lake sediment sequences have allowed us to determine the main environmental processes that controlled the terrigenous inputs and organic productivity in each lake for the last two millennia and to qualitatively reconstruct the climatic conditions in the ICR for this period. Moreover, the integration of both reconstructions with other relevant Iberian reconstructions have finally permitted us to determine the interplay of climate modes and forcing mechanisms acting in the IP for the last two millennia. Chapter 7 presents the reconstruction of the quantitative impact of the NAO in the ICR for the last two millennia obtained using a random walk-modularised Bayesian model and geochemical elements in the Cimera Lake record measured via X-Ray Fluorescence analysis. This chapter also contains a discussion of the model validation and a comparison of the reconstructed NAO impact with other NAO approaches. Finally, Chapter 8 provides the concluding remarks of the thesis grouped according to their methodological, limnological or climatic implications, and future works are proposed. The raw data obtained during the experimental processes are contained in the appendices.

2. STUDY SITE

2.1. The Iberian Central Range

The ICR is a mountainous region located to the west of the centre of the IP. It extends approximately 700 km from NE to SW and rises in some places to a height of over 2500 m asl (Rivas-Martínez et al., 1987; Ubanell 1994). The ICR divides the basins of the Duero and Tajo rivers (northern and southern Iberian plateau, respectively) and comprises several mountainous ranges known as 'sierras' separated by depressions or troughs that form natural corridors between the two plateaus (De Vicente et al., 1994) (Fig. 2.1). These sierras, and their corresponding highest peak, are from east to west: Pela (1548 m asl), Ayllón (2274 m asl), Guadarrama (2428 m asl), Gredos (with the highest peak of the ICR, Almanzor, at 2592 m asl), Béjar (2429 m asl), Francia (1735 m asl), Gata (1519 m asl), all located in the Spanish region, and Estrela (1993 m asl), located in Portugal (López-Sáez et al., 2014) (Fig. 2.1).

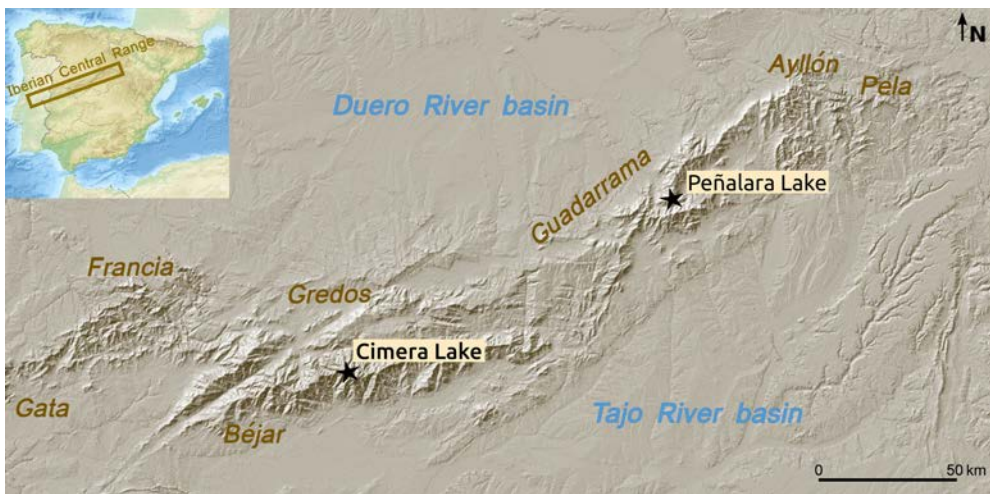


Figure 2.1. Topographical map of the Iberian Central Range showing the geographical location of the different 'sierras' that comprise this mountainous region in the Spanish area and the Duero and Tajo basins. The locations of Peñalara and Cimera lakes are identified.

The ICR is an intraplate mountain range that forms part of an ancient Hercynian and pre-Hercynian massif that developed during the Mesozoic and was reactivated during the Alpine Orogeny in the Palaeogene (Pedraza, 1989, 1994a; Ubanell, 1994). The result is a chain of horsts and grabens (Pedraza, 1994b) that is sorted into different tectonic styles depending on the local lithology, including igneous (granite and gneiss) or metamorphic (slates) rocks from the late Palaeozoic (De Vicente et al., 1994, Pedraza 1994a). In this sense, the central section has the characteristic structure of blocks, while at the edges this structure tends to be masked by the influence of folds. A consequence

of these block dynamics is the asymmetry between the northern and southern slopes of the ICR, particularly in the western sector, because of the high altitude of the northern plateau with respect to the deeply set valleys in the Tajo River basin.

Glacial morphologies in the ICR developed only above 1900 m asl throughout the Quaternary (Pedraza and Carrasco, 2006; Palacios et al., 2011, 2012). Consequently, well-developed glaciated morphologies, such as mountain glaciers, small ice caps, ice fields, valley slope, or cirque glaciers, are found on the summits of different sectors of the ICR (Pedraza and Carrasco, 2006). Some of these glacial geomorphologies favoured the formation of lakes, whose basins can be classified accord to this genesis (e.g., cirque, moraine, and bottom valley) (Wetzel, 2001). Lakes are only found in Sierra de Guadarrama (Spain), Sierra de Gredos (Spain) and Serra da Estrela (Portugal), where the glacial activity was more intense (Pedraza and Carrasco, 2006).

The vegetation in low and middle altitudes of the ICR is dominated by oak forests of *Quercus ilex* subsp. *ballota*, *Quercus suber* and *Quercus pyrenaica* (Devesa, 1995; Pulido et al., 2007). The timberline, located between 1900 and 2100 m asl, is represented by pine forests of *Pinus sylvestris* and *Pinus nigra*, which are especially prominent in Sierra de Gredos and Sierra de Guadarrama (Martínez, 1999). Higher areas are occupied by shrublands, where brooms, such as *Cytisus oromediterraneus*, *Echinospartum ibericum*, and *Echinospartum barnadesii*, or heathlands of *Erica australis* in more humid areas, are the prevailing vegetation (Rivas-Martínez, et al., 1987; Sánchez-Mata, 1989; Fernández-González, 1991). Psychroxerophilous grasslands are the dominant vegetation in the highest areas (Toro et al., 2006; López-Sáez et al. 2014).

The climate of the ICR is an alpine type immersed in a Mediterranean climate with a strong continental influence (Durán et al., 2013). The arrival of Atlantic depressions from the SW frequently occurs in fall, winter and spring; however, in summer, the Azores anticyclone is persistent and does not favour moisture transport from the west. Consequently, the ICR climate is characterized by a significant amount of solid precipitation and low temperatures in winter and warm and dry conditions in summer (Sánchez-López et al., 2015). The minimum and maximum temperatures estimated for the period 1951–1999 AD oscillate between 0 and 2 °C and between 20 and 22 °C, respectively. The total mean annual rainfall estimated for the period 1951–1999 AD is ca. 1400 mm and occurs in the humid ombrotype region (Ninyerola et al., 2005).

2.2. Peñalara Lake

Peñalara Lake ($40^{\circ}50'N$ – $3^{\circ}57'W$) is a tiny (0.6 ha, 115 m long, and 71.5 m wide) and shallow (4.8 m maximum depth) alpine lake (2016 m asl) located on the southeastern slope of the Peñalara Massif in the Sierra de Guadarrama (Fig. 2.1). It is located in an over-excavated depression of a glacial cirque, and its catchment (140 ha) is composed of metamorphic rocks (gneiss) partially covered by Late Pleistocene glacial moraine deposits (Palacios et al., 2003) (Fig. 2.2). The watershed exhibits small zones of shrubs (*Cytisus* sp., *Juniperus* sp.), psychroxerophytic grassland (*Festuca* sp.),

meadows (*Nardus* sp.) and peat bogs (*Sphagnum* spp.), but the acidic nature of the catchment bedrock does not allow the development of thick soils (Toro et al., 2006).

The deepest sector of the lake is located in the northern portion of the lake, and it is dominated by fine sediments. In contrast, the southern sector is shallower (< 2 m deep) and accumulates cobble to boulder deposits transported by rock avalanches from a scree field developed at the base of a steep relief (Fig. 2.2). Peñalara has various temporary water inflows and a single outlet located on its southern shore (Fig. 2.2).

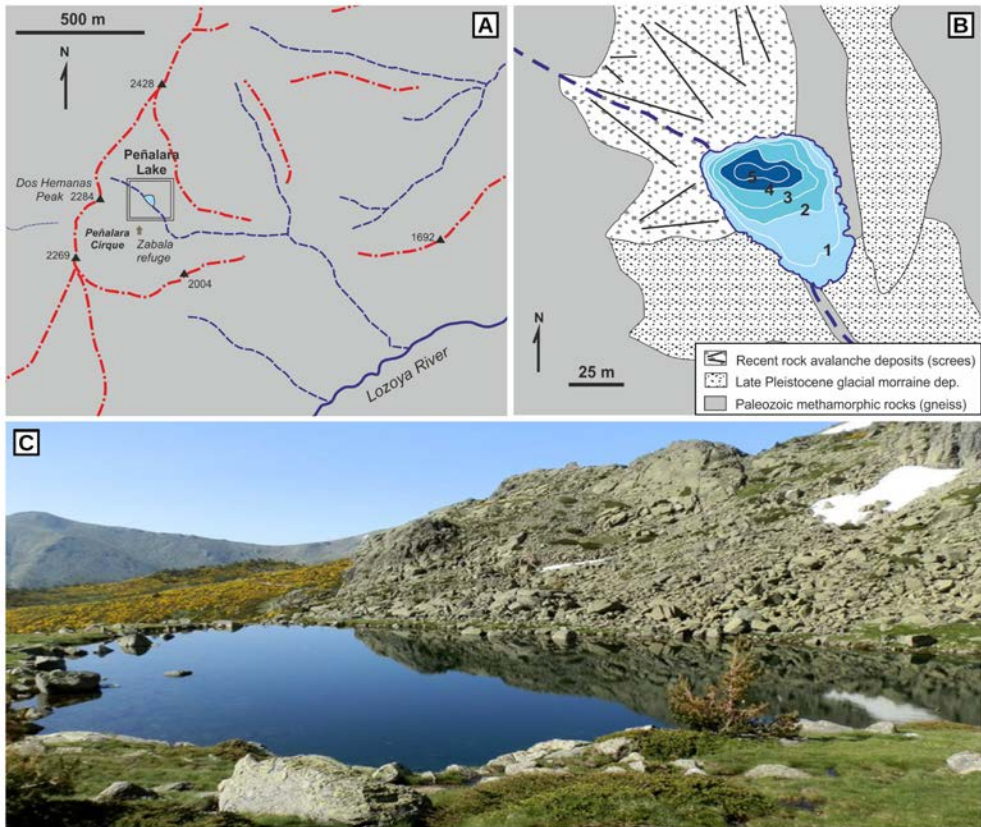


Figure 2.2. A) Topographic and B) bathymetric maps of Peñalara Lake according to Toro and Granados (2002). C) Panoramic view of Peñalara Lake from its northern side in May 2013 AD.

Peñalara Lake has been monitored since 1992 AD, and there are accurate physico-chemical and biological datasets that have allowed for the characterization of the lacustrine dynamics. The lake is usually ice-covered from November-December to March-April, with a mean ice-cover duration of approximately 115 Julian days, although the ice cover can extend until May in severe winters (Fig. 2.3). In addition, the lake can exhibit two clearly differentiated ice covers in years with irregular winters that present unusual warm periods of 2 or 3 weeks, such as 1999 and 2012 AD (Granados et al., 2006; Sánchez-López et al., 2015). The lake is monomictic, with thermal

stratification of its waters occurring during the winter period under the ice cover. The rest of the year, the water column remains largely homogeneous (Fig. 2.3). The dissolved oxygen of the water column has an annual periodic fluctuation (4–12 mg/l) with winter depletion below the ice cover. The lake water is very diluted, with a low conductivity (10 µS/cm at 25°C), an extremely low alkalinity (with mean values range 40–60 µeq/l) and slightly acidic pH (a pH value of 6.2) (Toro and Granados, 2002; Granados et al., 2006).

During the early 1990s, the lake presented a marked tendency towards eutrophication, but the Spanish authorities began to carry out control policies to reduce tourist impacts and the lake rapidly returned to its original trophic status (Toro and Granados, 2002). Currently, Peñalara Lake can be considered an oligotrophic lake according to its low values of total phosphorus (mean values of 7 µg P-PO₄ l⁻¹), chlorophyll (maximum and mean values of 8 µg Chl-a l⁻¹, 1.8 µg Chl-a l⁻¹, respectively) and Secchi disk depth (maximum depth of 4.8 m) (Toro and Granados, 2002; Toro et al., 2006).

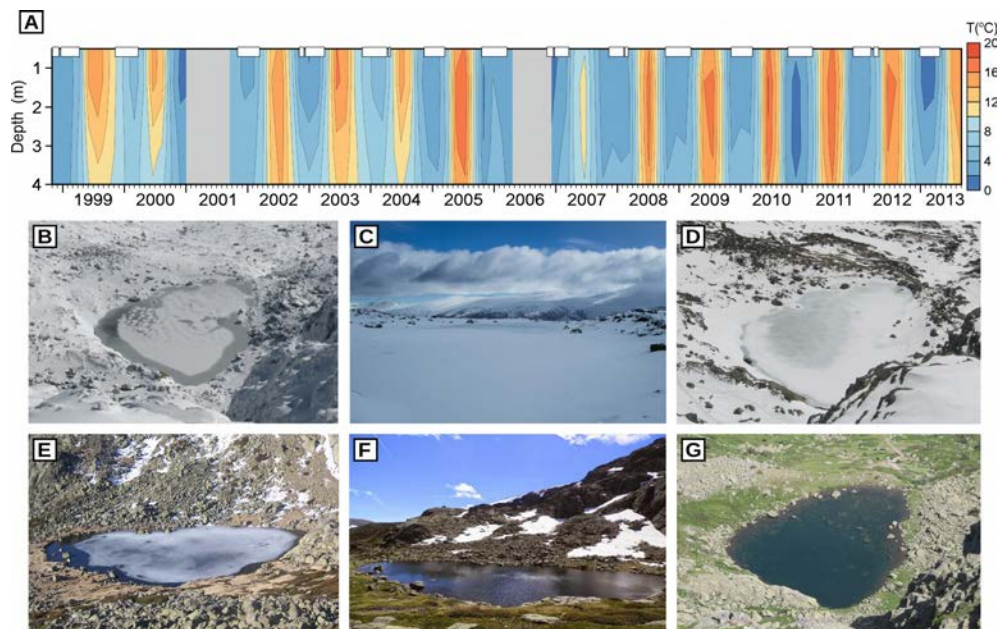


Figure 2.3. A) Monthly lake water temperatures at different depths, from lake surface (0.5 m) to lake bottom (4 m), and ice-cover duration in Julian days (white rectangles) for Peñalara Lake for the period 1998–2013 AD. The grey bands correspond to periods without lake water temperature data. B–G) Views of Peñalara Lake showing the different phases of the ice phenology from the formation of the ice cover to the totally ice-free phase. Photos by I. Granados and M. Toro.

The weather station at Puerto de Navacerrada (40°46'N – 4°19'W; 1860 m asl), 8 km southwest of Peñalara Lake, provides the only available meteorological data for the lake area for the period between 1950 and 2011 AD. The mean annual air temperature in this area is approximately 6 °C, and the temperature is typically below 0 °C from December to February. The mean maximum and minimum air temperatures are 20 °C

and -5 °C, respectively. The mean annual precipitation is 1339 mm, ranging from ca. 805 mm and ca. 2380 mm per year, with the wettest period occurring from early October to late May. Snowfall primarily occurs from November to April (Fig. 2.4).

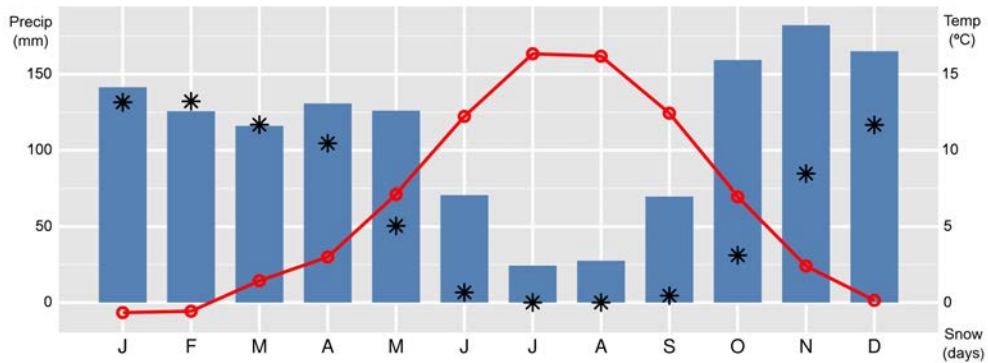


Figure 2.4. Climograph of the Peñalara Lake area including average monthly precipitation (blue bars), temperature (red lines) and snow days (black asterisks) for the period 1950–2011 AD. Climatic data are from the Navacerrada weather station.

2.3. Cimera Lake

Cimera Lake ($40^{\circ}15'N$ – $5^{\circ}18'W$) is the highest (2140 m asl) of a series of 5 alpine lakes located in a glacial cirque in the Massif Central of Sierra de Gredos (Figs. 2.1 and 2.5; Palacios et al., 2011). Cimera is a shallow lake (9.4 m maximum depth) with a small surface area (5 ha, 384 m long, 177 m wide), and its catchment (75.6 ha) is primarily composed of exposed plutonic rocks (granites) and exhibits scarce developed soils and small grasslands and psychroserophytic meadows (*Nardus* sp.) (Granados and Toro, 2000) (Fig. 2.5). The southern sector has a mean water depth of 5.5 m, and its sediment is dominated by coarse gravel scree deposits. There are two temporary stream inlets in the southern littoral zone of the lake and one outlet on the northern side that becomes dry in late summer (Fig. 2.5). Flood currents from these streams are the origin of the major volume of fine sediment inputs accumulated in the offshore zone of the northern part of the lake (Fig. 2.5).

Although Cimera has not been monitored for a long period because of its remoteness, different limnological studies conducted in the lake have determined its main physico-chemical features and characterized its lacustrine dynamics. Cimera is a discontinuous, cold, polymictic lake (Toro et al., 2006) that usually starts to freeze between November and December, and it becomes completely ice-free in May-June (Sánchez-López et al., 2015) (Fig. 2.6). The ice cover has a mean duration of 190 days, and the duration depends on the severity of the winter, with a difference of ca. 2 months between mild and severe winters (Granados and Toro, 2000; Sánchez-López et al., 2015) (Fig. 2.6). Cimera can also be classified as an oligotrophic lake because of the total mean phosphorus values ($7 \mu\text{g P-PO}_4 \text{l}^{-1}$), maximum and mean annual chlorophyll values ($11.5 \mu\text{g Chl-a l}^{-1}$ and $2.1 \mu\text{g Chl-a l}^{-1}$, respectively) and mean Secchi disk depth

(5 m) (Catalan et al., 2002; Granados and Toro, 2000). The dissolved oxygen concentration in the water column has an annual periodic fluctuation (0–12 mg/l) and usually presents 80–120% oxygen saturation values during the open water period and intense bottom depletion in winter because of the thick ice cover. The lake water is slightly acidic (mean pH value of 6.8) and exhibits low conductivity (<10 µS/cm at 25 °C) and nutrient contents (N and P) (Catalan et al., 2002; Granados and Toro, 2000).

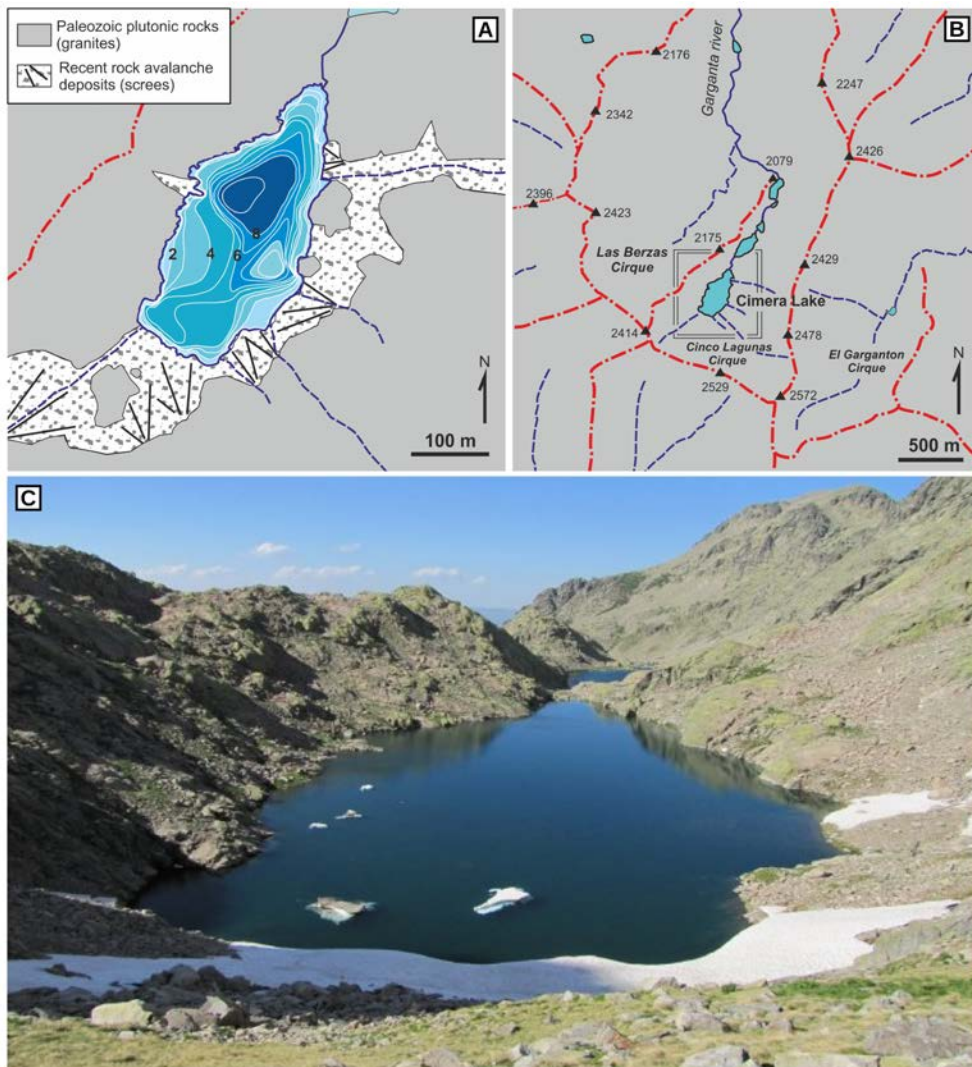


Figure 2.5. A) Topographic and B) bathymetric maps of Cimera Lake according to Granados and Toro (2000). C) View of Cimera Lake from its southern side in July 2011 AD.

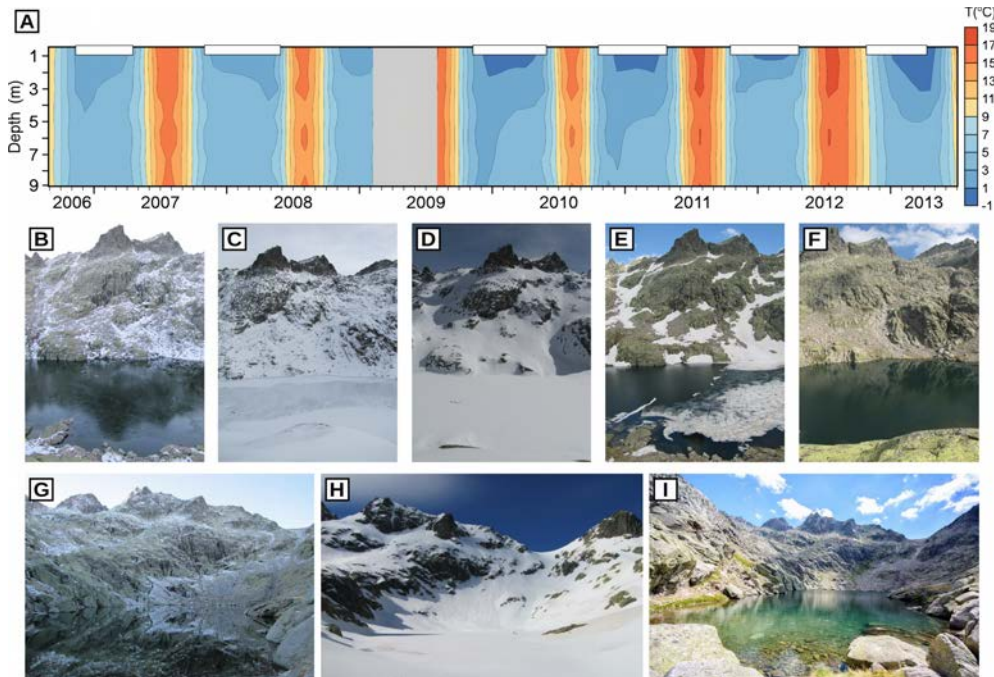


Figure 2.6. A) Monthly lake water temperatures at different depths, from lake surface (0.5 m) to lake bottom (9 m), and ice-cover duration in Julian days (white rectangles) for Cimera Lake for the period 2006–2013 AD. The grey band corresponds to a period without lake water temperature data. B–F) Chronological views of Cimera Lake showing the different phases of the ice phenology from the formation of the ice cover to totally ice-free conditions during the period of 2010/2011 AD. G–I) Views from the northern side of Cimera Lake catchment of different phases of the ice cover from the formation phase to the totally ice-free phase. Photos by I. Granados and M. Toro.

There are no weather stations near Cimera Lake because of its remoteness. Nevertheless, the total annual precipitation and average air temperature have been previously estimated to be slightly higher and lower, respectively, than those in the Peñalara Lake area (Toro et al., 2006). The snow season in this region is longer than Peñalara Lake area due to the higher altitude.

3. DATA , MATERIALS AND METHODOLOGY

3.1. Instrumental data

3.1.1. Climate index

The monthly NAO index dataset spanning the period 1825–2013 AD was obtained from the Climatic Research Unit (CRU) of the University of East Anglia (UK) (<http://www.cru.uea.ac.uk/cru/data/nao>). This NAO index is defined as the difference between the normalized monthly sea-level pressure anomalies recorded at Reykjavik (Iceland) and those observed at Gibraltar (UK) (Jones et al., 1997). The NAO subset from 1950 to 2013 AD was selected to determine the relationships between this climate mode and the climatic and limnological data (i.e., conceptual lakes models) for both Peñalara and Cimera lakes (Table 3.1). The NAO subset from 1930 to 2010 AD was used to conduct the initial calibration step of the Bayesian model, whereas the data from 1825 to 1930 AD were employed to test the Bayesian NAO reconstruction (Table 3.1).

Sections of the PhD	Data	Period (yrs AD)
Peñalara Lake conceptual model	NAO index	1950–2013
	Climatic data (<i>precip., temp. and snow days</i>)	1950–2011
	Limnological data (<i>lake water temperature</i>)	1998–2013
	Limnological data (<i>ice phenology</i>)	1993–2013
Cimera Lake conceptual model	NAO index	1950–2013
	Climatic data (<i>precipitation and temperature</i>)	1950–2011
	Climatic data (<i>snow depth</i>)	2010–2013
	Limnological data (<i>lake water temp. and ice phenology</i>)	2006–2013
Bayesian model	NAO index	1930–2012
		1825–1930

Table 3.1. Summary of the time periods of the instrumental data used to construct Peñalara and Cimera lakes conceptual models and the Bayesian model.

3.1.2. Climatic data

For the Peñalara Lake region, monthly total precipitation, mean air temperature and snow days datasets for the period 1950–2011 AD were obtained from the Puerto de Navacerrada weather station (40°46'N – 4°19'W; 1860 m asl) (Fig. 3.1 and Table 3.1).

Monthly precipitation and temperature data from the Puerto Navacerrada weather station shows that snow days data for the studied period can be considered an

equivalent measure of snow depth. The percentage of precipitation days and the amount of precipitation (mm) when the maximum temperature is below 4 °C is approximately 80% in December, January and February (Fig. 3.2). Therefore, there is a direct relationship between the number of precipitation days and the total amount of precipitation and the majority of the precipitation that falls during these winter months is in the form of snow (Fig. 3.2).

No high-altitude meteorological stations exist close to Cimera Lake. Thus, regional climate series were used for this area. Regional monthly anomalies of precipitation and maximum and minimum air temperatures from 16 meteorological stations located in the surrounding area and covering the period 1950–2011 AD were selected (Fig. 3.1 and Table 3.1). The snow depth dataset for the period 2010–2013 AD was obtained from the Puerto Peones snow gauge dataset ($40^{\circ}15'N - 5^{\circ}26'W$; 2165 m asl) (Table 3.1), which is located approximately 10 km west of the lake (Fig. 3.1).

All the climatic data time series were quality controlled and homogenized following the recommended protocols of Aguilar et al. (2003) and Brunet et al. (2008).

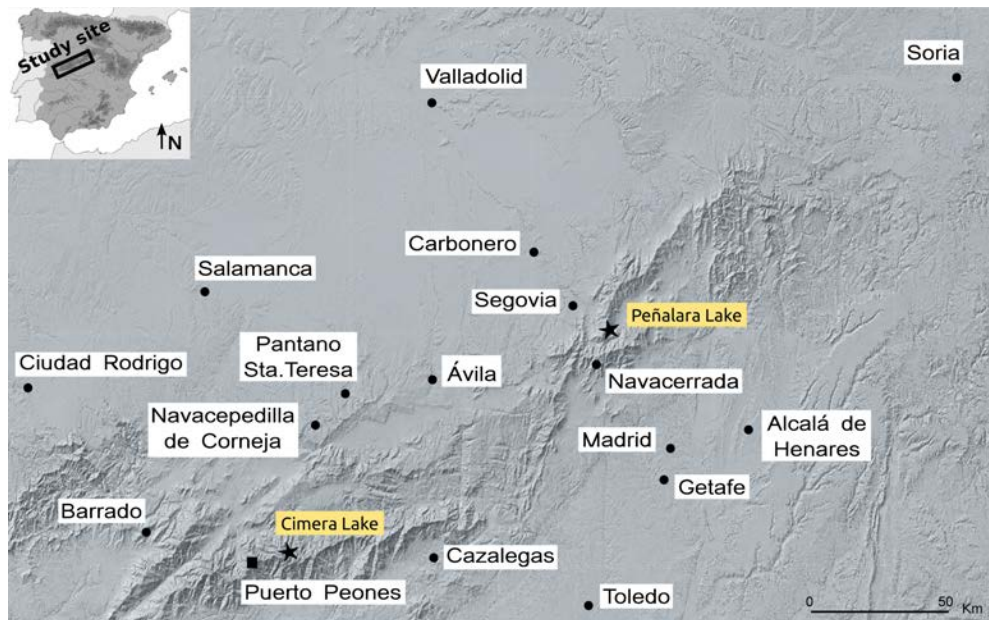


Figure 3.1. Map of the topography of the Iberian Central Range showing the locations of the weather stations (black circles), the snow gauge (black square) and Peñalara and Cimera lakes (black stars).

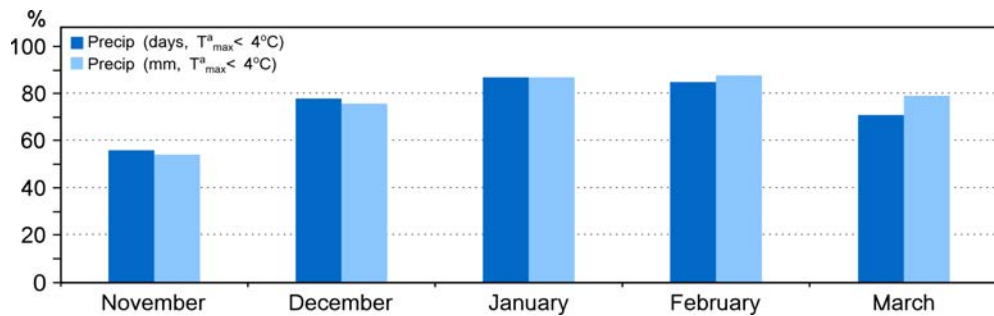


Figure 3.2. Percentages of monthly precipitation data from the Puerto Navacerrada meteorological station for the period 1946–2010 AD expressed in total days (blue bars) and amount of precipitation in mm (light blue bars) with maximum temperatures below 4 °C.

3.1.3. Limnological data

- Lake water column temperatures

Measures of lake water column temperatures at different depths, different time intervals and for different time periods were obtained using thermistor chains located in Peñalara and Cimera lakes (Table 3.1, Figs. 2.3A and 2.6A)

In Peñalara Lake, lake water temperatures were measured at 0.5, 1, 2, 3 and 4 m of water depth at intervals of ten minutes, two hours and four hours for the period 1998–2013 AD. Different thermistors were used: one Tinytalk II thermistor was used at 0.5 m deep between 1998 and 2005 AD, and HOBO Water Temp Pro V1 & V2 thermistor chains were used at 0.5, 1, 2, 3 and 4 m deep from 2005 to 2013 AD (Fig. 3.3). Linear regression models were employed to inter-calibrate the different devices and to obtain a mean daily homogeneous dataset covering the complete period (Fig. 3.4).

In Cimera Lake, lake water temperatures were measured hourly with HOBO Water Temp Pro V1 & V2 thermistors (Fig. 3.3) at water depths of 0.5, 3, 6, and 9 m for the period 2006–2013 AD. Daily temperature data were obtained from these measurements by calculating the mean daily values.



Figure 3.3. Photos of A) HOBO Water Temp Pro V2 and B) Tinytalk II thermistors.

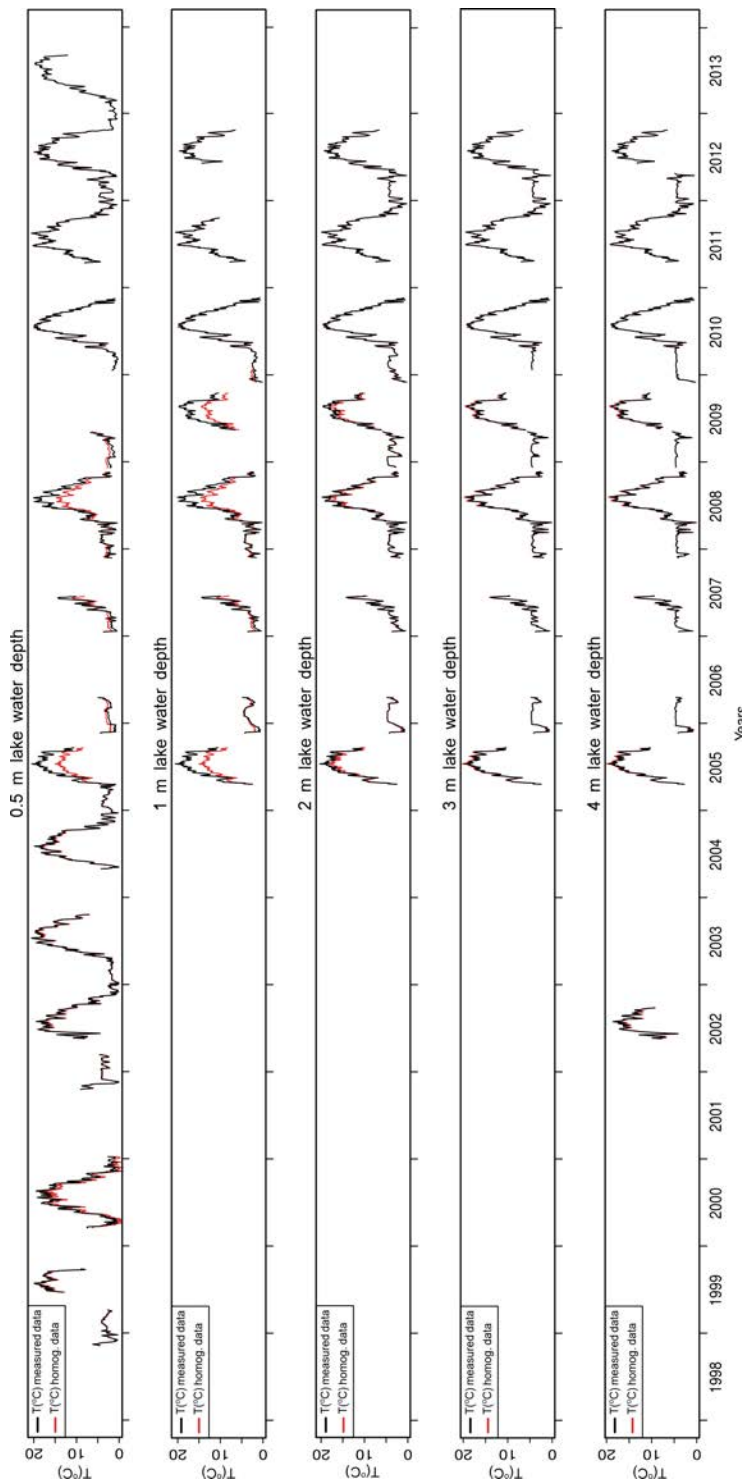


Figure 3.4. Mean daily datasets of lake water temperature measured at 0.5, 1, 2, 3 and 4 m of water depth (black lines) and their corresponding homogeneous datasets (red lines) from Peñalara Lake for the period 1998–2013 AD.

- Ice phenology

The ice phenology data include freeze-up and break-up dates and ice-cover duration. The freeze-up date is defined as the first day the lake is completely ice-covered as determined by a visual inspection. The break-up date is defined as the first day the ice cover begins to break. The ice-cover duration is expressed as the number of days that the lake is completely ice-covered (Ruibo et al., 2012). These definitions require nearly daily observations of each lake to collect the ice phenology data.

In Peñalara Lake, the ice data were obtained from daily visual observations of the lake and span the period 1993–2013 AD (Table 3.2). The ice cover on Peñalara does not continuously cover the lake surface during irregular winters with warm periods of above-mean air temperatures that persist for 2 or 3 weeks. In these years, the lake exhibits two clearly differentiated ice-covered periods, with the second ice-covered period usually occurring either at the beginning or the end of the winter (Table 3.2). Nevertheless, the ice-free period between these two ice-covered periods is typically less than 13% of the total ice-cover duration, with the exception of 1998 AD, in which the ice-free period accounted for 34.4% of the total ice-covered period (Table 3.2). Therefore, the ice-cover duration in Peñalara Lake is represented by the sum of the two ice-covered periods and excluding the in-between ice-free days. The ice data corresponding to the year 1998 AD were considered outliers and were not included in the subsequent statistical analyses.

There are no daily available observations for Cimera Lake because of its remote location. Hence, ice phenology dates for this lake were deduced from lake water temperatures measured by the thermistor chains (Table 3.3). The freeze-up date was defined as the date when the lake water temperature changed from an autumn overturning pattern to winter stratification, and the break-up date was defined as the date when the lake water temperature changed from winter stratification to a spring overturning pattern (Fig. 2.5A). This method of deriving the ice phenology metric in Cimera Lake was verified using Peñalara Lake data. The differences between the freeze-up and break-up dates based on daily visual observations and those based on water temperatures measured using the thermistors at different water depths in Peñalara Lake were calculated (Table 3.4). These differences show that dates based on the measured water temperature data were typically earlier than those obtained based on daily visual observations. However, the differences in the freeze-up and break-up dates between the daily observations and the water temperatures measured using thermistors were less than five days. Therefore, these differences were considered negligible and ice data deduced from measured water temperature can be considered similar to ice data from visual observation of the lake. The ice phenology data deduced from water temperature span the period 2006–2013 AD.

All ice date data from both lakes were expressed in Julian days, and the observation year for both dates is given as the year of break-up. The ice-cover duration is expressed in number of days (Tables 3.2 and 3.3).

NAO imprints in the Central Iberian Peninsula for the last two millennia

Data year considered	Freeze-up date	Julian day	Break-up date	Julian day	Ice-cover duration in days	Number of covers	Total days	% Ice-free days between covers
1993	08/12/92	343	01/04/93	90	114	1	114	–
1994	27/12/93	361	–	–	–	–	–	–
1995	–	–	–	–	–	–	–	–
1996	05/12/95	339	25/04/96	115	142	1	142	–
1997	24/12/96	359	13/03/97	71	79	1	79	–
1998	<i>01/01/98</i> <i>10/04/98</i>	<i>1</i> <i>100</i>	<i>08/03/98</i> <i>10/05/98</i>	<i>66</i> <i>129</i>	<i>66</i> <i>30</i>	<i>2</i>	<i>96</i>	<i>34.4</i>
1999	30/11/98 16/12/98	334 350	12/12/98 13/04/99	345 102	12 118	2	130	3.1
2000	16/11/99	320	29/02/00	59	105	1	105	–
2001	19/12/00	354	–	–	–	1	–	–
2002	16/11/01	320	25/03/02	83	129	1	129	–
2003	23/11/02 05/01/03	327 5	25/12/02 22/04/03	358 111	32 107	2	139	7.9
2004	03/12/03 06/05/04	337 127	27/04/04 19/05/04	117 139	146 13	2	159	5.7
2005	04/12/04	339	10/04/05	99	127	1	127	–
2006	14/11/05	318	17/04/06	106	154	1	154	–
2007	10/12/06 23/01/07	344 23	19/01/07 22/04/07	18 111	40 89	2	129	3.1
2008	14/12/07 23/03/08	348 83	15/03/08 08/04/08	74 98	92 16	2	108	7.4
2009	25/11/08	330	25/04/09	114	151	1	151	–
2010	19/12/09	353	26/04/10	115	128	1	128	–
2011	23/11/10	327	14/04/11	103	142	1	142	–
2012	18/12/11 14/04/12	352 105	29/03/12 10/05/12	88 130	102 26	2	128	12.5
2013	13/01/13	13	23/05/13	142	130	1	130	–

Table 3.2. Ice phenology records for Peñalara Lake obtained by visual observations of the lake. The data in grey italics correspond to the anomalous year 1998 AD and were not included in the analyses.

Data year considered	Freeze-up date	Julian day	Break-up date	Julian day	Ice-cover duration in days
2007	28/11/2006	331	07/05/2007	126	160
2008	20/11/2007	323	20/06/2008	171	213
2009	05/11/2008	309	—	—	—
2010	03/12/2009	336	22/06/2010	172	201
2011	15/11/2010	318	26/05/2011	145	192
2012	14/11/2011	317	24/05/2012	144	192
2013	26/11/2012	330	16/06/2013	166	202

Table 3.3. Ice phenology records for Cimera Lake deduced from lake water column temperatures measured by thermistor chains at different water depths.

Daily visual observation		From lake water temperatures		Differences between dates (days)	
Freeze-up date	Break-up date	Freeze-up date	Break-up date	Freeze-up date	Break-up date
14/11/2005	17/04/2006	—	19/04/2006	—	2
10/12/2006	19/01/2007	—	—	—	—
23/01/2007	22/04/2007	23/01/2007	20/04/2007	0	-2
14/12/2007	15/03/2008	10/12/2007	15/03/2008	-4	0
23/03/2008	08/04/2008	23/03/2008	07/04/2008	0	-1
25/11/2008	25/04/2009	—	22/04/2009	—	-3
19/12/2009	26/04/2010	—	25/04/2010	—	-1
23/11/2010	14/04/2011	—	—	—	—
18/12/2011	29/03/2012	18/12/2011	25/03/2012	0	-4
14/04/2012	10/05/2012	14/04/2012	08/05/2012	0	-2
13/01/2013	23/05/2013	13/01/2013	23/05/2013	0	0

Table 3.4. Ice phenology dates from Peñalara Lake obtained by visual observations of the lake and deduced from lake water column temperatures measured by thermistor chains at different water depths.

3.2. Lake coring campaigns

In February 2012, seven sediment cores (6.6 and 9 cm inner diameters and up to 152 cm long) using the UWITEC® piston recovering system and three sediment cores (6.6 cm inner diameter and up to 45.5 cm long) using the UWITEC® gravity system were retrieved from Peñalara Lake (Fig. 3.5). In March 2012, ten cores (6.6 cm inner diameter and up to 124.8 cm long) were recovered from Cimera Lake using the UWITEC® gravity system (Fig. 3.5). The sediment cores were sealed, transported to the Instituto de Ciencias de la Tierra Jaume Almera-Consejo Superior de Investigaciones Científicas (ICTJA-CSIC; Barcelona, Spain) laboratory and stored in a cold room at + 4 °C until sampling.



Figure 3.5. UWITEC® A) piston and B) gravity recovering systems. C) Cutting a sediment core recovered from Cimera Lake in March 2012 before to be sealed the core with foam. D) Sediment cores recovered from Peñalara Lake in February 2012.

3.3. Core selection, image acquisition and sediment characterization

All the sediment cores were split longitudinally into two halves, and after a visual lithological description, the cores PE12-01-01 (126.5 cm long) from Peñalara Lake and CIM12-04A (124.8 cm long) from Cimera Lake were selected as the most representative of the main offshore facies of both lakes (Fig. 3.6).

After the selection of the cores, the best preserved half of each core was imaged with a Charged Coupled Device (CCD) colour line-scan camera mounted in an X-Ray Fluorescence (XRF) Avaatech core scanner located at the University of Barcelona (Spain) to obtain a visual record of both cores (Fig. 3.7).

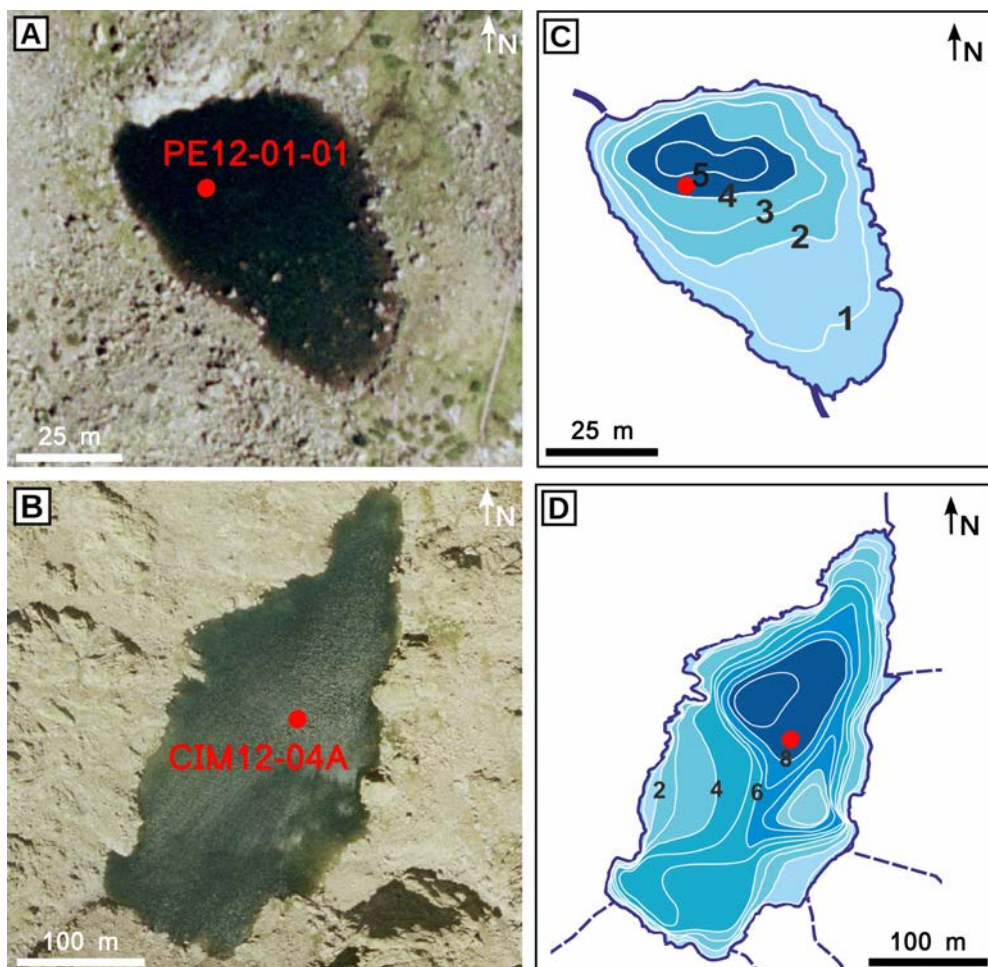


Figure 3.6. A) Aerial photo from the Instituto Geológico y Minero de España (IGME) and B) bathymetric map of Peñalara Lake. C) Aerial photo from the IGME and D) bathymetric map of Cimera Lake. Red points indicate the location of the cores used in this study, i.e., PE12-01-01 and CIM12-04A from Peñalara and Cimera lakes, respectively.



Figure 3.7. Core images acquired with a colour line-scan camera of A) the PE-12-01-01 core from Peñalara Lake and B) the CIM12-04A core from Cimera Lake. Top of both cores on the left.

Smear slides were conducted every 5 cm and in the most relevant sedimentary layers in both cores in order to identify and describe the main components of the sediments and their temporal evolution. Thus, 30 smear slides were collected from PE12-01-01, and 41 smear slides were collected from CIM12-04A (Fig. 3.8). In the smear slide procedure, a tiny sediment sample was taken using a toothpick and placed on a clear glass microscope slide, and the sample was then dispersed using a drop of distilled water. The sediment water/mixture was smeared out using the toothpick. The slide was allowed to dry over 24 hours to evaporate the water. A few drops of UV Loctite® 358 adhesive was then placed on the sample, and a glass cover slip was applied. Then, the smear slide was placed under UV light during 30 seconds to harden the adhesive (Rothwell, 1998) (Fig. 3.8). Microscopic observations under a high-end polarization microscope (Leica® DM4500 P with x630 magnification) located in the ICTJA-CSIC were then conducted (Fig. 3.8).

The uppermost 56.5 cm of the core PE12-01-01 is composed of dark brown organic-rich lacustrine sediments, whereas the lowermost 70 cm is composed of light grey and light brown sandy disturbed sediments, which probably accumulated under glacial-lacustrine conditions (Fig. 3.7). Hence, only the organic-rich lacustrine sediments from PE12-01-01 were considered when conducting the analyses.

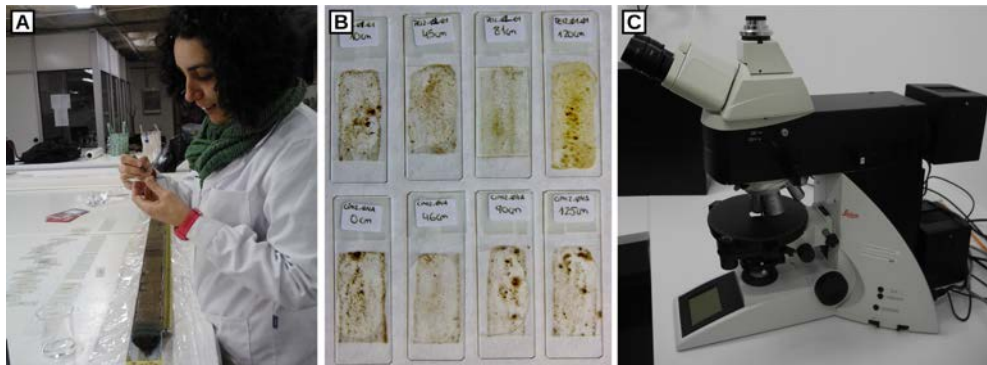


Figure 3.8. A) Smear slide preparation from lacustrine sediments using a toothpick (photo by S. Giralt). B) Image of smear slides from the PE12-01-01 and CIM12-04A cores (photo by S. Giralt). C) High-end polarization microscope Leica® DM4500 P located in ITCJA-CSIC (Barcelona, Spain) used in the observation of the smear slides (photo by E. Montoya).

3.4. Radiometric dating

3.4.1. ^{210}Pb and ^{137}Cs dating

The concentration profiles of ^{210}Pb along the lacustrine section of PE12-01-01 and in the uppermost 20 cm of the core CIM12-04A were determined by quantifying its decay product ^{210}Po by alpha spectroscopy following Sánchez-Cabeza et al. (1998) (Tables 3.5 and 3.6). The procedure consisted of adding a given amount of ^{209}Po as the internal tracer and then totally dissolving 200–300-mg sediment aliquots of each sample in an acid medium using an analytical microwave oven. Polonium isotopes were plated onto pure silver discs in HCl (1 N) at 70 °C while being stirred for 8 h. Polonium emissions were subsequently counted with alpha spectrometers equipped with low-background silicon surface barrier detectors for 4×10^5 s in the Laboratori de Radioactivitat Ambiental of the Institut de Ciència i Tecnologia Ambientals at the Universitat Autònoma de Barcelona (LaRAM ICTA-UAB, Barcelona, Spain) (Fig. 3.9).

Six samples from between 25 and 29 cm in the core PE12-01-01 were analysed for ^{226}Ra (via ^{214}Pb through its 351 keV gamma emission line) by gamma spectrometry using a high-purity intrinsic germanium detector located in the LaRAM ICTA-UAB (Fig. 3.9). The excess ^{210}Pb ($^{210}\text{Pb}_{\text{ex}}$) concentrations were calculated by subtracting ^{226}Ra (assumed to equal to the supported ^{210}Pb activity) from the total ^{210}Pb concentrations (Table 3.5). The supported ^{210}Pb concentration of the core CIM1204A was estimated by averaging the concentration of ^{210}Pb below 9 cm, where it remained constant because there was not enough material available to conduct measurements by gamma spectrometry (Table 3.6). The $^{210}\text{Pb}_{\text{ex}}$ -derived sediment accumulation rates of both cores were calculated by applying the constant flux: constant sedimentation model (CF:CS) (Krishnaswamy et al., 1971). The ^{137}Cs concentrations of six samples between 25 and 29 cm in the PE12-01-01 core were determined from the gamma measurements and used to constrain and verify the ^{210}Pb age model (Masqué et al., 2003).



Figure 3.9. A) ORTEC® and B) Canberra® alpha spectrometers used for the ^{210}Pb analyses. C) HPGe gamma spectrometer and its D) coaxial Ge detector used for the ^{226}Ra and ^{137}Cs analyses. All the equipment is located in the LaRAM ICTA-UAB (Barcelona, Spain). Photos by J.J. Bruach.

PE12-01-01 core depth (cm)	Accumulated mass (g·cm⁻²)	²¹⁰Pb total (Bq·kg⁻¹)	²¹⁰Pb excess (Bq·kg⁻¹)	¹³⁷Cs (Bq·kg⁻¹)	²²⁶Ra (Bq·kg⁻¹)
0	0.22	190 ± 10	112 ± 12	–	–
3.5	1.08	216 ± 11	137 ± 13	–	–
8	2.47	234 ± 11	155 ± 13	–	–
12	3.49	253 ± 11	175 ± 13	–	–
16	4.61	243 ± 9	164 ± 11	–	–
20	5.71	246 ± 10	167 ± 12	–	–
24	7.07	252 ± 11	174 ± 12	–	–
24.5	7.27	244 ± 17	166 ± 18	–	–
25	7.44	300 ± 15	151 ± 16	70 ± 5	82 ± 3
25.5	7.64	229 ± 9	151 ± 11	65 ± 2	87 ± 3
26	7.82	212 ± 14	134 ± 15	65 ± 5	83 ± 9
26.5	8.00	197 ± 15	118 ± 16	–	–
27	8.26	180 ± 7	102 ± 9	–	–
27.5	8.47	173 ± 11	95 ± 12	–	–
28	8.69	149 ± 7	71 ± 9	62 ± 3	75 ± 5
28.5	8.98	142 ± 5	63 ± 8	38 ± 1	72 ± 2
29	9.18	–	–	42 ± 1	72 ± 3
29.5	9.33	147 ± 8	68 ± 10	–	–
30	9.55	138 ± 7	60 ± 9	–	–
31.6	10.16	122 ± 5	44 ± 8	–	–
33	10.75	102 ± 4	24 ± 8	–	–
34.6	11.42	108 ± 5	30 ± 8	–	–
36	–	150 ± 6	71 ± 9	–	–
37.5	–	144 ± 7	65 ± 9	–	–
39	–	–	–	–	–
40.5	–	143 ± 7	65 ± 9	–	–
42	–	–	–	–	–
43.5	–	154 ± 6	75 ± 9	–	–
45	–	147 ± 6	68 ± 9	–	–

PE12-01-01 core depth (cm)	Accumulated mass (g·cm ⁻²)	²¹⁰ Pb total (Bq·kg ⁻¹)	²¹⁰ Pb excess (Bq·kg ⁻¹)	¹³⁷ Cs (Bq·kg ⁻¹)	²²⁶ Ra (Bq·kg ⁻¹)
46.5	—	—	—	—	—
48	—	141 ± 6	62 ± 9	—	—
49.5	—	—	—	—	—
51	—	154 ± 9	76 ± 11	—	—
52.5	—	146 ± 6	67 ± 8	—	—
54	—	—	—	—	—
56.5	—	98.0 ± 5.2	19.4 ± 8.1	—	—

Table 3.5. Total and excess ²¹⁰Pb, ¹³⁷Cs and ²²⁶Ra concentrations in the core PE12-01-01.

CIM12-04A core depth (cm)	Accumulated mass (g·cm ⁻²)	²¹⁰ Pb total (Bq·kg ⁻¹)	²¹⁰ Pb excess (Bq·kg ⁻¹)
0.1	0.04	1211 ± 39	993 ± 41
0.3	0.07	1249 ± 48	1032 ± 50
0.5	0.09	1176 ± 45	959 ± 47
0.7	0.12	1041 ± 57	823 ± 58
0.9	0.13	1262 ± 48	1044 ± 49
1.1	0.17	1123 ± 49	905 ± 50
1.3	0.19	1215 ± 67	997 ± 68
1.5	0.22	1170 ± 67	952 ± 68
1.7	0.26	1109 ± 58	891 ± 60
1.9	0.31	1027 ± 52	808 ± 54
2.1	0.39	1154 ± 52	936 ± 53
2.3	0.44	1014 ± 55	795 ± 56
2.5	0.48	1063 ± 50	845 ± 51
2.7	0.55	949 ± 53	730 ± 54
2.9	0.62	1036 ± 57	818 ± 58
3.1	0.69	1055 ± 37	837 ± 38
3.3	0.76	946 ± 56	727 ± 57
3.5	0.79	929 ± 54	710 ± 55

CIM12-04A core depth (cm)	Accumulated mass (g·cm ⁻²)	²¹⁰ Pb total (Bq·kg ⁻¹)	²¹⁰ Pb excess (Bq·kg ⁻¹)
3.7	0.83	919 ± 42	700 ± 43
3.9	0.93	874 ± 45	656 ± 47
4.1	1.01	683 ± 33	465 ± 35
4.3	1.07	751 ± 42	533 ± 44
4.5	1.13	701 ± 38	483 ± 39
4.7	1.17	659 ± 34	441 ± 36
4.9	1.23	616 ± 34	398 ± 36
5.1	1.32	549 ± 19	330 ± 22
5.3	1.39	539 ± 34	321 ± 36
5.5	1.46	439 ± 20	221 ± 22
5.7	1.51	527 ± 32	308 ± 33
5.9	1.60	587 ± 29	368 ± 31
6.1	1.68	499 ± 23	281 ± 25
6.3	1.74	434 ± 24	216 ± 26
6.5	1.80	411 ± 16	193 ± 19
6.7	1.90	424 ± 25	206 ± 27
6.9	1.95	404 ± 24.4	185 ± 27
7.1	2.06	439 ± 15	220 ± 18
7.3	2.11	454 ± 26.7	236 ± 29
7.5	2.18	459 ± 25.9	241 ± 28
7.7	2.25	437 ± 15.3	218 ± 19
7.9	2.35	453 ± 26.4	235 ± 27
8.1	2.43	447 ± 15.1	229 ± 18
8.3	2.49	453 ± 25	235 ± 27
8.5	2.56	—	—
8.7	2.68	446 ± 16	228 ± 19
8.9	2.79	404 ± 19	186 ± 21
9.1	2.94	351 ± 16	133 ± 20

Table 3.6. Total and excess ²¹⁰Pb concentrations in the core CIM12-04A.

3.4.2. AMS ^{14}C radiocarbon dating

^{14}C radiocarbon dating was performed on terrestrial plant macroremains and pollen concentrates. The pollen concentrates were obtained following the protocol of Rull et al. (2010):

- Transfer 2 cc of sediment sample into 50 ml test glass tubes
- Add 15 ml of potassium hydroxide solution (10%), stir and heat in a water bath for 20 minutes
- Add distilled water up to 50 ml, stir, centrifuge and decant
- Rinse a minimum of two times with water until the pH of distilled water is attained
- Sieve through a 200 μm mesh
- Add 15 ml of hydrochloric acid (37%), stir and heat in a water bath for 10 minutes
- Add distilled water up to 50 ml, stir, centrifuge and decant
- Rinse a minimum of two times with water until the pH of distilled water is attained
- Transfer the sample to a Teflon test tube, centrifuge and decant
- Add 15 ml of hydrofluoric acid (70%), stir and heat in a water bath for 20 minutes, centrifuge and decant
- Add 15 ml of HF, stir and leave overnight (~12 hours)
- Add distilled water up to 50 ml, stir, centrifuge and decant
- Rinse a minimum of two times with water until the pH of distilled water is attained
- Transfer the suspension to a small glass vial with a screw cap

A total of 6 and 7 AMS ^{14}C samples were obtained for PE12-01-01 and CIM12-04A cores, respectively. Samples for radiocarbon dating were analysed at either the Beta Analytic Laboratory (USA) or the Poznan Radiocarbon Laboratory (Poland). Radiocarbon ages were calibrated to calendar years (BP and AD/BC) using the online CALIB 7.1 software (Stuiver and Reimer, 1993) and INTCAL13 curve (Reimer et al., 2013) by selecting the median of the 95.4% distribution (2σ probability interval).

3.4.3. Chronological models

The age-depth model for PE12-01-01 core was constructed by linear interpolation between selected ^{14}C dates together with ^{210}Pb and ^{137}Cs profiles, and the age-depth model for the CIM12-04A core was established using ^{210}Pb profiles and the R-code package 'clam' and a smooth spline (type 4) with a 0.3 smoothing value and 1000 iterations applied to the selected ^{14}C dates (Blaauw, 2010).

3.5. Geochemical analyses

3.5.1. X-Ray Fluorescence (XRF) core scanning

An XRF Avaatech® core scanner (Fig. 3.10A) was employed to determine the chemical composition of the sediments from both cores. The core scanner is installed in a seagoing container, and the measurement system moves along one half of the core (Fig. 3.10B). A prism is lowered onto the sediment surface at each measurement position, and radiation generated in the X-ray tube enters at an angle of 45°. The incoming X-ray radiation provokes an electron of a given chemical element to be ejected from an inner shell of the atom, and the resulting vacancy is subsequently filled by an electron falling back from an outer shell. The energy difference between the two shells is emitted as electromagnetic radiation. The wavelength of the emitted radiation is characteristic for each element, and the amplitudes of peaks in the XRF spectrum are proportional to the concentrations of the corresponding elements in the analysed sample. The detector of the outgoing radiation is likewise installed at an angle of 45° (Fig. 3.10C). The entire measurement system is flushed with helium to prevent partial or complete absorption of emitted soft radiation from the sample by air. A net counting time of 30 seconds is commonly applied, although major element analysis can be achieved with shorter counting times (Richter et al., 2006). The XRF settings for the PE12-01-01 and CIM12-04A core analyses were as follows: 2 mm spatial resolution; 2 mA; 15 s count time and 10 kV for lighter elements; and 55 s count time and 30 kV for heavier elements. Thirty chemical elements were measured, although only ten light (Al, Si, K, Ca, Ti, V, Cr, Mn, Fe and Zn) and three heavy (Rb, Sr and Zr) elements had sufficient counts to be considered statistically consistent.



Figure 3.10. A) Image of the XRF Avaatech core scanner at the University of Barcelona (Spain). B) XRF Avaatech core scanner measurement system moving along a core half. C) The prism of the XRF Avaatech core scanner measurement system (photos by J. Frigola)

3.5.2. Bulk X-Ray Diffraction (XRD)

Different sampling resolutions were selected in the upper and lower parts of both cores for determining bulk mineralogical composition by XRD. These sampling resolutions were based on previous chronological models conducted on Peñalara (Toro and Granados, 2002) and Cimera sediments (Granados and Toro, 2000). The PE12-01-01 core was sampled every 2 mm between 0 and 37 cm depth (186 samples), and every 5 mm between 37 and 56.5 cm depth (39 samples). The CIM12-04A core was sampled every 2 mm between depths of 0 and 36 cm (181 samples) and every 5 mm between

depths of 36 and 124.8 cm (178 samples). All of the samples were dried at 60 °C for 48 h and manually ground using an agate mortar. The XRD analysis was conducted using a SIEMENS®-D500 automatic X-Ray diffractometer (Cu K-alpha, 40 kV, 30 mA, with a graphite monochromator) at the ICTJA-CSIC (Barcelona, Spain) (Fig. 3.11A). Powder samples were added to measurement plates with a diameter of 25 mm and a height of 1 mm and manually compacted prior to loading into the diffractometer (Fig. 3.11B). The XRD patterns revealed that the samples were primarily composed of a crystalline fraction (highlighted by different peaks) and a negligible amorphous one. The identification and quantification of the relative abundances of the different mineralogical species were conducted following the standard procedure (Chung, 1974a, 1974b).

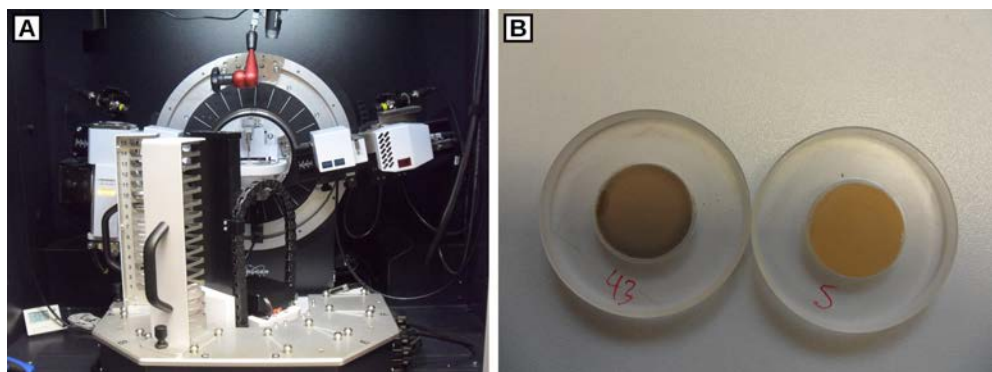


Figure 3.11. A) Image of the SIEMENS®-D500 automatic X-ray diffractometer at the ICTJA-CSIC (Barcelona, Spain) used to determine the mineralogical composition via bulk XRD. B) Image of two compacted samples prepared on measurement plates for XRD analysis.

3.5.3. Clay X-Ray Diffraction (XRD)

Among the samples used for bulk XRD analysis, 35 samples from PE12-01-0 and 63 samples from CIM12-04A were selected for identification of clay minerals composition via XRD. The XRD analysis was conducted using the X-Ray diffractometer located at the ICTJA-CSIC (Barcelona, Spain) (Fig. 3.11A). The clay fraction separation was performed according to Moore and Reynolds (1997). A clay suspension of each sample was pipetted onto a glass slide and air dried for 24 h to obtain oriented aggregates. Then, glycolation and heat treatment (350 °C) were applied to the dried samples. XRD analysis of the treated samples (dried, glycolated and heated) was finally employed to identify the clays. The identification and quantification of the relative abundance of the different clay minerals were conducted following the same standard procedure as for mineral species (Chung, 1974 a, b). The clay composition of a sample of a dust collected after a dust deposition episode in June 2014 in the Cimera Lake catchment was also determined (Fig. 3.12).



Figure 3.12. Photos of a dust deposition episode in Cimera Lake catchment taken in June 2014. A dust sample of this episode was collected for XRD analysis.

3.5.4. Bulk elemental (TC, TN) and stable isotope ($\delta^{13}\text{C}$, $\delta^{15}\text{N}$) organic chemistry

The same samples employed to measure the bulk mineralogical composition via XRD were also used to determine the TC, TN and stable isotope values ($\delta^{13}\text{C}$, $\delta^{15}\text{N}$) in both cores. For these organic chemistry analyses, 2.5 mg of each ground sample was weighed in a CPA225D electronic microbalance (0.01 mg readability, 100 g weighting capacity) at the ICTJA-CSIC and packed in a tin (Sn) capsule (4 mm of diameter and 6 mm long) (Fig. 3.13). Vanadium pentoxide (VO_5) was added to all the samples prior to encapsulation to catalyse oxidation.

The TC, TN (RSD, 5% of the measurements) and stable isotope ($\delta^{13}\text{C}$, $\delta^{15}\text{N}$, 0.2‰ analytical precision) analyses were conducted using a Finnigan DELTAplus® TC/EA-CF-IRMS spectrometer at the Centres Científics i Tecnològics of the Universitat de Barcelona (CCiT-UB, Barcelona, Spain) (Fig. 3.14). The CF-IRMS transforms the sample into a gas that is then introduced into the spectrometer automatically. The procedure consists of sample combustion, gas treatment (CO_2 , N_2 , CO) and gas separation in a chromatographic column in order to separately analyse the gases using a mass spectrometer. Combustion takes place in an oven with an oxygen atmosphere into which the small tin capsule is introduced. The reference substances used to calibrate the stable isotope measurements are shown in Table 3.7.

The carbonate content of the samples was below the detection limit (< 1%) of the XRD analysis; thus, the TC was considered equivalent to the total organic carbon (TOC).

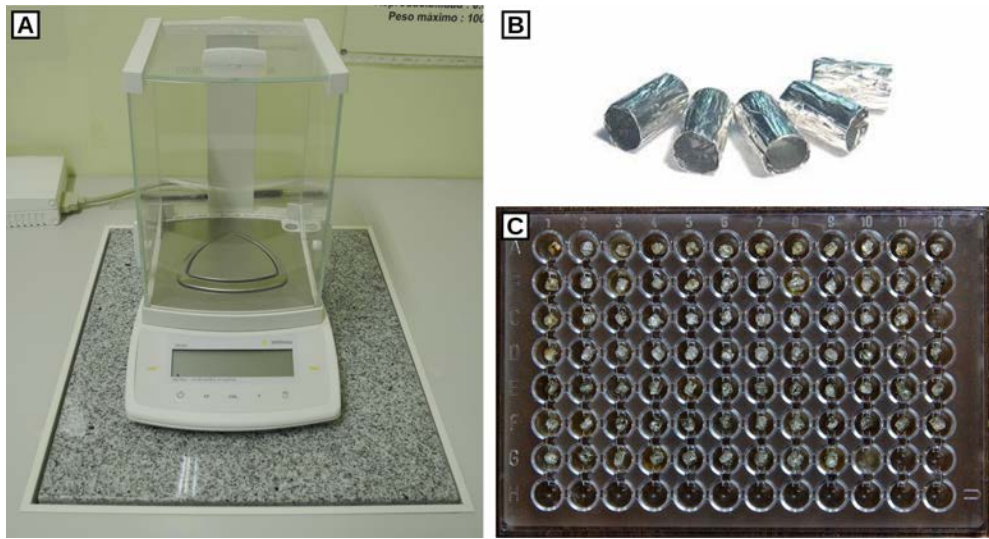


Figure 3.13. A) CPA225D electronic microbalance located in the ICTJA-CSIC (Barcelona, Spain) used to weigh ground samples for TC, TN, $\delta^{13}\text{C}$ and $\delta^{15}\text{N}$ analyses (photo by E. Montoya). B) Tin capsules used to package the samples (<http://www.ludiswiss.com>). C) Microtiter plate used to contain the samples after packing (photo by S. Giralt).



Figure 3.14. Image of the Finnigan DELTAplus® TC/EA-CF-IRMS spectrometer at the CCiT-UB (Barcelona, Spain) (photo by J.J. Pueyo).

Stable isotope	Reference	Isotopic signature (‰)	Standard deviation
$\delta^{13}\text{C}$	Antropina	-28.8	—
	IAEA CH7	-32.2	0.050
	IAEA CH6	-10.4	0.033
	USGS 40	-26.3	0.042
	UCGEMA-F	-26.3	—
	UCGEMA-S	-24.9	—
$\delta^{15}\text{N}$	IAEA N2	4.7	0.2
	IAEA N1	20.5	0.2
	IAEA NO3	4.7	—
	USGS 40	-4.3	—
	UCGEMA-F	4.9	—

Table 3.7. References used for the stable isotope analyses, their corresponding isotopic signature values and standard deviations.

3.5.5. Elemental chemical analyses ($[\text{NO}_3^-]$, $[\text{SO}_4^{2-}]$, [TP])

Nitrate (NO_3^-), total phosphorus (TP) and sulphate (SO_4^{2-}) concentrations were also measured in the dust sample collected from the Cimera Lake catchment in June 2014 (Fig. 3.12). An aliquot of this sample was treated with a hot 5% HCl solution to extract soluble nitrogen, phosphorus and sulphate compounds. Nitrate and sulphate were measured in the solution by ion chromatography, and phosphorus was measured by inductively coupled plasma mass spectrometry (ICP-MS) at the CCiT-UB (Fig. 3.15).



Figure 3.15. A) Plasma source of the inductively coupled plasma mass spectrometer (ICP-MS) and B) ion chromatography line, both at the CCiT-UB (Barcelona, Spain). C) A detail of its column and injection pump.

3.6. Statistical treatment of data

3.6.1. Pearson product-moment correlation coefficients

The freeze-up process begins in early winter (November-December) in both lakes, whereas the break-up process ranges from late winter to early spring (March-April) for Peñalara Lake to late spring (May-June) for Cimera Lake (Tables 3.2 and 3.3). Due to these differences, two seasons were defined to obtain comparable relationships between the NAO index, climatic and ice phenology instrumental datasets in each lake. The winter season, which spans from January to March (hereafter JFM), and the spring season, which spans from March to May (hereafter MAM). Pearson's correlation analyses at 1%, 5%, and 10% significance levels were used to obtain correlation coefficients and their respective p-values between the different instrumental datasets for JFM and MAM in each lake (Table 3.1). In addition, because the freezing process is quicker than the melting process, monthly data from September to December were also used in the analysis of the freezing process in both lakes. In the following text and unless otherwise stated, significance (p-value) always refers to $p < 0.01$.

Pearson's correlation analyses at 1% and 5% significance levels were conducted for the thirteen chemical elements obtained by XRF analysis in both cores to eliminate redundant information and simplify the results. From the elements with highly significant correlations ($r > 0.8$, p -value < 0.01 ; Table 3.8), the most representative elements with the largest number of XRF counts (i.e., Ti, Si, V, Cr, Mn, Zn, Rb and Zr) were selected to conduct the following statistical analyses for the PE12-01-01 and CIM12-04A cores.

3.6.2. Redundancy Data Analyses (RDA)

It was necessary to resample the XRF data using linear interpolation to obtain the same spatial resolution among all the proxies used in the RDAs. The XRF data were resampled with a regular spacing of 5 mm between 37 and 56.5 cm depth for PE12-01-01 core and between 36 and 124.8 cm depth for CIM12-04A core using the function 'approxTime' from the package 'simecol' (Petzoldt and Rinke, 2007) in the R software (R Core Team, 2015).

RDAs were conducted between the geochemical datasets (i.e., XRF, TOC, TN, $\delta^{13}\text{C}$ and $\delta^{15}\text{N}$ data) as the response variable and the mineralogical datasets obtained from XRD analyses as the explanatory variable in each core. The mineralogical composition of the sediment was used as a constraining matrix because each mineralogical species represents a 'compendium' of geochemical elements (Giralt et al., 2008). The RDA was used to establish the origin of the geochemical parameters and their relationships with the associated mineral phases. This statistical treatment of the data was performed using the package 'vegan' (Oksanen et al., 2013) in the R software (R Core Team, 2015).

A)

	Al	Si	K	Ca	Ti	V	Cr	Mn	Fe	Zn	Rb	Sr	Zr
Al	1												
Si	0.99	1											
K	0.97	0.97	1										
Ca	0.96	0.96	0.98	1									
Ti	0.96	0.96	0.98	0.97	1								
V	0.48	0.48	0.48	0.47	0.5	1							
Cr	0.59	0.59	0.6	0.6	0.58	0.33	1						
Mn	0.90	0.89	0.94	0.93	0.93	0.48	0.58	1					
Fe	0.93	0.92	0.97	0.95	0.98	0.48	0.57	0.94	1				
Zn	0.23	0.25	0.15	0.14	0.26	0.23	<i>0.03</i>	0.16	0.24	1			
Rb	0.89	0.88	0.95	0.93	0.93	0.46	0.56	0.91	0.95	0.12	1		
Sr	0.64	0.62	0.75	0.75	0.7	0.32	0.45	0.72	0.73	-0.29	0.82	1	
Zr	0.44	0.47	0.49	0.55	0.51	0.3	0.28	0.5	0.5	0.15	0.49	0.43	1

B)

	Al	Si	K	Ca	Ti	V	Cr	Mn	Fe	Zn	Rb	Sr	Zr
Al	1												
Si	0.99	1											
K	0.84	0.88	1										
Ca	0.41	0.47	0.69	1									
Ti	0.69	0.74	0.94	0.79	1								
V	0.31	0.34	0.5	0.54	0.59	1							
Cr	0.6	0.62	0.62	0.46	0.62	0.37	1						
Mn	0.34	0.34	0.31	0.34	0.32	0.14	0.31	1					
Fe	0.52	0.59	0.84	0.69	0.92	0.58	0.54	0.19	1				
Zn	0.23	0.26	0.4	0.63	0.55	0.38	0.37	0.4	0.53	1			
Rb	0.2	0.22	0.42	0.37	0.4	0.21	0.1	-0.02	0.29	<i>0.01</i>	1		
Sr	<i>0.06</i>	<i>0.08</i>	0.26	0.44	0.29	0.24	<i>0.08</i>	<i>0</i>	0.17	<i>0.06</i>	0.81	1	
Zr	0.13	0.17	0.41	0.53	0.56	0.38	0.27	0.18	0.58	0.57	0.24	0.18	1

Table 3.8. Pearson's correlation coefficients among the elements obtained by XRF analysis from A) PE12-01-01 and B) CIM12-04A cores, respectively. All of the correlations are significant at the 0.01 level except for the numbers in italics and grey, which indicate no significant correlations; $n>250$.

3.6.3. Principal Component Analyses (PCA)

The geochemical datasets (i.e., the XRF previously resampled for the RDAs, TOC, TN, $\delta^{13}\text{C}$ and $\delta^{15}\text{N}$ data) used in PCAs were previously normalised to avoid problems arising from their different orders of magnitude.

PCAs were applied to the normalized geochemical datasets to determine the main environmental processes that controlled the input, distribution and deposition of the sediments in both lakes. This statistical treatment of the data was performed using the package 'vegan' (Oksanen et al., 2013) in the R software (R Core Team, 2015).

3.6.4. The Bayesian model: random walk-modularised model

The employed modelling approach was based on a Bayesian model of Parnell et al. (2015), which used raw pollen data to infer past climate conditions. The parallelism between the environmental and climate implications derived from a pollen study and the chemical data from XRF analysis of the core CIM12-04A have allowed us to reproduce this approach. In spite of the methodological differences between the two proxies, the palynological composition of the sediments is commonly determined for a given number of sediment layers (depths) in the same way as the chemical composition of the sediments, which consists of measuring the counts per second of the sediment core at regular depths (i.e., every 2 mm) for a given number of different chemical elements. In this case, it was unnecessary to eliminate the redundancy information from the XRF data because the model performs an automatic selection of the geochemical data most related to climate. Hence, this Bayesian model can reconstruct the evolution of the NAO impact in the ICR (NAO_{ICR}) for the last two millennia from raw chemical elements obtained by XRF analysis (see below for further information). The notation of the model is outlined here:

- m and f superscripts denote modern and fossil elements, respectively.
- i and j subscripts correspond to the number of the core layers (i.e., depth) and the chemical elements from XRF proxy, respectively.
- t represents the age of all depths in the sediment core. t^m_i corresponds to modern ages of the overlapping period in Anno Domini (AD) years, and t^f_i corresponds to fossil ages not included in the overlapping period in AD and Before Christ (BC) years.
- XRF_{ij} (expressed as counts per second) represents the chemical element j measured at the depth i in the CIM12-04A core. XRF^m_{ij} corresponds to modern data in the overlapping period whereas XRF^f_{ij} denotes fossil data not included in the overlapping period.
- NAO^m_i is modern annual index data for each t^m_i in the overlapping period.
- NAO^{grid} is a grid of NAO values of length k .
- θ is a set of parameters $(\beta_0, \beta_1, \beta_2, \mu, \sigma)$ governing the relationship between NAO and XRF in the overlapping period. μ corresponds to the mean and σ represents the standard deviation.
- NAO' is the fossil impact of NAO estimated by the model (i.e., NAO_{ICR}).

Using the notation above, we created the following general model equation:

$$p(NAO^f | XRF^f, NAO^m, XRF^m) \propto p(XRF^m | NAO^m) \cdot p(XRF^f | NAO^f) \cdot p(NAO^f)$$

where $p(NAO^f | NAO^m, XRF^m, XRF^f)$ is the posterior distribution, $p(XRF^m | NAO^m)$ is the 'modern' likelihood (i.e., modern calibration model), $p(XRF^f | NAO^f)$ is the 'fossil' likelihood and $p(NAO^f)$ is the fossil prior distribution.

The model is a random walk because the NAO reconstruction depends on modern time, and it is a modularised model because it is divided into different steps, which are detailed below. We used the JAGS package (Just Another Gibbs Sampler; Plummer, 2003) to fit the model via Gibbs sampling and the R software (R Core Team, 2015). The reader is referred to the Appendix A (Text A.1), which provides a theoretical R session with all the mathematical details. The model steps are as follows:

I) Initial calibration step: The aim of this first step is to estimate the causal link between climate (NAO^m) and the proxy (XRF^m) during the overlapping instrumental period. The selected overlapping instrumental period is 1930–2012 AD because the constructed age-depth model from the recovered sedimentary record of Cimera Lake showed a multidecadal uncertainty prior to the 1930s. XRF^m data were resampled with a yearly resolution for the overlapping period using the R function 'approxTime' from the package 'simecol' (Petzoldt and Rinke, 2007). NAO^m and XRF^m corresponding to 2010 AD were excluded from the modern dataset because the NAO index in this year is considered an anomalous value. It had a largely negative probability distribution when compared with the rest of the NAO data during the overlapping period.

The statistical link between climate (NAO^m) and the proxy (XRF^m) is obtained by estimating the posterior probability distributions of the θ parameters ($\beta_0, \beta_1, \beta_2, \mu, \sigma$) during the selected overlapping period. The Bayesian equation used to estimate this relationship was the following:

$$p(\theta | XRF^m, NAO^m) \propto p(XRF^m | NAO^m, \theta) \cdot p(NAO^m) \cdot p(\theta)$$

where $p(\theta)$ is the prior probability distribution of $\beta_0, \beta_1, \beta_2, \mu_0$ and σ , $p(NAO^m)$ is the random walk prior probability distribution, $p(XRF^m | NAO^m, \theta)$ is the likelihood probability distribution and $p(\theta | XRF^m, NAO^m)$ is the posterior probability distribution of the parameters.

$p(XRF^m | NAO^m, \theta)$ was approximated as a gamma distribution (Ga):

$$p(XRF_{ij}^m) \sim Ga(\alpha_{ij}, \delta_{ij})$$

$$\alpha_{ij} = \frac{\mu_{ij}^2}{\sigma_{ij}^2}, \quad \delta_{ij} = \frac{\mu_{ij}}{\sigma_{ij}^2}$$

$$\mu_{ij} = e^{\left(\beta_{0j} + \beta_{1j} \cdot NAO_i + \beta_{2j} \cdot NAO_i^2\right)}, \quad \sigma_{ij} = e^{\mu_{0j}}$$

μ_{ij} and σ_{ij} correspond to mean and standard deviations of the gamma distribution, respectively.

We approximated the prior probability distributions of β_{0j} , β_{1j} , β_{2j} , μ_{0j} , as normal distributions and approximated the prior probability distribution of σ as a uniform distribution, defining their means and their precisions as follows:

$$p(\beta_{0j}) \sim N(0, 100), \quad p(\beta_{1j}) \sim N(0, 100), \quad p(\beta_{2j}) \sim N(0, 100),$$

$$p(\mu_j) \sim N(0, 100), \quad p(\sigma) \sim U(0, 100)$$

$p(\text{NAO}^m)$ was approximated as a time-dependent normal distribution through the precision (prec):

$$p(\text{NAO}_i^m) \sim N(\text{NAO}_{i-1}^m, \text{prec}_i)$$

$$\text{prec}_i = \frac{1}{(t_i^m - t_{i-1}^m) \cdot \sigma^2}$$

Finally, we ran the model to obtain the posterior probability distributions of the Θ parameters, $p(\Theta | XRF^m, \text{NAO}^m)$. The settings of the JAGS package were 4 chains, 3000 iterations and 2000 burn-ins.

II) Creating Marginal Data Posteriors (MDPs) step: The objective of this second step is to obtain the posterior distributions of the NAO given only the information in that layer of the core. These are known as Marginal Data Posteriors (MDPs) of NAO.

The MDPs of NAO for each layer were obtained using an NAO^{grid} of k=50 values between -3 and 3, the posterior probability distribution of the Θ parameters from the calibration step and the XRF^f data. The k MDPs of each layer were the sum of the gamma distributions of each j chemical element:

$$p(MDP_{ik}) \sim Ga(\alpha_j, \delta_j)$$

$$\alpha_j = \frac{\mu_j^2}{\sigma_j^2}, \quad \delta_j = \frac{\mu_j}{\sigma_j^2}$$

$$\mu_j = e^{\left(\beta_{0j} + \beta_{1j} \cdot \text{NAO}_k^{grid} + \beta_{2j} \cdot \text{NAO}_k^{grid^2}\right)}, \quad \sigma_j = e^{\mu_{0j}}$$

Finally, we calculated the precision (precis_{MDP}) and the mean (μ_{MDP}) of the k MDPs obtained for each layer (MDP_{ik}) and their maximum and minimum uncertainties (ε_{max} , ε_{min}):

$$\mu_{MDPi} = MDP_i^{final} \cdot \text{NAO}^{grid}, \quad MDP_i^{final} = \frac{MDP_i}{\sum_k MDP_k}$$

$$\sigma_{MDP_i} = \sqrt{MDP_i^{final} \cdot NAO^{grid^2} - \mu_i^2}, \quad precis_{MDP_i} = \frac{1}{\sigma_{MDP_i}^2}$$

$$\varepsilon_{max_i} = \mu_{MDP_i} + 2 \cdot sd_{MDP_i}, \quad \varepsilon_{min_i} = \mu_{MDP_i} - 2 \cdot \sigma_{MDP_i}$$

III) Model fitting step: We create the posterior distribution of NAO^f using the $MDPs$. In other words, we obtained the NAO_{ICR} for the last two millennia. The posterior distribution of NAO^f is created using the mean (μ_{MDP}) and precision ($precis_{MDP}$) of the $MDPs$ from step II. The Bayesian equation of this step is as follows:

$$p(NAO^f | MDPs) \propto p(MDPs | NAO^f) \cdot p(NAO^f)$$

where $p(NAO^f)$ is the random walk prior probability distribution, $p(MDPs | NAO^f)$ is the likelihood probability distribution and $p(NAO^f | MDPs)$ is the posterior probability distribution of the NAO^f .

$p(NAO^f)$ was approximated as a time-dependent normal distribution through the precision ($precis_f$). The first NAO^f should have a vague prior distribution:

$$p(NAO_i^f) \sim N(NAO_{i-1}^f, precis_{f_i}) \quad i=2,3,4 \dots n \text{ layers}$$

$$p(NAO_1^f) \sim N(0, 100) \quad i=1$$

$$precis_{f_i} = \frac{1}{(t_i^f - t_{i-1}^f) \cdot \sigma^2}$$

The $p(MDPs | NAO^f)$ likelihood is approximated as a normal distribution:

$$\mu_{MDP_i} \sim N(NAO_i^f, precis_{MDP_i})$$

In the data model, we also include the first NAO^m as it depends on the last NAO^f value. This is approximated as a normal distribution. The sd has a log-normal distribution with the parameters a and b :

$$NAO_1^m \sim N(NAO_i^f, precis_{mf}) \quad i=n \text{ layers}$$

$$precis_{mf} = \frac{1}{(t_{m_1} - t_{f_i}) \cdot \sigma^2} \quad i=n \text{ layers}$$

$$\sigma \sim \exp(a, b)$$

Once we defined all the data for the model, we ran the model to obtain the posterior probability distribution of NAO^f , $p(NAO^f|MDPs)$. The settings of the JAGS package (Plummer, 2003) were 3 chains, 3000 iterations and 2000 burn-ins. Finally, the impact of the NAO in the ICR (NAO_{ICR}) for the last two millennia were calculated as the median of NAO^f obtained from the model and its uncertainties as the 5th and 95th quantiles.

IV) Model validation step: As in any reconstruction, the last step of the model is involves statistical validation. A 5-fold cross-validation of the modern data was conducted to evaluate the model performance. The predicted geochemical data were obtained as the median of the predicted values and the uncertainty bounds containing the true (i.e., measured) data for 80% of the samples. The correlation between the true and predicted data was also calculated.

In addition, the NAO_{ICR} obtained was visually compared with the multidecadal NAO index from CRU for the period 1930–1825 AD, which was not included in the calibration of the model. This multidecadal NAO index was calculated using a loess function and smoothing span degree of 0.10. The non-stationary variability of the uncertainties associated with the chronological model of Cimera Lake hampered the mathematical comparison between the instrumental and the reconstructed data.

Finally, to determine whether some global aspects could be depicted in the reconstructed NAO impacts for the ICR, the NAO_{ICR} was visually compared with three different NAO approaches: i) the approach from Trouet et al. (2009), which is a simplistic approach based on two records (from Scotland and Morocco) (Fig. 3.16); ii) the variability in NAO obtained by Olsen et al. (2012), which is also a simplistic approach based on a palaeo-redox proxy (Mn/Fe ratio) in a sediment record from a small lake near Kangerlussuaq (Greenland) (Fig. 3.16); and iii) the much more robust reconstruction by Ortega et al. (2015), which employed multi-proxy data from different locations in the Northern Hemisphere (i.e., 48 proxies) (Fig. 3.16).

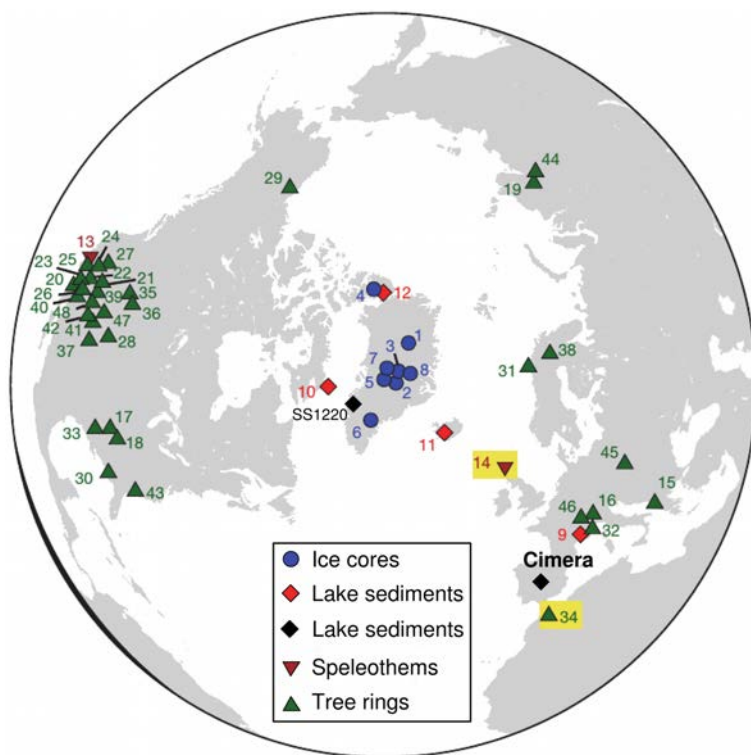


Figure 3.16. Location of the initial 48 proxy records (ice cores, lake sediments, speleothems and tree rings) used for the reconstruction of the NAO by Ortega et al. (2015). The two proxies used in the NAO approach of Trouet et al. (2009) are highlighted with yellow boxes. Records from Lake SS1220 (Kangerlussuaq, $67^{\circ}03'N$ - $51^{\circ}13'W$) used in the NAO approach by Olsen et al. (2012) and the Cimera Lake record are shown with black diamonds. The figure was modified from Ortega et al. (2015).

4. RESULTS

4.1. Relationships between climate index, climatic and limnological data

The results of Pearson's correlation analyses between the studied series for JFM and MAM and between monthly data from September to December are shown in Tables 4.1 and 4.2 for Peñalara Lake and in Tables 4.3 and 4.4 for Cimera Lake, respectively.

4.1.1. Peñalara Lake

During JFM, the NAO is positively correlated with air temperature ($r= 0.69$) and negatively with precipitation ($r= -0.67$) and snow days ($r= -0.64$). Air temperature displays negative correlations with precipitation ($r= -0.59$), snow days ($r= -0.75$), ice-cover duration ($r= -0.59$, p-value < 0.05) and ice-off ($r= -0.65$), whereas precipitation is positively correlated with snow days ($r= 0.69$), ice-cover duration ($r= 0.52$, p-value < 0.05) and ice-off ($r= 0.53$, p-value < 0.05). Snow days show positive correlations with ice-cover duration and ice-off ($r= 0.66$ and $r= 0.70$, respectively) (Table 4.1). During MAM, the NAO is positively correlated with air temperature ($r= 0.36$) and negatively with precipitation and snow days ($r= -0.50$ and $r= -0.31$, respectively; p-value < 0.05). Air temperature displays negative correlations with precipitation ($r= -0.43$) and snow days ($r= -0.85$), whereas precipitation is positively correlated with snow days ($r= 0.51$) (Table 4.1). Finally, the correlations between ice records are the same in both seasons (winter and spring) because data are annual and do not depend on seasonality. Only ice-off and ice-cover duration are positively correlated each other ($r= 0.67$) (Table 4.1). Finally, with respect to monthly data and the freezing process, the freeze-up date is only positively correlated with November temperature ($r= 0.54$, p-value < 0.05) (Table 4.2).

4.1.2. Cimera Lake

During JFM, the NAO is positively correlated with maximum temperature ($r= 0.70$) and negatively with precipitation ($r= -0.71$). Maximum air temperature shows a positive correlation with the minimum air temperature ($r= 0.51$) and a negative correlation with precipitation ($r= -0.62$). The remaining variables do not display significant correlations in this season (Table 4.3). In MAM, the NAO displays a positive correlation with maximum air temperatures ($r= 0.42$) and negative correlations with precipitation ($r= -0.51$). Maximum air temperature is also positively correlated with the minimum air temperature ($r= 0.79$) and negatively correlated with precipitation ($r= -0.59$) (Table 4.3). Finally, the correlations between ice records are also the same in both winter and spring because they have an annual character. Only ice-off and ice-cover duration are positively correlated ($r= 0.91$) (Table 4.3). With respect to monthly data and the freezing process, the freeze-up date is not significantly correlated with any data (Table 4.4).

WINTER (JFM)	NAO	Temp	Precip	Snow days	Freeze-up	Ice-cover	Break-up
NAO	1						
Temp	0.69***	1					
Precip	-0.67***	-0.59***	1				
Snow days	-0.64***	-0.75***	0.69***	1			
Freeze-up	-0.09	0.05	0.00	-0.01	1		
Ice-cover	-0.53**	-0.59**	0.52**	0.66***	-0.37	1	
Break-up	-0.52**	-0.65***	0.53**	0.70***	0.41	0.67***	1

SPRING (MAM)	NAO	Temp	Precip	Snow days	Freeze-up	Ice-cover	Break-up
NAO	1						
Temp	0.36***	1					
Precip	-0.50***	-0.43***	1				
Snow days	-0.31**	-0.85***	0.51***	1			
Freeze-up	—	—	—	—	1		
Ice-cover	0.35	-0.14	-0.04	0.22	-0.37	1	
Break-up	0.04	-0.30	-0.14	0.16	0.41	0.67***	1

Table 4.1. Pearson's correlation coefficients in winter (JFM) (top) and spring (MAM) (bottom) between limnological data, climatic data and the NAO index for Peñalara Lake. * denotes that the correlation is significant at the 0.1 level, ** at the 0.05 level and *** at the 0.01 level. The numbers in italics are annual correlations.

Results

<i>September</i>	NAO	Temp	Precip	Snow days	Freeze-up
NAO	1				
Temp	0.61	1			
Precip	-0.47**	-0.31	1		
Snow days	-0.27***	-0.53	-0.23	1	
Freeze-up	0.18	-0.05	-0.36	-	1
<i>October</i>	NAO	Temp	Precip	Snow days	Freeze-up
NAO	1				
Temp	0.50**	1			
Precip	-0.60***	-0.49**	1		
Snow days	-0.42*	-0.81***	0.45**	1	
Freeze-up	-0.08	-0.10	-0.15	0.31	1
<i>November</i>	NAO	Temp	Precip	Snow days	Freeze-up
NAO	1				
Temp	0.51**	1			
Precip	-0.10	0.08	1		
Snow days	-0.47**	-0.71***	0.40*	1	
Freeze-up	0.30	0.54**	0.34	0.01	1
<i>December</i>	NAO	Temp	Precip	Snow days	Freeze-up
NAO	1				
Temp	0.48**	1			
Precip	-0.70***	-0.34	1		
Snow days	-0.54**	-0.66***	0.64***	1	
Freeze-up	0.06	0.19	0.15	0.21	1

Table 4.2. Pearson's correlation coefficients between monthly (September, October, November and December) freeze-up date, climatic data and the NAO index for Peñalara Lake. * denotes that the correlation is significant at the 0.1 level, ** at the 0.05 level and *** at the 0.01 level. The numbers in italics are annual correlations. Bold numbers highlight significant correlations of freeze-up.

WINTER (JFM)	NAO	Temp Max	Temp Min	Precip	Snow depth	Freeze-up	Ice-cover	Break- up
NAO	1							
Temp Maximum	0.70***	1						
Temp Minimum	0.12	0.51***	1					
Precip	-0.71***	-0.62***	0.20	1				
Snow depth	-0.47	—	—	—	1			
Freeze-up	-0.41	-0.58	0.46	-0.22	0.22	1		
Ice-cover	-0.34	0.07	0.05	-1.00	-0.02	-0.13	1	
Break-up	-0.61	-0.15	-0.04	-1.00	0.16	0.28	0.91***	1

SPRING (MAM)	NAO	Temp Max	Temp Min	Precip	Snow depth	Freeze-up	Ice-cover	Break- up
NAO	1							
Temp Maximum	0.42***	1						
Temp Minimum	0.21	0.79***	1					
Precip	-0.51***	-0.59***	-0.18	1				
Snow depth	-0.28	-1.00	-1.00	-	1			
Freeze-up	—	—	—	—	—	1		
Ice-cover	-0.79*	-0.05	0.06	0.25	0.77	-0.13	1	
Break-up	-0.87**	-0.35	-0.17	0.01	0.84	0.28	0.91***	1

Table 4.3. Pearson's correlation coefficients in winter (JFM) (top) and spring (MAM) (bottom) between limnological data, climatic data and the NAO index for Cimera Lake. * denotes that the correlation is significant at the 0.1 level, ** at the 0.05 level and *** at the 0.01 level. The grey numbers indicate correlations where $n < 5$. The numbers in italics are annual correlations.

Results

<i>September</i>	NAO	Temp Max	Temp Min	Precip	Snow depth	Freeze-up
NAO	1					
Temp Maximum	-0.12	1				
Temp Minimum	0.46	0.53	1			
Precip	-0.49	-0.53		1		
Snow depth	-0.31	1.00	1.00	-	1	
Freeze-up	-0.51	-0.23	-0.52	0.78	-0.77	1
<i>October</i>	NAO	Temp Max	Temp Min	Precip	Snow depth	Freeze-up
NAO	1					
Temp Maximum	-0.01	1				
Temp Minimum	0.67	0.53	1			
Precip	0.40	-0.70		1		
Snow depth	-0.43	-1.00	-1.00	-	1	
Freeze-up	0.17	-0.78	-0.03	0.19	-0.17	1
<i>November</i>	NAO	Temp Max	Temp Min	Precip	Snow depth	Freeze-up
NAO	1					
Temp Maximum	0.61	1				
Temp Minimum	0.16	0.45	1			
Precip	1.00	0.65		1		
Snow depth	0.57	1.00	1.00	-	1	
Freeze-up	-0.23	-0.86	-0.79	0.52	-0.30	1
<i>December</i>	NAO	Temp Max	Temp Min	Precip	Snow depth	Freeze-up
NAO	1					
Temp Maximum	0.80	1				
Temp Minimum	0.74	0.56	1			
Precip	-0.99	-0.58	0.06	1		
Snow depth	0.51	1.00	1.00	-	1	
Freeze-up	-0.10	-0.03	0.03	-0.43	0.08	1

Table 4.4. Pearson's correlation coefficients between monthly (September, October, November and December) freeze-up date, climatic data and the NAO index for Cimera Lake. * denotes that the correlation is significant at the 0.1 level, ** at the 0.05 level and *** at the 0.01 level. The grey numbers indicate correlations where $n < 5$. The numbers in italics are annual correlations.

4.2. Facies description

4.2.1. Peñalara Lake

Two sedimentary facies were identified in the uppermost 56.5 cm of the PE12-01-01 core (Fig. 4.1). Facies M1 is composed of brown silty mud with abundant amorphous aggregates of organic matter and few preserved terrestrial plant remains (i.e., phytoclasts) (Fig. 4.1). In the M1 facies, the diatom content is high and dominated by *Aulacoseira* sp. colony chains, whereas the mineral content is low and features rounded grains (Fig. 4.1). Facies M2 is composed of brown silty mud with dispersed fine sand. This facies presents a higher mineral content and less organic matter and diatoms than facies M1. Organic matter is present in this second facies as scattered amorphous aggregates with a very low composition of phytoclasts (Fig. 4.1). Minerals present more angular shapes than in facies M1. These two facies represent a single lithostratigraphic unit.

The facies description, together with previous visual observations, allowed us to create a synthetic stratigraphic column of the core PE12-01-01. The brown silty mud (facies M1) is the dominant facies and presents interbedded layers of different thicknesses of brown silty mud with dispersed fine to very fine sand (facies M2) (Fig. 4.1).

4.2.2. Cimera Lake

Three sedimentary facies were identified in the core CIM12-04A (Fig. 4.2). Facies M1 is composed of massive brown silty mud with dispersed grains of fine sand. Organic matter is present as predominant amorphous aggregates and a low content of altered terrestrial plant remains (i.e., phytoclasts) (Fig. 4.2). Facies M2 is characterized by poorly defined layers of brown silty mud and fine to medium sand. The sand grain shape appears to be more angular than in facies M1, and there are amorphous aggregates of organic material, although in a lower proportion than in facies M1 (Fig. 4.2). Facies S is composed of white to ochre coarse sand with granules forming well-defined tabular layers, some of which include pebble clasts. Most of the grains show a more angular shape than those in facies M2, and the terrigenous fraction in facies S is significantly higher than the organic matter content (Fig. 4.2).

The facies description, together with previous visual observations, allowed us to create a synthetic stratigraphic column of the core CIM12-04A. The brown silty mud (facies M1) is the dominant facies with interbedded layers of poorly defined brown silty mud with fine to medium sand (facies M2) and layers of coarse sand (facies S). The latter facies are more common in the lower part of the sequence (Fig. 4.2).

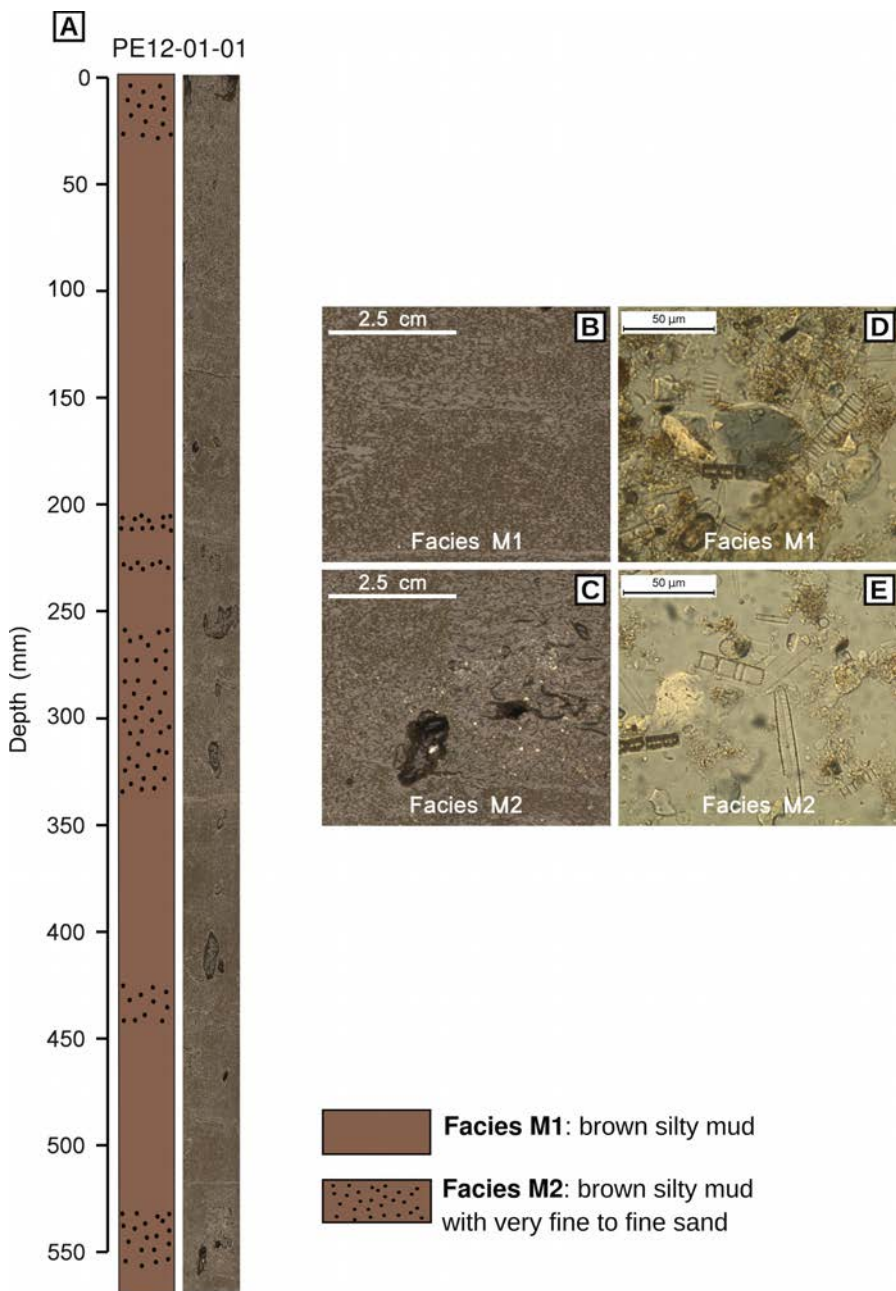


Figure 4.1. A) Synthetic lithological columns with the defined facies and image of the PE12-01-01 core taken with the colour line-scan camera. B, C) Detailed core image of facies M1 and M2, respectively. D, E) Images of facies M1 and M2 acquired from smear slides with a camera installed in the high-end polarization microscope Leica® DM4500 P, respectively.

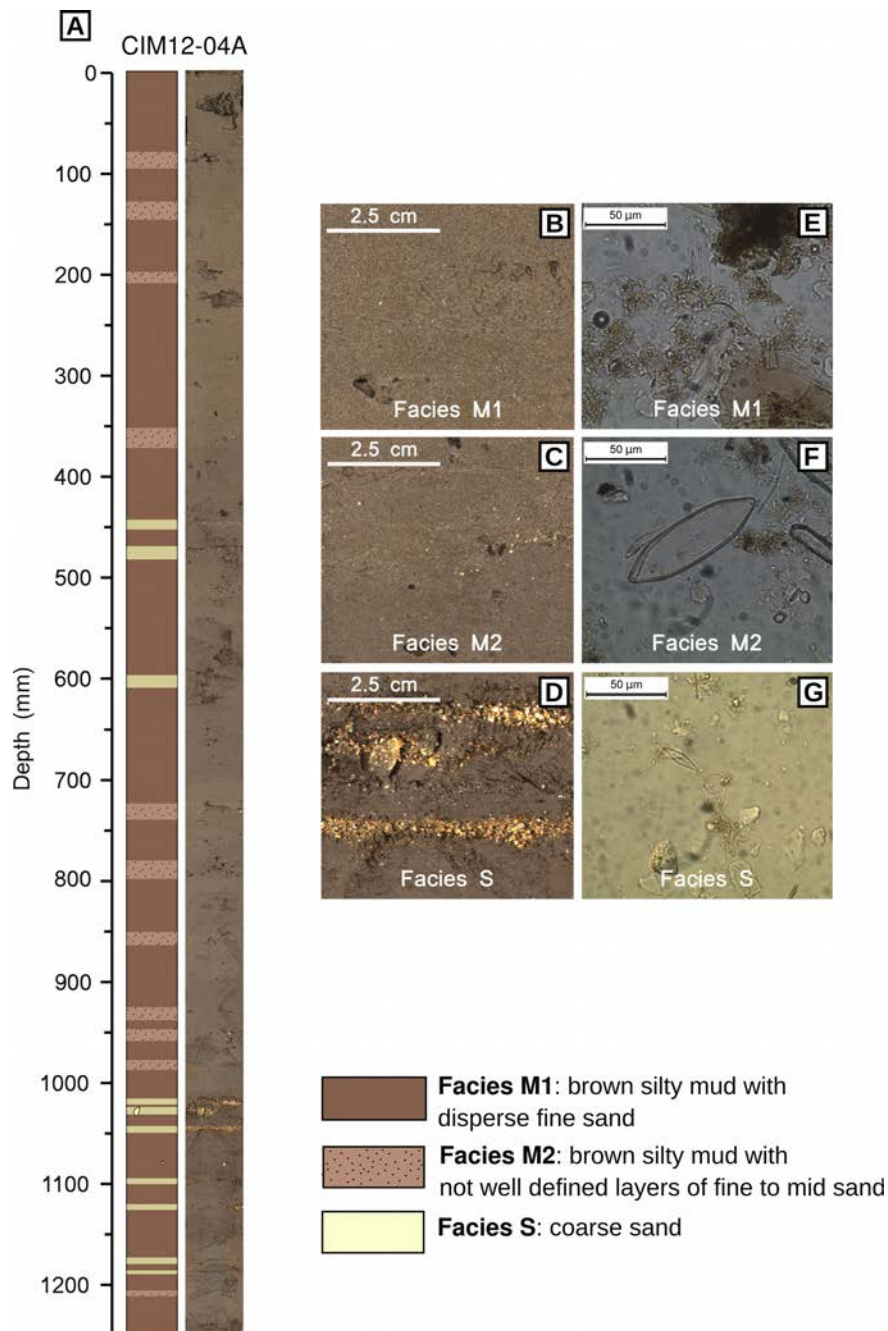


Figure 4.2. A) Synthetic lithological columns with the defined facies and image of CIM12-04A core taken with the colour line-scan camera. B-D) Detailed core image of facies M1, M2 and S, respectively. E-G) Images of facies M1, M2 and S acquired from smear slides with a camera installed in the high-end polarization microscope Leica® DM4500 P, respectively.

4.3. Chronological models

4.3.1. Peñalara Lake

The ^{210}Pb concentration profile of the core PE12-01-01 displays a complex pattern (Fig. 4.3). The ^{210}Pb concentration increases from the surface (190 Bq/kg) to 12 cm (250 Bq/kg) and remains constant down to 25 cm of core depth. Then, the ^{210}Pb concentration gradually decreases to values of approximately 100 Bq/kg at 35 cm of core depth. From this depth to 52 cm, the ^{210}Pb concentration is approximately 150 Bq/kg (Fig. 4.3). ^{137}Cs is detected in all the analysed samples between 25 and 29 cm of core depth, showing a clear decreasing-downwards trend. These results indicate that this material accumulated after the 1950s AD (Fig. 4.3). The interpretation of these data is that the uppermost 25 cm correspond to the deposition and reworking of sediment since the 1990s when the area was declared a Natural Park and the resulting removal of garbage previously deposited into the lake. (Toro and Granados, 2002) (Fig. 4.3). The excess ^{210}Pb concentration profile between 25 and 35 cm of core depth and the ^{137}Cs data were used to obtain an average sedimentation rate (SR) of $1.6 \pm 0.1 \text{ mm/yr}$ for this zone by applying the CF:CS model. The age of this zone thus ranges between the early 1920s and the late 1980s AD.

Four of the six ^{14}C dates from PE12-01-01 were not included in the construction of the linear age-depth model (Table 4.5 and Fig. 4.4). On one hand, the ages at 10 and 28 cm are inconsistent with the presence of $^{210}\text{Pb}_{\text{ex}}$ because they are older than the ^{210}Pb -derived ages. This may be explained by sediment reworking. On the other hand, the ^{14}C dates at 41.5 and 48 cm overlap but the lithology of the core does not suggest the presence of an instantaneous event, such as a fine-grained mass wasting deposit (Fig. 4.1). Hence, the ^{14}C date at 48 cm was rejected because it was younger than the date at 41.5 cm, likely as a result of reworking of younger sediment. The fourth date rejected was found at 55.5 cm of core depth, and it is much younger than the previous radiocarbon date (Table 4.5).

Therefore, the obtained SRs from the linear age-depth model were 0.07 mm/yr and 0.11 mm/yr for the 25 – 41.5 cm and 41.5 – 55 cm intervals, respectively (Fig. 4.4). Hence, the resultant age-depth for Peñalara Lake record indicates that the 25 – 55 cm sediment sequence spans from $263 \pm 95.5 \text{ BC}$ to $1986 \pm 1 \text{ AD}$ (Fig. 4.4).

Depth (cm)	Lab Code	Material	^{14}C years BP	Cal. years BP (2σ)	Cal. years AD/BC (2σ)
10	Beta - 333757	Pollen c.	730 ± 30	681 ± 28	$1269 \pm 28 \text{ AD}$
28	Beta - 333758	Pollen c.	1190 ± 30	1118 ± 65	$832 \pm 65 \text{ AD}$
41.5	Poz-61899	Pollen c.	1060 ± 30	966.5 ± 39.5	$983.5 \pm 39.5 \text{ AD}$
48	Poz-61900	Pollen c.	1085 ± 30	974 ± 40	$976 \pm 40 \text{ AD}$
55	Beta - 333759	Pollen c.	2180 ± 30	2213.5 ± 95.5	$263.5 \pm 95.5 \text{ BC}$
55.5	Beta - 333760	Wood	120 ± 30	80 ± 69	$1870 \pm 69 \text{ AD}$

Table 4.5. Radiocarbon dates and calibrated ages for the PE12-01-01 core. Results are reported with 2σ uncertainty. Samples in italics were discarded. 'Pollen c.' denotes pollen concentrate.

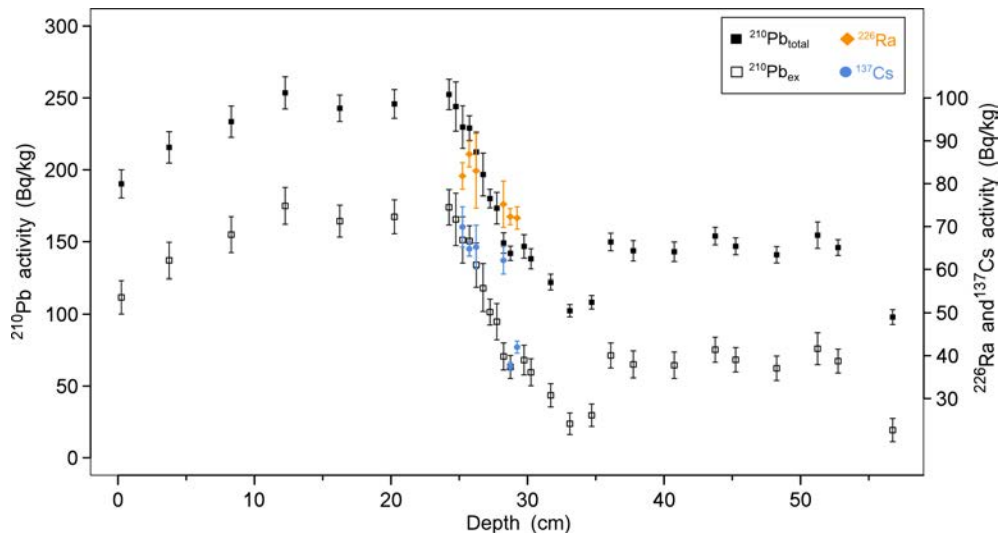


Figure 4.3. Activity depth profiles of total ^{210}Pb (solid black squares), excess ^{210}Pb (open black squares), ^{226}Ra (orange diamond) and ^{137}Cs (blue circles) for core PE12-01-01, with error bars representing 1σ uncertainties.

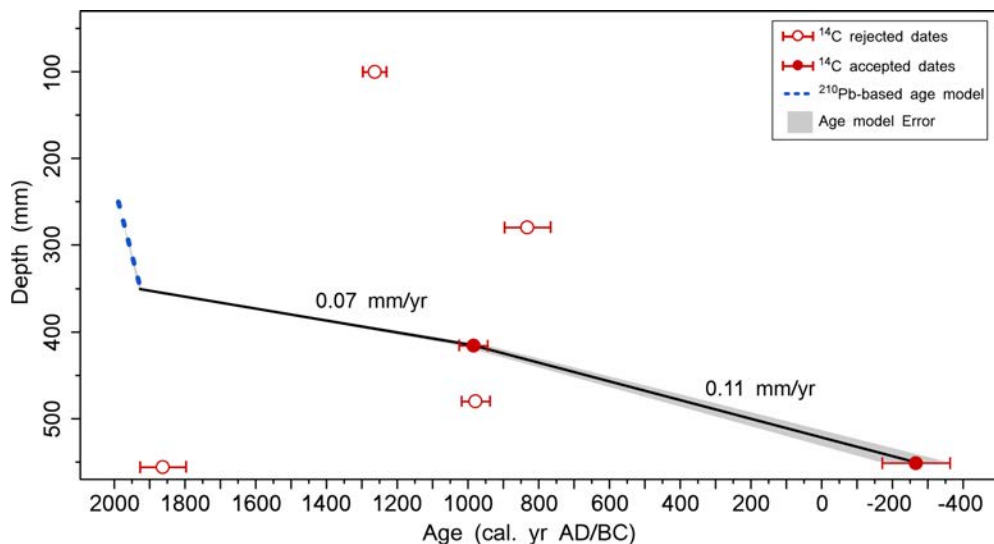


Figure 4.4. Age-depth linear model of the core PE12-01-01 based on the AMS ^{14}C dates and ^{210}Pb activity depth profile. The error bars of the red points represent the $\pm 2\sigma$ calibrated age range for the AMS ^{14}C dates. The black continuous line represents the age-depth function framed by a grey area that corresponds to the error model. The blue dashed line represents the zone of ^{210}Pb dates.

4.3.2. Cimera Lake

The concentration profile of the excess ^{210}Pb can be divided into three intervals according to its slopes: 0 – 4 cm, 4 – 6.5 cm and 6.5 – 9 cm. The supported ^{210}Pb horizon is attained at 9.2 cm. Relatively lower concentrations of $^{210}\text{Pb}_{\text{ex}}$ were measured in the sandy layers and excluded from the estimation of the sedimentation rates for each zone (Fig. 4.5). The sedimentation rates obtained by applying the CF:CS model were $4.1 \pm 0.8 \text{ mm/yr}$ for 0 – 4 cm and $0.65 \pm 0.02 \text{ mm/yr}$ for 4 – 6.5 cm. Hence, these two zones cover the period from 2012 to $1954 \pm 2 \text{ AD}$. The concentration of $^{210}\text{Pb}_{\text{ex}}$ was constant in the 6.5 – 9 cm interval; thus, a chronology could not be derived.

The seven AMS ^{14}C dates determined between 10 and 124.5 cm exhibit stratigraphic coherence, except for the sample located at 10 cm because the age of this sample was too old for its stratigraphic location (Table 4.6), likely due to reworking of older sediment. Therefore, this sample was not used in the construction of the age-depth model (Fig. 4.5).

The resulting age-depth model constructed using the ^{210}Pb profiles and a smooth spline (Blaauw, 2010) shows that the uppermost 124.5 cm of sedimentary infill spans from $172 \pm 65 \text{ BC}$ ($2122 \pm 65 \text{ cal yr BP}$) to 2012 AD (Fig. 4.5). The four distinct SR intervals that can be differentiated in the age-depth model correspond to a) 4.1 mm/yr for 0 – 4 cm and b) 0.65 mm/yr for 4 – 6.5 cm from the CF:CS mode; and c) 0.2 mm/yr for 6.5 – 29.5 cm and d) 0.9 mm/yr for 29.5 – 124.5 from the linear interpolation between selected radiocarbon dates.

Depth (cm)	Lab Code	Material	^{14}C years BP	Cal. years BP (2 σ)	Cal. years AD/BC (2 σ)
10	Beta - 333752	Pollen c.	1420 ± 30	1329 ± 39	$621 \pm 39 \text{ AD}$
29.5	Poz-61896	Pollen c.	1140 ± 30	1032 ± 63	$918 \pm 63 \text{ AD}$
49	Beta - 333753	Pollen c.	1170 ± 30	1113 ± 66	$837 \pm 66 \text{ AD}$
67.5	Poz-61897	Pollen c.	1425 ± 30	1332 ± 40	$618 \pm 40 \text{ AD}$
86	Beta - 333754	Pollen c.	1940 ± 30	1885 ± 64.5	$64.5 \pm 64.5 \text{ AD}$
105.5	Poz-61898	Pollen c.	1875 ± 30	1803.5 ± 76.5	$146.5 \pm 76.5 \text{ AD}$
124.5	Beta - 333755	Pollen c.	2160 ± 30	2122.5 ± 65.5	$172.5 \pm 65.5 \text{ BC}$

Table 4.6. Radiocarbon dates and calibrated ages for CIM12-04A core from Cimera Lake. Results are reported with 2 σ uncertainty. Samples in italics were discarded. 'Pollen c.' denotes pollen concentrate.

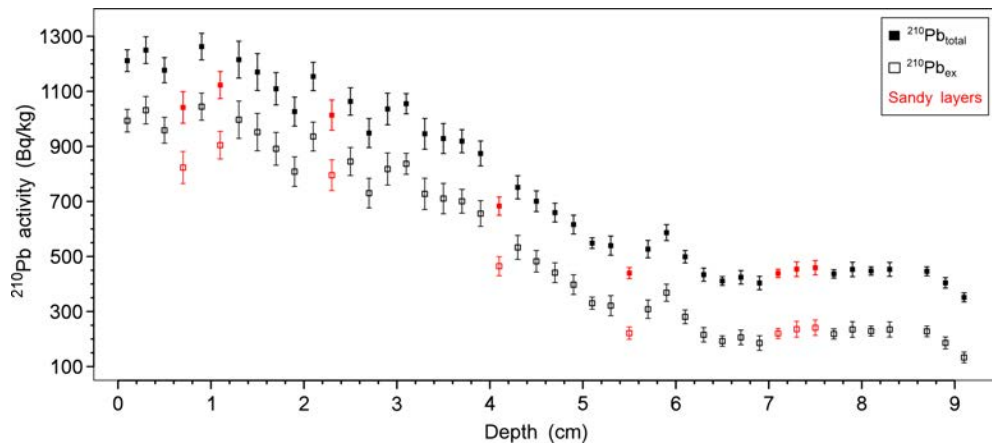


Figure 4.5. Activity depth profiles of total ^{210}Pb (solid black and red squares) and excess ^{210}Pb (open black squares) for the core CIM12-04A, with error bars representing 1σ uncertainties.

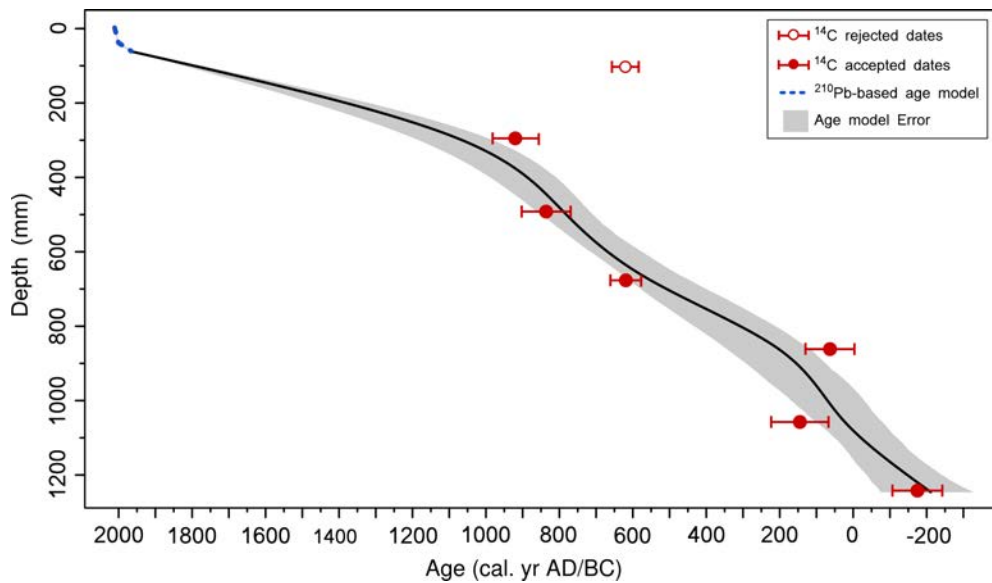


Figure 4.6. Age-depth model of the core CIM12-04A based on the AMS ^{14}C dates and ^{210}Pb activity depth profile and constructed using the R-code package 'clam'. The error bars of the red points represent the $\pm 2\sigma$ calibrated age range for the AMS ^{14}C dates. The black continuous line represents the age-depth function framed by a grey area that corresponds to the error model. The blue dashed line represents the zone of ^{210}Pb dates.

4.4. Geochemical and mineralogical characterization of the lake sediments

4.4.1. Peñalara Lake

The average TOC content is approximately 4 wt%, with a range from 2 to 5.5 wt %, and the TN content is approximatly 0.4 on average, with a range from 0 and 0.55 wt %. Both proxies covary positively and display lower values in facies M2 (Fig. 4.7). The carbon-nitrogen atomic ratio (TOC/TN) remains constant with values of approximately 14, from the bottom to 25 cm of the core depth sequence (Fig. 4.7). The isotopic composition of the organic matter ranges between -26‰ and -25‰ and from 3 to 4.5‰ for $\delta^{13}\text{C}$ and $\delta^{15}\text{N}$, respectively. The most prominent change in $\delta^{13}\text{C}$ values occurs at 27.5 cm, where the values abruptly drop to around -26‰ and remain unchanged until 25 cm of core depth (Fig. 4.7). The $\delta^{15}\text{N}$ values are almost invariable along the core (Fig. 4.7). The chemical elements that display the most remarkable oscillations are Al, Si, K, Ca, Ti and Fe, which peak in the silty intervals (i.e., facies M2; Fig. 4.7). The chemical elements V, Cr, Mn and Zn show noisy signals. The profiles of Rb, Sr and Zr decrease upwards (Fig. 4.7). The mineralogical composition of the PE12-01-01 sediment record shows that the percentages of muscovite slightly decrease upwards, whereas the proportions of quartz increase. The rest of the mineral proportions remain roughly constant (Fig. 4.7). The clay mineral analyses confirm the presence of palygorskite in the Peñalara Lake record (Fig. 4.7).

4.4.2. Cimera Lake

The TOC and TN contents of the CIM12-04A sequence display average values of approximately 3.5 and 0.35 wt%, respectively. From the bottom to a depth of 6 cm, both parameters positively covary around their respective mean values (Fig. 4.8). Above this interval, the TOC and TN percentages largely increase until the top of the core. From the core bottom to a depth of 14.5 cm, the TOC/TN ratio remains constant at around 12. Subsequently, the TOC/TN ratio increases to 14 in the 14.5 – 6.5 cm depth interval (Fig. 4.8). Above 6.5 cm, the ratio decreases to 11, and a final sudden increase occurs at the top of the core (Fig. 4.8). The $\delta^{13}\text{C}$ isotopic composition ranges between -25.5 and -24‰ and the $\delta^{15}\text{N}$ isotopic composition between 0 and 3‰ (Fig. 4.8). The $\delta^{13}\text{C}$ values display an enrichment trend above 35 cm and a sudden depletion at the top of the core, whereas the $\delta^{15}\text{N}$ values show a noticeable depletion trend from 14.5 cm to the top of the core (Fig. 4.8). Al, Si, K, Ca, Ti and Fe display the largest oscillations, whereas V, Cr and Mn are the noisiest. The Mn profile decreases upwards, whereas Zr displays the opposite pattern (Fig. 4.8). All of the inorganic elements show fewer counts in the uppermost centimetres (Fig. 4.8). The mineral species exhibit roughly constant percentages from the core bottom up to 35 cm of core depth. Above this interval, kaolinite and clinochlore increase, whereas quartz and microcline display the opposite trend (Fig. 4.8). Between 35 and 10 cm, muscovite diminishes from 29% to 24 wt%, and albite remains constant. The uppermost 10 cm is characterized by an increase in muscovite and major oscillations of albite (Fig. 4.8). Finally, the clay mineral analyses confirm a significant amount of palygorskite in the Cimera Lake sediments (Fig. 4.8).

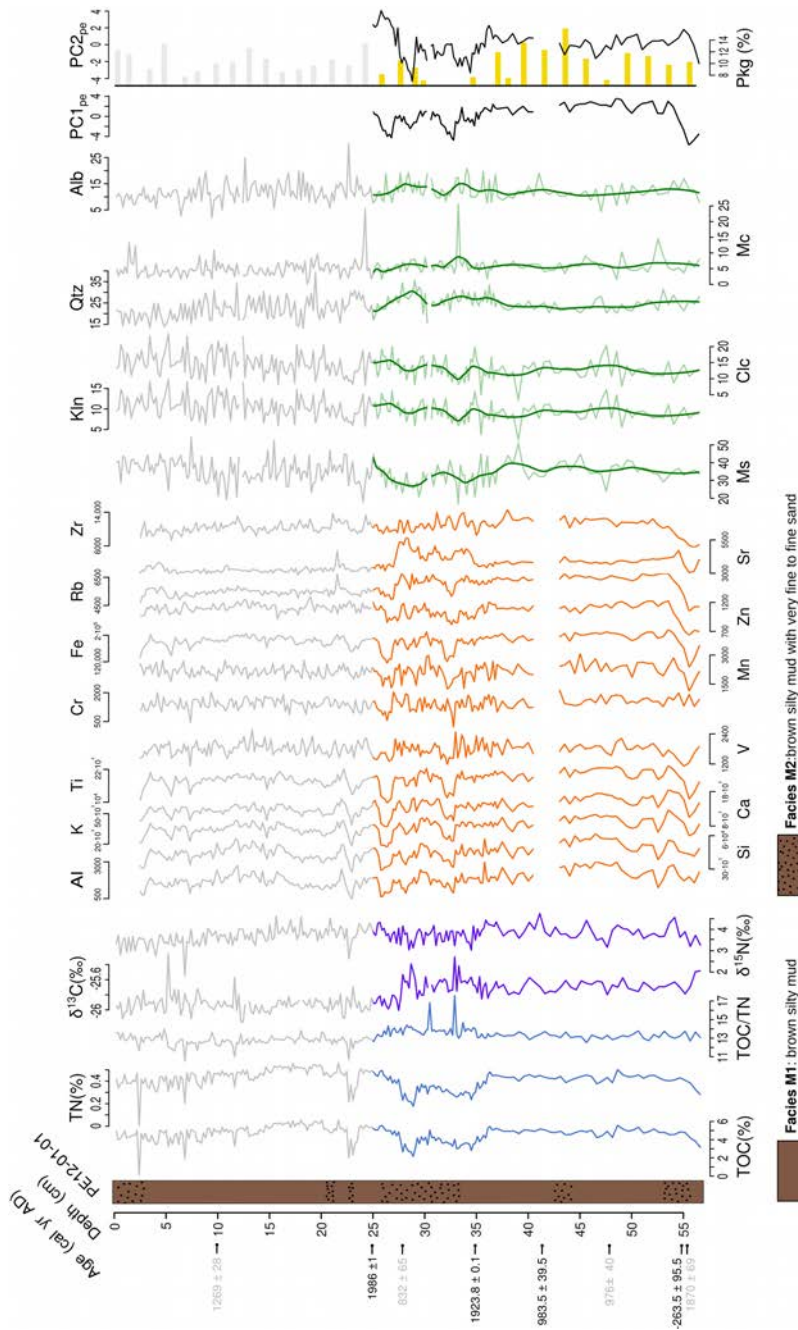


Figure 4.7. Stratigraphic column of the PE12-01-01 core, with facies, elemental (TOC, TN, TOC/TN ratio; light-blue lines) and isotopic compositions ($\delta^{13}\text{C}$ and $\delta^{15}\text{N}$; dark-blue lines), XRF profiles (expressed in counts per second; orange lines), mineralogy (expressed as percentages of total dry weight, Ms=muscovite, Mc=quartz, Clc=clinochlore, Kln=kaolinite, Alb=albite; light-green lines correspond to original data and dark-green lines correspond to smoothed data calculated with the loess function and a span degree of 0.10), clay fraction (Pkg=polygorskite, yellow bars), and the first and second eigenvector scores (PC_{1pe} and PC_{2pe}; black lines) with depth. The grey lines and grey bars correspond to areas of reworked sediments in the core (i.e., uppermost 25 cm).

Results

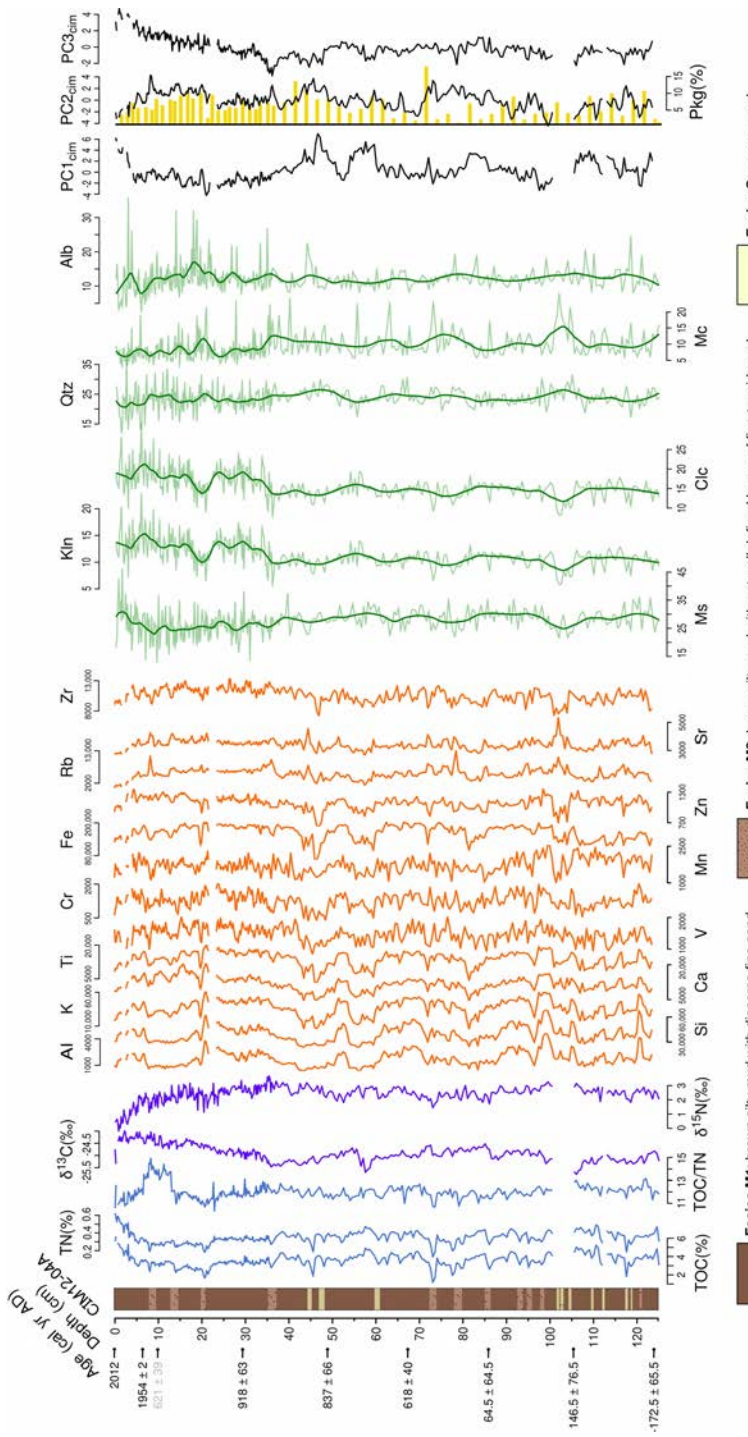


Figure 4.8. Stratigraphic column of the CIM12-04A core, with facies, elemental (TOC, TN, TOC/TN ratio; light-blue lines) and isotopic compositions ($\delta^{13}\text{C}$ and $\delta^{15}\text{N}$; dark-blue lines), XRF profiles (expressed in counts per second; orange lines), mineralogy (expressed as percentages of total dry weight, Ms=muscovite, Mc=quartz, Kln=kainite, Clc=clinochlore, Alb=albite; light-green lines correspond to original data and dark-green lines correspond to smoothed data calculated with the loess function and a span degree of 0.10), clay fraction ($\text{Pkg} \equiv \text{polygorskite}$, yellow bars), and the first, second and third eigenvector scores (PC1_{cm} , PC2_{cm} and PC3_{cm} ; black lines) with depth.

4.5. Geochemical and mineralogical characterization of an aeolian dust sample

The clay minerals analyses also confirm the presence of palygorskite in the dust sample from Cimera Lake collected in June 2014 (Fig. 4.9). The concentrations of nitrate, sulphate and total phosphorus ($[NO_3^-]$, $[SO_4^{2-}]$, and [TP]) in this dust sample were 190 ppm, 530 ppm and 0.5 ppm, respectively.

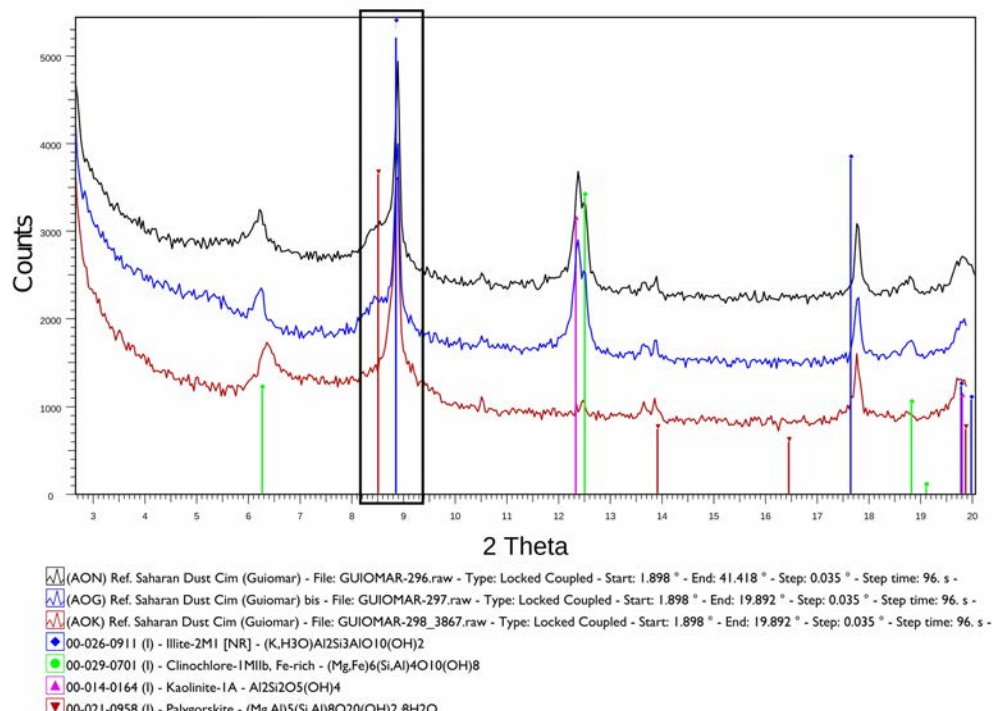


Figure 4.9. Diffractogram obtained by XRD of the clay composition of the dust event sample collected in Cimera Lake in June 2014. Palygorskite is present in the sample.

4.6. Redundancy Data Analyses (RDAs)

4.6.1. Peñalara Lake

The results from the reworked sediments in the uppermost 25 cm of the PE12-01-01 core have been neglected, and they have not been taken into account in neither of the following statistical analyses (Fig. 4.7).

The RDA biplot of PE12-01-01 displays three main groups (Fig. 4.10A): group A encompasses the $\delta^{13}C$ values and is associated with quartz, albite and microcline; group B only includes muscovite related with Mn, Si, and the TOC and TN profiles; and group C is associated with kaolinite and clinochlore. The remaining chemical elements (i.e., Ti, Cr, V, Zr, and Rb) and the $\delta^{15}N$ values are located between groups A and B, whereas Zn is located between groups B and C.

4.6.2. Cimera Lake

The RDA biplot from the core CIM12-04A has allowed us to define three main groups (Fig. 4.10B): group A includes Ti, Rb and $\delta^{15}\text{N}$ values and is associated with quartz, albite and microcline; group B is associated with muscovite and the TOC and TN proportions; and group C includes Zn and $\delta^{13}\text{C}$ values and is associated with kaolinite and clinochlore. Zr is located between groups A and B, although most of the geochemical elements (i.e., Si, V, Cr and Mn) are generally located in the centre of the biplot.

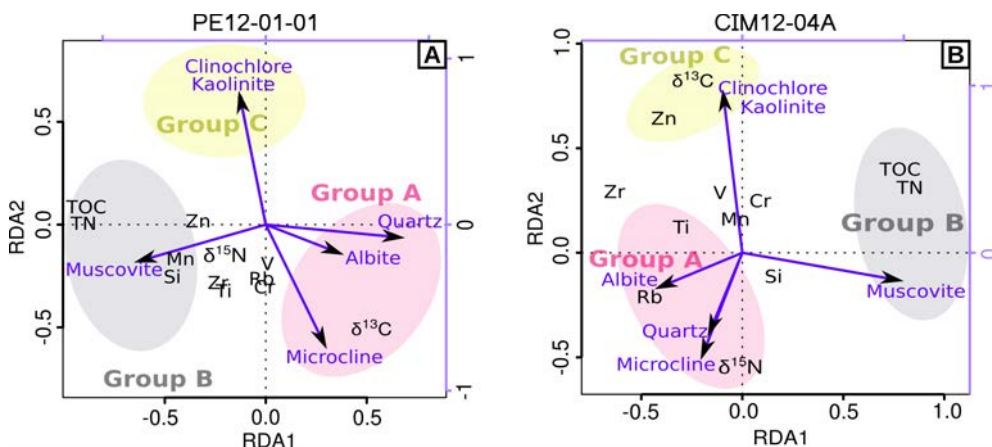


Figure 4.10. RDA biplots for the cores A) PE12-01-01 and B) CIM12-04A. Light red, grey and yellow areas indicate groups A, B and C, respectively.

4.7. Principal Component Analyses (PCAs)

4.7.1. Peñalara Lake

The PCA of the geochemical dataset from the PE12-01-01 core shows that the two first eigenvectors account for 57% of the total variance (Table 4.7). The first eigenvector (PC1_{pe}) represents 36% of the total variance, and it is primarily controlled by all the geochemical elements at the positive end (Fig. 4.11A and Table 4.7). The second eigenvector (PC2_{pe}) accounts for 21% of the total variance. This is tied by TOC, TN and, to minor extent, by $\delta^{15}\text{N}$ and Zn at its positive end and by $\delta^{13}\text{C}$ with a minor contribution of Rb at the negative end (Fig. 4.11A and Table 4.7). The other eigenvectors defined by the PCA analysis were not considered because they explain <11% of the total variance, and according to the broken-stick model, only the first two axes from the PCA can be considered significant (Table 4.7 and Fig. 4.11B).

Component	Initial eigenvalues			Component	
	Total	% of variance	% Cumulative	1	2
1	2.08	36.01	36.01	TOC	0.22
2	1.60	21.46	57.46	TN	0.24
3	1.15	10.94	68.40	$\delta^{13}\text{C}$	-0.45
4	0.91	6.91	75.32	$\delta^{15}\text{N}$	0.19
5	0.89	6.55	81.87	Si	0.37
6	0.85	5.97	87.83	Ti	0.42
7	0.68	3.87	91.70	V	0.24
8	0.66	3.65	95.35	Cr	0.22
9	0.54	2.45	97.80	Mn	0.33
10	0.42	1.50	99.30	Zn	0.37
11	0.27	0.60	99.91	Rb	0.37
12	0.11	0.09	100	Zr	0.24

Table 4.7. Principal component analysis (PCA) results for the PE12-01-01 core. Eigenvalues for the twelve obtained components, the percentage of the variance explained and the cumulative percentage for every axis are shown (left). Factor loads for every variable in the main axes from the PCA are also shown (right). The hyphens correspond to loadings of <0.

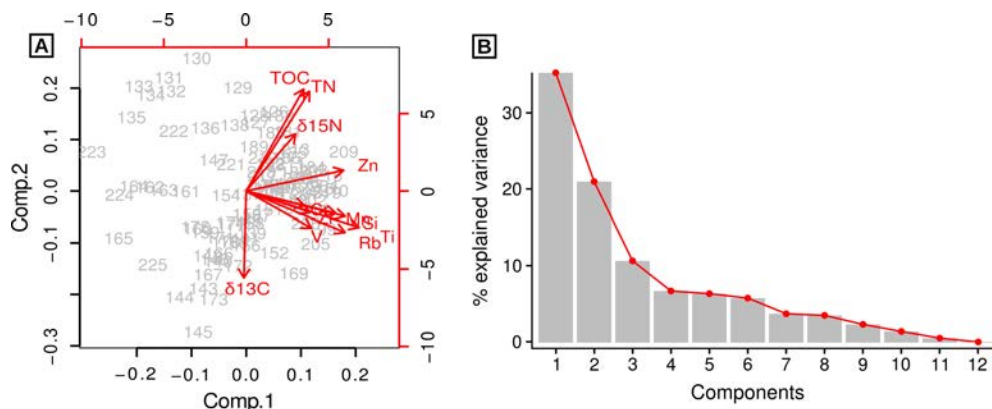


Figure 4.11. A) PCA biplots showing the first and second eigenvectors for the PE12-01-01 sequence. B) Scree plot displaying the proportion of the total variance explained by each of the components from PCA of PE12-01-01 sequence.

4.7.2. Cimera Lake

The PCA of the geochemical dataset from CIM12-04A sequence shows that the first three eigenvectors account for 67% of the total variance (Table 4.8). The first eigenvector (PC1_{cim}) explains 34% of the total variance and is primarily controlled by Ti and, to a lesser extent, by the remaining geochemical elements at the negative end and by TOC and TN percentages at the positive end (Fig. 4.12 and Table 4.8). The second eigenvector (PC2_{cim}) represents 18.5% of the total variance and is mainly controlled by TOC, TN, Si, Mn and Cr at the negative end, and by Rb and $\delta^{13}\text{C}$ at the positive end (Fig. 4.12 and Table 4.8). The third eigenvector (PC3_{cim}) accounts for 14% of the total variance and is mostly controlled by $\delta^{13}\text{C}$ values at the positive end and by $\delta^{15}\text{N}$ values at the negative end (Fig. 4.12 and Table 4.8). The other eigenvectors defined by the PCA analysis were not considered because they explain considerably lower percentages of the total variance, and according to the broken-stick model, only the first three axes from the PCA can be considered significant (Table 4.8 and Fig. 4.12C).

Component	Initial eigenvalues			Component	
	Total	% of variance	% Cumulative	1	2
1	2.01	33.81	33.81	TOC	0.29 -0.49
2	1.49	18.51	52.32	TN	0.30 -0.50
3	1.31	14.31	66.63	$\delta^{13}\text{C}$	-0.14 0.24
4	0.98	7.97	74.6	$\delta^{15}\text{N}$	— —
5	0.93	7.24	81.84	Si	-0.29 -0.39
6	0.75	4.72	86.56	Ti	-0.44 -0.19
7	0.67	3.7	90.26	V	-0.32 -0.11
8	0.63	3.27	93.53	Cr	-0.30 -0.31
9	0.61	3.07	96.6	Mn	-0.19 -0.28
10	0.53	2.32	98.92	Zn	-0.33 —
11	0.32	0.86	99.78	Rb	-0.29 0.26
12	0.17	0.23	100	Zr	-0.34 —

Table 4.8. Principal component analysis (PCA) results for the CIM12-04A core. Eigenvalues for the twelve obtained components, the percentage of the variance explained and the cumulative percentage for every axis are shown (left). Factor loads for every variable in the main axes from the PCA are also shown (right). The hyphens correspond to loadings of <0.

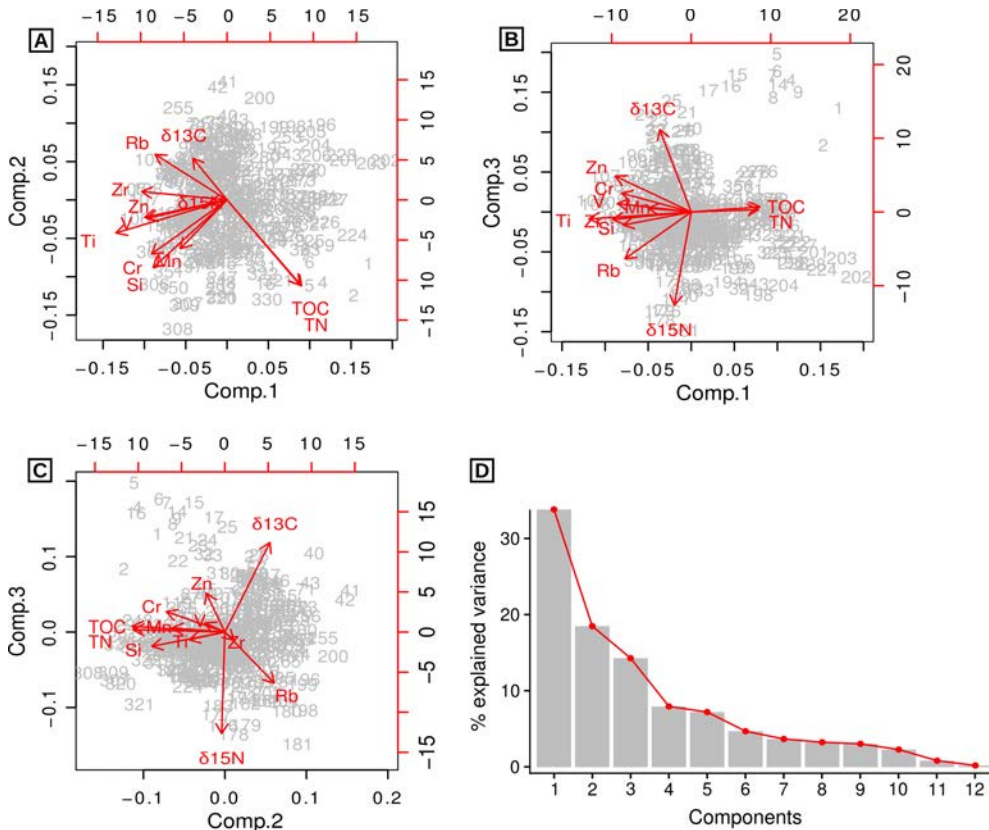


Figure 4.12. A, B, C) PCA biplots showing the first, second and third eigenvectors for the CIM12-04A sequence, respectively. D) Scree plot displaying the proportion of the total variance explained by each of the components from PCA of CIM12-04A sequence.

4.8. Bayesian model: random walk-modularised

The trace plots of the θ parameters ($\beta_0, \beta_1, \beta_2, \mu, \sigma$) for the thirteen chemical elements display chains beginning at different initial values, and they indicate good mixing and convergence. Furthermore, all the parameters exhibit a normal posterior distribution (Fig. 4.13).

The Fig. 4.14 exhibits the mean of the MDPs (μ_{MDP}) obtained in the second step of the Bayesian model with their uncertainties ($\varepsilon_{max}, \varepsilon_{min}$) and the ancient NAO (i.e., median of NAO) obtained from all the geochemical elements of CIM12-04A sequence in the third step of the model. This NAO fossil ranges between -2 and 2 values and represent a quantitative impact of the NAO in the ICR over the last two millennia, i.e., the NAO_{ICR} . From 200 BC to ca. 400 AD, the NAO_{ICR} presents a predominance of negative values, and for the period ca. 400 – 650 AD, it shows the opposite conditions (Fig. 4.14B). After that, negative values prevail until ca. 900 AD. Then, between ca. 900 AD and 1450 AD, the ancient NAO remains constant and shows positive values.

Results

Finally, NAO_{ICR} displays a trend towards negative values for the period ca. 1450 – 1900 AD, with a predominant negative scenario during the last 50 years of this period (Fig. 4.14B).

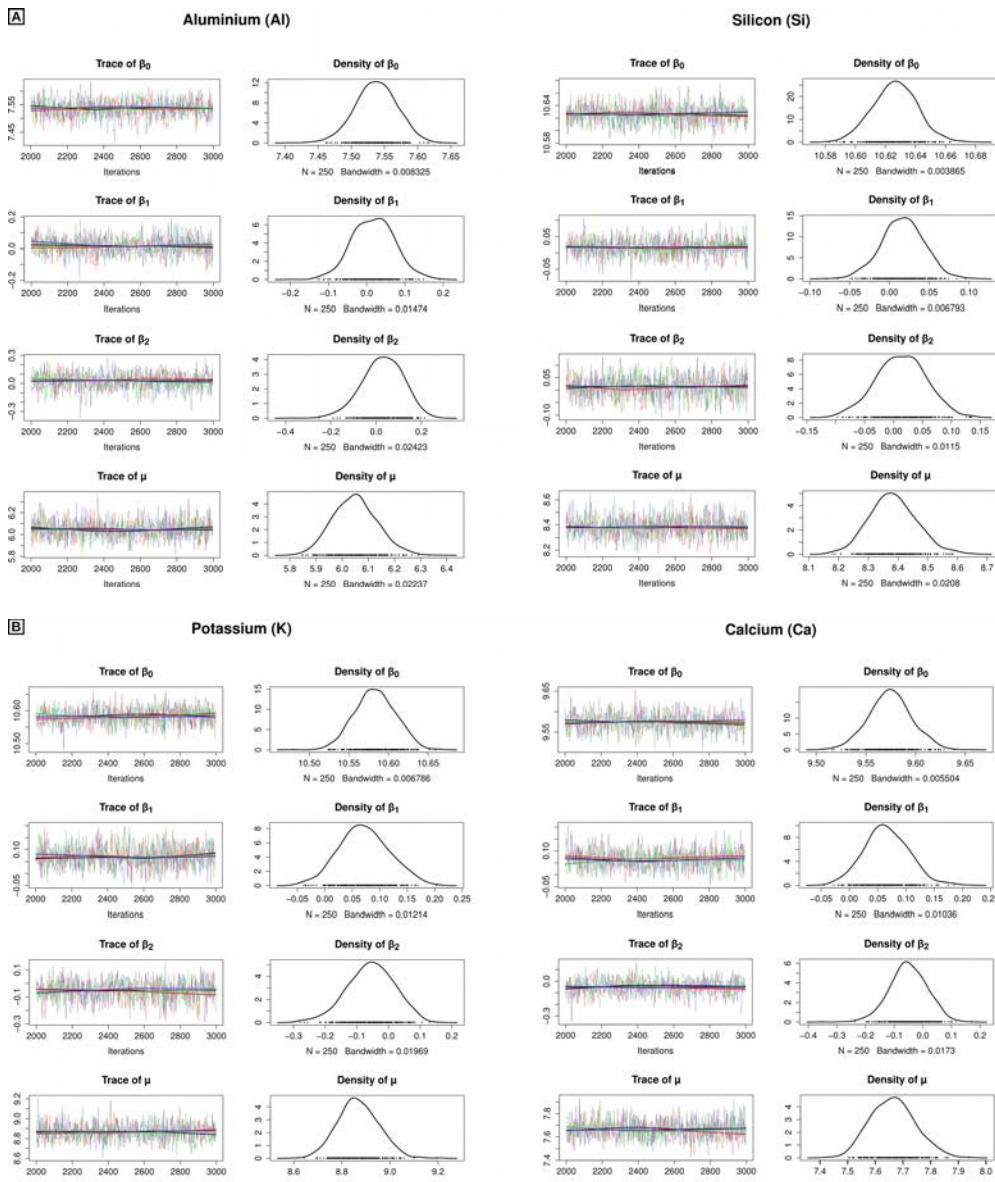


Figure 4.13. A-G) Trace plots of the four chains of the Θ parameters ($\beta_0, \beta_1, \beta_2, \mu, \sigma$) (red, green, blue and black lines) (left) and density distributions of these Θ parameters, both obtained from the initial calibration step (right) for each geochemical element. Note that a unique figure of the σ parameter is common for all the geochemical elements.

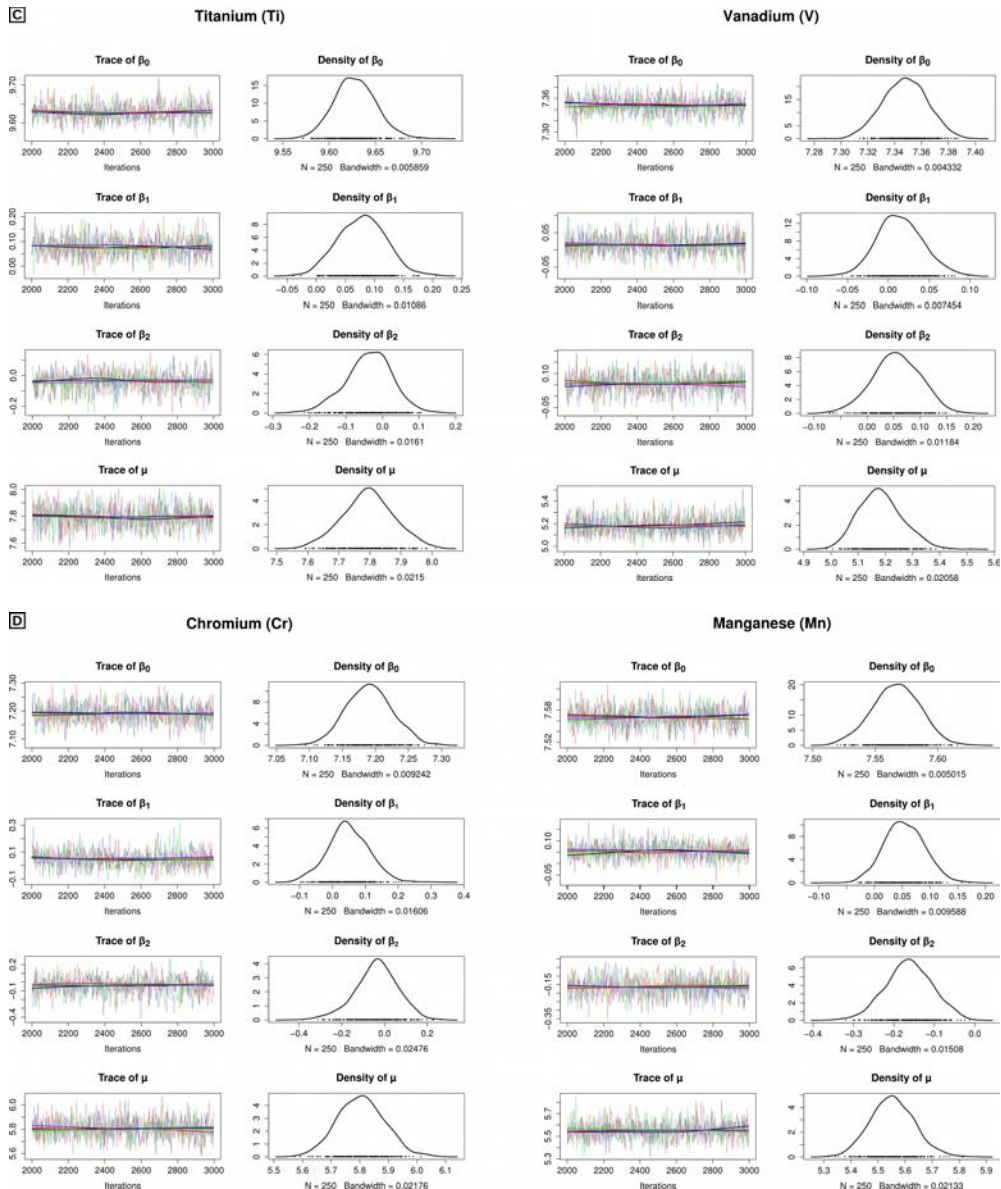


Figure 4.13. A-G) Trace plots of the four chains of the Θ parameters ($\beta_0, \beta_1, \beta_2, \mu, \sigma$) (red, green, blue and black lines) (left) and density distributions of these Θ parameters, both obtained from the initial calibration step (right) for each geochemical element. Note that a unique figure of the σ parameter is common for all the geochemical elements.

Results

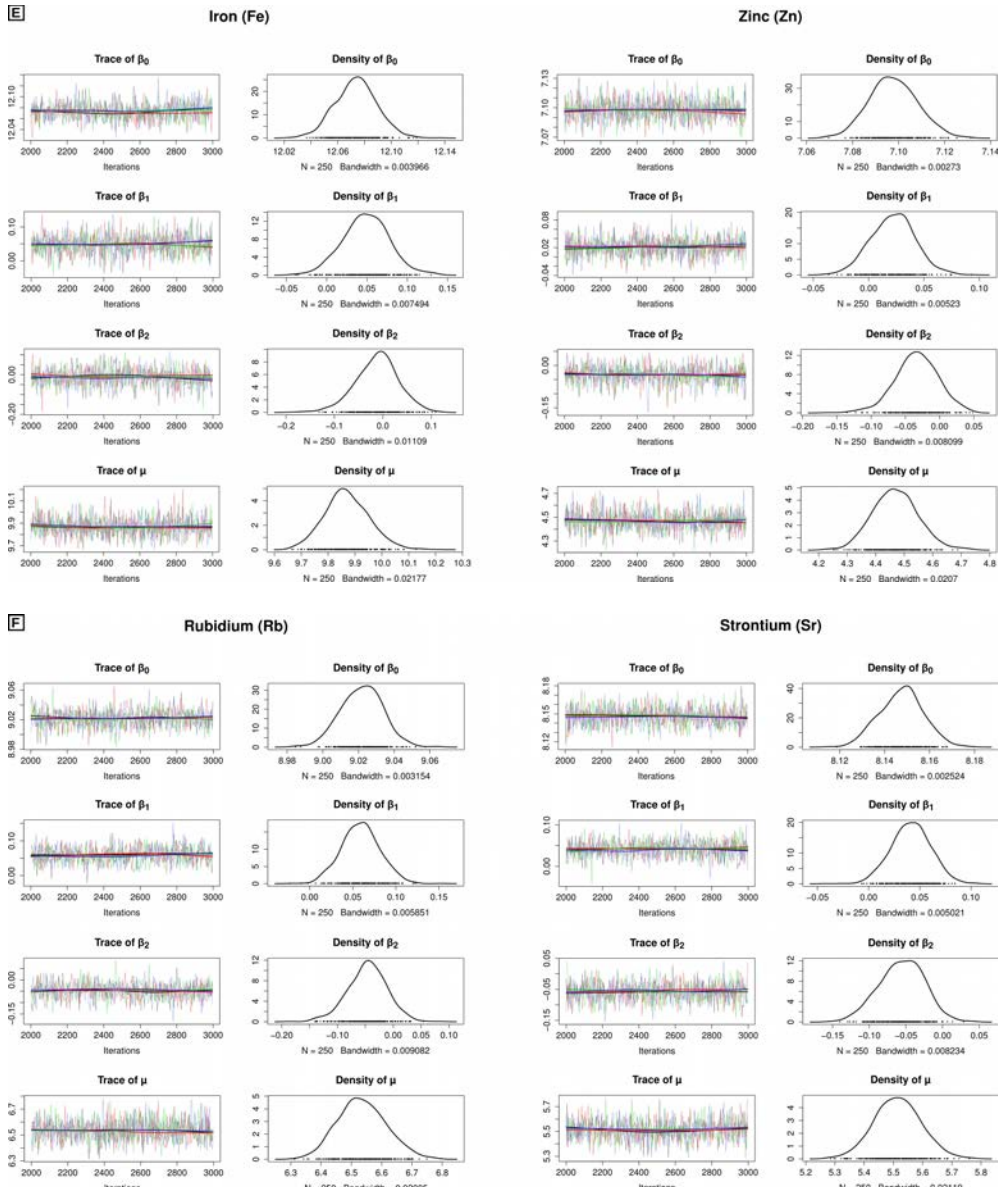


Figure 4.13. A-G) Trace plots of the four chains of the Θ parameters ($\beta_0, \beta_1, \beta_2, \mu, \sigma$) (red, green, blue and black lines) (left) and density distributions of these Θ parameters, both obtained from the initial calibration step (right) for each geochemical element. Note that a unique figure of the σ parameter is common for all the geochemical elements.

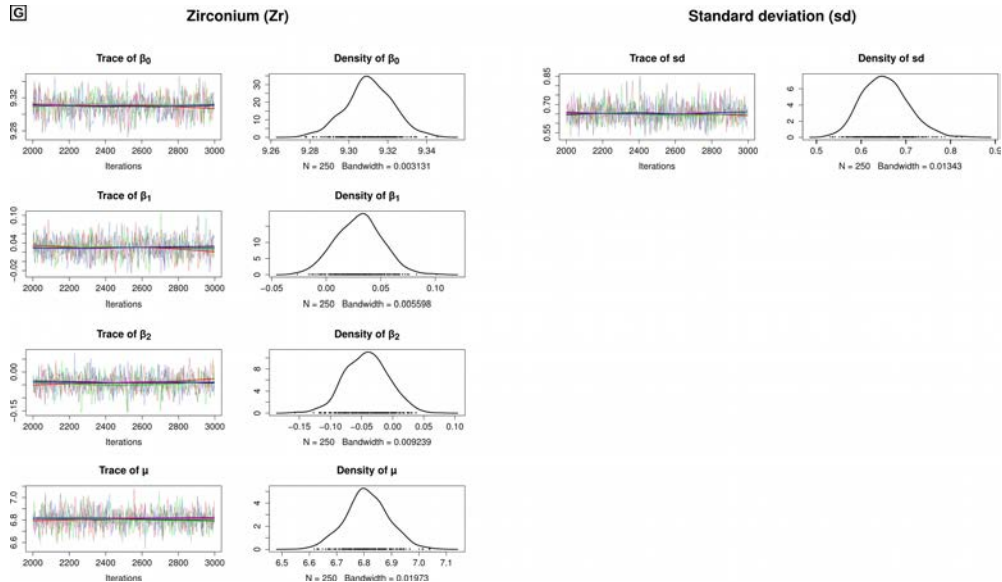


Figure 4.13. A-G) Trace plots of the four chains of the Θ parameters ($\beta_0, \beta_1, \beta_2, \mu, \sigma$) (red, green, blue and black lines) (left) and density distributions of these Θ parameters, both obtained from the initial calibration step (right) for each geochemical element. Note that a unique figure of the σ parameter is common for all the geochemical elements.

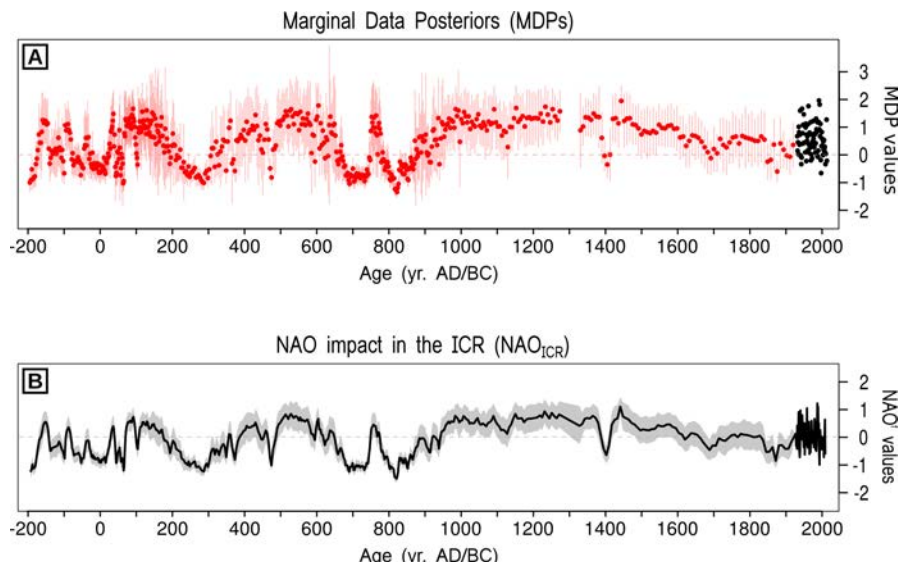


Figure 4.14. A) Black points correspond to the annual NAO index data for the overlapping period 1930–2012 AD (i.e., NAO^m). Red points show the Marginal Data Posteriors (MDPs) of NAO obtained in the second step of the Bayesian model. The red horizontal bars show the uncertainty bounds (twice the standard deviation of each MDP). B) Values of the ancient NAO impact (NAO_{ICR}) obtained using the Bayesian model (black line) and the uncertainty model (grey band) for the last two millennia. The first values without the uncertainty band correspond to the NAO index data for the overlapping period (NAO^m).

Results

The 5-fold cross-validation shows that the predicted values of the modern geochemical elements (XRF^m) obtained using the Bayesian model and the true values (i.e., the measured XRF values) do not follow a linear regression trend for any of the elements. Consequently, the correlations between the two datasets are low for all the geochemical elements (Fig. 4.15).

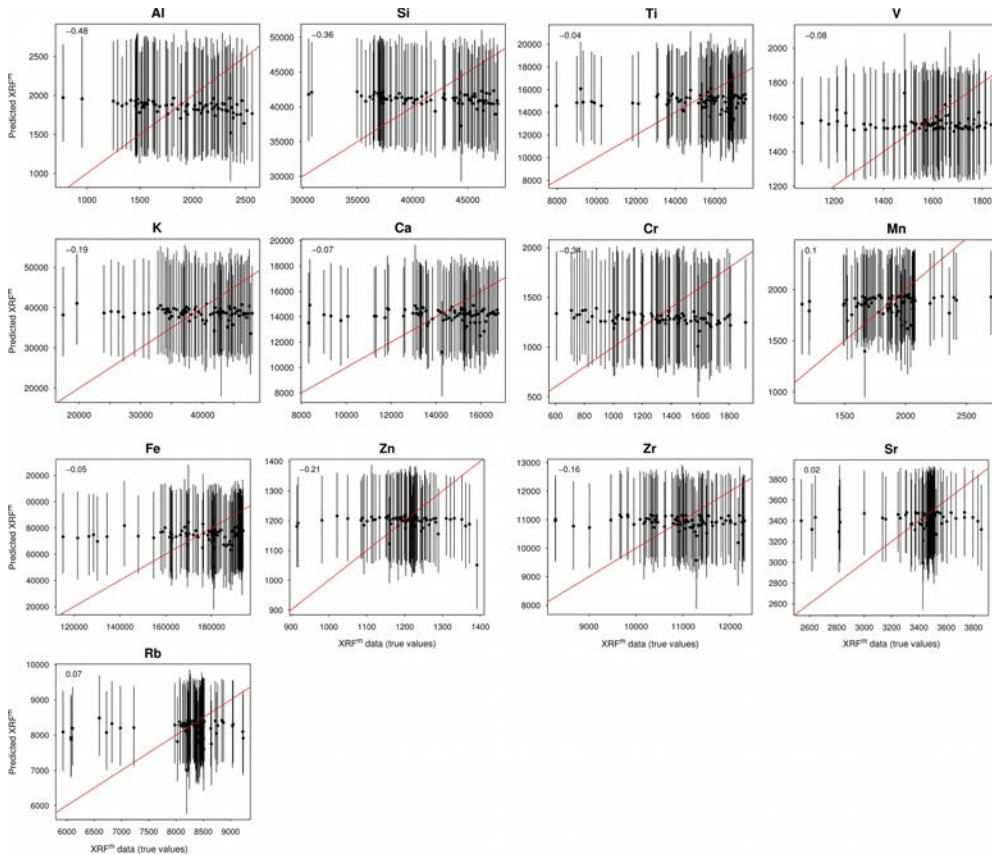


Figure 4.15. Cross-validation of the modern training set used in the Bayesian model. The figures show the true (i.e., measured) vs. predicted value of each chemical element, with vertical lines representing the uncertainty of the prediction (80% of the true samples). The red lines represent a linear regression line with intercept=0 and slope=1 values. The number located in the upper left corner of the plots indicates the correlation between the true and predicted values.

5. THE PRESENT-DAY NAO EFFECTS ON THE ICE PHENOLOGY OF IBERIAN ALPINE LAKES

5.1. Conceptual lake model

The effects of the NAO on the relationships between climate variables and ice phenology in Iberian alpine lakes have been established using a conceptual lake model. Peñalara Lake has the longest and most complete dataset (Table 3.1) for development of a conceptual model.

The Pearson correlation analyses suggest that the climatic data from the Peñalara Lake area are highly influenced by the winter NAO (Table 4.1). In winters with a prevalent negative phase of the NAO, a well-defined effect on air temperature (colder) and on precipitation (rainier) is found; hence, there are more snow days (Table 4.1). These climatic conditions control ice processes (i.e., freezing and thawing) at different time scales because freezing occurs faster than melting due to the different physical properties of water and ice.

Neither the winter (JFM) nor the spring (MAM) climatic variables exhibit significant relationships with the freeze-up dates; only the monthly mean air temperature in November is related to the freeze-up dates (Table 4.2). The freezing process is primarily driven by lake properties (e.g., surface area and mean depth) that determine the heat lost from lakes before freezing (Korhonen, 2006). Moreover, the freezing process is highly dependent on specific daily synoptic conditions (e.g., an anticyclone centred over the IP). Once the lake has lost its heat content during autumn, ice cover forms quickly after the surface water temperature falls below the freezing point, which typically occurs after a cold night with no wind (Bengtsson, 2012) (Fig. 5.1). Therefore, the freezing process is often not reflected in seasonal-scale data (i.e., autumn or early winter).

In contrast, the results show that the ice-cover duration and break-up date are negatively correlated with the winter air temperature and positively correlated with winter snow days (Table 4.1). The thawing process is slower than the freezing process and is primarily dependent on solar radiation and seasonal climatic conditions (Palecki and Barry, 1986). The melting process begins when the air temperature initially rises in late winter or early spring (Fig. 5.2). However, the snow that previously accumulated over the ice cover reduces the heat absorbed due to its lower thermal conductivity with respect to ice (Adams, 1981). Thus, the winter air temperatures coupled with the insulating effect of snow largely control the duration of ice cover and the subsequent break-up date (Figs. 5.2 and 5.3A).

At the regional scale, the effects of the NAO on the selected climatic variables are weaker in spring than in winter (Table 4.1 and Figs. 5.4 and 5.5). Moreover, for Peñalara Lake, the thawing process is typically controlled by late winter or early spring climatic conditions; the lake is often ice free during spring (Toro et al., 2006).

Therefore, the NAO effects are only transmitted to the thawing process in winter (Table 4.1 and Fig. 5.3A).

Nevertheless, some non-climatic factors (e.g., lake morphometry, altitude, and latitude) can partially control the lake ice phenology and the effects of the NAO. Therefore, the conceptual lake model developed for Peñalara Lake was adjusted for Cimera Lake to account for some of these non-climatic factors (Fig. 5.3B). In addition, the conceptual lake model for Redon Lake (Fig. 5.3C), an alpine lake (2240 m asl, 24 ha, 655 m long, 565 m wide and 73 m maximum depth) located in the Central Spanish Pyrenees that is typically ice-covered from early December to May-June (Pla-Rabes and Catalan, 2011), is also discussed to account for these non-climatic factors (Sánchez-López et al., 2015).

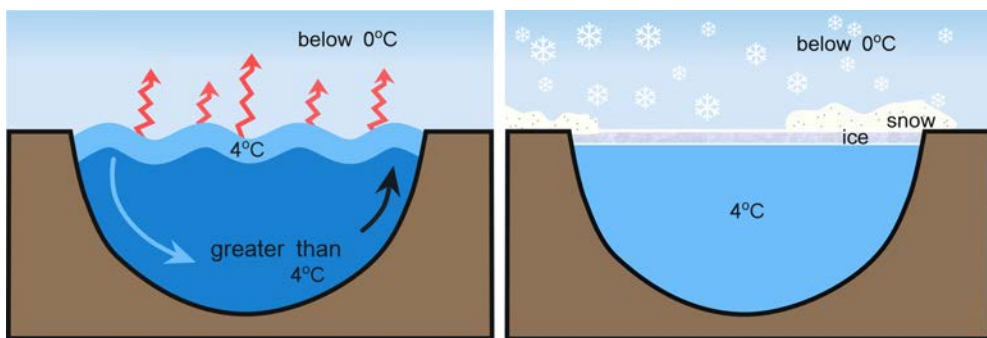


Figure 5.1. Two different stages of lake ice formation. A) During autumn, the lake surface progressively loses its heat to the cooler air. This cooled surface water sinks and is replaced by warmer and less dense water from the bottom of the lake (water temperature $> 4^{\circ}\text{C}$). The mixing continues until all the lake water has reached a maximum-density temperature of approximately 4°C . B) The end of the mixing process means that the cooled water does not sink and that it remains at the surface, allowing it to cool further. Once this water reaches the freezing point (below 0°C), solid ice forms on the surface of the lake. Snowfall during winter accumulates on the ice cover, acting as a blanket due to its insulating effect.

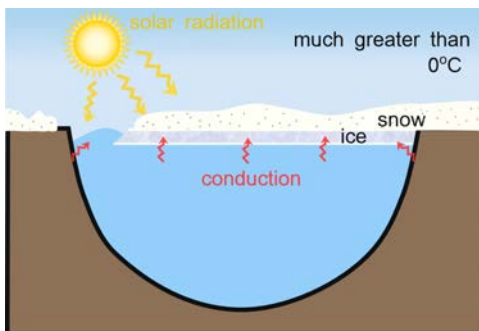


Figure 5.2. Lake ice thawing process. As temperatures increase, the accumulated snow on the ice cover begins to melt. Once the snow melts off the top of the ice cover, the ice is exposed to the sun and it decays through two methods: 1) melting caused by solar radiation and pools of meltwater on the surface of the ice and 2) heat conduction from the surrounding land and warmer water flowing under the ice from streams or runoff.

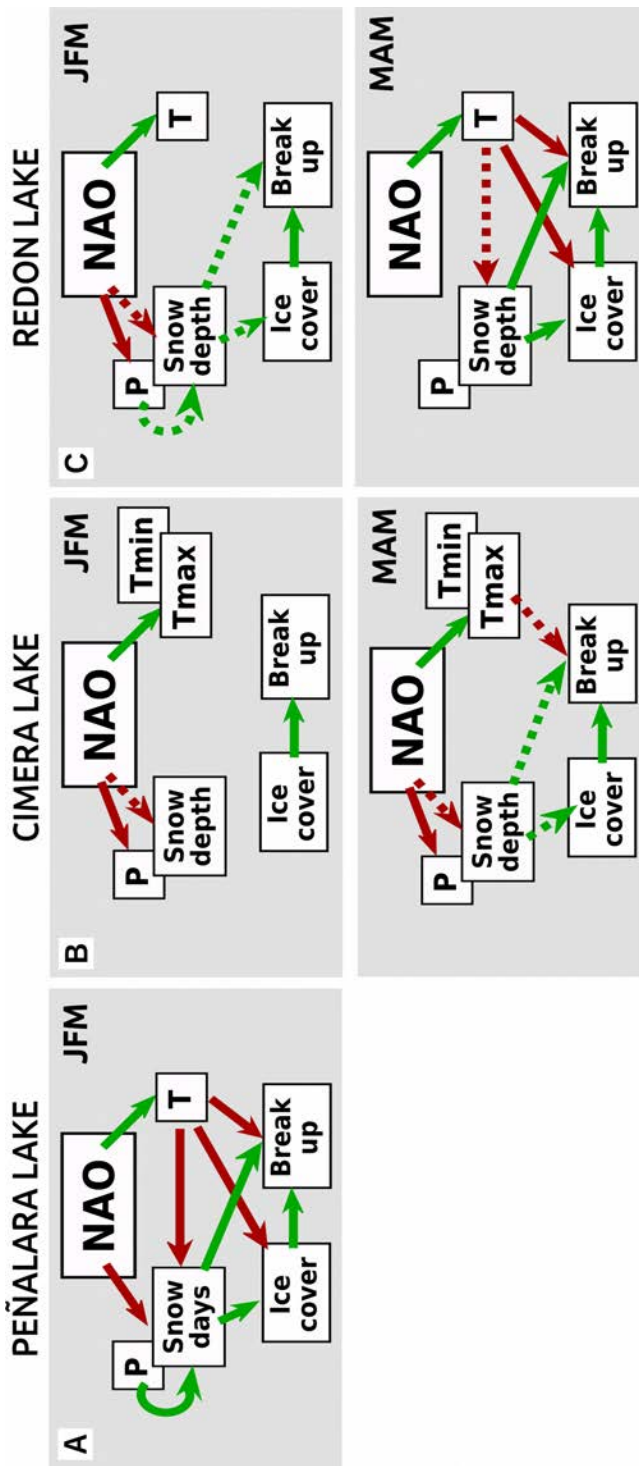


Figure 5.3. Conceptual models for A) Peñalara Lake, B) Cimera Lake and C) Redon Lake (Sánchez-López et al., 2015) in winter (JFM) (top) and spring (MAM) (bottom). The green lines represent positive correlations, and the red lines represent negative correlations. Dashed lines represent non-significant correlations. The arrowhead indicates the direction of the effect.

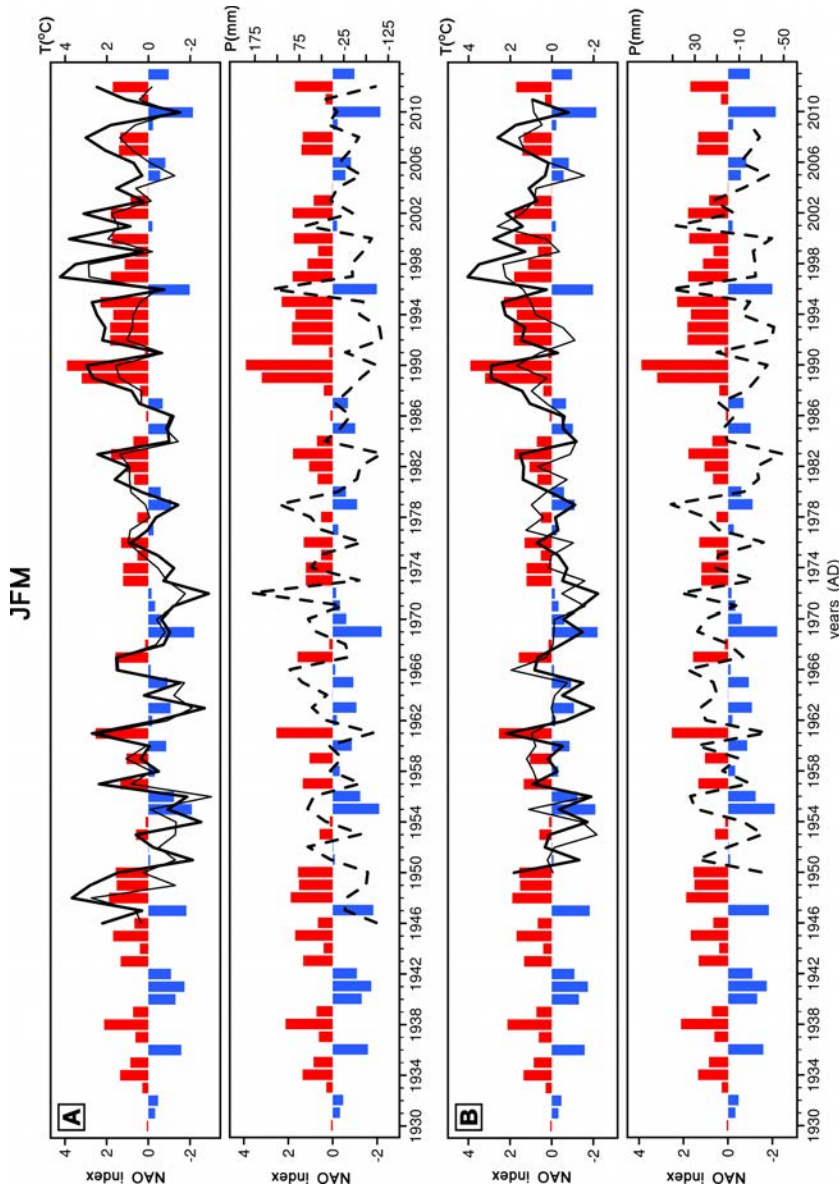


Figure 5.4. Bar graphs of the winter (JFM) NAO index (i.e., positive phase in red bars and negative phase in blue bars). The lines correspond to winter (JFM) anomalies in the maximum (black line, top) and minimum (thin line, top) temperatures and precipitation (black dashed line, bottom) from A) the Navacerrada weather station and B) regional data from the Cimera Lake area.

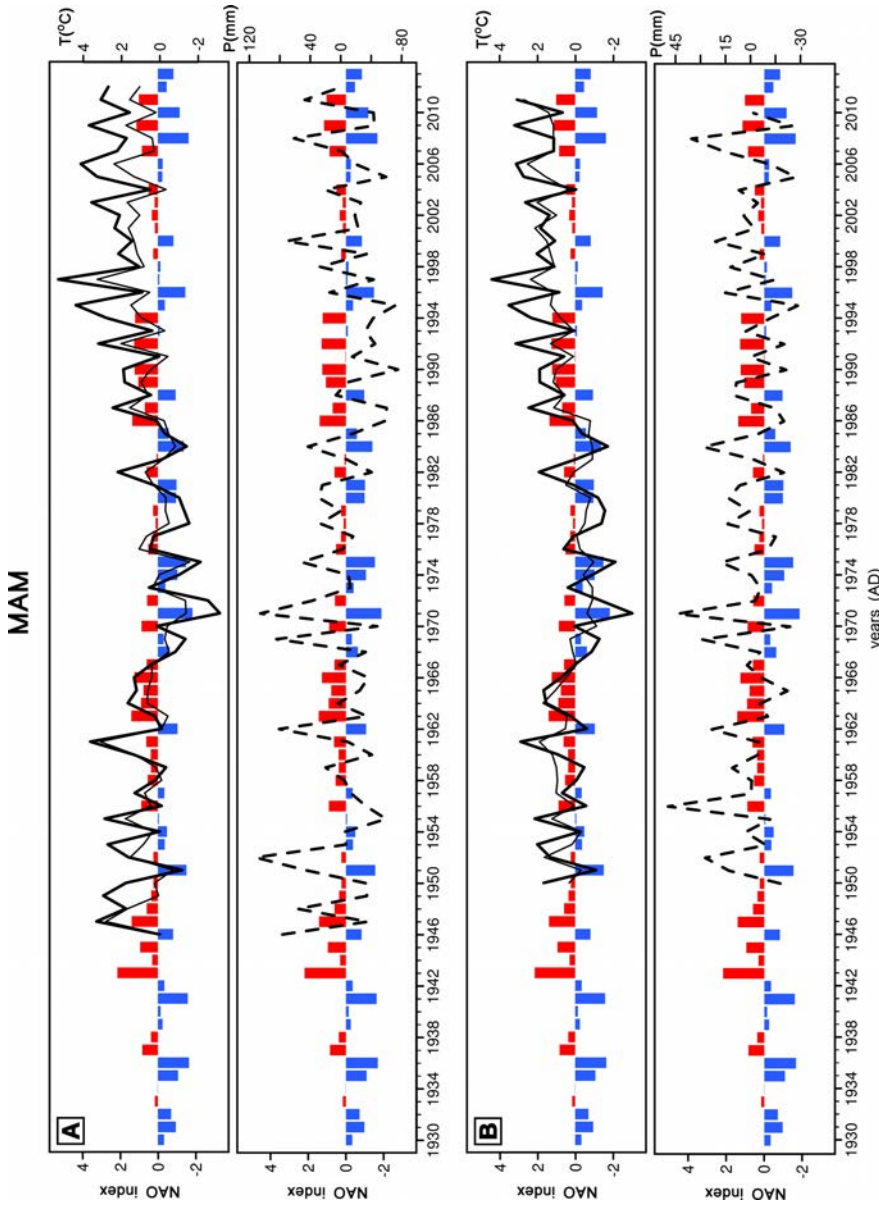


Figure 5.5. Bar graphs of the spring (MAM) NAO index (i.e., positive phase in red bars and negative phase in blue bars). The lines correspond to spring (MAM) anomalies in the maximum (black line, top) and minimum (thin line, top) temperatures and precipitation (black dashed line, bottom) from A) the Navacerrada weather station and B) regional data from the Cimera Lake area.

5.2. Differences in winter NAO effects

5.2.1. Morphometric factors

Redon Lake is larger and deeper than Peñalara and Cimera lakes; thus, dissimilarities exist between the ice phenologies of these lakes (Fig. 5.6). Lake morphometry is an important factor that controls ice cover because it affects the strength of wind action, water circulation, water temperature, and heat storage in the lake (Jeffries and Morris, 2007). Although lake morphometry is an important factor for the freezing process, it has been determined to be less important for predicting the break-up date compared with air temperature, latitude and elevation (Williams and Stefan, 2006). For Cimera Lake, there is an escarpment on the southern side of the catchment that exerts a shading effect conducive to extended ice cover and later break-up dates (Fig. 2.5). Nevertheless, our results show that the NAO effects on ice phenology are more prominent than the shading effect. Thus, neither morphometric dissimilarities between lakes nor the shading effect over Cimera require the introduction of any adjustment to the conceptual models (Fig. 5.3).

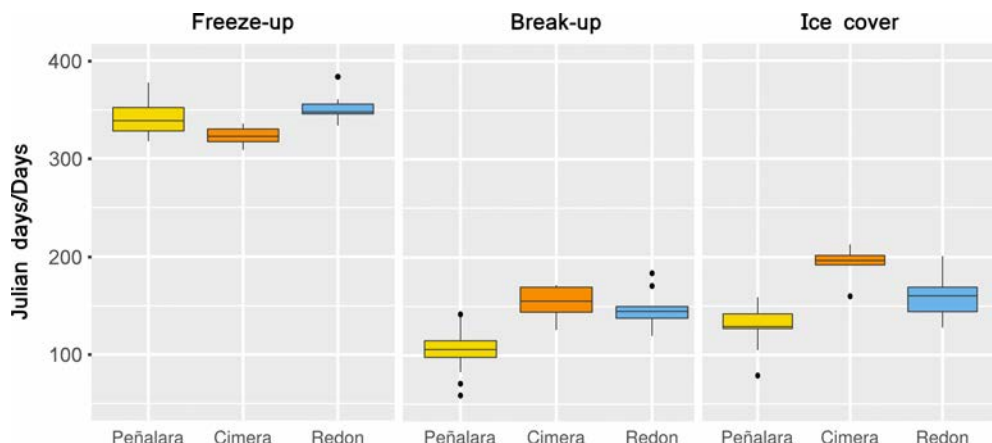


Figure 5.6. Boxplots of ice phenology for Peñalara Lake (yellow), Cimera Lake (orange) and Redon Lake (blue). The black circles correspond to outliers. Freeze-up and break-up are in Julian days whereas ice-cover duration is in number of days. The data periods are 1993–2013, 2006–2013 and 1997–2013 for Peñalara, Cimera and Redon lakes, respectively.

5.2.2. The altitude effect

The conceptual model developed for Peñalara Lake (2016 m asl) (Fig. 5.3A) exhibits some variability for Cimera Lake (2140 m asl) and Redon Lake (2240 m asl) (Figs. 5.3B and 5.3C) because the lake altitude strongly affects the break-up date (Šporka et al., 2006; Brown and Duguay, 2010).

In winter, the results demonstrate that the NAO has smaller effects on precipitation and on air temperature for Redon Lake ($r= -0.41$ and $r= 0.43$, respectively)

(Sánchez-López et al., 2015) than for Peñalara Lake ($r = -0.67$ and $r = 0.69$, respectively; Table 4.1). The Redon Lake snow data are not sufficient to obtain significant correlations; however, these data suggest a higher dependency of snow accumulation on precipitation than on air temperature (Sánchez-López et al., 2015). In contrast, snow days in the Peñalara Lake area depend on air temperature ($r = -0.75$) and precipitation ($r = 0.69$). Moreover, the significant relationships between winter climatic variables (i.e., air temperature and snow days) and ice records (i.e., break-up and ice-cover duration) found for Peñalara Lake only occur in spring in the Redon Lake area (Fig. 5.3). Therefore, the ice-cover duration and break-up date are negatively correlated with the spring air temperature and positively correlated with the spring snow depth in the Redon Lake area (Fig. 5.3). However, the spring snow depth exhibits a small and non-significant correlation with precipitation in this season; thus, the spring snow depth primarily corresponds to winter and early spring accumulations (Fig. 5.3) (López-Moreno, 2005; Sánchez-López et al., 2015). These results demonstrate the increasing importance of air temperature relative to snowfall as the altitude decreases. At high-elevation sites, air temperatures are typically below 0 °C for longer periods; thus, the snow accumulation primarily depends on precipitation rather than the air temperature. However, the air temperature increases as the elevation decreases; thus, snowfall is controlled by precipitation and air temperature (López-Moreno et al. 2011a). In addition, the winter snow cover lasts longer at higher-altitude sites, which extends the insulating effect of the snow cover, which influences the melting process. Therefore, the winter NAO effects on the melting process are uncoupled with both the snow accumulation (i.e., winter snow depth) and the air temperature (i.e., spring air temperature) in the highest studied lake (i.e., Redon Lake) until spring, whereas the effects are coupled at lower sites (i.e., Peñalara Lake) and only occur in winter (Fig. 5.3).

For Cimera Lake, the NAO appears to control regional air temperatures and precipitation in winter ($r = 0.70$ and $r = -0.71$, respectively) and spring ($r = 0.42$ and $r = -0.51$, respectively) (Table 4.3 and Figs. 5.4 and 5.5). Therefore, it is expected that the NAO effects on ice phenology in the Cimera Lake region should reflect a combination of the effects found in the Peñalara Lake and Redon Lake regions. Unfortunately, the scarcity of available data only permits a partial establishment of these relationships for this lake (Tables 4.3 and 4.4, and Fig. 5.3B).

5.2.3. The latitude effect

Latitude is also an important factor that primarily affects the break-up date (Brown and Duguay, 2010), modulating the NAO effects on the ice melting process.

Despite the differences between the effects of the NAO on climatic variables in the Peñalara Lake and Redon Lake areas (Fig. 5.3) that are primarily due to altitude effects, the results show that the effects of the NAO on precipitation and snow accumulation increase as the latitude decreases (Fig. 5.3). Therefore, the effects of the NAO on the selected climatic variables become more complex as the latitude decreases. At high latitudes, the NAO largely controls the air temperature. However, at low latitudes, the NAO effects on precipitation increase (Trigo et al., 2002). For example,

López-Moreno et al. (2011b) showed that the NAO primarily controls the differences between cold and warm conditions over the Alps; nevertheless, the NAO produces significant differences between wet and dry conditions in the ICR and the Pyrenees. Consequently, the NAO effects on snowpack evolution and ice phenology will be different in each region. Moreover, the air temperature primarily governs snow accumulation in the Swiss Alps, whereas precipitation exhibits a variable effect on snow accumulation in this region. However, the snowpack is controlled by precipitation rather than by air temperature in the Pyrenees (López-Moreno et al., 2011a).

Latitude controls ice phenology via solar radiation due to the strong dependence of ice dynamics on the radiative balance at the surface of a lake (Leppäranta, 2010). High-latitude locations have air temperatures that are often below 0 °C for a substantial period of time in winter; this trend is also reflected in lake ice behaviour. Previous studies that focussed on predicting break-up dates introduced latitude as an important factor in determining this ice parameter (e.g., Weyhenmeyer et al., 2011; Livingstone and Adrian, 2009). These studies are usually based on the break-up dates of lakes located in higher-latitude sites where the air temperature is the primary factor that determines ice phenology, as opposed to other factors such as precipitation or snow accumulation (Thompson et al., 2009).

At higher latitudes, such as Lake Baikal (Livingstone, 1999), the Baltic region (Yoo and D'Odorico, 2002) and the English Lake District (George, 2007), the NAO signal primarily affects ice phenology via the air temperature, whereas at lower latitudes (e.g., the IP), the NAO effects on ice cover are transmitted via both the air temperature and precipitation. The latter factor plays an important role in the amount of snow that accumulates on the ice cover, which is important due to the insulating effect of snow (Tables 4.1, 4.3 and Fig. 5.3).

6. THE EA PATTERN AND NAO INTERPLAY OVER THE IBERIAN PENINSULA FOR THE LAST TWO MILLENNIA

6.1. Sedimentology and interpretation of statistical analyses (RDAs and PCAs)

The RDAs of the Peñalara and Cimera lake records show that some geochemical elements can be used as indicators of physico-chemical processes that control the sedimentary deposition in the lakes (Fig. 6.1). The similarities between both RDAs indicate that these processes are analogous in both lakes and that the differences between the indicators might be primarily ascribed to differences in parent rocks (gneiss in Peñalara Lake and granites in Cimera Lake) and, to a lesser extent, to lake morphometry. In the PE12-01-01 record, chemical elements such as Si, Mn, Zr, and Ti, as well as the organic content, are related to fine material (i.e., muscovite), whereas these elements do not have any association with coarse material from the gneiss (i.e., quartz, albite and microcline). In the CIM12-04A record, Ti, Zr and Rb are associated with coarse material from the granites (i.e., quartz, albite and microcline), whereas the organic content is associated with fine material (i.e., muscovite). These relationships suggest that the first RDA eigenvector in both records can be interpreted in terms of the hydrological sorting of siliciclastic inputs (Fig. 6.1).

The $PC1_{pe}$ is related to most of the chemical elements and partially to the TOC and TN contents (Fig. 6.1 and Table 4.7). The $PC1_{cim}$ is associated with most of the chemical elements and with Ti in particular, and it is derived from detrital minerals that are not affected by diagenetic processes. Furthermore, the lack of association between these detrital elements and the organic matter suggests that both PC1s ($PC1_{pe}$ and $PC1_{cim}$) reflect changes in the input of siliciclastic material from the catchment (Fig. 6.1 and Table 4.7). Negative (positive) values of the two first eigenvectors indicate higher (lower) siliciclastic inputs with a major (minor) presence of coarse material (Fig. 6.1). Thus, higher siliciclastic inputs imply lower hydrological sorting because of fine and coarse detrital material entering the lakes, and vice versa. These coarser siliciclastic inputs lead to the dilution of the in-lake organic matter production, thereby reducing its percentages in the deposited lake sediments, whereas fine siliciclastic material inputs (i.e., muscovite) result in the opposite conditions. In alpine lakes, one of the main transport processes governing siliciclastic inputs is runoff derived from snowmelt and rainfall. The intensity of the runoff is controlled by the occurrence of a well-defined melt season in terms of temperature and rainfall variations (Pelto, 2008). Hence, during periods characterized by warmer springs caused by an earlier increase in temperature, the snowmelt coincides with the arrival of spring rainfall, thereby leading to rain-on-snow events, which are responsible for intense runoff episodes (Asikainen et al., 2006; Nesje et al., 2001; Parris et al., 2010; Fig. 6.2). These higher-energy runoff currents reduce the hydrological sorting and increase the proportion of coarse-grained material

from less weathered parent rock (i.e., quartz, albite and microcline) in the sediments.

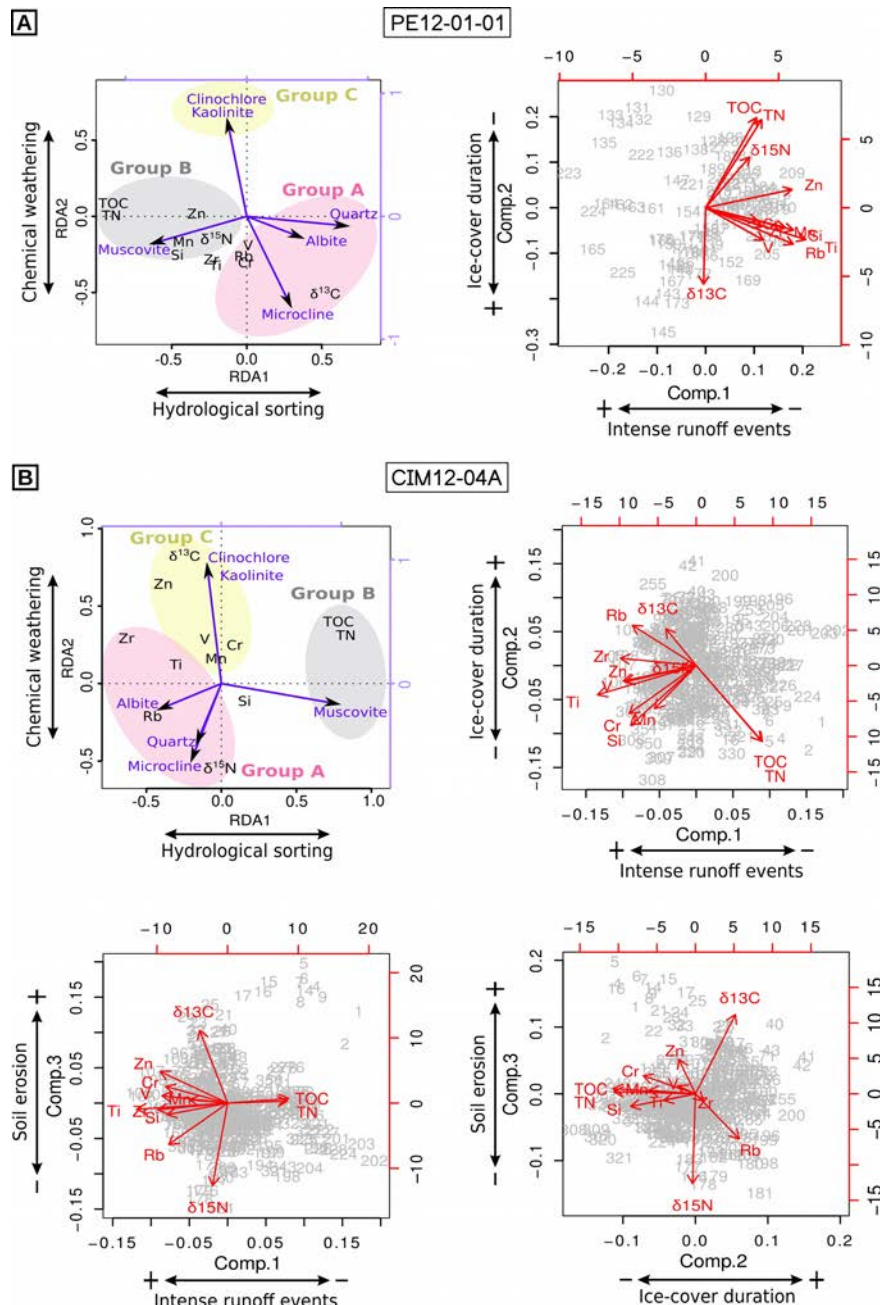


Figure 6.1. RDA and PCA biplots for the A) PE12-01-01 and B) CIM12-04A records. Light red, grey and yellow areas indicate groups A, B and C, respectively.

However, during periods characterized by later increases in temperature, a percentage of the spring precipitation occurs in the form of snow, which reduces the rain-on-snow events and diminishes the possibility of extreme runoff currents (Fig. 6.2). The gradual snowmelt with lower-energy transport enhances the hydrological sorting and increases the proportion of fine material (i.e., muscovite mud grains) in the lake sediments.

As Peñalara Lake is located at a lower altitude than Cimera Lake, it has a shorter and earlier snowmelt season than Cimera Lake, which can sometimes result in an uncoupled influence of snowmelt and spring rainfall on the runoff, resulting in few to no rain-on-snow events in this area. Nevertheless, the sum effect of both uncoupled effects on Peñalara Lake runoff is expected to be similar to the effect of rain-on-snow events on Cimera Lake runoff.

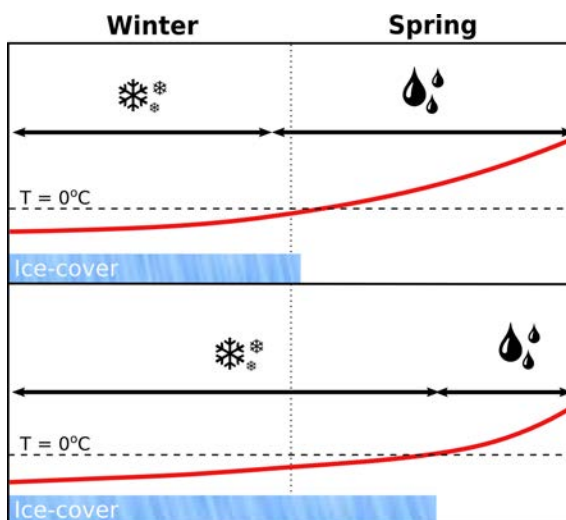


Figure 6.2. Diagram explaining the meteorological winter-spring conditions that determine the occurrence of rain-on-snow events. The black dashed lines correspond to a temperature of 0 °C, and red lines represent the temperature evolution.

Although the two variables that mainly influence the siliciclastic inputs are snowmelt and spring rainfall, summer and autumn storms can also represent an important factor that controls the input of terrigenous material in both lakes. Hence, it can be hypothesized that the sandy facies, i.e., the M2 and S layers of the records, might correspond to high-energy flood events derived from these storms (Figs. 4.1 and 4.2).

The second eigenvector of both RDA analyses opposes unaltered siliciclastic material (i.e., quartz, albite and microcline). This eigenvector is associated with $\delta^{13}\text{C}$ values and elements such as V, Cr, and Rb in the PE12-01-01 record, with Rb and weathered minerals in the CIM12-04A record (i.e., kaolinite and clinochlore), and partially with the organic fraction in both records (Fig. 6.1). The RDA analysis of the CIM12-04A core also shows that $\delta^{13}\text{C}$ enrichments are linked to increases in the proportion of chemically weathered material and that $\delta^{15}\text{N}$ depletions are associated with decreases in coarse-grained unaltered material (Figs. 4.8 and 6.1). Hence, these eigenvectors can be interpreted in terms of the chemical weathering of the parent rocks present in the soil catchment of both lakes.

The PC_{2pe} is related to $\delta^{13}\text{C}$ values and TOC and TN contents (Fig. 6.1 and Table

4.7A). The PC_{2cim} is mostly related to the TOC, TN and Rb values (Fig. 6.1 and Table 4.7B). The TOC concentration is a bulk value that represents the fraction of organic matter that escaped remineralization during sedimentation, and it is commonly considered a good indicator of the organic productivity of a lake (Meyers and Teranes, 2001). The burial of organic matter is frequently followed by the rapid loss of N (Cohen, 2003), and the positive covariance of the two proxies in both lakes indicates negligible organic matter degradation. In addition, the TOC/TN ratio, featuring a value of approximately 13 in both records (Figs. 4.7 and 4.8), suggests that the accumulated organic matter has a mainly algal origin (Meyers and Lallier-Vergès, 1999). Therefore, both PC_{2pe} and PC_{2cim} are associated with variations in the lake organic productivity. In PC_{2pe}, positive (negative) values of the second eigenvector represent a decrease (increase) in lake productivity associated with both the internal recycling of nutrients and, to a lesser extent, the input of weathered material from the catchment (Fig. 6.1). In PC_{2cim}, the variations in lake productivity show the opposite pattern (Fig. 6.1). The weathered material is produced by a series of chemical reactions that occur in the soil (Catalan et al., 2014) and that generate a pool of micronutrients that, when released by soil erosion, might enhance the in-lake productivity. In alpine lakes, the ice-cover duration modulates lake productivity through its influence on the growing season length, summer stratification, and lake overturning strength and timing, which determine the internal lake nutrient cycle (Catalan and Fee, 1994; Catalan et al., 2002; Pla-Rabes and Catalan, 2011). The ice cover of Iberian alpine lakes depends on both the winter-spring temperature and accumulated precipitation in the form of snow on the ice cover. Cold (warm) and wet (dry) conditions will lead to longer (shorter) ice-cover durations, which is partly a result of the enhanced (reduced) insulating effect of the snow deposited on the ice cover (Sánchez-López et al., 2015). Therefore, during periods characterized by colder spring temperatures and a prolonged snow season, the ice cover will last longer (Fig. 6.2), which will lead to a shorter growing season and thus lower lake productivity. However, the opposite situation occurs during periods characterized by shorter ice-cover durations as a result of warmer spring temperatures and a shorter snow season (Fig. 6.2).

Additionally, the presence of other factors, such as the nutrient inputs from outside the catchment, can also influence the productivity of alpine lakes. A number of studies have shown that the arrival of African dust is an important source of limiting nutrients, such as phosphorus and nitrogen, for these oligotrophic environments (Toro et al., 2006; Reche et al., 2009; Camarero and Catalan, 2012). Thus, dust events can enhance lake productivity. African dust events are clearly recorded in the Cimera lake sequence, as evidenced by the accumulation of palygorskite (Fig. 4.8). This clay is formed in very arid conditions, such as deserts, or in alkaline environments (Singer and Norrish, 1974). Therefore, it was most likely deposited in Cimera Lake during Sahara-Sahel dust events that affect the IP (Rodríguez et al., 2015). These external inputs of nutrients are also supported by the results obtained from the sample collected in the Cimera catchment after a dust episode, which revealed concentrations of nitrate, sulphate and total phosphorous several orders of magnitude higher than those of the water in the lake (Table 6.1; Toro et al., 2006). Nevertheless, the relationship between these external nutrient inputs (reflected by the palygorskite percentages) and lake

productivity (reflected by the TOC and TN contents through the negative scores of PC_{2cim}) appears to be opposite to the expected relationship (i.e., $r_{PC2} = 0.38$, p-value < 0.01). More palygorskite is related to lower lake productivity, and vice versa. The respiration of the organic matter accumulated in the lake bottom provokes a release of CO₂, which, in turn, produces a decrease in the pH of the water layers closer to the sediments (Catalan and Camarero, 1993). The stability of palygorskite depends on both pH and concentrations of Mg and Si, being more stable under alkaline pH conditions (Velde, 1995). Therefore, lake productivity decreases during long-lasting ice-cover, and palygorskite is preserved due to the higher alkalinity in the first millimetres of lake sediment (Velde, 1995). On the contrary, when lake productivity increases due to either extra nutrient inputs or shorter ice-cover durations, bacterial activity in the sediment also increases (Reche et al., 2009), provoking an increase in CO₂ concentration and a decrease in the pH. Under these conditions, the palygorskite deposited in the sediment is less stable. As a result, enhanced Cimera Lake productivity reflects intense arid episodes associated with short-lasting ice cover and enhanced African dust inputs. In Peñalara Lake, the mineralogical data showed that the influence of African dust inputs on lake productivity is less clear (Fig. 4.7). No apparent relationship was found in the correlation coefficients between lake productivity (reflected in the positive scores of the second eigenvector) and palygorskite ($r_{PC2} = 0.05$, p-value > 0.1), although positive but non-significant correlations were found between this clay and the TOC and TN percentages.

Samples/Analyses	[NO ₃ ⁻]	[SO ₄ ⁻²]	TP
Dust sample (ppm)	190	530	0.5
Lake water (ppb)	36	0.3	9

Table 6.1. Concentration of nitrate (NO₃⁻), sulphate (SO₄⁻²) and total phosphorous (TP) in the dust sample collected in the Cimera Lake catchment (in ppm) and in a water sample from Cimera Lake (in ppb; Toro et al., 2006).

The third eigenvector is only significant in Cimera Lake (PC_{3cim}), and the interpretation of PC_{3cim} is related to variations in the isotopic composition (i.e., δ¹³C and δ¹⁵N values) of the organic matter (Fig. 6.1). Because the RDA eigenvector has been previously interpreted in terms of the inputs of weathered material produced in soils, the PC_{3cim} could be a rough indicator of soil erosion. Neither of the isotopic signatures shows a trend from the bottom to a depth of 35 cm in the studied core. Above this interval, δ¹³C enrichment and δ¹⁵N depletion occur, with the latter change more prominent in the uppermost 7.5 cm of the sequence (Fig. 4.8). These variations coincide with remarkable increases in the contents of clay minerals (Fig. 4.8). The TOC/TN ratio increases between 22.5 cm and 7.5 cm of core depth, and together with the δ¹³C fluctuations located between 35 and 7.5 cm, it may be related to inputs of organic matter from the erosion of the catchment soil (Meyers and Lallier-Vergès, 1999; Meyers and Teranes, 2001). Soil organic matter is usually enriched with respect to δ¹³C values because of remineralization and depleted with respect to δ¹⁵N values because of its

atmospheric origin (Meyers and Teranes, 2001). Therefore, the supply of this organic matter to the lake might explain the variations in the isotope records. The positive covariance between the PC3_{cim} and the increased clay mineral proportions also support the soil erosion hypothesis (Fig. 4.8).

However, in the uppermost 7.5 cm, the TOC and TN percentages increase significantly and the $\delta^{15}\text{N}$ depletion is more prominent (Fig. 4.8), and these changes could be related to global climate change (Catalan et al., 2013). The lake productivity could have been enhanced because of temperature increases and large inputs of atmospheric nitrogen ($\delta^{15}\text{N}$ depleted) resulting from the increase in the global pool of reactive nitrogen (Bergstrom and Jansson, 2006). Fossil fuel combustion and the Haber-Bosch process have altered the global nitrogen cycle (Galloway and Cowling, 2002). A large number of sediment records from remote lakes in the Northern Hemisphere also show this $\delta^{15}\text{N}$ depletion during the Industrial Era (Hastings et al., 2009; Holtgrieve et al., 2011). The enhancement of chemical weathering over a short time scale because of the present global warming trend (Catalan et al., 2014) might also intensify the biogeochemical reactions within the lake, thereby contributing to the observed increases in TOC and TN and decreases in the TOC/TN ratio during the Industrial Era. Hence, the PC3_{cim} in this last interval could provide an indicator of the effects of global warming and/or human pollution, which could have similar effects on the $\delta^{15}\text{N}$ values because of the organic matter inputs derived from soil erosion.

In summary, from the bottom to a depth of 7.5 cm in the Cimera sequence, positive values of the PC3_{cim} reflect an enhancement of soil erosion episodes, whereas in the uppermost 7.5 cm, this eigenvector might also reflect the influence of global warming and/or human pollution on lake productivity.

6.2. Climatic and environmental changes in the Iberian Central Range and the Iberian Peninsula over the last two millennia

The multivariate RDA and PCA analyses of geochemical and mineralogical datasets from Peñalara and Cimera records have allowed us to determine climatic and environmental changes in the ICR. This reconstruction has been primarily focussed on the Cimera Lake sequence because it presents a much better constrained chronology than the Peñalara sequence, although the latter sequence supports the climatic and environmental conditions described for the ICR (Fig. 6.3). This reconstruction includes five main climate chrono-zones: The Roman Period (RP; ca. 250 BC – 500 AD), the Early Middle Ages (500 – 900 AD), The Medieval Climate Anomaly (MCA; 900 – 1300 AD), The Little Ice Age (1300 – 1850 AD) and the Industrial Era (1850 – 2012 AD).

Comparisons with the main IP sedimentary records have been used to establish the contextual climatic and environmental conditions over the last two millennia in the IP in these climatic chrono-zones (Fig. 6.4).

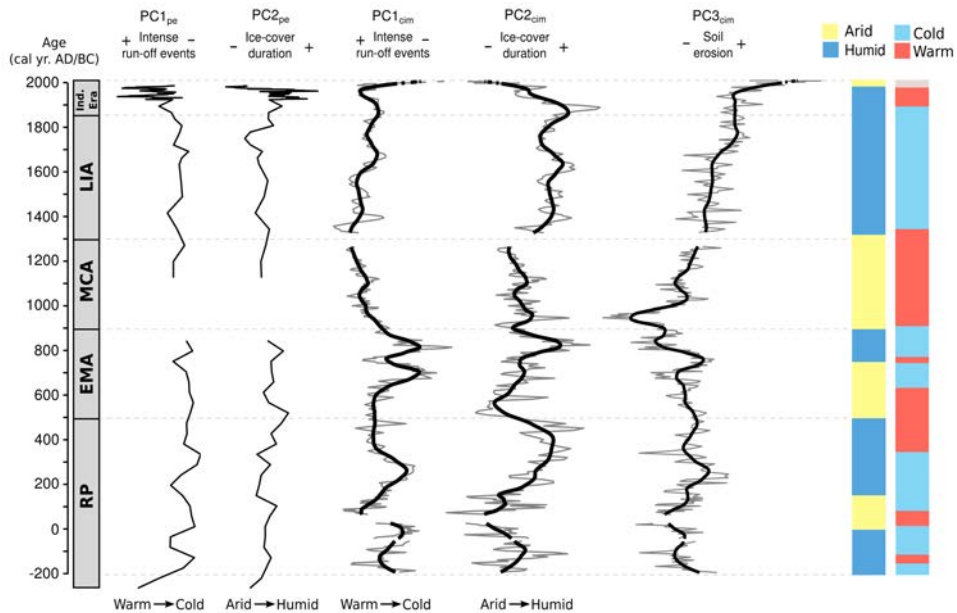


Figure 6.3. Variations in the $PC1_{pe}$ and $PC2_{pe}$ scores relative to age in the Peñalara Lake sequence and in the $PC1_{cim}$, $PC2_{cim}$ and $PC3_{cim}$ scores relative to age in the Cimera Lake sequence. Main climate periods are indicated with grey dashed lines. Original data are plotted in grey lines, and smoothed data calculated with the loess function and a span degree of 0.10 are represented by thicker black lines. Vertical bars correspond to thermal and hydrological conditions suggested by the processes assigned to $PC1_{cim}$ and $PC2_{cim}$. Note that the $PC2_{pe}$ values have been inverted to be in agreement with the ice-cover duration of $PC2_{cim}$.

6.2.1. The Roman Period (RP; ca. 250 BC – 500 AD)

In terms of thermal conditions, the sedimentary records from the NW of the IP indicate predominantly warm conditions during this period (Martínez-Cortizas et al., 1999; Desprat et al., 2003; Álvarez et al., 2005; Martín-Chivelet et al., 2011;). In the Pyrenees, Redon Lake displayed low winter-spring temperatures (~200 BC – 400 AD) and a warming trend at the end (Pla and Catalan, 2005, 2011), whereas the summer-autumn temperatures showed a transition from cold to warm conditions (Catalan et al., 2009). In the centre of the IP, Almenara de Adaja (López-Merino et al., 2009) and Tablas de Daimiel (Gil-García et al., 2007) registered a centennial-scale alternation of cold and warm periods, whereas the Peñalara and Cimera lakes sequences exhibited decadal short-lived periods of rain-on-snow events, which suggest cold and warm oscillations (Figs. 6.3 and 6.4). These differences in the frequency of climatic oscillations can be partially ascribed to the lower temporal resolution of the first Iberian records. Finally, the Tajo Prodelta recorded a warm period (Abrantes et al. 2005; Rodrigues et al., 2009). To the best of our knowledge, records from the southern IP have not been employed in temperature reconstructions.

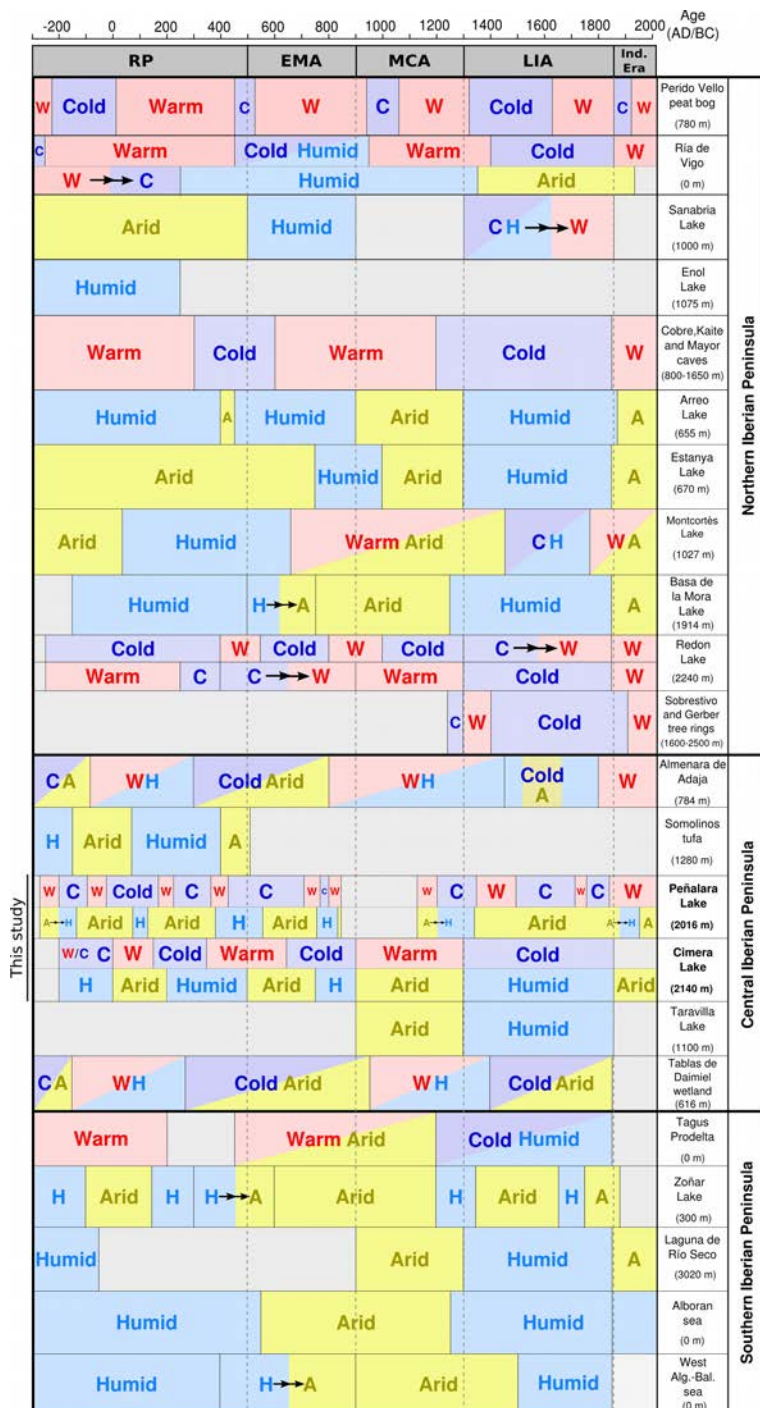


Figure 6.4. Summary of the climatic conditions reconstructed using different records from the IP. A=arid, H=humid, C=cold, and W=warm, and arrows indicate climate transitions. Fig. 1.21 shows the locations of these records. The records from the northern to southern IP include the Penido Vello peat bog (Martínez-Cortizas et al., 1999); Ría de Vigo (Desprat et al., 2003; Álvarez et al., 2005); Sanabria Lake (Iambriña-Enriquez et al., 2014); Estany Lake (Morelón et al. 2009, 2011); Cobre, Kaité and Mayor caves (Martín-Chivel et al., 2011); Arreó Lake (Corella et al., 2013); Montcortès Lake (Corella et al., 2011); Basa de la Mora Lake (1914 m; Moreno et al., 2012; Pérez-Sanz et al., 2013); Redon Lake (Pia and Catalán, 2005, 2011; Catalán et al., 2009); Sobrestrobo and Gerber tree rings (Bünigen et al., 2008); Almenara de Adaja (López-Merino et al., 2009); Sonolinos tufa lake (Carrás et al., 2012); Peñalara and Cimera lakes (this study); Taravilla Lake (Moreno et al., 2008); Tablas de Daimiel wetland (Gil García et al., 2007); Tajo Prodelta (Abrantes et al., 2005; Rodrigues et al., 2009); Zohar Lake (Martín-Puertas et al., 2008); Laguna de Río Seco (Jiménez-Espejo et al., 2014); Alboran sea (Martín-Puertas et al., 2010); and West Algerian-Balearic sea (Nieto-Moreno et al., 2011).

In terms of humidity, the northwestern IP presented an arid phase that was observed in the marine and lacustrine records (Bernárdez et al., 2008; Jambrina-Enríquez et al., 2014), although towards the east, Enol Lake showed the opposite conditions (Moreno et al., 2011). In the Pyrenees, Estanya Lake displayed a dry climate scenario (Morellón et al., 2009), whereas the remaining records (Arreo, Montcortès and Basa de la Mora Lakes) displayed large increases in water availability (Corella et al., 2011, 2013; Pérez-Sanz et al., 2013). In the Central IP, all of the records showed an alternation between arid and humid phases (Gil-García et al., 2007; López-Merino et al., 2009; Currás et al., 2012). Peñalara and Cimera lakes showed multidecadal alternations of long and short ice-cover durations derived from variations in lake productivity (Figs. 6.3 and 6.4) resulting from fluctuations between periods of longer winter snow seasons during colder and/or wetter conditions and the opposite conditions. These multidecadal alternations led to periodic oscillations in soil erosion in Cimera Lake (Fig. 6.3). In addition, the presence of facies S and M2 in the ICR sequences might be associated with frequent autumn/summer storms in this region (Figs. 4.7 and 4.8). In the southern IP and western Mediterranean region, marine records (Alboran Sea and west Algerian-Balearic Basin) and terrestrial records (Zoñar Lake) displayed prevalent wet conditions (Martín-Puertas et al., 2008, 2010; Nieto-Moreno et al., 2011). This humid interval was not favourable to African aeolian inputs in the IP (Martín-Puertas et al., 2010; Nieto-Moreno et al., 2011; Jiménez-Espejo et al., 2014); thus, the Cimera Lake productivity was not enhanced (Fig. 6.3).

Therefore, during the RP, the northern IP was characterized by a E–W longitudinal gradient in terms of humidity (Fig. 6.4), with humid conditions prevailing at higher altitudes towards the eastern areas and dry conditions prevailing at lower altitudes towards the western areas. A broad N–S humidity gradient also occurred, with humid conditions generally occurring in the southern part of the IP and dominant arid conditions occurring in the northern part (Fig. 6.4). These E–W and N–S humidity gradients highlight the complex interplay between geography, topography and climate.

6.2.2. The Early Middle Ages (EMA; 500 – 900 AD)

General humid and cold conditions were registered by the marine and lacustrine records in the NW IP (Desprat et al., 2003; Álvarez et al., 2005; Jambrina-Enríquez et al., 2014) during the EMA. However, spatial heterogeneity was also observed as indicated by the predominantly warm temperatures of the Penido Vello peat bog (Martínez-Cortizas et al., 1999) and speleothem records from the Cobre, Mayor and Kaite caves (Martín-Chivelet et al., 2011) (Fig. 6.4). In the Pyrenees, the records showed a strong disparity in humidity, with Arreo Lake displaying wet conditions caused by less saline conditions and high lake levels (Moreno et al., 2011; Corella et al., 2013) and Estanya Lake presenting a dominant dry scenario between 500 and 750 AD (Morellón et al., 2009). Montcortès and Basa de la Mora lakes displayed a shift from humid to arid conditions (Corella et al., 2011; Pérez-Sanz et al., 2013). In terms of the thermal conditions in the Pyrenees, the summer-autumn temperatures in Redon Lake exhibited a transition from cold to warm temperatures (Catalan et al., 2009), whereas the winter-spring temperatures remained cold (Pla and Catalan, 2005, 2011). In the central IP, the Almenara

de Adaja (López-Merino et al., 2009) and Tablas de Daimiel (Gil-García et al., 2007) records registered a cold and arid EMA, although the first record indicated the opposite conditions at the end of this period. Peñalara Lake sequence recorded less intense runoff events and shorter ice-cover durations, possibly as a consequence of predominant cold and dry conditions. Between 500 and 630 AD, Cimera Lake was characterized by more rain-on-snow events and shorter ice-cover durations, as reflected in enhanced lake productivity, which suggested warm temperatures and arid conditions and shorter snow seasons. In contrast, from 630 to 900 AD, the Cimera Lake record presented the opposite conditions (Figs. 6.3 and 6.4). These long-term climate conditions may also indicate a progressive inhibition of soil erosion surrounding Cimera Lake. The lack of facies M2 in the Peñalara sequence and the low frequency of facies S in the Cimera sequence (Figs. 4.7 and 4.8) are consistent with the low number of floods observed in the Tajo River basin during this climate period (Benito et al., 2003a, 2003b). In the southern IP and western Mediterranean region, the marine and terrestrial records displayed a trend towards drier conditions (Martín-Puertas et al., 2008, 2010; Nieto-Moreno et al., 2011).

Therefore, the E–W humidity gradient only occurred in the northern IP, and progressively more arid conditions occurred westwards. Nevertheless, the N–S humidity gradient affected the entire IP and produced generally humid conditions in the northern area, a transition from arid to humid conditions in the ICR, and a dry scenario in the southern area (Fig. 6.4). The progressive increase in humidity in the ICR suggests a southwards displacement of this humidity gradient over time.

6.2.3. The Medieval Climate Anomaly (MCA; 900 – 1300 AD)

Moreno et al. (2012) conducted a comprehensive characterization of the MCA climate evolution for the IP and showed that the selected continental records from the Mediterranean IP generally registered drier conditions, as indicated by lower water levels and higher chemical concentrations. Marine cores also indicated a decrease in the fluvial supply and an increase in African dust particles. Records from the NW IP indicated an increase in humidity during the MCA, which reflects the opposite behaviour to that of the Mediterranean IP. Thus, Morellón et al. (2012) focussed on the available climatic evidence from the Pyrenees and concluded that warmer and more arid conditions prevailed during the MCA in this region, as evidenced by lower lake levels, decreased runoff and a significant development of xerophytes and Mediterranean vegetation. The only climate reconstruction that presented an opposite behaviour was that of Redon Lake, and the opposite behaviour might have been related to the combination of multiple local factors, such as the geographical location and orientation (Morellón et al., 2012).

Climate records that were not included in the previous reviews suggest that high temperatures occurred in the northern IP (Martín-Chivelet et al., 2011) and arid conditions occurred in the south IP (Martín-Puertas et al., 2010) (Fig. 6.4). In the ICR, the Peñalara Lake record only contains the last 150 years of the MCA, during which it registered a transition from a warm-arid to a cold-humid scenario. The Cimera Lake record displayed a predominant warm and arid scenario, as indicated by the prevalent rain-on-snow events, an increasing trend in lake productivity caused by short ice-cover

durations related to the shorter snow season, and an increase in African aeolian inputs (Fig. 6.3). Furthermore, the development and weathering of soils in the Cimera Lake catchment caused by these optimal climatic conditions resulted in soil erosion, which is indicated by a marked increase in erosion (Fig. 6.3). The scarce presence of facies M2 (Fig. 4.8) might be associated with a low frequency of autumn/summer storms in the ICR. Benito et al. (2003a) found that large flood events decreased in the Tajo River basin during the period 1205–1450 AD, which might partially support our hypothesis.

The integration of the previous works with these new climate records (Fig. 6.4) indicates that although wet conditions were recorded in the marine records from the northwest end of the IP, arid and dry conditions were mostly predominant throughout the entire IP (Moreno et al., 2012). Thus, compared with the conditions during the RP and EMA, evident N–S or E–W humidity gradients did not occur during the MCA.

6.2.4. The Little Ice Age (LIA; 1300–1850 AD)

Morellón et al. (2012) also included a detailed reconstruction of the main climate changes during the LIA in the Pyrenees. To the best of our knowledge, additional comprehensive LIA evolutions for the entire IP are not available.

Northern Iberian records consistently show that the onset of the LIA resulted in cold and humid climate conditions that progressively became warmer. Only the Ría de Vigo record displays arid conditions (Desprat et al., 2003; Álvarez et al., 2005). In the Pyrenees, Morellón et al. (2012) demonstrated that cold and humid conditions with higher lake levels and increased runoff prevailed during this period. All of the records in the mid-latitudes of the IP recorded cold conditions, although they displayed differences in terms of humidity, with Taravilla Lake (Moreno et al., 2008) and Tajo Prodelta (Abrantes et al., 2005; Rodrigues et al., 2009) showing predominantly wet conditions and Almenara de Adaja (López-Merino et al., 2009) and Tablas de Daimiel (Gil-García et al., 2007) displaying predominantly arid conditions (Fig. 6.4). The Cimera Lake record was characterized by a decreasing trend of intense runoff events and prevalent low lake productivity with decadal oscillations, which indicated predominantly long ice-cover durations caused by prolonged snow seasons (Fig. 6.3). These conditions on the ICR were likely provoked by a colder period with dry-wet-dry decadal oscillations within the framework of a generally humid scenario (Fig. 6.4). This climatic scenario was broadly reflected in the Cimera Lake soil erosion, which was generally constant and likely caused by cold conditions hampering the development and disintegration of soils (Fig. 6.3). The high frequency of facies M2 in the Cimera sequence (Fig. 4.8) might also indicate the major presence of autumn/summer storms in the ICR, which was also observed for the Tajo River (Benito et al., 2003a, 2003b). The Peñalara sequence also showed a minor presence of run-off events, thereby indicating a predominantly cold scenario, although the prevalence of dry conditions and the lack of the facies M2 recorded in this sequence suggest a dry scenario (Figs. 6.3, 6.4 and 4.7). The differences between ICR lakes can be partially attributed to differences in altitude. Finally, in the southern IP and western Mediterranean, humid conditions with a decadal oscillating pattern were observed (Martín-Puertas et al., 2010; Nieto-Moreno et al., 2011). The generally low levels of lake productivity present in the central and southern Iberian re-

cords (Martín-Puertas et al., 2008; Jiménez-Espejo et al., 2014) may be explained by the dominantly humid conditions that prevailed during the LIA and likely inhibited the deposition of nutrient inputs from North African dust.

Therefore, despite minor discrepancies, prevalent wet and cold climatic conditions were recorded throughout the entire IP during the LIA (Fig. 6.4).

6.2.5. The Industrial Era (1850 – 2012 AD)

The records included in this study show that, over the last 150 years, the IP has been characterized by predominantly warm and arid conditions (Fig. 6.4), which are most likely associated with the current global warming trend. Nevertheless, the intensity of human activities during the Industrial Era and their impact on natural ecosystems have increased the difficulty of discerning and evaluating climate signals (Fig. 6.4).

The Peñalara Lake sequence exhibited long ice-cover durations during the first part of this period, although presented a conspicuous decrease during the second part and a marked increase of intense run-off events during the whole period (Fig. 6.3). These conditions are in concordance with the global warming scenario. The Cimera Lake sequence showed an increasing trend of lake productivity that was partially triggered by progressively shorter ice-cover durations, which were likely caused by less prolonged snow seasons and suggest prevalent arid conditions in the ICR (Fig. 6.3). However, between 1850 and 1950 AD, the Cimera sequence presented a shift from a low to a high frequency of intense runoff episodes, whereas over the last 50 years, the sequence displayed a marked decrease in these episodes (Fig. 6.3). These environmental conditions suggest an earlier warming and a rapid shift to cold conditions over the last decades. These colder conditions for the last 50 years clearly contradict the current global warming scenario. Granados and Toro (2000) indicated that the Cimera Lake summer water has warmed by more than 1.5 °C since the 1980s, which is consistent with the rise in temperatures caused by global warming. The PC3_{cin} might also reflect the influence of global warming in Cimera Lake. An explanation for this apparent contradiction may be found in the rapid increase in organic matter (i.e., TOC and TN) in the sediments. This increase in the proportion of organic matter has most likely diluted the inorganic fraction of the sediments, thereby lowering the signal of almost all the elements measured with XRF (Fig. 4.8).

6.3. Climate-forcing mechanisms driving climate variability in the Iberian Peninsula over the last two millennia

The climate evolution of the IP over the last 2,000 years indicates that two spatiotemporal climate patterns have occurred. During the RP and EMA periods, E–W and N–S humidity gradients co-occurred, whereas during the MCA and LIA, these climate gradients were not observed (Fig. 6.4).

The NAO has been shown to be the climate mode responsible for the largest share of the climate variability in the North Atlantic and European regions in recent decades (Hurrell et al., 2003). Thus, the majority of Iberian climate reconstructions over

the last 1000 years have attributed most of the observed climate variability to variations in the NAO (e.g., Nieto-Moreno et al., 2011; Morellón et al., 2012; Moreno et al., 2012). These climate reconstructions commonly ascribe the warm and arid climate conditions of the MCA to the dominant positive phases of the NAO and the humid and cold conditions of the LIA to the predominance of negative phases of the NAO (Trouet et al., 2009; Ortega et al., 2015).

Nevertheless, as initially stated, recent works suggest that other North Atlantic climate modes, such as the EA and SCAND climate patterns, significantly influence most climate variables in Europe (Jerez and Trigo, 2013; Comas-Bru and McDermott, 2014). Furthermore, the influence of the combined influence of the NAO and EA over Europe has been extended to vegetation dynamics and carbon uptake (Bastos et al., 2016) and to precipitation dynamics and the $\delta^{18}\text{O}$ –NAO relationship (Comas-Bru et al., 2016).

The EA and SCAND modulate variations in the strength and location of the NAO dipoles at the multidecadal scale (Comas-Bru and McDermott, 2014). The combined influence of the NAO–EA and NAO–SCAND leads to shifts in the winter temperature and precipitation anomaly patterns in Western Europe (Comas-Bru and McDermott, 2014). When the NAO and EA modes have the same sign, the precipitation and temperature patterns present a homogeneous spatial distribution, whereas when these modes have the opposite sign, the precipitation and temperature patterns present heterogeneous spatial distributions (Bastos et al., 2016; Comas-Bru and McDermott, 2014) (Fig. 1.11). In the IP, Hernández et al. (2015) showed that the NAO mainly governs winter precipitation and that the EA governs winter and summer temperatures (Fig. 1.14). These authors also showed that the Iberian lake dynamics are sensitive to the seasonal effects of interannual variations in these three patterns.

The role of these other climate modes and their interactions could explain the spatiotemporal climate variability observed in the IP over the last millennia. The humidity gradients recognized during the RP and EMA periods in the IP might have been caused by a predominant coincidence of the NAO and EA in opposite phases ($\text{NAO}^+ - \text{EA}^-$ or $\text{NAO}^- - \text{EA}^+$). The thermal conditions and the humidity gradients present during the RP suggest that the prevalent climate was dominated by the phase combination $\text{NAO}^- - \text{EA}^+$ (Fig. 6.4), which Hernández et al. (2015) indicated led to wet and warm winters and warm summers (Fig. 1.14). Conversely, the EMA presented an arid gradient with generally cold conditions, which suggests that the $\text{NAO}^+ - \text{EA}^-$ combination dominated the main climate variability and led to dry and cold winters and cold summers (Fig. 6.4).

However, the spatially homogeneous climate conditions that dominated the MCA and LIA also might have been caused by a predominance of both climate modes acting in the same phase. Thus, the MCA would be marked by a predominance of the positive phases of the NAO and EA ($\text{NAO}^+ - \text{EA}^+$), leading to dry and warm winters and warm summers, whereas the LIA would be dominated by the opposite phases ($\text{NAO}^- - \text{EA}^-$), leading to cold and wet winters and cold summers (Fig. 6.4).

The relationship between climate (e.g., NAO) and external climatic forcings, such as volcanic and solar forcings (e.g., in the frequency domain), is a controversial is-

sue because of their complex relationships (Mann, 2007; Sigl et al., 2015; Stoffel et al., 2015). Despite the complex relationships, the predominant NAO and EA phases during the RP, EMA, MCA and LIA appear to be associated with a large-scale dynamic response of the climate system to explosive volcanic and solar forcings. During the RP and MCA, the solar irradiance was relatively high, and there were few tropical explosive volcanic eruptions, whereas during the EMA and LIA, the solar irradiance was characterized by several periods of solar minima, and there were more frequent tropical volcanic eruptions (Table 6.2; Steinhilber et al., 2009; Sigl et al., 2015). These forcings might have modulated the NAO and EA phases over the last two millennia (Table 6.2). Most of the climate reconstructions for the last millennium have assumed a linear relationship between the solar activity and the NAO because other climate modes have not been considered (Morellón et al., 2012). However, our results suggest that, at the multi-decadal scale, the solar activity fluctuations are reflected in the EA.

Climate period	RP	EMA	MCA	LIA
Tropical volcanic eruptions	-	+	-	+
Solar irradiance forcing	high	low	high	low
Blocking events frequency	low	high	low	high
Ocean and continent conditions during blocking events	---	Cold ocean Warm continent	---	Warm ocean Cold continent
EA phase	+	-	+	-
NAO phase	-	+	+	-
ITCZ position	southern	northern	northern	southern
General climate conditions over Iberian Peninsula	Wet and warm winters and summers	Dry and cold winters and summers	Dry and warm winters and summers	Wet and cold winters and summers

Table 6.2. Frequency of tropical volcanic eruptions from Sigl et al. (2015), intensity of solar irradiance forcing obtained from Steinhilber et al. (2009), presence of blocking events, and the ocean and continent conditions ascribed to these forcings, the NAO and EA phases and general climate conditions over the IP during the RP, EMA, MCA and LIA climate periods.

Another consequence of the relationship between solar activity and climate modes is the development of atmospheric blocking events, which consist of a quasi-stationary high-pressure system in the eastern North Atlantic region that modifies the flow of the westerly winds (Trigo et al., 2004; Barriopedro et al., 2008). Low solar irradiance promotes the development of frequent and persistent atmospheric blocking events (Moffa-Sánchez et al., 2014). The duration of these blocking events is usually sufficiently long (i.e., between 1 and 3 weeks) to induce significant climate anomalies over a wide area of Europe (Trigo et al., 2004), although the occurrence of these anomalies is dependent on the location (Sousa et al., 2015). Recently, the location and persistence of

these blocking events over the eastern North Atlantic has also been associated with the phase of the EA pattern (Moffa-Sánchez et al., 2014). The position, frequency and persistence of these blocking events on the central North Atlantic Ocean are mainly conditioned by the phase of the NAO (Shabbar et al., 2001). The NAO⁺ phase leads to a 'cold ocean/warm land' pattern, which is unfavourable for the development and persistence of blocking events, whereas the NAO⁻ phase leads to a 'warm ocean/cold land' pattern, which promotes the formation and persistence of blocking events (Shabbar et al., 2001).

During the EMA and LIA, low solar irradiance promoted the development of frequent and persistent atmospheric blocking events (Moffa-Sánchez et al., 2014). The dominance of EA⁻ climate phase conditions during these two climate periods suggests that blocking events developed on the North Atlantic Ocean (Table 6.2). However, the NAO phase of these climate periods determined the main humidity and thermal dominance conditions. The NAO⁺ phase dominated the EMA and led to a 'cold ocean/warm land' pattern (Shabbar et al., 2001), which inhibited ocean water evaporation. This pattern, together with the low-frequency and less persistent blocking events, generally led to arid and relatively cold conditions in the IP (Table 6.2). Conversely, the LIA was governed by a NAO⁻ phase, which led to a 'warm ocean/cold land' pattern (Shabbar et al., 2001) that enhanced ocean water evaporation. This second pattern, together with the high-frequency and persistent blocking events, promoted a generally humid and cold scenario during this period (Table 6.2).

The delivery of African dust to Cimera Lake is related to climate conditions and is therefore representative of underlying forcing mechanisms over the last two millennia. On one hand, the meridional transport of African dust is related to cyclone activity inside and around the Mediterranean basin (Alpert and Ziv, 1989; Bergametti et al., 1989), and transport occurs when the westerly regime is weak, disrupted or displaced northwards (e.g., Rodríguez et al., 2001; Torres-Padrón et al., 2002; Ginoux et al., 2004). On the other hand, an arid source region and sufficient storminess and air turbulence to entrain dust and inject it into the atmosphere are necessary conditions for the availability of dust. These processes are mostly controlled by the latitudinal migration of the ITCZ and its associated wind cycle and rainfall belt (e.g., Engelstaedter et al., 2006; Bout-Roumazeilles et al., 2007). Hence, variability in the African dust inputs in the IP over the last two millennia could be the result of coupled movements between the NAO and the ITCZ. A predominance of NAO⁺ provokes lower precipitation over southern Europe and Northern Africa, and the related northern position of the ITCZ enhances dust emissions from Northern Africa (western and northern Saharan). Both of these factors favour a higher intensity of dust uptake and transport towards the IP, particularly during summer. Conversely, a NAO⁻ phase coupled with a more southern position of the ITCZ results in wet summer conditions in Northern Africa, reducing dust emission from the hyper-arid region of the Sahara desert. Consequently, the evidence of African dust inputs in Cimera Lake during dry periods, such as the EMA and MCA, may suggest a predominant NAO⁺ coupled with a more northern position of the ITCZ during this period. Furthermore, from this scenario, a particular predominance of dry summers in the IP during both periods could be derived (Table 6.2). In contrast, less evidence of these inputs during wetter periods, such as the RP and the LIA, hint at the opposite scenario and support the hypothesis of a predominance of NAO⁻ phases coupled with a more southern

position of the ITCZ during these periods. This situation would also indicate the existence of more frequent wet summers in the IP (Table 6.2). Different palaeorecords have extensively indicated ITCZ migrations at millennial time scale during the Holocene (e.g., Haug et al., 2001; Schneider et al., 2014), as well as possible coupling with the NAO during these migrations (Wanner and Brönnimann, 2012; Wirth et al., 2013). However, to our knowledge, these shifts in the ITCZ have not been documented yet for shorter time scales, such multidecadal or centennial time scales.

7. THE NAO IMPRINTS ON THE IBERIAN CENTRAL RANGE FOR THE LAST TWO MILLENNIA RECONSTRUCTED USING A BAYESIAN APPROACH

7.1. The NAO impact on the Iberian Central Range

The ancient NAO (NAO_{ICR}) obtained from the random walk-modularised Bayesian model is a record of the NAO impact in the ICR for the last two millennia. To evaluate the reliability of these reconstructed values and of the model, a 5-fold cross-validation of the modern data was conducted. However, the obtained results did not allow us to statistically validate the Bayesian model (Juggins and Birks, 2012). Consequently, to determine the degree to which the model can be validated, the obtained ancient NAO_{ICR} was compared with multidecadal NAOi data from CRU for the period 1930–1825 AD. This NAOi was not included in the calibration of the model (Fig. 7.1). The visual inspection of this comparison showed that both lines displayed similar multidecadal variations, although the mean value of the NAO_{ICR} impacts was dominated by negative values, whereas the instrumental NAO index presented oscillations between positive and negative values (Fig. 7.1). However, taking into account the uncertainty values of the reconstructed NAO impacts, the NAO_{ICR} displayed similar values to the instrumental NAO (Fig. 7.1). Hence, although the model cannot be validated by cross-validation, the NAO_{ICR} impacts reproduce similar inter-decadal oscillations and values as those present in the instrumental NAO record.

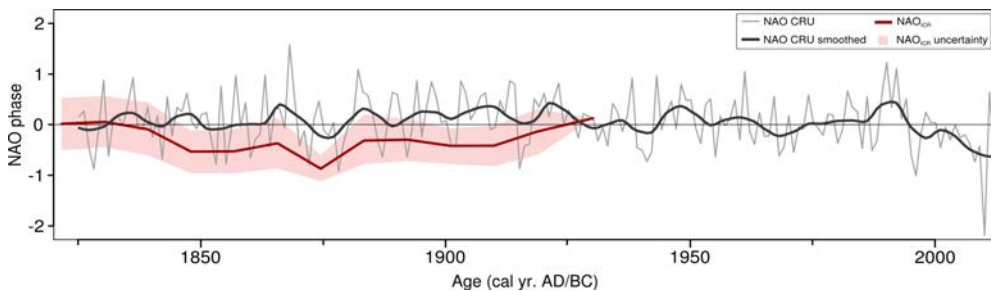


Figure 7.1. The light grey line corresponds to the annual NAOi calculated from the monthly NAOi from CRU for the period 1825–1930 AD and the dark grey line correspond to a smoothed version of these data calculated with the loess function and a span degree of 0.10. The red line correspond to the median value of the NAO impact in the Iberian Central Range (NAO_{ICR}) obtained in this study for the period 1825–1930 AD, and the red light band shows the uncertainty of the model obtained based on the 5th and 95th quantiles.

As previously mentioned on page 30, another important aspect necessary for a model to be valid is that it must make ecological sense. The NAO_{ICR} must be in accordance with the reconstructed temperature and precipitation conditions determined in the ICR for the last two millennia from the multi-proxy approach applied to sediments of

the CIM12-04A (Fig. 7.2). Another important aspect of this comparison is that both reconstructions were obtained by independent statistical methods: PCA was used to reconstruct the climate conditions in the ICR from the Cimera Lake sediments, whereas NAO_{ICR} was obtained by Bayesian statistics using the random walk-modularised model (see section 3.6 for further details). The NAO_{ICR} during the RP showed multidecadal alternations between both phases, although it presented a predominance of negative values (Fig. 7.2), which is in accordance with the humid scenario suggested by the reconstructed precipitation. The dominant temperature conditions during this period shifted between colder and warmer periods (Fig. 7.2). The EMA onset was characterized by a positive NAO_{ICR} coinciding with warm conditions in the ICR, although the opposite phase prevailed during the rest of the period, coinciding with a change from dominantly arid conditions to humid conditions (Fig. 7.2). A positive impact of the NAO_{ICR} prevailed in the region during the MCA together with a predominantly warm and arid scenario (Fig. 7.2). In contrast, the LIA was characterized by a trend towards a prevalent negative phase and a colder period with dry-wet-dry decadal oscillations in the context of a generally humid scenario (Fig. 7.2). Finally, this negative phase predominated until the onset of the Industrial Era, coinciding with a short markedly humid period (Fig. 7.2). Hence, temperature and humidity conditions obtained from the Cimera Lake sequence appear to be consistent with the possible climate conditions ascribed to NAO_{ICR} (Fig. 7.2).

7.2. Global aspects of the NAO impact on the Iberian Central Range

Finally, to determine whether some global aspects are depicted in the NAO_{ICR} and may therefore be roughly considered regional indices for the entire IP, the NAO_{ICR} reconstruction has been compared with the three different NAO approaches: i) the NAO index from Trouet et al. (2009) (NAO_{Tro}), which can be considered a simplistic approach based on two records from Scotland and Morocco (Figs. 3.16 and 7.3); ii) the multidecadal NAO index obtained by Olsen et al. (2012) (NAO_{Ols}), which can also be considered a simplistic approach based on a palaeo-redox proxy (Mn/Fe ratio) in a sediment record from a small lake near Kangerlussuaq (Greenland, Figs. 3.16 and 7.3); and iii) the much more robust NAO reconstruction from Ortega et al. (2015) (NAO_{Ort}), which employed multi-proxy data from different locations in the Northern Hemisphere (Figs. 3.16 and 7.3). None of the three NAO indices completely cover the last two millennia. Therefore, the comparisons have been carried out for the respective overlapping periods.

The NAO_{Ols} presented a predominant positive phase of NAO for the last two millennia, which contrasts with the other two NAO indices (Fig. 7.3). During the RP and EMA, only the NAO_{Ols} and the NAO_{ICR} are available. A more positive phase predominated in the NAO_{Ols} during the RP and a more negative one prevailed in the EMA, while the NAO_{ICR} presented both approximately opposite values and different variability during these two climate periods (Fig. 7.3). All four indices almost cover the MCA period, and NAO_{Ols} , NAO_{Tro} , and NAO_{ICR} showed prevalent positive phases, whereas the NAO_{Ort} index, despite presenting increasingly positive values, did not display a marked persistent positive phase during the Medieval period (Fig. 7.3). The similarity between

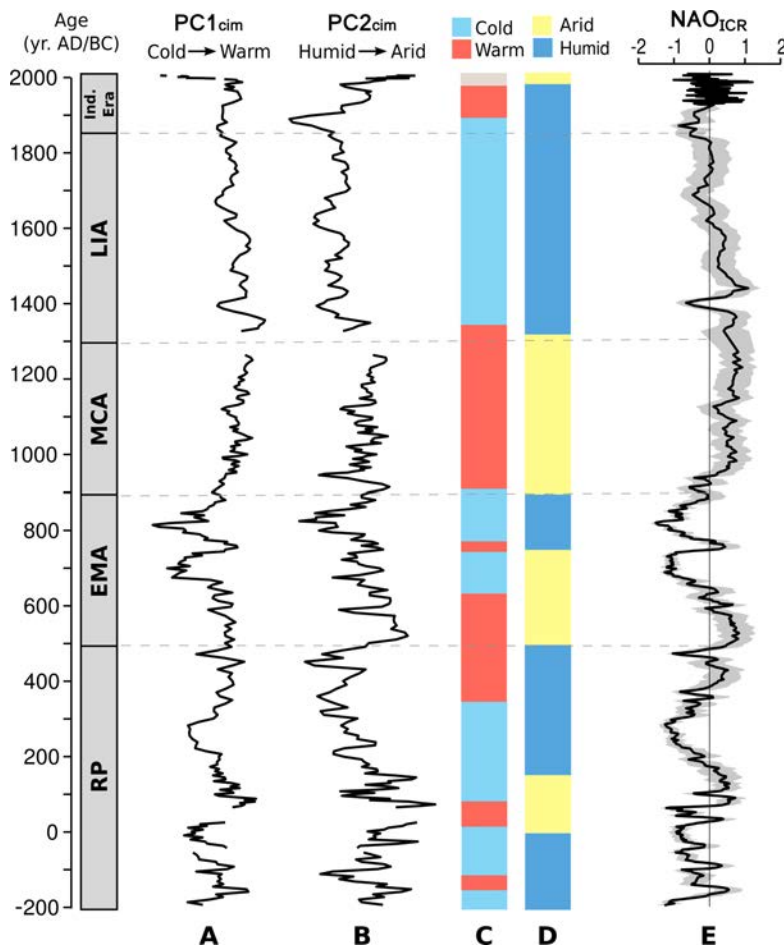


Figure 7.2. A) Scores of the first ($PC1_{cim}$) and B) second ($PC2_{cim}$) eigenvectors obtained from the multiproxy analysis of Cimera Lake sediments; these eigenvectors reflect thermal and humid conditions, respectively. C) and D) bars with cold and warm conditions, and arid and humid conditions deduced from A) and B), respectively. E) Values of the NAO impact in the ICR obtained in this study (black line) and the associated uncertainty (grey band).

NAO_{Tro} and NAO_{Ols} can be partly ascribed to the fact that the latter index was based on the first one in the construction of the reconstruction, whereas the major agreement between NAO_{Icr} and NAO_{Tro} can be ascribed to the geographical location of the proxy used as the southern node in the NAO_{Tro} calculations. The relative geographical proximity between Cimera Lake and Morocco most likely indicates that both sites mostly experienced similar climate conditions and that both records therefore registered similar NAO impacts. Additionally, the differences between the different instrumental indices of NAO support this hypothesis. Jones et al. (2003) showed that, although different NAO indices were highly correlated on interannual and longer time scales, the choice of the southern station in the calculation of the indices produced some significant differ-

ences. In contrast, the specific location of the northern node was not critical because the temporal variability over this region was much larger than the spatial variability.

Fewer discrepancies were found during the LIA, where all NAO reconstructions showed values predominantly lower than those during the MCA (Fig. 7.3). The cold temperatures registered during the LIA in most of the North Hemisphere (Mann, 2007) have been extensively related to the high frequency of solar minimum events (Steinhilber et al., 2009), which could have produced a predominance of negative NAO phases. Furthermore, the predominance of these periods of solar minima may also have contributed to the prevalence of negative EA phases, producing a dominance of cold summers in the IP (Table 6.2). However, taking into account the age-depth model errors, only one solar minimum event may be reflected in all the NAO reconstructions (Fig. 7.3). This event corresponds to the Spörer Minimum (1450 – 1550 AD), one of the longest (90 years) and lowest periods of total solar irradiance in the last two millennia (Steinhilber et al., 2009).

Finally, during the onset of the Industrial Era, the NAO_{ICR} and NAO_{Ort} showed negative values, whereas the NAO_{Tro} presented the opposite phase values preceded by a negative phase period.

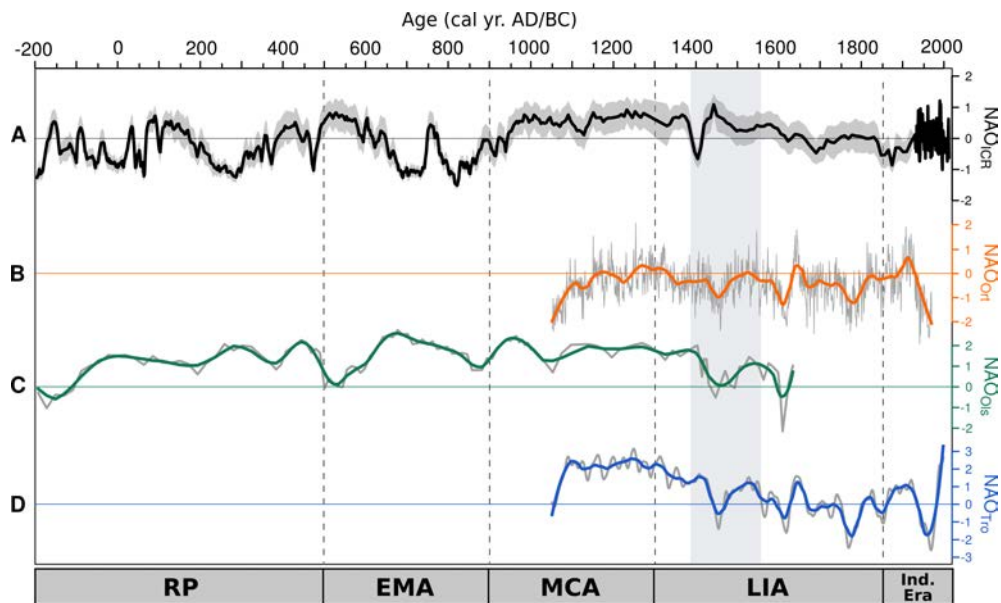


Figure 7.3. A) The black line denotes the NAO impact values in the ICR for this study (NAO_{ICR}); the light grey band shows the uncertainty of the model obtained from 5th and 95th quantiles. In B), C) and D) the grey lines denote NAO approaches from Ortega et al. (2015) (NAO_{Ort}), Olsen et al. (2012) (NAO_{Ols}) and Trouet et al. (2009) (NAO_{Tro}), respectively. The coloured lines (NAO_{Ort} orange line, NAO_{Ols} green line and NAO_{Tro} blue line) correspond to smoothed data calculated using the loess function and a span degree of 0.10. The grey band denotes the period Spörer Minimum (1450 – 1550 AD), which has been slightly spanning for taking into account the age model uncertainty of the NAO_{ICR} .

Hence, the differences between these reconstructions showed that a simplistic NAO approach can sometimes reflect local or regional aspects of this climate mode. Thus, the NAO_{ICR} reconstruction can be considered a regional NAO index, although such a simplistic approach should not be considered a global index.

The main strength of the approach followed here is that it provides many opportunities to obtain robust and accurate high-resolution NAO reconstructions using non-biological proxies, such as the chemical composition of the sediments. Performing a number of these NAO reconstructions in a relatively small geographical area and integrating them into a unique index might permit researchers to obtain robust and high-resolution reconstructions of the regional NAO impacts, and that might improve the current knowledge of the spatio-temporal evolution of this climate mode. Furthermore, reconstructing the impacts of other climate modes, such as the EA, might accurately characterize their spatio-temporal interactions and determine whether their relationships are non-stationary.

However, there are two drawbacks resulting from a simplistic NAO approach that should be taken into account: 1) the accuracy of the low-resolution reconstruction, which primarily depends on the resolution of the employed proxy, such as the two records (from Scotland and Morocco) used by Trouet et al. (2009), which featured a multidecadal resolution that partly undermined this aspect (e.g., Lehner et al., 2012), and 2) the role of other climate modes in the climate evolution and their interactions with the NAO over the last millennia have not been well addressed, despite the many lines of evidence showing their relevance in both current (Jerez and Trigo, 2013; Comas-Bru and McDermott, 2014) and past climate reconstructions (Hernández et al. 2015; Comas-Bru et al., 2016). To a large extent, the first limitation has been thoroughly addressed by Ortega et al. (2015), who developed an improved NAO reconstruction index that features an annual resolution and is based on multiple records (Figs. 3.16 and 7.3). The second weakness might be improved by the identification of regions where proxies can be used to robustly reconstruct changes in NAO or climate conditions without the concomitant influence of the EA (Comas-Bru et al., 2016).

8. CONCLUSIONS AND FUTURE WORKS

8.1. Concluding remarks

The study of NAO impacts in the Central IP and the integration with other reconstructions yield the following methodological, limnological and climatic conclusions.

8.1.1. Methodological conclusions

- The climatic impacts of the NAO on Iberian alpine lakes has been characterized by means of a conceptual lake model, which has contributed to better understanding of the transmission of the NAO signal to Iberian alpine lake sediments.

- The method involving geochemical data obtained from the XRF core scanner and a random walk-modularised Bayesian model has proven to be an accurate tool for conducting a high-resolution climate reconstruction with low costs in terms of time, sample collection and analyses.

- A local reconstruction of the impacts of the NAO can also show global aspects of this climate mode and thus, this reconstruction can be considered a first step to obtain an accurate regional NAO index for the entire IP. Additionally, this regional index can be integrated into more robust global NAO reconstructions that employ gridded proxy data from many different regions.

- The interplay between the NAO and other climate modes can be a key factor for the causal relationship between the proxy and climatic data and it should be taken into account in any NAO reconstruction.

8.1.2. Limnological conclusions

- The melting process of Iberian alpine lakes is strongly affected by the NAO, whereas the freezing process is dependent on short-term synoptic conditions (e.g., an anticyclone centred over the IP) and non-climatic factors that determine the heat loss rate, such as lake morphometry.

- The break-up date and ice-cover duration of Iberian alpine lakes reflect the NAO effects via the winter air temperature and snow accumulation. This result highlights the important role of the insulating effect of snow during the thawing period in mid-latitude areas, such as the IP, and in the transmission of the NAO signal to Iberian alpine lake sediments.

- The sedimentation in Peñalara and Cimera lakes is dominated by runoff lake productivity, as well as by soil erosion in the Cimera Lake. These environmental processes are primarily controlled by rain-on-snow events and the ice-cover duration.

8.1.3. Climatic conclusions

- At lower altitudes, the NAO signal is manifested via the coupled behaviour of the air temperature and precipitation during winter in Iberian alpine lakes. In contrast, at higher altitudes, the NAO affects the ice phenology by means of precipitation in winter (snow deposited over the lake ice cover) and air temperature in spring; thus, these climatic variables exhibit uncoupled behaviour at higher altitudes.

- The NAO effects on ice cover are largely related to air temperature at higher latitudes and to precipitation (snow accumulation) at lower latitudes because the latitude affects ice dynamics via solar radiation. Consequently, in northern Europe, the NAO signal primarily affects lake ice phenology via air temperature, whereas in southern Europe, the NAO affects the ice cover through both precipitation and air temperature changes.

- The generally warm conditions and humidity gradients recorded in the IP during the RP suggest a predominance of the NAO^- – EA^+ phases, whereas the opposite climatic conditions during the EMA suggest the NAO^+ – EA^- phases predominated in this region. In contrast, the spatially homogeneous warm and arid conditions during the MCA and the opposite conditions during the LIA in the IP indicate NAO^+ – EA^+ and NAO^- – EA^- interactions, respectively.

- The high solar irradiance and fewer tropical volcanic eruptions during the RP and MCA may support the hypothesis of a predominant EA^+ phase during these periods. The opposite scenario during the EMA and LIA (i.e., low solar irradiance and more tropical volcanic eruptions) may indicate a predominance of the EA^- phase, which would promote the formation of frequent and persistent atmospheric blocking events in the Atlantic region during these periods.

- The evidence of African dust inputs in Cimera Lake during dry periods such as the EMA and MCA may also suggest a predominant NAO^+ phase coupled with a more northern position of the ITCZ during these periods. Furthermore, this scenario suggests a particular predominance of dry summers in the IP during both periods. In contrast, less evidence of these inputs during wetter periods, such as the RP and the LIA, suggest the opposite scenario.

- The evolution and impact of the NAO in the Central IP have been reconstructed for the last 2,000 years. These impacts show a multidecadal time-scale resolution with predominantly negative values during the RP and the second half of the EMA, positive values during the first part of the EMA and the MCA, and a decreasing trend towards the opposite conditions during the LIA. Furthermore, this NAO approach is in accordance with other NAO reconstructions with different degrees of methodological robustness and lower time resolutions.

8.2. Perspectives and future works

This PhD thesis provides valuable insights into the use of Iberian alpine lakes as sensors of the influences of climate modes, such as the NAO, and into the use of Bayesian statistics to precisely determine these climate mode influences in the past.

However, further work can be proposed to complete and improve the interpretations, which is reflected in the following points:

- To explore the combined influence of various climate modes (i.e., NAO, EA and SCAND) on ice phenology.
- To obtain a more accurate origin of the African dust inputs and compare the results with other records, such as those from the Cariaco basin, to better constrain the ITCZ migrations over the last two millennia.
- To examine the role of SCAND and/or AMO and their interactions with the NAO in the present and past climate variability of the IP.
- To improve the validation of the implemented Bayesian model, such as by means of a bootstrap cross-validation.
- To integrate more geochemical data from other Iberian lakes in order to construct a longer and more precise spatio-temporal NAO index for the entire IP.
- To integrate the NAO–EA and/or NAO–SCAND intercations in the quantitative reconstructions of NAO impact in the ICR. This may consist in creating a 'new' climate index which contain these interactions, such as a linear combinations of these indeces, and to use it during the intial calibration step of the Bayesian model.

REFERENCES

- Abrantes, F., Lebreiro, S., Rodrigues, T., Gil, I., Bartels-Jónsdóttir, H., Oliveira, P., Kissel, C., Grimalt, J.O., 2005. Shallow-marine sediment cores record climate variability and earthquake activity off Lisbon (Portugal) for the last 2000 years. *Quaternary Science Reviews* 24, 2477–2494.
- Adams, W.P., 1981. Snow and ice on lakes. In *Handbook of Snow: Principles, Processes, Management and Use*. Gray, D.M., Male, D.H. (eds). Pergamon Press, Canada, pp. 437–474.
- Adrian, R., O'Reilly, C.M., Zagarese, H., Baines, S.B., Hessen, D.O., Keller, W., Livingstone, D.M., Sommaruga, R., Straile, D., Van Donk, E., Weyhenmeyer, G.A., Winderl ,M., 2009. Lakes as sentinels of climate change. *Limnology and Oceanography* 54(6), 2283.
- Aguilar, E., Auer, I., Brunet, M., Peterson, T.C., Wieringa, J., 2003. Guidelines on climate metadata and homogenization. World Meteorological Organization, Geneva. WCDMP-No.53, WMO-TD No.1186.
- Agustí-Panareda, A., Thompson, R., 2002. Reconstructing air temperature at eleven remote alpine and arctic lakes in Europe from 1781 to 1997 AD. *Journal of Paleolimnology* 28, 7–23.
- Alexander, M.A., Bladé, I., Newman, M., Lanzante, J.R., Lau, N.C., Scott, J.D., 2002. The atmospheric bridge: The influence of ENSO teleconnections on air-sea interaction over the global oceans. *Journal of Climate* 15(16), 2205–2231.
- Alpert, P., Ziv, B., 1989. The Sharav cyclone: observations and some theoretical considerations. *Journal of Geophysical Research: Atmospheres* 94(D15), 18495–18514.
- Álvarez, M.C., Flores, J.A., Sierro, F.J., Díz P., Francés, G., Pelejero, C., Grimalt, J.O., 2005. Millennial surface water dynamics in the Ría de Vigo during the last 3000 years as revealed by coccoliths and molecular biomarkers. *Palaeogeography, Palaeoclimatology, Palaeoecology* 218(1), 1–13.
- Alverson, K., Oldfield, F., Bradley, R.S., 1999. *Past Global Changes and Their Significance for the Future*. Elsevier, Amsterdam, 479 pp.
- Alverson, K.D., Bradley, R.S., Pedersen, T.F., 2003. *Paleoclimate, global change and*

the future. Springer Verlag, Berlin, 220 pp.

Anderson, L., Abbott, M.B., Finney, B.P., Burns, S.J., 2007. Late Holocene moisture balance variability in the southwest Yukon Territory, Canada. *Quaternary Science Reviews* 26, 130–141.

Appenzeller, C., Stocker, T.F., Anklin, M., 1998. North Atlantic oscillation dynamics recorded in Greenland ice cores. *Science* 282, 446–449.

Asami, R., Yamada, T., Iryu, Y., Quinn, T.M., Meyer, C.P., Paulay, G., 2005. Interannual and decadal variability of the western Pacific sea surface condition for the years 1787–2000: reconstruction based on stable isotope record from a Guam coral. *Journal of Geophysical Research* 110, C05018.

Ashpole, I., Washington, R., 2013. Intraseasonal variability and atmospheric controls on daily dust occurrence frequency over the central and western Sahara during the boreal summer. *Journal of Geophysical Research: Atmospheres* 118, 12915–12926.

Asikainen, C.A., Francus, P., Brigham-Grette, J., 2007. Sedimentology, clay mineralogy and grain-size as indicators of 65 Ka of climate change from El'gygytgyn Crater Lake, Northeastern Siberia. *Journal of Paleolimnology* 37, 105–122.

Bai, X., Wang, J., Sellinger, C., Clites, A., Assel, R., 2012. Interannual variability of ice cover and its relationship to NAO and ENSO. *Journal of Geophysical Research: Oceans* 117, CO3002.

Bakke, J., Lie, Ø., Heegaard, E., Dokken, T., Haug, G.H., Birks, H.J.B., Dulski, P., Nilsen, T., 2010. Rapid oceanic and atmospheric changes during the Younger Dryas cold period. *Nature Geoscience* 2, 202–205.

Bao, R., Hernández, A., Sáez, A., Giralt, S., Prego, R., Pueyo, J.J., Moreno, A., Valero-Garcés, B.L., 2015. Climatic and lacustrine morphometric controls of diatom paleoproductivity in a tropical Andean lake. *Quaternary Science Reviews* 129, 96–10.

Barboni, R., Bonnefille, R., Alexandre, A., Meunier, J.D., 1999. Phytoliths as paleoenvironmental indicators, West Side Middle Awash Valley, Ethiopia. *Palaeogeography, Palaeoclimatology, Palaeoecology* 152, 87–100.

Barnston, A.G., Livezey, R. E., 1987. Classification, seasonality and persistence of low-frequency atmospheric circulation patterns. *Monthly weather review* 115(6), 1083–1126.

Barreiro-Lostres, F., Brown, E., Moreno, A., Morellón, M., Abbott, M., Hillman, A., Giralt, S., Valero-Garcés, B., 2015. Sediment delivery and lake dynamics in a

- Mediterranean mountain watershed: Human-climate interactions during the last millennium (El Tobar Lake record, Iberian Range, Spain). *Science of the Total Environment* 533, 506–519.
- Barriopedro, D., García-Herrera, R., Lupo, A.R., Hernández, E., 2006. A climatology of Northern Hemisphere blocking. *Journal of Climate* 19(6), 1042–1063.
- Barriopedro, D., García-Herrera, R., Huth, R., 2008. Solar modulation of Northern Hemisphere winter blocking. *Journal of Geophysical Research: Atmospheres* 113, D14118.
- Bartlein, P.J., Anderson, K.H., Anderson, P.M., Edwards, M.E., Mock, C.J., Thompson, R.S., Webb, R.S., Webb III, T., Whitlock, C., 1998. Paleoclimate simulations for North America over the past 21,000 years: features of the simulated climate and comparisons with paleoenvironmental data. *Quaternary Science Reviews* 17, 549–585.
- Bastos, A., Janssens, I.A., Gouveia, C.M., Trigo, R.M., Ciais, P., Chevallier, F., Peñuelas, J., Rödenbeck, C., Piao, S., Friedlingstein, P., Running, S.W., 2016. European land CO₂ sink influenced by NAO and East-Atlantic Pattern coupling. *Nature Communications* 7, 10315.
- Battarbee, R.W., Smol, J.P., Meriläinen, J., 1986. Diatoms as indicators of pH: a historical review. In *Diatoms and lake acidity*. Smol, J.P., Battarbee, R.W., Davis, R.B., Meriläinen, J. (eds). Junk Publications, Dordrecht, pp. 5–14.
- Battarbee, R.W., 2000. Palaeolimnological approaches to climate change, with special regard to the biological record. *Quaternary Science Reviews* 19, 107–124.
- Battarbee, R.W., Jones, V.J., Flower, R.J., Cameron, N.G., Bennion, H., Carvalho, L., Juggins, S., 2001. Diatoms. In *Tracking Environmental Change Using Lake sediments*, vol. 3. Smol, J.P., Birks, H.J.B., Last, W.M. (eds.). Kluwer Academic, Dordrecht, pp. 155–202.
- Bengtsson, L., 2012. Ice covered lakes. In *Encyclopedia of lakes and reservoirs*. Bengtsson, L., Herschy, R.W., Fairbridge, R.W. (eds). Springer, New York, pp. 357–360.
- Benito, G., Sopeña, A., Sánchez-Moya, Y., Machado, M.J., Pérez-González, A., 2003a. Palaeoflood record of the Tagus River (Central Spain) during the Late Pleistocene and Holocene. *Quaternary Science Reviews* 22, 1737–1756.
- Benito, G., Diéz-Herrero, A., Fernández de Villalta, M., 2003b. Magnitude and frequency of flooding in the Tagus basin (Central Spain) over the last millennium. *Climatic Change* 58(1–2), 171–192.

- Bergametti, G., Gomes, L., Remoudaki, E., Desbois, M., Martin, D., Buat-Ménard, P., 1989. Present transport and deposition of dust to the north-western Mediterranean. In *Paleoclimatology and Paleometeorology: Modern and past patterns of global atmospheric transport*. Leinen, M., Sarnthein, M. (eds). Kluwer Academic, Boston, Mass, pp. 227–252.
- Bergstrom, A.K., Jansson, M., 2006. Atmospheric nitrogen deposition has caused nitrogen enrichment and eutrophication of lakes in the northern hemisphere. *Global Change Biology* 12, 635–643.
- Bernárdez, P., González-Álvarez, R., Francés, G., Prego, R., Bárcena, M.A., Romero, O.E., 2008. Late Holocene history of the rainfall in the NW Iberian peninsula – evidence from a marine record. *Journal of Marine Systems* 72, 366–382.
- Berner, E.K., Berner, R.A., 2012. Introduction to the Global Environment: The Water and Energy Cycles and Atmospheric and Oceanic Circulation. In *Global environment: water, air, and geochemical cycles*. Princeton University Press, pp. 1–23.
- Besonen, M.R., Bradley, R.S., Mudelsee, M., Abbott, M., Francus, P., 2008. A 1,000 year record of hurricane activity from Boston, Massachusetts. *Geophysical Research Letters* 35, L14705.
- Birks, H.J.B., Line, J.M., Juggins, S., Stevenson, A.C., ter Braak, C.J.F., 1990. Diatoms and pH reconstruction. *Philosophical Transactions of the Royal Society B* 327, 263–278.
- Birks, H.J.B., 1995. Quantitative palaeoenvironmental reconstructions. In *Statistical modelling of Quaternary science data. Technical guide 5*. Maddy, D., Brew, J. (eds). Quaternary Research Association, Cambridge, pp. 161–254.
- Birks, H.J.B., 2003. Quantitative palaeoenvironmental reconstructions from Holocene biological data. In *Global change in the Holocene*. Mackay, A., Battarbee, R.W., Birks, H.J.B., Oldfield, F. (eds). Arnold, London, pp. 107–123.
- Birks, H.J.B., Heiri, O., Seppä, H., Bjune, A.E., 2010. Strengths and weaknesses of quantitative climate reconstructions based on late-Quaternary biological proxies. *The Open Ecology Journal* 3, 68–110.
- Birks, H.J.B., 2012. Overview of numerical methods in palaeolimnology. In *Tracking environmental change using lake sediments*. Birks, H.J.B., Lotter, A.F., Juggins, S., Smol, J.P. (eds). Springer Netherlands, pp. 19–92.
- Bjerknes J., 1964. Atlantic air–sea interaction. *Advances in Geophysics* 10, 1–82.

- Blaauw, M., Christen, J.A., 2005. Radiocarbon peat chronologies and environmental change. *Journal of the Royal Statistical Society: Series C (Applied Statistics)* 54, 805–816.
- Blaauw, M., Bakker, R., Christen, J.A., Hall, V.A., van der Plicht, J., 2007. A Bayesian framework for age-modelling of radiocarbon-dated peat deposits: case studies from the Netherlands. *Radiocarbon* 49, 357–367.
- Blaauw, M., 2010. Methods and code for ‘classical’ age-modelling of radiocarbon sequences. *Quaternary Geochronology* 5, 512–518.
- Bladé, I., Liebmann, B., Fortuny, D., van Oldenborgh, G.J., 2012. Observed and simulated impacts of the summer NAO in Europe: implications for projected drying in the Mediterranean region. *Climate dynamics* 39(3-4), 709–727.
- Blessing, S., Fraedrich, K., Junge, M., Kunz, T., Linkheit, F., 2005. Daily North-Atlantic Oscillation (NAO) index: statistics and its stratospheric polar vortex dependence. *Meteorologische Zeitschrift* 14(6), 763–769.
- Bolstad, W.M., 2007. Introduction to Bayesian Statistics. John Wiley and Sons (eds). Hoboken, New Jersey.
- Bos, D.G., Cumming, B.F., Smol, J.P., 1999. Cladocera and Anostraca from the interior plateau of British Columbia, Canada, as paleolimnological indicators of salinity and lake level. *Hydrobiologia* 392, 129–141.
- Bout-Roumazeilles, V., Nebout, N.C., Peyron, O., Cortijo, E., Landais, A., Masson-Delmotte, V., 2007. Connection between South Mediterranean climate and North African atmospheric circulation during the last 50,000 yr BP North Atlantic cold events. *Quaternary Science Reviews* 26(25), 3197–3215.
- Bradley, R.S., Eddy, J.A., 1991. Records of past global changes. In *Global Changes of the Past*. Bradley, R.S. (ed). University Corporation for Atmospheric Research, Boulder, pp. 5–9.
- Bradley, R.S., 2008. Holocene perspectives on future climate change. In *Natural Climate Variability and Global Warming: A Holocene Perspective*. Battarbee, R.W., Binney, H.A. (eds). Wiley-Blackwell, Chichester, pp. 254–268.
- Bradley, R.S., 2015. *Paleoclimatology: reconstructing climates of the Quaternary*. Academic Press, Amsterdam.
- Bronk Ramsey, C., 2007. Deposition models for chronological records. *Quaternary Science Reviews* 27, 42–60.

- Brown, L.C., Duguay, C.R., 2010. The response and role of ice cover in lake-climate interactions. *Progress in Physical Geography* 34, 671–704.
- Brunet, M., Aguilar, E., Saladié, O., Sigró, J., López, D., 2001. The Spanish temperature series. Time variations and trends over the last 150 years. In *Geophysical Research Abstracts Vol. 3, No. GRA3*, pp. 5333–5376.
- Brunet, M., Jones, P.D., Sigró, J., Saladié, O., Aguilar, E., Moberg, A., Della-Marta, P.M., Lister, D., Walther, A., López, D., 2007. Temporal and spatial temperature variability and change over Spain during 1850–2005. *Journal of Geophysical Research: Atmospheres* 112(D12).
- Brunet, M., Saladié O., Jones P., Sigró, J., Aguilar, E., Moberg, A., Lister, D., Walther, A., Almarza, C., 2008. A case-study/guidance on the development of long-term daily adjusted temperature datasets. World Meteorological Organization, Geneva. WCDMP-66/ WMO-TD-1425.
- Buck, C.E., Christen, J.A., James, G.N., 1999. BCAL: an on-line Bayesian radiocarbon calibration tool. *Internet Archaeology* 7. http://intarch.ac.uk/journal/issue7/buck_toc.html.
- Bueh, C., Nakamura, H., 2007. Scandinavian pattern and its climatic impact. *Quarterly Journal of the Royal Meteorological Society* 133(629), 2117–2131.
- Büntgen, U., Frank, D., Grudd, H., Esper, J., 2008. Long-term summer temperature variations in the Pyrenees. *Climate Dynamics* 31(6), 615–631.
- Cacho, I., Grimalt, J.O., Pelejero, C., Canals, M., Sierro, F.J., Flores, J.A., Shackleton, N., 1999. Dansgaard-Oeschger and Heinrich event imprints in the Alboran Sea paleotemperatures. *Paleoceanography* 14, 698–705.
- Cahill, N., Kemp, A.C., Horton, B.P., Parnell, A.C., 2016. A Bayesian hierarchical model for reconstructing relative sea level: from raw data to rates of change. *Climate of the Past* 12, 525–542.
- Camarero, L., Catalan, J., 2012. Atmospheric phosphorus deposition may cause lakes to revert from phosphorus limitation back to nitrogen limitation. *Nature Communications* 3, 1118.
- Campelo, F., Nabais, C., García-González, I., Cherubini, P., Gutiérrez, E., Freitas, H., 2009. Dendrochronology of *Quercus ilex* L. and its potential use for climate reconstruction in the Mediterranean region. *Canadian Journal of Forest Research* 39, 2486–2493.
- Castañeda, I., Schouten, S., 2011. A review of molecular organic proxies for examining

- modern and ancient lacustrine environments. *Quaternary Science Reviews* 30, 2851–2891.
- Castro-Díez, Y., Pozo-Vázquez, D., Rodrigo, F.S., Esteban-Parra, M.J., 2002. NAO and winter temperature variability in southern Europe. *Geophysical Research Letters* 29(8), 1160.
- Casty, C., Raible, C.C., Stocker, T.F., Wanner, H., Luterbacher, J., 2007. A European pattern climatology 1766–2000. *Climate Dynamics* 29, 791–805.
- Catalan, J., Camarero, L., 1993. Seasonal changes in alkalinity and pH in two Pyrenean lakes of very different water residence time. *Internationale Vereinigung für Theoretische und Angewandte Limnologie Verhandlungen* 25(2), 749–753.
- Catalan, J., Fee, E.J., 1994. Interannual variability in limnic ecosystems: origin, patterns and predictability. In *Limnology Now: A Paradigm of Planetary Problems*. Margalef, R., (ed). Elsevier Science, New York, pp. 81–97.
- Catalan, J., Ventura, M., Brancelj, A., Granados, I., Thies, H., Nickus, U., Korhola, A., Lotter, A.F., Barbieri, A., Stuchlík, E., Lien, L., Bitušík, P., Buchaca, T., Camarero, L., Goudsmit, G.H., Kopáček, J., Lemcke, G., Livingstone, D.M., Müller, B., Rautio, M., Sisko, M., Sorvari, S., Sporka, F., Struneycky, O., Toro, M., 2002. Seasonal ecosystem variability in remote mountain lakes: implications for detecting climatic signals in sediment records. *Journal of Paleolimnology* 28, 25–46.
- Catalan, J., Camarero, L., Felip, M., Pla, S., Ventura, M., Buchaca, T., Bartumeus, F., de Mendoza, G., Miró, A., Casamayor, E.O., Medina-Sánchez, J.M., Bacardit, M., Altuna, M., Bartrons, M., Díaz de Quijano, D., 2006. High mountain lakes: extreme habitats and witnesses of environmental changes. *Limnetica* 25(1-2), 551–584.
- Catalan, J., Pla, S., García, J., Camarero, L., 2009. Climate and CO₂ saturation in an alpine lake throughout the Holocene. *Limnology and Oceanography* 54, 2542–2552.
- Catalan, J., Pla-Rabés, S., Wolfe, A., Smol, J.P., Rühland, K.M., Anderson, N.J., Kopáček, J., Stuchlík, E., Schmidt, R., Koinig, K., Camarero, L., Flower, R., Heiri, O., Kamenik C., Korhola, A., 2013. Global change revealed by palaeolimnological records from remote lakes: a review. *Journal of Paleolimnology* 49, 513–535.
- Catalan, J., Pla-Rabés, S., García, J., Camarero, L., 2014. Air temperature-driven CO₂ consumption by rock weathering at short timescales: Evidence from a Holocene lake sediment record. *Geochimica et Cosmochimica Acta* 136, 67–79.
- Cattiaux, J., Vautard, R., Cassou, C., Yiou, P., Masson-Delmotte, V., Codron, F., 2010. Winter 2010 in Europe: a cold extreme in a warming climate. *Geophysical Research Letters* 37, L20704.

- Chiapello, I., Moulin, C., 2002. TOMS and METEOSAT satellite records of the variability of Saharan dust transport over the Atlantic during the last two decades (1979–1997). *Geophysical Research Letters* 29(8), 1176.
- Christensen, J.H., Krishna, K., Kumar, Aldrian, E., An, S.I., Cavalcanti, I.F.A., de Castro, M., Dong, W., Goswami, P., Hall, A., Kanyanga, J.K., Kitoh, A., Kossin, J., Lau, N.C., Renwick, J., Stephenson, D.B., Xie, S.P., Zhou, T., 2013. Climate Phenomena and their Relevance for Future Regional Climate Change. In *Climate Change 2013: The Physical Science Basis. Contribution of Working Group I to the Fifth Assessment Report of the Intergovernmental Panel on Climate Change*. Stocker, T.F., Qin, D., Plattner, G.K., Tignor, M., Allen, S.K., Boschung, J., Nauels, A., Xia, Y., Bex, V., Midgley, P.M. (eds). Cambridge University Press, Cambridge, United Kingdom and New York, NY, USA.
- Chronis, T., Raitsos, D.E., Kassis, D., Sarantopoulos, A., 2011. The summer North Atlantic Oscillation influence on the eastern Mediterranean. *Journal of Climate* 24(21), 5584–5596.
- Chung, F.H., 1974a. Quantitative interpretation of X-ray diffraction patterns of mixtures. I. Matrix-flushing method for quantitative multicomponent analysis. *Journal of Applied Crystallography* 7, 519–525.
- Chung, F.H., 1974b. Quantitative interpretation of X-ray diffraction patterns of mixtures. II. Adiabatic principle of X-ray diffraction analysis of mixtures. *Journal of Applied Crystallography* 7, 526–531.
- Clement, A., Bellomo, K., Murphy, L.N., Cane, M.A., Mauritzen, T., Rädel, G., Stevens, B., 2015. The Atlantic Multidecadal Oscillation without a role for ocean circulation. *Science* 350(6258), 320–324.
- Cohen, A.S., 2003. In *Paleolimnology: The History and Evolution of Lake Systems*. Oxford University Press, p. 528.
- Cole, J.J., Caraco, N.F., Kling, G.W., Kratz, T.K., 1994. Carbon-dioxide supersaturation in the surface waters of lakes. *Science* 265, 1568–1570.
- Cole, J.J., Prairie, Y.T., Caraco, N.F., McDowell, W.H., Tranvik, L.J., Striegl, R.G., Duarte, C.M., Kortelainen, P., Downing, J.A., Middelburg, J.J., Melack, J., 2007. Plumbing the global carbon cycle: Integrating inland waters into the terrestrial carbon budget. *Ecosystems* 10, 171–184.
- Comas-Bru, L., McDermott, F., 2014. Impacts of the EA and SCA patterns on the European twentieth century NAO-winter climate relationship. *Quarterly Journal of the Royal Meteorological Society* 140, 354–363.

- Comas-Bru, L., McDermott, F., Werner, M., 2016. The effect of the East Atlantic pattern on the precipitation $\delta^{18}\text{O}$ -NAO relationship in Europe. *Climate Dynamics* 1, 1–11.
- Compo, G.P., Whitaker, J.S., Sardeshmukh, P.D., Matsui, N., Allan, R.J., Yin, X., Gleason, B.E., Vose, R.S., Rutledge, G., Bessemoulin, P., Brönnimann, S., Brunet, M., Crouthamel, R.I., Grant, A.N., Groisman, P.Y., Jones, P.D., Kruk, M.C., Kruger, A.C., Marshall, G.J., Maugeri, M., Mok, H.Y., Nordli, Ø., Ross, T.F., Trigo, R.M., Wang, X.L., Woodruff, S.D., Worley, S.J., 2011. The Twentieth Century Reanalysis Project. *Quarterly Journal of the Royal Meteorological Society* 137(654), 1–28.
- Cook, E.R., D'Arrigo, R.D., Mann, M.E., 2002. A well verified, multiproxy reconstruction of the winter North Atlantic Oscillation index since A.D. 1400. *Journal of Climate* 15, 1754–1764.
- Cook, E.R., Seager, R., Cane, M.A., Stahle, D.W., 2007. North American drought: reconstructions, causes, and consequences. *Earth-Science Reviews* 81(1), 93–134.
- Corella, J.P., Valero-Garcés, B., Moreno, A., Morellón, M., Rull, V., Giralt, S., Rico, M.T., and Pérez-Sanz, A., 2011. Climate and human impact on a meromictic lake during the last 6000 years (Montcortés Lake, Central Pyrenees, Spain). *Journal of Paleolimnology* 46, 351–367.
- Corella, J.P., Stefanova, V., El Anjoumi, A., Rico, E., Giralt, S., Moreno, A., Plata-Montero, A., Valero-Garcés, B.L., 2013. A 2500-year multi-proxy reconstruction of climate change and human activities in northern Spain: the Lake Arreo record. *Palaeogeography, Palaeoclimatology, Palaeoecology* 386, 555–568.
- Coudé-Gaussen, G., 1981. Etude détaillée d'un échantillon de poussières éoliennes prélevé au Tanezrouft, le 10 décembre 1980. *Recherches géographiques à Strasbourg* 16/17 121–30.
- Coudé-Gaussen, G., Hillaire-Marcel, C., Rognon, P., 1982. Origine et évolution pédologique des fractions carbonatées dans les loess des Matmata (Sud-Tunisien) d'après leurs teneurs en ^{13}C et ^{18}O . *Comptes Rendus de l'Académie des Sciences de Paris* 295, 939–942.
- Coudé-Gaussen, G., Rognon, P., Bergametti, G., Gomes, L., Strauss, B., Le Coustumer, M.N., 1987. Saharan dust on Fuerteventura island (Canaries): chemical and mineralogical characteristics, air mass trajectories, and probable sources. *Journal of Geophysical Research* 92, 9753–9771.
- Crantz, D., 1765. *The History of Greenland; Including an Account of the Mission Carried on by the United Brethren in that Country*. London: Longman, Hurst, Rees, Orme and Brown; xi, 359 pp; 2 volumes, vi, 323.

- Currás, A., Zamora, L., Reed, J.M., García-Soto, E., Ferrero, S., Armengol, X., Mezquita-Joanes, F., Marqués, M.A., Riera, S., Julià, R., 2012. Climate change and human impact in central Spain during Roman times: high-resolution multi-proxy analysis of a Tufa lake record (Somolinos, 1280 m asl). *Catena* 89, 31–53.
- Dansgaard, W., Johnsen, S.J., Clausen, H.B., Dahl-Jensen, D., Gundestrup, N.S., Hammer, C.U., Hvidberg, C.S., Steffensen, J.P., Sveinbjørnsdóttir, A.E., Jouzel, J., Bond, G., 1993. Evidence for general instability of past climate from a 250-kyr ice-core record. *Nature* 364, 218–220.
- Deevey, E.S., 1955. The obliteration of the hypolimnion. *Memorie Dell’istituto Italiano Di Idrobiologia* 8(suppl), 9–38.
- Defant, A., 1924. Die Schwankungen der atmosphärischen Zirkulation über dem Nordatlantischen Ozean im 25-jährigen Zeitraum 1881–1905. *Geogr Ann* 6, 13–41.
- Delworth, T.L., Mann, M.E., 2000. Observed and simulated multidecadal variability in the Northern Hemisphere. *Climate Dynamics* 16, 661–676.
- De Pedraza, J., López, J., 1980. Gredos. Geología y glaciarismo. Trazo-Editorial. Zaragoza. 31 pp.
- Deser, C., Alexander, M.A., Xie, S.P., Phillips, A.S., 2010. Sea surface temperature variability: Patterns and mechanisms. *Annual Review of Marine Science* 2, 115–143.
- Desprat, S., Sanchez Goñi, M.F., Loutre, M.F., 2003. Revealing climatic variability of the last three millennia in northwestern Iberia using pollen influx data. *Earth and Planetary Science Letters* 213(1), 63–78.
- De Vicente, G., González, J.M., Calvo, J.P., Muñoz, A., Giner, J., Rodríguez, M., 1994. Evolución y estructuras alpinas en la zona del centro peninsular. *Cadernos do Laboratorio Xeolóxico de Laxe* 19, 175–190.
- Devesa, J.A., 1995. Vegetación y Flora de Extremadura. Universitas Editorial, Badajoz.
- Diao, Y., Li, J., Luo, D., 2006. A new blocking index and its application: blocking action in the Northern Hemisphere, *Journal of Climate* 19, 4819–4839.
- Dinsmore, W.P., Scrimgeour, G.J., Prepas, E.E., 1999. Empirical relationships between profundal macroinvertebrate biomass and environmental variables in boreal lakes of Alberta, Canada. *Freshwater Biology* 41, 91–100.
- Dove, H.W., 1839. Über die geographische Verbreitung gleichartiger Witterungserscheinungen. Erste Abhandlung: Über die nicht periodischen Änderungen der Temperaturvertheilung auf der Oberfläche der Erde. *Abh. Königl. Akad. Wiss. Berlin*, 1839, 287–415.

- Durán, L., Sánchez, E., Yagüe, C., 2013. Climatology of precipitation over the Iberian Central System mountain range. *International Journal of Climatology* 33, 2260–2273.
- Durán, L., Rodríguez-Fonseca, B., Yagüe, C., Sánchez, E., 2014. Water vapour flux patterns and precipitation at Sierra de Guadarrama mountain range (Spain). *International Journal of Climatology* 35(7), 1593–1610.
- Egede, H., 1745. History of Greenland - A Description of Greenland: Shewing the Natural History, Situation, Boundaries, and Face of the Country; the Nature of the Soil; the Rise and Progress of the Old Norwegian Colonies; the Ancient and Modern Inhabitants; their Genius and Way of Life, and Produce of the Soil; their Plants, Beasts, Fishes, &c.' (translated from the Danish). Picadilly, London: Pickering Book-seller; 220.
- Eglinton, T.I., Eglinton, G., 2008. Molecular proxies for paleoclimatology. *Earth and Planetary Science Letters* 275, 1–16.
- El Kenawy, A., López-Moreno, J.I., Vicente-Serrano, S.M., 2012. Trend and variability of surface air temperature in northeastern Spain (1920–2006): linkage to atmospheric circulation. *Atmospheric Research* 106, 159–180.
- El Mouden, A., Bouchaou, L., Snoussi, M., 2005. Constraints on alluvial clay mineral assemblages in semiarid regions. The Souss Wadi Basin (Morocco, Northwestern Africa). *Geologica Acta* 3(1), 3–13.
- Enfield, D.B., Mestas-Nuñez, A.M., Trimble, P.J., 2001. The Atlantic multidecadal oscillation and its relationship to rainfall and river flows in the continental US. *Geophysical Research Letters* 28, 2077–2080.
- Engelstaedter, S., Tegen, I., Washington, R., 2006. North African dust emissions and transport. *Earth-Science Reviews* 79(1), 73–100.
- Engelstaedter, S., Washington, R., 2007. Atmospheric controls on the annual cycle of North African dust. *Journal of Geophysical Research: Atmospheres* 112, D17111.
- Esteban-Parra, M.J., Pozo-Vazquez, D., Rodrigo, F.S., Castro-Diez, Y., 2003. Temperature and precipitation variability and trends in Northern Spain in the context of the Iberian Peninsula climate. In *Mediterranean Climate: Variability and Trends*. Bolle, H.J. (ed), Springer, New York, pp. 259 – 276.
- Eugster, H.P., Hardiem, L.A., 1978. Saline lakes. In *Lakes: Chemistry, Geology, Physics*. Lerman, A. (ed). Springer-Verlag, New York, pp. 237–293.
- Fagan, B., 2009. The long summer: how climate changed civilization. Basic books, New York.

- Feldstein, S.B., 2000. The timescale, power spectra, and climate noise properties of teleconnection patterns. *Journal of Climate* 13, 4430–4440.
- Felis, T., Pätzold, J., Loya, Y., Fine, M., Nawar, A.H., Wefer, G., 2000. A coral oxygen isotope record from the northern Red Sea documenting NAO, ENSO, and North Pacific teleconnections on Middle East climate variability since the year 1750. *Paleoceanography* 15, 679–694.
- Fernández-González, F., 1991. La vegetación del valle del Paular (Sierra de Guadarrama, Madrid), I. Lazaroa 12, 153–272.
- Fischer, E.M., Luterbacher, J., Zorita, E., Tett, S.F.B., Casty, C., Wanner, H., 2007. European climate response to tropical volcanic eruptions over the last half millennium. *Geophysical Research Letters* 34, L05707.
- Folland, C.K., Palmer, T.N., Parker, D.E., 1986. Sahel rainfall and worldwide sea temperatures, 1901 – 85. *Nature* 320(6063), 602 – 606.
- Folland, C.K., Colman, A.W., Rowell, D.P., Davey, M.K., 2001. Predictability of northeast Brazil rainfall and real-time forecast skill, 1987–1998. *Journal of Climate* 14(9), 1937–1958.
- Folland, C.K., Knight, J., Linderholm, H.W., Fereday, D., Ineson, S., Hurrell, J.W., 2009. The summer North Atlantic Oscillation: past, present, and future. *Journal of Climate* 22(5), 1082–1103.
- Franzke, C., Fraedrich, K., Lunkheit, F., 2000. Low frequency variability in a simplified atmospheric global circulation model: storm track induced ‘spatial resonance’. *Quarterly Journal of the Royal Meteorological Society* 126, 2691–2708.
- Fredlund, G.G., Tieszen, L.L., 1997. Calibrating grass phytolith assemblages in climatic terms: application to late Pleistocene assemblages from Kansas and Nebraska. *Palaeogeography Palaeoclimatology, Palaeoecology* 136, 199–211.
- Fritz, S.C., 1990. Twentieth century salinity and water-level fluctuations in Devils Lake, North Dakota: test of a diatom-based transfer function. *Limnology and Oceanography* 35, 1771–1781.
- Fritz, S.C., 2008. Deciphering climatic history from lake sediments. *Journal of Paleolimnology* 39, 5–16.
- Gaines, S.M., Eglinton, G., Rullkötter, J., 2009. *Echoes of Life: What Fossil Molecules Reveal About Earth History*. Oxford University Press, Oxford, 357 pp.
- Galloway, J.N., Cowling, E.B., 2002. Reactive nitrogen and the world: 200 years of change. *Ambio* 31, 64–71.

- García-Alix, A., Jimenez-Espejo, F.J., Lozano, J.A., Jiménez-Moreno, G., Martínez-Ruiz, F., García Sanjuán, L., Aranda Jiménez, G., García Alfonso, E., Ruiz-Puertas, G., Scott Anderson, R., 2013. Anthropogenic impact and lead pollution throughout the Holocene in Southern Iberia. *Science of the Total Environment* 449, 451–460.
- Gasse, F., Barker, P., Gell, P.A., Fritz, S.C., Chalié, F., 1997. Diatom-inferred salinity in palaeolakes: an indirect tracer of climate change. *Quaternary Science Review* 16, 547–563.
- George, D.G., Maberly, S.C., Hewitt, D.P., 2004. The influence of the North Atlantic Oscillation on the physical, chemical and biological characteristics of four lakes in the English Lake District. *Freshwater Biology* 49, 760–774.
- George, D.G., 2007. The impact of the North Atlantic Oscillation on the development of ice on Lake Windermere. *Climatic Change* (3–4) 81, 455–468.
- Ghanbari, R.M., Bravo, H.R., Magnuson, J.J., Hyzer, W.G., Benson, B.J., 2009. Coherence between lake ice cover, local climate and teleconnections (Lake Mendota, Wisconsin). *Journal of Hydrology* 374, 282–293.
- Gil-García, M., Ruiz Zapata, M., Santisteban, J., Mediavilla, R., López-Pamo, E., Dabrio, C., 2007. Late holocene environments in Las Tablas de Daimiel (south central Iberian peninsula, Spain). *Vegetation History and Archaeobotany* 16, 241–250.
- Ginoux, P., Prospero, J.M., Torres, O., and Chin, M., 2004. Long-term simulation of global dust distribution with the GOCART model: Correlation with North Atlantic Oscillation. *Environmental Modelling and Software* 19, 113–128.
- Ginoux, P., Prospero, J.M., Gill, T.E., Hsu, N.C., Zhao, M., 2012. Global-scale attribution of anthropogenic and natural dust sources and their emission rates based on MODIS Deep Blue aerosol products, *Reviews of Geophysics* 50, RG3005.
- Giralt, S., Moreno, A., Bao, R., Sáez, A., Prego, R., Valero-Garcés, B.L., Pueyo, J.J., González-Sampériz, P., Taberner, C., 2008. A statistical approach to disentangle environmental forcings in a lacustrine record: the Lago Chungara case (Chilean Altiplano). *Journal of Paleolimnology* 40, 195–215.
- Glueck, M.F., Stockton, C.W., 2001. Reconstruction of the North Atlantic oscillation. *International Journal of Climatology* 21, 1453–1465.
- Goldenberg, S.B., Landsea, C.W., Mestas-Nuñez, A.M., Gray, W.M., 2001. The recent increase in Atlantic hurricane activity: causes and implications. *Science* 293, 474–479.

- Goodkin, N.F., Hughen, K.A., Doney, S.C., Curry, W.B., 2008. Increased multidecadal variability of the North Atlantic Oscillation since 1781. *Nature Geoscience* 1, 1844–848.
- Goodkin, N.F., Druffel, E.R.M., Hughen, K.A., Doney, S.C., 2012. Two centuries of limited variability in subtropical North Atlantic thermocline variability. *Nature Communications* 3, 803.
- Goosse, H., Barriat, P.Y., Lefebvre, W., Loutre, M.F., Zunz, V., 2010. Introduction to climate dynamics and climate modeling. Université catholique de Louvain. Online textbook available at <http://www.climate.be/textbook>.
- Granados, I., Toro, M., 2000. Recent Warming in a High Mountain Lake (Laguna Cimera, Central Spain) inferred by means of fossil chironomids. *Journal of Limnology* 59 (1), 109–119.
- Granados, I., Toro, M., Rubio-Romero, A., 2006. Laguna Grande de Peñalara 10 años de seguimiento limnológico. Dirección General del Medio Natural, Consejería de Medio Ambiente y Ordenación del Territorio, Comunidad de Madrid. 198 pp.
- Gray, W.M., 1997. Role of the ocean conveyor belt as a cause of global multidecadal climate, paper presented at Meeting on Atlantic Climate Variability, Lamont-Doherty Earth Obs., Earth Inst. at Columbia Univ., Palisades, New York.
- Gronau, K.L., 1811. Das Klima der Polarländer. In *Repertorium des Neuesten und Wissenwurdigsten aus der gesamten Naturkunde*. Flörke, H.F. (eds). Berlin.
- Grootes, P.M., Stuiver, M., 1997. Oxygen 18/16 variability in Greenland snow and ice with 10– 3-to 105-year time resolution. *Journal of Geophysical Research: Oceans* 102(C12), 26455–26470.
- Gu, R., Stefan, H.G., 1990. Year-round temperature simulation of cold climate lakes. *Cold Regions Science and Technology* 18, 147–160.
- Guerzoni, S., Molinaroli, E., Chester, R., 1997. Saharan dust inputs to the western Mediterranean sea: depositional patterns, geochemistry and sedimentological implications. *Deep-Sea Research II* 44 (3–4), 631–654.
- Guiot, J., de Vernal, A., 2007. Transfer functions: methods for quantitative paleoceanography based on microfossils. *Developments in marine geology* 1, pp. 523–563.
- Gutro, R., 2005. What's the difference between weather and climate?. NASA. Retrieved June 8, 2016, from http://www.nasa.gov/mission_pages/noaa-n/climate/climate_weather.html

- Haine, T., 2008. What did the Viking discoverers of America know of the North Atlantic Environment?. *Weather* 63, 60–65.
- Hannon, G.E., Gaillard, M.J., 1997. The plant-macrofossil record of past lake-level changes. *Journal Paleolimnology* 18, 15–28.
- Harris, M.B., 1998. Basic statistics for behavioral science research.
- Hartmann, Dennis L., 2015. Global physical climatology. Vol. 103. Newnes.
- Haslett, J., Whiley, M., Bhattacharya, S., Salter-Townsend, M., Wilson, S., Allen, J., Huntley, B., Mitchell, F., 2006. Bayesian palaeoclimate reconstruction. *Journal of the Royal Statistical Society: Series A (Statistics in Society)* 169, 395–438.
- Haslett, J., Parnell, A., 2008. A simple monotone process with application to radiocarbon-dated depth chronologies. *Journal of the Royal Statistical Society: Series C (Applied Statistics)* 57, 399–418.
- Hastenrath, S., 1991. Climate Dynamics of the Tropics. Atmospheric sciences library, 8.
- Hastie, T., Tibshirani, R., Friedman, J., 2001. The elements of statistical learning. Springer, New York.
- Hastings, M.G., Jarvis, J.C., Steig, E.J., 2009. Anthropogenic impacts on nitrogen isotopes of ice-core nitrate. *Science* 324, 1288.
- Haug, G.H., Hughen, K.A., Sigman, D.M., Peterson, L.C., Röhl, U., 2001. Southward migration of the intertropical convergence zone through the Holocene. *Science* 293, 1304–1308.
- Hense, A., Glowienka-Hense, R., 2010. Comments on: on the weather history of North Greenland, west coast by Julius Hann. *Meteorologische Zeitschrift* 19(2), 207–211.
- Hernández, A., Trigo, R.M., Pla-Rabes, S., Valero-Garcés B.L., Jerez, S., Rico-Herrero, M., Vega, J.C., Jambrina-Enríquez, M., Giralt, S., 2015. Sensitivity of two Iberian lakes to North Atlantic atmospheric circulation modes, *Climate Dynamics* 45, 3403–3417.
- Herschy, R.W., 2012. Lakes sediments. In Encyclopedia of lakes and reservoirs. Bengtsson, L., Herschy, R.W., Fairbridge, R.W. (eds). Springer, New York, pp. 458–463.
- Hervàs, A., Camarero, L., Reche, I., Casamayor, E.O., 2009. Viability and potential for immigration of airborne bacteria from Africa that reach high mountain lakes in Europe. *Environmental Microbiology* 11(6), 1612–1623.

- Hodell, D.A., Curtis, J.H., Brenner, M., 1995. Possible role of climate in the collapse of Classic Maya civilization. *Nature*. 375, 391–394.
- Hodell, D.A., Brenner, M., Curtis, J.H., 2005. Terminal Classic drought in the northern Maya lowlands inferred from multiple sediment cores in Lake Chichancanab (Mexico). *Quaternary Science Reviews* 24, 1413–1427.
- Hoerling, M.P., Hurrell, J.W., Xu, T., 2001. Tropical origins for recent North Atlantic climate change. *Science* 292, 90–92.
- Holden, P., Mackay, A., Simpson, G.L., 2008. A Bayesian palaeoenvironmental transfer function model for acidified lakes. *Journal Paleolimnology* 39, 551–566.
- Holmes, J.A., 1998. A late Quaternary ostracod record from Wallywash Great Pond, a Jamaican marl lake. *Journal Paleolimnology* 19, 115–128.
- Holmes, J.A., 2001. Ostracoda. In *Tracking Environmental Change Using Lake sediments*, vol. 4. Smol, J.P., Birks, H.J.B., Last, W.M. (eds.). Kluwer Academic, Dordrecht, pp. 125–151.
- Holtgrieve, G.W., Schindler, D.E., Hobbs, W.O., Leavitt, P.R., Ward, E.J., Bunting, L., Chen, G., Finney, B.P., Gregory-Eaves, I., Holmgren, S., Lisac, M.J., Lisi, P.J., Nydick, K., Rogers, L.A., Saros, J.E., Selbie, D.T., Shapley, M.D., Walsh, P.B., Wolfe, A.P., 2011. A coherent signature of anthropogenic nitrogen deposition to remote watersheds of the northern hemisphere. *Science* 334, 1545–1548.
- Hu, Q., Feng, F., 2008. Variation of the North American summer monsoon regimes and the Atlantic multidecadal oscillation. *Journal of Climate* 21, 2371–2383.
- Huntington, E., 1922. *Civilization and climate*. Yale University Press.
- Hurrell, J.W., 1995. Decadal trends in the North Atlantic Oscillation: regional temperatures and precipitation. *Science* 269(5224), 676–679.
- Hurrell, J.W., van Loon, H., 1997. Decadal variations in climate associated with the North Atlantic Oscillation. *Climatic Change* 36, 301–326.
- Hurrell, J.W., Kushir, Y., Ottersen, G., Visbeck, M., 2003. An overview of the North Atlantic Oscillation. In *The North Atlantic Oscillation, Climatic Significance and Environmental Impact*. Hurrell, J.W., Kushir, Y., Ottersen, G., Visbeck, M. (eds.). Geophysical Monograph 134. American Geophysical Union, Washington, pp. 1–35.
- Hurrell, J.W., Visbeck, M., Busalacchi, A., Clarke, R.A., Delworth, T.L., Dickson, R.R., Johns, W.E., Koltermann, K.P., Kushnir, Y., Marshall, D., Mauritzen, C., Mccartney, M.S., Piola, A., Reason, C., Reverdin, G., Schott, F., Sutton, R., Wainer, I., Wright,

- D., 2006. Atlantic climate variability and predictability: A CLIVAR perspective. *Journal of Climate* 19(20), 5100–5121.
- Hurrell, J.W., 2015. Climate Variability: North Atlantic and Arctic Oscillation. In *Encyclopedia of Atmospheric Sciences*, second volume, pp. 47–60.
- Hutchinson, G.E., Loffler, J., 1956. The thermal classification of lakes. *Proceedings of the National Academy of Sciences* 42, 84–86.
- Hutchinson, G.E., 1969. Eutrophication, past and present. In *Eutrophication: Causes, Consequences, Correctives*. National Academy of Sciences, Washington DC, pp. 17–26.
- Imboden, D.M., Wüest, A., 1995. Mixing mechanisms in lakes. In *Physics and chemistry of lakes*. Lerman, A., Imboden, D., Gat, J. (eds). Springer-Verlag, Berlin, pp. 83–138.
- Imbrie, J., Kipp, N.G., 1971. A new micropaleontological method for quantitative paleoclimatology: application to a Late Pleistocene Caribbean core. In *The Late Cenozoic glacial ages*. Turekian, K.K. (ed). Yale University Press, New Haven, pp. 77–181.
- Jackson, S.T., Overpeck, J.T., Webb III, T., Keatitch, S.E., Anderson, K.H., 1997. Mapped plant-macrofossils and pollen records of late Quaternary vegetation in eastern North America. *Quaternary Science Reviews* 16, 1–70.
- Jambrina-Enríquez, M., Rico, M., Moreno, A., Leira, M., Bernández, P., Prego, R., Recio, C., Valero-Garcés, B.L., 2014. Timing of deglaciation and postglacial environmental dynamics in NW Iberia: the Sanabria Lake record. *Quaternary Science Reviews* 94, 136–158.
- James, I.N., James, P.M., 1989. Ultra-low frequency variability in a simple atmospheric circulation model. *Nature* 342, 53–55.
- Jeffries, M.O., Morris, K., 2007. Some aspects of ice phenology on ponds in central Alaska, USA. *Annals of Glaciology* 46, 397–403.
- Jensen, O.P., Benson, B.J., Magnuson, J.J., Card, V.M., Futter, M.N., Soranno, P.A., Stewart, K.M., 2007. Spatial analysis of ice phenology trends across the Laurentian Great Lakes region during a recent warming period. *Limnology and Oceanography* 52(5), 2013–2026.
- Jerez, S., Trigo, R.M., 2013. Time-scale and extent at which large-scale circulation modes determine the wind and solar potential in the Iberian Peninsula. *Environmental Research Letters* 8(4), 044035.

- Jiménez-Espejo, F.J., García-Alix, A., Jiménez-Moreno, G., Rodrigo-Gámiz, M., Anderson, R.S., Rodríguez-Tovar, F.J., Martínez-Ruiz, F., Giralt, S., Delgado Huertas, A., Pardo-Igúzquiza, E., 2014. Saharan aeolian input and effective humidity variations over western Europe during the Holocene from a high altitude record. *Chemical Geology* 374–375, 1–12.
- Jones, P.D., Jonsson, T., Wheeler, D., 1997. Extension to the North Atlantic Oscillation using early instrumental pressure observations from Gibraltar and south-west Iceland. *International Journal of Climatology* 17, 1433–1450.
- Jones, P.D., Osborn, T.J., Briffa, K.R., 2001. The evolution of climate over the Last Millennium. *Science* 292, 662–667.
- Jones, P.D., Osborn, T.J., Briffa, K.R., 2003. Pressure-Based Measures of the North Atlantic Oscillation (NAO): A Comparison and an Assessment of Changes in the Strength of the NAO and in its Influence on Surface Climate Parameters. In *The North Atlantic Oscillation, Climatic Significance and Environmental Impact*. Hurrell, J.W., Kushir, Y., Ottersen, G., Visbeck, M. (eds). *Geophysical Monograph* 134. American Geophysical Union, Washington, pp. 51–62.
- Jones, P.D., Mann, M.E., 2004. Climate over the past millennia. *Reviews of Geophysics*. 42, RG2002.
- Jones, P.D., Briffa, K.R., Osborn, T.J., Lough, J.M., Van Ommen, T.D., Vinther, B.M., Luterbacher, J., Wahl, E.R., Zwiers, F.W., Mann, M.E., Schmidt, G.A., Ammann, C.M., Buckley, B.M., Cobb, K.M., Esper, J., Goosse, H., Graham, N., Jansen, E., Kiefer, T., Kull, C., Küttel, M., Mosley-Thompson, E., Overpeck, J.T., Riedwyl, N., Schulz, M., Tudhope, A.W., Villalba, R., Wanner, H., Wolff, E., Xoplaki, E., 2009. High-resolution palaeoclimatology of the last millennium: A review of current status and future prospects. *The Holocene* 19, 3–49.
- Jouzel, J., Masson-Delmotte, V., Cattani, O., Dreyfus, G., Falourd, S., Hoffmann, G., Nouet, J., Barnola, J.M., Chappellaz, J., Fischer, H., Gallet, J.C., Johnsen, S., Leuenberger, M., Loulergue, L., Luethi, D., Oerter, H., Parrenin, F., Raisbeck, G., Raynaud, D., Schwander, J., Spahni, R., Souchez, R., Selmo, E., Schilt, A., Steffensen, J.P., Stenni, B., Stauffer, B., Stocker, T., Tison, J.-L., Werner, M., Wolff, E.W., 2007. Orbital and millennial Antarctic climate variability over the last 800,000 years. *Science* 317(5839), 793–796.
- Juggins, S., Birks, H.J.B., 2012. Quantitative environmental reconstructions from biological data. In *Tracking environmental change using lake sediments*. Birks, H.J.B., Lotter, A.F., Juggins, S., Smol, J.P. (eds). Springer Netherlands, pp. 431–494.
- Jung, T., Vitart, F., Ferranti, L., Morcrette, J.J., 2011. Origin and predictability of the extreme negative NAO winter of 2009/10. *Geophysical Research Letters* 38, L07701.

- Kaplan, A., Cane, M.A., Kushnir, Y., Clement, A.C., 1998. Analyses of global sea surface temperatures 1856–1991. *Journal of Geophysical Research: Oceans* 103, 18575–18589.
- Kerr, R.A., 2000. A North Atlantic climate pacemaker for the centuries. *Science* 288, 1984–1985.
- Kjellström, E., Thejll, P., Rummukainen, M., Christensen, J.H., Boberg, F., Christensen, O.B., Maule, C.F., 2013. Emerging regional climate change signals for Europe under varying large-scale circulation conditions. *Climate Research* 56, 103–119.
- Knight, J.R., Allan, R.J., Folland, C.K., Vellinga, M., Mann, M.E., 2005. A signature of persistent natural thermohaline circulation cycles in observed climate, *Geophysical Research Letters* 32, L20708.
- Knight, J.R., Folland, C.K., Scaife, A.A., 2006. Climate impacts of the Atlantic multidecadal oscillation. *Geophysical Research Letters* 33, L17706.
- Knippertz, P., Todd, M.C., 2012. Mineral dust aerosols over the Sahara: Meteorological controls on emission and transport and implications for modeling. *Reviews of Geophysics* 50, RG1007.
- Knudsen, M.F., Seidenkrantz, M.S., Jacobsen, B.H., Kuijpers, A., 2011. Tracking the Atlantic Multidecadal Oscillation through the last 8,000 years. *Nature Communications* 2, 178.
- Korhola, A., Vasko, K., Toivonen, H.T.T., Olander, H., 2002. Holocene temperature changes in northern Fennoscandia reconstructed from chironomids using Bayesian modelling. *Quaternary Science Reviews* 21, 1841–1860.
- Korhonen, J., 2006. Long-term changes in lake ice cover in Finland. *Hydrology Research* 37(4–5), 347–363.
- Krichak, S.O., Alpert, P., 2005. Decadal trends in the east Atlantic–west Russia pattern and Mediterranean precipitation. *International Journal of Climatology* 25(2), 183–192.
- Krishnaswamy, S., Lal, D., Martin, J.M., Meybeck, M., 1971. Geochronology of lake sediments. *Earth and Planetary Science Letters* 11(1–5), 407–414.
- Küttel, M., Xoplaki, E., Gallego, D., Luterbacher, J., Garcia-Herrera, R., Allan, R., Barriendos, M., Jones, P.D., Wheeler, D., Wanner, H., 2010. The importance of ship log data: reconstructing North Atlantic, European and Mediterranean sea level pressure fields back to 1750. *Climate Dynamics* 34, 115–1128.

- Kushnir, Y., 1994. Interdecadal variations in North Atlantic sea surface temperature and associated atmospheric conditions. *Journal of Climate* 7, 141 – 157.
- Lau, N.C., 1997. Interactions between global SST anomalies and the midlatitude atmospheric circulation. *Bulletin of the American Meteorological Society* 78, 21–33.
- Leckebusch, G.C., Kapala, A., Mächel, H., Pinto, J.G., Reyers, M., 2008. Indices of the North Atlantic and Arctic Oscillations/Indices der Nordatlantischen und Arktischen Oszillation. *Promet (Meteorologische Fortbildung)*, special issue on the North Atlantic Oscillation (NAO) 3-4, 95–100.
- Lehner, F., Raible, C.C., Stocker, T.F., 2012. Testing the robustness of a precipitation proxy-based North Atlantic Oscillation reconstruction. *Quaternary Science Reviews* 45, 85–94.
- Leland, H.V., Berkas, W.R., 1998. Temporal variation in plankton assemblages and physicochemistry of Devils Lake, North Dakota. *Hydrobiologia* 377, 57–71.
- Leng, M.J., Marshall, J.D., 2004. Palaeoclimate interpretation of stable isotope data from lake sediment archives. *Quaternary Science Reviews* 23(7), 811–831.
- Leng, M.J., 2006. Isotopes in palaeoenvironmental research (Vol. 10). New York, Springer.
- Leng, M.J., Henderson, A.C.G., 2013. Recent advances in isotopes as palaeolimnological proxies. *Journal Palaeolimnology* 49, 481–496.
- Leppäranta, M., 2010. Modelling the formation and decay of lake ice. In *The Impact of Climate Change on European lakes*. George, G. (ed). Springer, Berlin, pp. 63–83.
- Le Treut, H., Somerville, R., Cubasch, U., Ding, Y., Mauritzen, C., Mokssit, A., Peterson, T., Prather, M., 2007. Historical overview of climate change. In *Climate Change 2007: The Physical Science Basis. Contribution of Working Group I to the Fourth Assessment Report of The Intergovernmental Panel on Climate Change*. Solomon, S., Qin, D., Manning, M., Chen, Z., Marquis, M., Averyt, K.B., Tignor, M., Miller, H.L. (eds). Cambridge University Press, Cambridge, United Kingdom, and New York, NY, USA.
- Lewis, W.M. Jr., 1983. A revised classification of lakes based on mixing. *Canadian Journal of Fisheries and Aquatic Sciences* 40, 1779–1787.
- Li, B., Nychka, D.W., Amman, C.M., 2010. The value of multiproxy reconstruction of past climate. *Journal of the American Statistical Association* 105, 883–895.
- Likens, G.E., Davis, M.B., 1975. Post-glacial history of Mirror Lake and its watershed in New Hampshire, USA: an initial report. *Verhandlungen Internationale Vereinigung*

- Limnologie 19, 982–993.
- Likens, G.E., 1985. An ecosystem approach to aquatic ecology. Mirror lake and its environment. Springer, New York.
- Liu, Z., Alexander, M., 2007. Atmospheric bridge, oceanic tunnel, and global climatic teleconnections. *Reviews of Geophysics* 45(2).
- Livingstone, D.A., 1957. On the sigmoid growth phase in the history of Linsley Pond. *American Journal of Science* 255, 364–373.
- Livingstone, D.M., 1999. Ice break-up on southern Lake Baikal and its relationship to local and regional air temperatures in Siberia and to the North Atlantic Oscillation. *Limnology and Oceanography* 44(6), 1486–1497.
- Livingstone, D.M., Adrian, R., 2009. Modeling the duration of intermittent ice cover on a lake for climate changes studies. *Limnology and Oceanography* 54(5), 1709–1722.
- López-Merino, L., López-Sáez, J.A., Sánchez, F.A., Pérez-Díaz, S., Shaad, D.A., Guerra Doce, E., 2009. Estudio polínico de una laguna endorreica en Almenara de Adaja (Valladolid, Meseta Norte): cambios ambientales y actividad humana durante los últimos 2800 años. *Revista Española de Micropaleontología* 41 (3), 333–348.
- López-Moreno, J.I., 2005. Recent variations of snowpack depth in the Central Spanish Pyrenees. *Arctic, Antarctic, and Alpine Research* 37 (2), 253–260.
- López-Moreno, J.I., Vicente-Serrano, S.M., Morán-Tejeda, E., Lorenzo-Lacruz, J., Zabalza, J., El Kenawy, A., Beniston, M., 2011a. Influence of Winter North Atlantic Oscillation Index (NAO) on Climate and Snow Accumulation in the Mediterranean Mountains. In *Hydrological, Socioeconomic and Ecological Impacts of the North Atlantic Oscillation in the Mediterranean Region*. Vicente-Serrano, S.M., Trigo, R.M. (eds). *Advances in Global Change Research* 46. Springer, New York, pp. 73–89.
- López-Moreno, J.I., Vicente-Serrano, S.M., Morán-Tejeda, E., Lorenzo-Lacruz, J., Kenawy, A., Beniston, M., 2011b. Effects of the North Atlantic Oscillation (NAO) on combined temperature and precipitation winter modes in the Mediterranean mountains: Observed relationships and projections for the 21st century. *Global and Planetary Change* 77(1), 62–76.
- López-Sáez, J.A., Abel-Schaad, D., Pérez-Díaz, S., Blanco-González, A., Alba-Sánchez, F., Dorado, M., Ruiz-Zapata, M.B., Gil-García, M.J., Gómez-González, C., Franco-Múgica, F., 2014. Vegetation history, climate and human impact in the Spanish Central System over the last 9,000 years. *Quaternary International* 353, 98–122.
- Lotter, A.F., Walker, I.R., Brooks, S.J., Hofmann, W., 1999. An intercontinental

- comparison of chironomid palaeotemperature inference models: Europe vs North America. *Quaternary Science Reviews* 18, 717–735.
- Luterbacher, J., Xoplaki, E., Dietrich, D., Jones, P.D., Davies, T.D., Portis, D., Gonzalez-Rouco, J.F., von Storch, H., Gyalistras, D., Casty, C., Wanner, H., 2002. Extending North Atlantic Oscillation Reconstructions Back to 1500. *Atmospheric Science Letters* 2, 114–124.
- Luterbacher, J., Brönnimann, S., Wanner, H., 2008. The history of scientific Research on the North Atlantic Oscillation/Historische Entwicklung der Nordatlantischen Oszillations-Erforschung. *Promet (Meteorologische Fortbildung)*, special issue on the North Atlantic Oscillation (NAO) 3-4, 79–88.
- Luterbacher, J., Werner, J.P., Smerdon, J.E., Fernández-Donado, L., González-Rouco, F.J., Barriopedro, D., Ljungqvist, F.C., Büntgen, U., Zorita, E., Wagner, S., Esper, J., McCarroll, D., Toreti, A., Frank, D., Jungclaus, J.H., Barriendos, M., Bertolin, C., Bothe, O., Brázil, R., Camuffo, D., 2016. European summer temperatures since Roman times. *Environmental Research Letters* 11, 024001.
- Mackay, A., Jones, V.J., Battarbee, R.W., 2003. Approaches to Holocene climate reconstruction using diatoms. In *Global Change in the Holocene*. Mackay, A., Battarbee, R., Birks, H.J.B., Oldfield, F. (eds). Arnold, London, pp. 294–309.
- Manly, B.F.J., 1997. Randomization, bootstrap and Monte Carlo methods in biology, 2nd edn. Chapman & Hall, London.
- Mann, M.E., 2007. Climate over the past two millennia. *Annual Review of Earth and Planetary Sciences* 35(1), 111.
- Margalef, R., 1983. Limnología. Ediciones Omega: Barcelona.
- Marshall, J., Kushnir, Y., Battisti, D., Chang, P., Czaja, A., Dickson, R., Hurrell, J., McCartney, M., Saravanan, R., Visbeck, M., 2001. North Atlantic climate variability: phenomena, impacts and mechanisms. *International Journal of Climatology* 21(15), 1863–1898.
- Marshall, J., Plumb, R.A., 2013. Atmosphere, ocean and climate dynamics: an introductory text (Vol. 21). Academic Press.
- Marticorena, B., Chatenet, B., Rajot, J.L., Traoré, S., Coulibaly, M., Diallo, A., Koné, I., Maman, A., NDiaye, T., Zakou, A., 2010. Temporal variability of mineral dust concentrations over West Africa: analyses of a pluriannual monitoring from the AMMA Sahelian Dust Transect. *Atmospheric Chemistry and Physics* 10, 8899–8915.
- Martín, M.L., Valero, F., Morata, A., Luna, M.Y., Pascual, A., Santos-Muñoz, D., 2010.

- Springtime coupled modes of regional wind in the Iberian Peninsula and large-scale variability patterns. *International Journal of Climatology* 31, 880–95.
- Martín-Chivelet, J., Muñoz-García, M.B., Lawrence Edwards, R., Turrero, M.M., Ortega, A.I., 2011. Land surface temperature changes in Northern Iberia since 4000 yr BP, based on $\delta^{13}\text{C}$ of speleothems. *Global and Planetary Change* 77, 1–12.
- Martín-Puertas, C., Valero-Garcés, B.L., Mata, M.P., González-Sampériz, P., Bao, R., Moreno, A., Stefanova, V., 2008. Arid and humid phases in southern Spain during the last 4000 years: the Zoñar Lake record, Córdoba. *The Holocene* 18, 907–921.
- Martín-Puertas, C., Jiménez-Espejo, F., Martínez-Ruiz, F., Nieto-Moreno, V., Rodrigo, M., Mata, M.P., Valero-Garcés, B.L., 2010. Late Holocene climate variability in the southwestern Mediterranean region: an integrated marine and terrestrial geochemical approach. *Climate of the Past* 6, 807–816.
- Martínez, F., 1999. Los bosques de P. Sylvestris del Sistema Central español. Distribución, Historia, Composición Florística y tipología. PhD Thesis, Universidad Complutense de Madrid. 701 pp.
- Martínez-Cortizas, A., Pontevedra-Pombal, X., García-Rodeja, E., Núvoa Muñoz, J.C., Shotyk, W., 1999. Mercury in a Spanish Peat Bog: archive of climate change and atmospheric metal deposition. *Science* 284, 939–942.
- Masqué, P., Fabres, J., Canals, M., Sánchez-Cabeza, J.A., Sánchez-Vidal, A., Cacho, I., Calafat, A.M., Bruach, J.M., 2003. Accumulation rates of major constituents of hemipelagic sediments in the deep Alboran Sea: A centennial perspective of sedimentary dynamics. *Marine Geology* 193, 207–233.
- McCarthy, G.D., Haigh, I.D., Hirschi, J.J.M., Grist, J.P., Smeed, D.A., 2015. Ocean impact on decadal Atlantic climate variability revealed by sea-level observations. *Nature* 521, 508–510.
- McGregor, S., Timmermann, A., Timm, O., 2010. A unified proxy for ENSO and PDO variability since 1650. *Climate of the Past* 6, 1–17.
- Medina-Elizalde, M., Burns, S.J., Lea, D.W., Asmerom, Y., Von Gunten, L., Polyak, V., Vuille, M., Karmalkar, A., 2010. High resolution stalagmite record from the Yucatán peninsula spanning the Maya terminal classic period. *Earth and Planetary Science Letters* 298, 255–262.
- Menut, L., Chiapello, I., Moulin, C., 2009. Predictability of mineral dust concentrations: The African Monsoon Multidisciplinary Analysis first short observation period forecasted with CHIMEREDUST. *Journal of Geophysical Research: Atmospheres* 114, D07202.

- Meyers, P.A., Lallier-Vergès, E., 1999. Lacustrine sedimentary organic matter records of Late Quaternary paleoclimates. *Journal of Paleolimnology* 21, 345–372.
- Meyers, P.A., Teranes, J.L., 2001. Sediment organic matter. In *Tracking Environmental Changes Using Lake Sediment*, Vol. 2: Physical and Geochemical Methods. Last, W.M., Smol, J.P. (eds). Dordrecht, Kluwer Academic, pp. 239–270.
- Middleton, N.J., Goudie, A.S., 2001. Saharan dust: sources and trajectories. *Transactions of the Institute of British Geographers* 26(2), 165–181.
- Mix, A.C., 1987. The oxygen-isotope record of glaciation. In *North America and Adjacent Oceans During the Last Deglaciation*. The Geology of North America, vol. K-3. Ruddiman, W.F., Wright Jr., H.E. (eds). Geological Society of America, Boulder, pp. 111–135.
- Mladenov, N., Sommaruga, R., Morales-Baquero, R., Laurion, I., Camarero, L., Dieguez, M.C., Camacho, A., Delgado, A., Torres, O., Chen, Z., Felip, M., Reche, I., 2011. Dust inputs and bacteria influence dissolved organic matter in clear alpine lakes. *Nature Communications* 2, 405.
- Moffa-Sánchez, P., Born, A., Hall, I.R., Thornalley, D.J., Barker, S., 2014. Solar forcing of North Atlantic surface temperature and salinity over the past millennium. *Nature Geoscience* 7(4), 275–278.
- Molfino, B., Kipp, N.G., Morley, J.J., 1982. Comparison of foraminiferal, coccolithophorid and Radiolarian paleotemperature equations: assemblage coherency and estimate concordancy. *Quaternary Research* 17, 279–313.
- Molinaroli, E., 1996. Mineralogical characterization of Saharan dust with a view to its final destination in Mediterranean sediments. In *The impact of desert dust across the Mediterranean*. Guerzoni, S., Chester, R. (eds). Springer Netherlands, pp.153–162.
- Mooney, C.Z., Duval, R.D., 1993. Bootstrapping: a non-parametric approach to statistical inference. Sage, Newbury Park.
- Moore, D.M., Reynolds, R.C., Jr., 1997. *X-ray Diffraction and the Identification and Analysis of Clay Minerals*. Oxford University Press, Oxford, 378 pp.
- Moore, G.W.K., Pickart, R.S., Renfrew, I.A., 2011. Complexities in the climate of the subpolar North Atlantic: a case study from the winter of 2007. *Quarterly Journal of the Royal Meteorological Society* 137, 757–767.
- Moore, G.W.K., Renfrew, I.A., 2012. Cold European winters: interplay between the NAO and the East Atlantic mode. *Atmospheric Science Letters* 13, 1–8.

- Moore, G.W.K., Renfrew, I.A., Pickart, R., 2013. Multi-decadal mobility of the North Atlantic Oscillation. *Journal of Climate* 26(8), 2453–2466.
- Morales-Baquero, R., Pulido-Villena, E., Reche, I., 2006. Atmospheric inputs of phosphorus and nitrogen to the southwest Mediterranean region: Biogeochemical responses of high mountain lakes. *Limnology and Oceanography* 51(2), 830–837.
- Morellón, M., Valero-Garcés, B., Vegas-Vilarrúbia, T., González-Sampériz, P., Romero, Ó., Delgado-Huertas, A., Mata, P., Moreno, A., Rico, M., Corella, J.P., 2009. Lateglacial and Holocene palaeohydrology in the western Mediterranean region: the Lake Estanya record (NE Spain). *Quaternary Science Reviews* 28, 2582–2599.
- Morellón, M., Valero-Garcés, B., González-Sampériz, P., Vegas-Vilarrúbia, T., Rubio, E., Rieradevall, M., Delgado-Huertas, A., Mata, P., Romero, Ó., Engstrom, D.R., López-Vicente, M., Navas, A., Soto, J., 2011. Climate and human signatures during the medieval warm period and the little ice age in the Spanish pre-Pyrenees: the Lake Estanya record. *Journal of Paleolimnology* 46(3), 423–452.
- Morellón, M., Pérez-Sanz, A., Corella, J.P., Büntgen, U., Catalán, J., González-Sampériz, P., González-Trueba, J.J., López-Sáez, J.A., Moreno, A., Pla-Rabes, S., Saz-Sánchez, M.A., Scussolini, P., Serrano, E., Steinhilbe, F., Stefanova, V., Vegas-Vilarrúbia, T., Valero-Garcés, B., 2012. A multi-proxy perspective on millennium-long climate variability in the Southern Pyrenees. *Climate of the Past* 8, 683–700.
- Moreno, A., Valero-Garcés, B.L., González-Sampériz, P., Rico, M., 2008. Flood response to rainfall variability during the last 2000 years inferred from the Taravilla Lake record (Central Iberian Range, Spain). *Journal of Paleolimnology* 40, 943–961.
- Moreno, A., Santoro, C.M., Latorre, C., 2009. Climate change and human occupation in the northernmost Chilean Altiplano over the last ca. 11 500 cal. a BP. *Journal of Quaternary Science*, 24(4), 373–382.
- Moreno, A., López-Merino, L., Leira, M., Marco Barba, J., González-Sampériz, P., Valero-Garcés, B.L., López-Sáez, J.A., Santos, L., Mata, P., Ito, E., 2011. Revealing the last 13,500 years of environmental history from the multiproxy record of a mountain lake (Lago Enol, N Iberian Peninsula). *Journal of Paleolimnology* 46(3), 327–349.
- Moreno, A., Pérez, A., Frigola, J., Nieto-Moreno, V., Rodrigo-Gámiz, M., González-Sampériz, P., Morellón, M., Martín-Puertas, C., Corella, J. P., Belmonte, A., Sancho, C., Cacho, I., Herrera, G., Canals, M., Jiménez-Espejo, F., Martínez-Ruiz, F., Vegas, T., Valero-Garcés, B.L., 2012. The Medieval Climate Anomaly in the Iberian Peninsula reconstructed from marine and lake records, *Quaternary Science Reviews* 43, 16–32.

- Moulin, C., Lambert, C.E., Dulac, F., Dayan, U., 1997. Control of atmospheric export of dust from north Africa by the north Atlantic Oscillation. *Nature* 387, 691–694.
- Müller, W.A., Frankignoul, C., Chouaib, N., 2008. Observed decadal tropical Pacific–North Atlantic teleconnections. *Geophysical Research Letters* 35, L24810.
- Næs, T., Isaksson, T., Fearn, T., Davies, T., 2002. A user-friendly guide to multivariate calibration and classification. NIR Publications, Chichester.
- Nesje, A., Dahl, S.O., Andersson, C., Matthews, J.A., 2000. The lacustrine sedimentary sequence in Sygnekskardvatnet, western Norway: a continuous, high-resolution record of the Jostedalsbreen ice cap during the Holocene. *Quaternary Science Reviews* 19, 1047–1065.
- Nesje, A., Dahl, S.O., Matthews, J.A., Berresford, M.S., 2001. A ~ 4500-yr record of river floods obtained from a sediment core in Lake Atnsjoen, eastern Norway. *Journal of Paleolimnology* 25, 329–342.
- Nichols, G., 2009. Sedimentology and stratigraphy. John Wiley and Sons.
- Nieto-Moreno, V., Martínez-Ruiz, F., Giralt, S., Jiménez -Espejo, F., Gallego-Torres, D., Rodrigo-Gámiz, M., García -Orellana, J., Ortega-Huertas, M., de Lange, G.J., 2011. Tracking climate variability in the Western Mediterranean during the Late Holocene: a multiproxy approach. *Climate of the Past* 7, 1395–1414.
- Nieto-Moreno, V., Martínez-Ruiz, F., Giralt, S., Gallego-Torres, D., García-Orellana, J., Masqué, P., Ortega-Huertas, M., 2013. Climate imprints during the 'Medieval Climate Anomaly' and the 'Little Ice Age' in marine records from the Alboran Sea basin. *Holocene* 23(9), 1227–1237.
- Ninyerola, M., Pons, X., Roure, J.M., 2005. Atlas Climático Digital de la Península Ibérica. Metodología y aplicaciones en bioclimatología y geobotánica. Universidad Autónoma de Barcelona, Bellaterra.
- Ojala, A.E.K., Alenius, T., 2005. 10,000 years of interannual sedimentation recorded in the Lake Nautajarvi (Finland) clastic-organic varves. *Palaeogeography, Palaeoclimatology, Palaeoecology* 219, 285–302.
- Oksanen, J., Blanchet, F.G., Kindt, R., Legendre, P., Minchin, P.R., O'Hara, R.B., Simpson, G.L., Solymos, P., Henry, M., Stevens, H., Wagner, H., 2013. Vegan: community ecology package. R package version 2.0-10. <http://CRAN.Rproject.org/package=vegan>.
- Oldfield, F., 1977. Lakes and their drainage basins as units of sediment-based ecological study. *Progress in Physical Geography* 1, 460–504.

- Olsen J., Anderson N.J., Knudsen, M.F., 2012. Variability of the North Atlantic Oscillation over the past 5,200 years. *Nature Geosciences* 5, 808–812.
- Ortega, P., Lehner, F., Swingedouw, D., Masson-Delmotte, V., Raible, C.C., Casado, M., Yiou, P., 2015. A model-tested North Atlantic Oscillation reconstruction for the past millennium. *Nature*, 523(7558), 71–74.
- O'Sullivan, P., Reynolds, C.S., 2008. The lakes handbook: limnology and limnetic ecology (Vol. 1). John Wiley & Sons.
- Palacios, D., de Andrés, N., Luengo, E., 2003. Distribution and effectiveness of nivation in Mediterranean mountains: Peñalara (Spain). *Geomorphology* 54, 157–178.
- Palacios, D., Marcos, J., Vázquez-Solem, L., 2011. Last Glacial Maximum and deglaciation of Sierra de Gredos, central Iberian Peninsula. *Quaternary International* 233, 16–26.
- Palacios, D., Andrés, N., Marcos, J., Vázquez-Solem, L., 2012. Maximum glacial advance and deglaciation of the Pinar Valley (Sierra de Gredos, Central Spain) and its significance in the Mediterranean context. *Geormorphology* 177–178, 51–61.
- Palecki, M.A., Barry, R.G., 1986. Freeze-up and break-up of lakes as an index of temperature changes during the transition seasons: a case study for Finland. *Journal of Climate and Applied Meteorology* 25 (7), 893–902.
- Paredes, D., Trigo, R.M., Garcia-Herrera, R., Trigo, I.F., 2006. Understanding precipitation changes in Iberia in early spring: weather typing and storm-tracking approaches. *Journal of Hydrometeorology* 7, 101–13.
- Park, J., Byrne, R., Böhnel, H., Garza, R.M., Conserva, M., 2010. Holocene climate change and human impact, central Mexico: a record based on maar lake pollen and sediment chemistry. *Quaternary Science Reviews* 29, 618–632.
- Parker, D., Folland, C., Scaife, A., Knight, J., Colman, A., Baines, P., Dong, B., 2007. Decadal to multidecadal variability and the climate change background. *Journal of Geophysical Research: Atmospheres* 112, D18115.
- Parnell, A.C., Sweeney, J., Doan, T.K., Salter-Townshend, M., Allen, J.R., Huntley, B., Haslett, J., 2015. Bayesian inference for palaeoclimate with time uncertainty and stochastic volatility. *Journal of the Royal Statistical Society: Series C (Applied Statistics)* 64(1), 115–138.
- Parris, A.S., Bierman, P.R., Noren, A.J., Prins, M.A., Lini, A., 2010. Holocene paleostorms identified by particle size signatures in lake sediments from northeastern United State. *Journal of Paleolimnology* 43, 29–49.

- Pedraza, J., 1989. La morfogénesis del Sistema Central y su relación con la morfología granítica. *Cadernos do Laboratorio Xeolóxico de Laxe* 13, 31–46.
- Pedraza, J., 1994a. Los modelos genético-evolutivos del Sistema Central Español: Implicaciones morfotectónicas. *Cadernos do Laboratorio Xeolóxico de Laxe* 13, 91–118.
- Pedraza, J., 1994b. Geomorfología del Sistema Central. In *Geomorfología de España*. Gutiérrez-Elorza, M. (ed). Editorial Rueda, Madrid, pp. 63–100.
- Pedraza, J., Carrasco, R.M., 2006. El glaciarismo Pleistoceno del Sistema Central. *Revista de la Asociación Española para la Enseñanza de las Ciencias de la Tierra* 13, 278–288.
- Pelto, M.S., 2008. Impact of Climate Change on North Cascade Alpine Glaciers, and Alpine Runoff. *Northwest Science* 82, 65–75.
- Pennington, W., Haworth, E.Y., Bonny, A.P., Lishman, J.P., 1972. Lake sediments in northern Scotland. *Philosophical Transactions of the Royal Society B* 264, 191–294.
- Pérez-Sanz, A., González-Sampériz, P., Moreno, A., Valero-Garcés, B., Gil-Romera, G., Rieradevall, M., Tarrats, P., Lasheras-Álvarez, L., Morellón, M., Belmonte, A., Sancho, C., Sevilla-Callejo, M., Navas, A., 2013. Holocene climate variability, vegetation dynamics and fire regime in the central Pyrenees: the Basa de la Mora sequence (NE Spain). *Quaternary Science Reviews* 73, 149–169.
- Perlitz, J., Graf, H.F., Voss, R., 2000. The leading variability mode of the coupled troposphere–stratosphere winter circulation in different climate regimes. *Journal of Geophysical Research* 105, 6915–6926.
- Petzoldt, T., Rinke, K., 2007. Simecol: an object-oriented framework for ecological modeling in R. *Journal of Statistical and Software* 22(9), 1–31. <http://www.jstatsoft.org/v22/i09/>.
- Pfahl, S., Wernli, H., 2012. Quantifying the relevance of atmospheric blocking for co-located temperature extremes in the Northern Hemisphere on (sub-) daily time scales. *Geophysical Research Letters* 39(12).
- Philander, S.G.H., 1983. El Niño southern oscillation phenomena. *Nature* 302, 295–301.
- Pinto, J.G., Zacharias, S., Fink, A.H., Leckebusch, G.C., Ulbrich, U., 2009. Factors contributing to the development of extreme North Atlantic cyclones and their relationship with the NAO. *Climate Dynamics* 32, 711–737.
- Pinto, J.G., Raible, C.C., 2012. Past and recent changes in the North Atlantic Oscillation. *Wiley Interdisciplinary Reviews: Climate Change* 3, 79–90.

- Pla, S., Catalan, J., 2005. Chrysophyte cysts from lake sediments reveal the submillennial winter/spring climate variability in the northwestern Mediterranean region throughout the Holocene. *Climate Dynamics* 24, 263–278.
- Pla-Rabes, S., Catalan, J., 2011. Deciphering chrysophyte responses to climate seasonality. *Journal of Paleolimnology* 46, 139–150.
- Plummer, M., 2003. JAGS: a program for analysis of Bayesian graphical models using Gibbs sampling. In *Proceedings of the 3rd International Workshop on Distributed Statistical Computing*.
- Polissar, P., Abbott, M.B., Wolfe, A.P., Bezada, M., Rull, V., Bradley, R.S., 2005. Solar modulation of Little Ice Age climate in the Tropical Andes. *Proceedings of the National Academy of Sciences US.A* 103(24), 8937–8942.
- Portis, D.H., Walsh, J.E., Hamly, M.E., Lamb, P.J., 2001. Seasonality of the North Atlantic Oscillation. *Journal of Climate* 14(9), 2069–2078.
- Powers, L.A., Werne, J.P., Sinninghe Damsté, J.S., Hopmans, E.C., Schouten, S., 2010. Applicability and calibration of the TEX86 paleothermometer in lakes. *Organic Geochemistry* 41, 404–413.
- Powers, L.A., Johnson, T.C., Werne, J.P., Castañeda, I.S., Hopmans, E.C., Damsté, J.S.S., Schouten, S., 2011. Organic geochemical records of environmental variability in Lake Malawi during the last 700 years, Part I: The TEX 86 temperature record. *Palaeogeography, Palaeoclimatology, Palaeoecology* 303(1), 133–39.
- Prebble, M., Schulmeister, J., 2002. An analysis of phytolith assemblages for the quantitative reconstruction of late Quaternary environments of the Lower Taieri Plain, Otago, South Island, New Zealand. II. Paleoenvironmental reconstruction. *Journal of Paleolimnology* 27, 415–427.
- Prentice, I.C., Guiot, J., Huntley, B., Jolly, D., Cheddadi, R., 1996. Reconstructing biomes from palaeoecological data: a general method and its application to European pollen data at 0 and 6 ka. *Climate Dynamics* 12, 185–194.
- Prospero, J.M., Carlson, T., 1980. Saharan air outbreaks over the Tropical North Atlantic. *Pure and Applied Geophysics* 119, 677–691.
- Prospero, J.M., 1981. Arid regions as sources of mineral aerosols in the marine atmosphere. *Geological Society of America, Special paper* 186, 71–86.
- Prospero, J.M., Nees, R.T., 1986. Impact of the North African Drought and El-Niño on mineral dust in the Barbados trade winds. *Nature* 320(6064), 735–738.

- Prospero, J.M., Ginoux, P., Torres, O., Nicholson, S.E., Gill, T.E., 2002. Environmental characterization of global sources of atmospheric soil dust identified with the Nimbus 7 Total Ozone Mapping Spectrometer (TOMS) absorbing aerosol product. *Reviews of Geophysics* 40, 1–31.
- Psenner, R., 1999. Living in a dusty world: airborne dust as a key factor for alpine lakes. *Water, Air and Soil Pollution* 112, 217–227.
- Pulido, F., Sanz, R., Abel-Schaad, D., Ezquerra, F.J., Gil, A., González, G., Hernández, A., Moreno, G., Pérez, J.J., Vázquez, F., 2007. Los bosques de Extremadura. Evolución, ecología y conservación. Junta de Extremadura, Mérida, p. 343.
- Pulido-Villena, E., Reche, I., Morales-Baquero, R., 2006. Significance of atmospheric inputs of calcium over the southwestern Mediterranean region: High mountain lakes as tools for detection. *Global Biogeochemical Cycles* 20(2).
- Pulido-Villena, E., Wagener, T., Guieu, C., 2008. Bacterial response to dust pulses in the western Mediterranean: Implications for carbon cycling in the oligotrophic ocean. *Global Biogeochemical Cycles* 22(1).
- Pye, K., 1987. Aeolian Dust and Dust Deposits. Academic Press, San Diego, USA.
- R Core Team, 2015. R: A Language and Environment for Statistical Computing. R Foundation for Statistical Computing, Vienna, Austria. <http://www.R-project.org>.
- Ramos, A.M., Lorenzo, M.N., Gimeno, L., 2010. Compatibility between modes of low-frequency variability and circulation types: a case study of the northwest Iberian Peninsula. *Journal of Geophysical Research: Atmospheres* 115, D02113.
- Ravelo, A.C., Hillaire-Marcel, C., 2007. The use of oxygen and carbon isotopes of foraminifera in paleoceanography. In Proxies in Late Cenozoic Paleoceanography. Hillaire-Marcel, C., de Vernal, A. (eds). Elsevier, Amsterdam, pp. 735–764.
- Reche, I., Ortega-Retuerta, E., Romera, O., Pulido-Villena, E., Morales-Baquero, R., Casamayor, E.O., 2009. Effect of Saharan dust inputs on bacterial activity and community composition in Mediterranean lakes and reservoirs. *Limnology and Oceanography* 54, 869–879.
- Reimer, P.J., Bard, E., Bayliss, A., Beck, J.W., Blackwell, P.G., Ramsey, C.B., Buck, C.E., Cheng, H., Edwards, R.L., Friedrich, M., Grootes, P.M., 2013. INTCAL13 and MARINE13 radiocarbon age calibration curves 0–50,000 years cal BP. *Radiocarbon* 55, 1869–1887.
- Richter, T.O., Van der Gaast, S., Koster, B., Vaars, A., Gieles, R., de Stigter, H.C., De Haas, H., van Weering, T.C., 2006. The Avaatech XRF Core Scanner: technical

- description and applications to NE Atlantic sediments. Geological Society, London, Special Publications 267(1), 39–50.
- Riera, S., Wansard, R., Julià, R., 2004. 2000-year environmental history of a karstic lake in the Mediterranean Pre-Pyrenees: the Estanya Lakes (Spain). *Catena* 55, 293–324.
- Rivas-Martínez, S., Belmonte, D., Cantó, P., Fernández-González, F., Fuente, V., Moreno, J.M., Sánchez-Mata, D., Sancho, L.G., 1987. Piornales, enebrales y pinares oromediterráneos (*Pino-Cytision oromediterranei*) en el Sistema Central. *Lazaroa* 7, 93–124.
- Robertson, I., Lucy, D., Baxter, L., Pollard, A.M., Aykroyd, R.G., Barker, A.C., Carter, A.H.C., Switsur, V.R., Waterhouse, J.S., 1999. A kernel-based Bayesian approach to climatic reconstruction. *Holocene* 9, 495–500.
- Rodrigues, T., Grimalt, J.O., Abrantes, F.G., Flores, J.A., Lebreiro, S.M., 2009. Holocene interdependences of changes in sea surface temperature, productivity, and fluvial inputs in the Iberian continental shelf (Tagus mud patch). *Geochemistry, Geophysics, Geosystems* 10(7).
- Rodríguez, S., Querol, X., Alastuey, A., Kallos, G., Kakaliagou, O., 2001. Saharan dust contributions to PM10 and TSP levels in Southern and Eastern Spain. *Atmospheric Environment* 35, 2433–2447.
- Rodríguez, S., Cuevas, E., Prospero, J.M., Alastuey, A., Querol, X., López-Solano, J., García, M.I., Alonso-Pérez, S., 2015. Modulation of Saharan dust export by the North African dipole. *Atmospheric Chemistry and Physics* 15(13), 7471–7486.
- Rodríguez-Puebla, C., Encinas, A.H., Nieto, S., Garmendia, J., 1998. Spatial and temporal patterns of annual precipitation variability over the Iberian Peninsula. *International Journal of Climatology* 18, 299–316.
- Rodríguez-Puebla, C., García-Casado, L.A., Frías, M.D., 2001. Trend and Interannual Variations in Air Temperature over Iberian Peninsula, In 13th Symposium on Global Change and Climate Variations, 13–17 January 2002, Orlando, Florida. American Meteorological Society, Boston, USA. 106–108.
- Romero, R., Guijarro, J.A., Ramis, C., Alonso, S., 1998. A 30-year (1864–1993) daily rainfall data base for the Spanish Mediterranean region: First exploratory study. *International Journal of Climatology* 18, 541–560.
- Ropelewski, C.F., Halpert, M.S., 1987. North American precipitation and temperature patterns associated with the El Niño/Southern Oscillation (ENSO). *Monthly Weather Review* 114(12), 2352–2362.

- Ropelewski, C.F., Jones, P.D. 1987. An extension of the Tahiti–Darwin Southern Oscillation Index. *Monthly Weather Review* 115, 2161–2165.
- Rosenthal, Y., 2007. Elemental proxies for reconstructing Cenozoic seawater paleotemperatures from calcareous fossils. In *Proxies in Late Cenozoic Paleoceanography*. Hillaire-Marcel, C., de Vernal, A. (eds). Elsevier, Amsterdam, pp. 765–797.
- Rothwell, R.G., 1998. The smear slide method. In *Minerals and Mineraloids in Marine Sediments*. Springer, Netherlands, pp. 21–24.
- Rothwell, R.G., Croudace, I., 2014. *Micro-XRF Studies of Sediment Cores: A Non-destructive Tool for the Environmental Sciences*. Springer, Berlin.
- Ruibo, L., Leppäranta, M., Cheng, B., Heil, P., Li, Z., 2012. Changes in ice-season characteristics of a European Arctic lake from 1964 to 2008. *Climatic Change* 115, 725–739.
- Rull, V., Stansell, N.D., Montoya, E., Bezada, M., Abbott, M.B., 2010. Palynological signal of the Younger Dryas in the tropical Venezuelan Andes. *Quaternary Science Reviews* 29, 3045–3056.
- Salabarnada, A., 2011. Recent Depositional evolution of a high altitude alpine lake: Marboré Lake (Ordesa - Monte Perdido National Park, Spanish Pyrenees). MSc Thesis, UIMP University, 42 pp.
- Salmaso, N., 2012. Influence of atmospheric modes of variability on a deep lake south of the Alps. *Climate Research* 51(2), 125.
- Sánchez-Cabeza, J.A., Masqué, P., Ani-Ragolta, I., 1998. ^{210}Pb and ^{210}Po analysis in sediments and soils by microwave acid digestion. *Journal of Radioanalytical and Nuclear Chemistry* 227 (1–2), 19–22.
- Sánchez-López G., Hernández A., Pla-Rabes, S., Toro M., Granados I., Sigró J., Trigo R.M., Rubio-Inglés M.J., Camarero L., Valero-Garcés B., Giralt. S., 2015. The effects of the NAO on the ice phenology of Spanish alpine lakes. *Climatic Change* 130, 101–113.
- Sánchez-Mata, D., 1989. Flora y vegetación del Macizo Oriental de la Sierra de Gredos (Ávila). Institución Gran Duque de Alba, Ávila.
- Scaife, A.A., Knight, J.R., Vallis, G., Folland, C.K., 2005. A stratospheric influence on the winter NAO and north Atlantic surface climate. *Geophysical Research Letters* 32, L18715.

- Schlesinger, M.E., Ramankutty, N., 1994. An oscillation in the global climate system of period 65–70 years. *Nature* 367, 723–726.
- Schneider, T., Bischoff, T., Haug, G.H., 2014. Migrations and dynamics of the intertropical convergence zone. *Nature* 513(7516), 45–53.
- Schwalb, A., 2003. Lacustrine ostracodes as stable isotope recorders of late-glacial and Holocene environmental dynamics and climate. *Journal Paleolimnology* 29, 265–351.
- Seierstad, I.A., Stephenson, D.B., Kvamsto, N.G., 2007. How useful are teleconnection patterns for explaining variability in extratropical storminess? *Tellus A* 59, 170–181.
- Serrano, A., García A.J., Mateos, V.L., Cancillo, M.L., Garrido, J., 1999. Monthly modes of variation of precipitation over the Iberian Peninsula. *Journal of Climate* 12, 2894–2919.
- Shabbar, A., Huang, J.P., Higuchi, K., 2001. The relationship between the wintertime North Atlantic Oscillation and blocking episodes in the North Atlantic. *International Journal of Climatology* 21, 355–369.
- Sharma, S., Magnuson, J.M., 2014. Oscillatory dynamics do not mask linear trend in the timing of ice breakup for Northern Hemisphere lakes from 1855 to 2004. *Climatic Change* 124, 835–847.
- Shemesh, A., Peteet, D., 1998. Oxygen isotopes in fresh water biogenic opal—northeastern U.S. Allerød-Younger Dryas temperature shift. *Geophysical Research Letters* 25, 1935–1938.
- Shindell, D.T., Schmidt, G.A., Mann, M.E., Rind, D., Waple, A., 2001. Solar forcing of regional climate change during the Maunder Minimum. *Science* 294, 2149–2152.
- Siedler, G., Griffies, S.M., Gould, J., Church, J.A., 2013. Ocean circulation and climate: a 21st century perspective (Vol. 103). Academic Press.
- Sigl, M., Winstrup, M., McConnell, J.R., Welten, K.C., Plunkett, G., Ludlow, F., Büntgen, U., Caffee, M., Chellman, N., Dahl-Jensen, D., Fischer, H., Kipfstuhl, S., Kostick, C., Maselli, O.J., Mekhaldi, F., Mulvaney, R., Muscheler, R., Pasteris, D.R., Pilcher, J.R., Salzer, M., Schüpbach, S., Steffensen, J.P., Vinther, B.M., Woodruff, T.E., 2015. Timing and climate forcing of volcanic eruptions for the past 2,500 years. *Nature* 523, 543–549.
- Sillmann, J., Croci-Maspoli, M., 2009. Present and future atmospheric blocking and its impact on European mean and extreme climate. *Geophysical Research Letters* 36, L10702.

- Sillmann, J., Croci-Maspoli, M., Kallache, M., Katz, R.W., 2011. Extreme cold winter temperatures in Europe under the influence of North Atlantic atmospheric blocking. *Journal of Climate* 24(22), 5899–5913.
- Simpson, G.L., Birks, H.J.B., 2012. Statistical Learning in Palaeolimnology. In Tracking environmental change using lake sediments. Birks, H.J.B., Lotter, A.F., Juggins, S., Smol, J.P. (eds). Springer Netherlands, pp. 249–339.
- Singer, A., Norrish, K., 1974. Pedogenic palygorskite occurrences in Australia. *American Mineralogist* 59, 508–517.
- Singer, A., Galan, E., 1984. Palygorskite–Sepiolite. Occurrences, Genesis and Uses. *Developments in Sedimentology*. Elsevier, Amsterdam.
- Smol, J.P., Cumming, B.F., 2000. Tracking long-term changes in climate using algal indicators in lake sediments. *Journal of Phycology* 36, 986–1011.
- Smol, J.P., Birks, H.J.B., Last, W.M., 2001. Using biology to study long-term environmental change. In *Tracking Environmental Change Using Lake Sediments: Terrestrial, Algal, and Siliceous Indicators*. Smol, J.P., Birks, H.J.B., Last, W.M. (eds). Kluwer Academic, Dordrecht, The Netherlands, Vol. 3, pp.1–4.
- Smol, J.P., 2008. Pollution of Lakes and Rivers: a paleoenvironmental perspective. Blackwell, Oxford, 383 pp.
- Smol, J.P., Stoermer, E.F., 2010. The Diatoms: Applications for the Environmental and Earth Sciences. Cambridge University Press, Cambridge, 667 pp.
- Smol, J.P., Birks, H.J.B., Lotter, A.F., Juggins, S., 2012. The march towards the quantitative analysis of palaeolimnological data. In Tracking environmental change using lake sediments. Birks, H.J.B., Lotter, A.F., Juggins, S., Smol, J.P. (eds). Springer Netherlands, pp. 3–17.
- Sousa, P.M., Barriopedro, D., Trigo, R.M., Ramos, A.M., Nieto, R., Gimeno, L., Turkman K.F., Liberato, M.L.R., 2015. Impact of Euro-Atlantic blocking patterns in Iberia precipitation using a novel high resolution dataset. *Climate Dynamics* 1–19.
- Spangehl, T., Cubasch, U., Raible, C.C., Schimanke, S., Körper, J., Hofer, D., 2010. Transient climate simulations from the Maunder Minimum to present day: role of the stratosphere. *Journal of Geophysical Research* 115, D00I10.
- Šporka, F., Livingstone, D.M., Stuchlík, E., Turek, J., Galas, J., 2006. Water temperatures and ice cover in lakes of the Tatra Mountains. *Biologia* 61(18), 77–90.
- Steinhilber, F., Beer, J., Fröhlich, C., 2009. Total solar irradiance during the Holocene.

- Geophysical Research Letters 36(19), L19704.
- Stephenson, D.B., Wanner, H., Brönnimann, S., Luterbacher, J., 2003. The North Atlantic oscillation. Climatic significance and environmental impact. Geophysical Monograph Series 134, 37–50.
- Stephenson, D.B., Pavan, V., Collins, M., Junge, M.M., Quadrelli, R., 2006. North Atlantic Oscillation response to transient greenhouse gas forcing and the impact on European winter climate: a CMIP2 multi-model assessment. Climate Dynamics 27(4), 401–420.
- Stine, R., 1990. An introduction to bootstrap methods: examples and ideas. In Modern methods of data analysis. Fox, J., Long, J.S. (eds). Sage, Newbury Park, pp. 325–373.
- Stoffel, M., Khodri, M., Corona, C., Guillet, S., Poulain, V., Bekki, S., Guiot, J., Luckman, B.H., Oppenheimer, C., Lebas, N., Beniston, M., Masson-Delmotte, V. 2015. Estimates of volcanic-induced cooling in the Northern Hemisphere over the past 1,500 years. Nature Geoscience 8, 784–788.
- Straile, D., Livingstone, D.M., Weyhenmeyer, G.A., George, D.G., 2003. The response of freshwater ecosystems to climate variability associated with the North Atlantic Oscillation. In The North Atlantic Oscillation, Climatic Significance and Environmental Impact. Hurrell, J.W., Kushir, Y., Ottersen, G., Visbeck, M. (eds). Geophysical Monograph 134. American Geophysical Union, Washington, pp. 263–279.
- Stuiver, M., Reimer, P.J., 1993. Extended C-14 data base and revised Calib 3.0 C-14 age calibration program. Radiocarbon 35, 215–230.
- Sutton, R.T., Hodson, D.L.R., 2005. Atlantic ocean forcing of North American and European summer climate. Science 309, 115–118.
- Swart, P.K., Dodge, R.E., Hudson, H.J., 1996. A 240-year stable oxygen and carbon isotopic record in a coral from South Florida: implications for the prediction of precipitation in southern Florida. Palaios 11, 362–375.
- Talbot, M.R., Allen, P.A., 1996. Lakes. In Sedimentary Environments. Reading, H.G. (ed). Blackwell, Oxford, pp. 83–124.
- Talley L.D., Pickard G.L., Emery W.J., Swift J.H., 2011. Descriptive Physical Oceanography: An Introduction (Sixth Edition). Elsevier, Boston, 560 pp.
- Talley, L.D., 2013. Closure of the global overturning circulation through the Indian, Pacific, and Southern Oceans: Schematics and transports. Oceanography 26, 80– 97.

- Teisserenc de Bort., 1883. Etude sur l'hiver de 1879–80 et recherches sur l'influence de la position des grands centres d'action de l'atmosphère dans les hivers anormaux. Ann de la Soc Météor de France 31, 70–79.
- ter Braak, C.J.F., 1995. Non-linear methods for multivariate statistical calibration and their use in palaeoecology: a comparison of inverse (k-nearest neighbours, partial least squares and weighted averaging partial least squares) and classical approaches. Chemometrics and Intelligent Laboratory Systems 28, 165–180.
- Thompson, D.W.J., Wallace, J.M., 2000. Annular modes in the extratropical circulation. Part I: Month-to-month variability. Journal of Climate 13, 1000–1016.
- Thompson, R., Ventura, M., Camarero, L., 2009. On the climate and weather of mountain and sub-arctic lakes in Europe and their susceptibility to future climate change. Freshwater Biology 54, 2433–2451.
- Tierney, J.E., Russell, J.M., Huang, Y., Damsté, J.S.S., Hopmans, E.C., Cohen, A.S., 2008. Northern hemisphere controls on tropical southeast African climate during the past 60,000 years. Science 322(5899), 252–255.
- Tierney, J.E., Mayes, M.T., Meyer, N., Johnson, C., Swarzenski, P.W., Cohen, A.S., Russell, J.M., 2010. Late-twentieth-century warming in Lake Tanganyika unprecedented since AD 500. Nature Geoscience 3(6), 422–425.
- Timmermann, A., Latif, M., Voss, R., Grötzner, A., 1998. North Atlantic interdecadal variability: a coupled air–sea mode. Journal of Climate 11, 1906–1931.
- Toivonen, H., Manilla, H., Korhola, A., Olander, H., 2001. Applying Bayesian statistics to organism-based environmental reconstruction. Ecological Applications 11(2), 618–630.
- Toro M., Granados, I., 2000. Las lagunas de la Sierra de Gredos. Monografías de la Red de Espacios Naturales de Castilla y León. Ed. Junta de Castilla y León, Valladolid, p.42.
- Toro, M., Granados, I., 2002. Restoration of a small high mountain lake after recent tourist impact: the importance of limnological monitoring and palaeolimnology. Water, Air, and Soil Pollution: Focus 2, 295–310.
- Toro, M., Granados, I., Robles, S., Montes, C., 2006. High mountain lakes of Central Range (Iberian Peninsula): Regional limnology and environmental changes. Limnetica 25(1-2), 217–252.
- Torres-Padrón, M.E., Gelado-Caballero, M.D., Collado-Sánchez, C., Siruela-Matos, V.F., Cardona-Castellano, P.J., Hernández-Brito, J.J., 2002. Variability of dust inputs

- to the CANIGO zone. *Deep-Sea Research II* 49, 3455–3464.
- Trenberth, K.E., Branstator, G.W., Karoly, D., Kumar, A., Lau, N.C., Ropelewski, C., 1998. Progress during TOGA in understanding and modeling global teleconnections associated with tropical sea surface temperatures. *Journal of Geophysical Research* 103, 14291–14324.
- Trenberth, K.E., Caron, J.M., 2001. Estimates of meridional atmosphere and ocean heat transports. *Journal of Climate* 14(16), 3433–3443.
- Trenberth, K.E., Stepaniak, D.P., 2003. Seamless poleward atmospheric energy transports and implications for the Hadley circulation. *Journal of Climate* 16(22), 3706–3722.
- Trenberth, K.E., Shea, D.J., 2006. Atlantic hurricanes and natural variability in 2005. *Geophysical Research Letters* 33, L12704.
- Trigo, R.M., Palutikof, J.P., 2001. Precipitation scenarios over Iberia: a comparison between direct GCM output and different downscaling techniques. *Journal of Climate* 14(23), 4422–4446.
- Trigo, R.M., Osborn, T.J., Corte-Real, J., 2002. The North Atlantic oscillation influence on Europe: climate impacts and associated physical mechanisms. *Climate Research* 20(1), 9–17.
- Trigo, R.M., Trigo, I.F., DaCamara, C.C., Osborn, T.J., 2004. Climate impact of the European winter blocking episodes from the NCEP/NCAR Reanalyses. *Climate Dynamics* 23(1), 17–28.
- Trigo, R.M., Valente, M.A., Trigo, I.F., Miranda, P.M.A., Ramos, A.M., Paredes, D., García-Herrera, R., 2008. The impact of north atlantic wind and cyclone trends on European precipitation and significant wave height in the Atlantic. *Annals of the New York Academy of Sciences* 1146, 212–34.
- Trouet, V., Esper, J., Graham, N. E., Baker, A., Scourse, J. D., and Frank, D.C., 2009. Persistent positive North Atlantic Oscillation mode dominated the Medieval Climate Anomaly. *Science* 324, 78–80.
- Ubanell, A.G., 1994. Los modelos tectónicos del Sistema Central Español. *Cadernos do Laboratorio Xeolóxico de Laxe* 19, 249–260.
- Valero-Garcés, B., González-Sampériz, P., Navas, A., Machín, J., Mata, P., Delgado-Huertas, A., Bao, R., Moreno, A., Carrión, J.S., Schwalb, A., González-Barrios, A., 2006. Human impact since medieval times and recent ecological restoration in a Mediterranean lake: the Laguna Zoñar, southern Spain. *Journal of Paleolimnology*

- 35, 441–465.
- Vasko, K., Toivonen, H., Korhola, A., 2000. A Bayesian multinomial Gaussian response model for organism-based environmental reconstruction. *Journal of Paleolimnology* 24, 243–250.
- Velde, B., 1995. Origin and mineralogy of clays: Clays and the Environment. Velde, B. (ed). Springer, Berlin, pp. 334.
- Verpoorter, C., Kutser, T., Seekell, D.A., Tranvik, L.J., 2014. A global inventory of lakes based on high-resolution satellite imagery. *Geophysical Research Letters* 41(18), 6396–6402.
- Vicente-Serrano, S.M., Trigo, R.M., 2011. Hydrological, socioeconomic and ecological impacts of the North Atlantic Oscillation in the Mediterranean region. *Advances in global change research*, vol. 46. Springer, New York.
- Vinther, B.M., Johnsen, S.J., Andersen, K.K., Clausen, H.B., Hansen, H.W., 2003a. NAO signal recorded in the stable isotopes of Greenland ice cores. *Geophysical Research Letters* 30, 1387.
- Vinther, B.M., Andersen, K.K., Hansen, A.W., Schmitt, T., Jones, P.D., 2003b. Improving the Gibraltar/Reykjavik NAO Index. *Geophysical Research Letters* 30, 2222.
- Viron, O., Dickey, J.O., Ghil, M., 2013. Global modes of climate variability. *Geophysical Research Letters* 40(9), 1832–1837.
- Visbeck, M.H., Hurrell, J.W., Polvani, L., Cullen, H.M., 2001. The North Atlantic Oscillation: past, present, and future. *Proceedings of the National Academy of Sciences* 98(23), 12876–12877.
- von Grafenstein, U., Erlenkeuser, H., Brauer, A., Jouzel, J., Johnsen, S.J., 1999. A mid-European decadal isotope-climate record from 15,500 to 5,000 years B.P. *Science* 284, 1654–1657.
- von Storch, H., 1999. On the use of “inflation” in statistical downscaling. *Journal of Climate* 12, 3505–3506.
- Walker, G.T., 1924. Correlation in seasonal variation of weather. IX *Memoirs of the India Meteorological Department* 25, 275–332.
- Walker, G.T., Bliss, E.W., 1932. World Weather V. *Memoirs of Royal Meteorological Society* 4, 53–84.

- Wallace, J.M., Gutzler, D.S., 1981. Teleconnections in the geopotential height field during the Northern Hemisphere winter. *Monthly Weather Review* 109, 784–812.
- Wallace, J.M., Hobbs, P.V., 2006. Atmospheric science: an introductory survey (2nd edition). International Geophysics Series 92, Associated press, pp. 484.
- Wang, Y.H., Magnusdottir, G., Stern, H., Tian, X., Yu, Y., 2012. Decadal variability of the NAO: Introducing an augmented NAO index. *Geophysical Research Letters* 39, L21702.
- Wanner, H., Brönnimann, S., Casty, C., Gyalistras, D., Luterbacher, J., Schmutz, C., Stephenson, D.B., Xoplaki, E., 2001. North Atlantic oscillation. Concepts and studies. *Surveys in Geophysics* 22(4), 321–382.
- Wanner, H., Beer, J., Bütkofer, J., Crowley, T.J., Cubasch, U., Flückiger, J., Goosse, H., Grosjean, M., Joos, F., Kaplan, J.O., Küttel, M., Müller, S.A., Prentice, I.C., Solomina, O., Stocker, T.F., Tarasov, P., Wagner, M., Widmann, M., 2008. Mid-to Late Holocene climate change: an overview. *Quaternary Science Reviews* 27(19), 1791–1828.
- Wanner, H., Brönnimann, S., 2012. Is there a global Holocene climate mode. *PAGES news* 20(1), 44–5.
- Washington, R., Todd, M.C., Middleton, N.J., Goudie, A.S., 2003. Dust-storm source areas determined by the total ozone monitoring spectrometer and surface observations. *Annals of the Association of American Geographers* 93 (2), 297–313.
- Webb, A., 2002. Statistical pattern recognition, 2nd ed. Arnold, London.
- Wetzel, R.G., 2001. Limnology. Lake and rivers ecosystems. 3rd ed. Academic Press, San Diego, USA.
- Williams, S.G., Stefan, H.G. 2006. Modeling of lake ice characteristics in North America using climate, geography, and lake bathymetry. *Journal of Cold Regions Engineering* 20(4), 140–167.
- Williamson, C.E., Saros, J.E., Vincent, W.F., Smold, J.P., 2009. Lakes and reservoirs as sentinels, integrators, and regulators of climate change. *Limnology and Oceanography* 54, 2273–2282.
- Wirth, S.B., Glur, L., Gilli, A., Anselmetti, F.S., 2013. Holocene flood frequency across the Central Alps–solar forcing and evidence for variations in North Atlantic atmospheric circulation. *Quaternary Science Reviews* 80, 112–128.
- Wirrman, D., Mourguia, P., 1995. Late Quaternary spatio-temporal limnological

- variations in the Altiplano of Bolivia and Peru. *Quaternary Research* 43, 344–354.
- Woollings, T.J., Hoskins, B.J., Blackburn, M., Berrisford, P., 2008. A New Rossby Wave-breaking Interpretation of the North Atlantic oscillation. *Journal of the Atmospheric Sciences* 65, 609–626.
- Woollings, T., Hannachi, A., Hoskins, B., 2010. Variability of the North Atlantic eddy-driven jet stream. *Quarterly Journal of the Royal Meteorological Society* 136, 856–868.
- Wright, H.E., 1966. Stratigraphy of lake sediments and the precision of the paleoclimatic record. In *World climate from 8000 to 0 BC*. Sawyer, J.S. (ed). Royal Meteorological Society, London, pp. 157–173.
- Xu, Q., Li, Y., Bunting, M.J., Tian, F., Liu, J., 2010. The effects of training set selection on the relationship between pollen assemblages and climate parameters: implications for reconstructing past climate. *Palaeogeography, Palaeoclimatology and Palaeoecology* 289, 123–133.
- Yamamoto, A., Palter, J.B., 2016. The absence of an Atlantic imprint on the multidecadal variability of wintertime European temperature. *Nature communications*, 7.
- Yancheva, G., Nowaczyk, N.R., Mingram, J., Dulski, P., Schettler, G., Negendank, J.F.W., Liu, J., Sigman, D.M., Peterson, L.C., Haug, G.H., 2007. Influence of the intertropical convergence zone on the East Asian monsoon. *Nature* 445, 74–77.
- Yao, Y., Luo, D., 2014. Relationship between zonal position of the North Atlantic Oscillation and Euro-Atlantic blocking events and its possible effect on the weather over Europe. *Science China Earth Sciences* 57(11), 2628–2636.
- Yoo, J., D'Odorico, P., 2002. Trends and fluctuations in the dates of ice break-up of lakes and rivers in Northern Europe: the effect of the North Atlantic Oscillation. *Journal of Hydrology* 268(1), 100–112.
- Zhang, Y.J., Wallace, M., Battisti, D.S., 1997. ENSO-like interdecadal variability: 1900–93. *Journal of Climate* 10, 1004–1020.
- Zhang, C., 2005. Madden-julian oscillation. *Reviews of Geophysics* 43(2).

Theoretical R session

Text A1. *Theoretical R session with all the mathematical details of the Random walk-modularised Bayesian model.*

```
###RANDOM WALK-MODULARIZED BAYESIAN MODEL SCRIPT FOR R IN LINUX VERSION###

## To install JAGS package (Just Another Gibbs Sampler; Plummer, 2003) is
#previously required.

#####Required Packages and Libraries#####
install.packages('rjags')
library(rjags)
install.packages('R2jags')
library(R2jags)
install.packages('coda')
library(coda)
install.packages('runjags')
library(runjags)
install.packages('MASS')
install.packages('fitdistrplus')
library(fitdistrplus)

##Set working directory
setwd("~/Directory")

## Load your data model:

#NAO_m a numerical integer vector of length m that corresponds to modern
#annual NAO index data of the overlapping period

#xrf_m a numerical integer matrix of m rows and n columns (i.e., number of
#geochemical elements) that corresponds to modern data in the overlapping
#period

#time_m a numerical vector of length n that corresponds to modern ages of the
#overlapping period in Anno Domini (AD) years. This data must be sorted in
#descending age, i.e., from older to punger ages.

#xrf_f a numerical integer matrix of l rows and n columns (i.e., number of
#geochemical elements) that denotes fossil data the rest of geochemical data
#data not included in the overlapping period

#time_f a numerical vector of length l that corresponds to fossil ages not
#included in the overlapping period in AD and Before Christ (BC) years. BC
#years must be negative values. Data sorted as t_m

load('DATA.Rdata')
```

```
##pow function used in a couple of places
pow = function(x,n) return(x^n)

#####
#####
#####
##Step1
##INITIAL CALIBRATION STEP. Run the first model on only the modern data
#####

data=list(N.rows_m =
nrow(xrf_m),N.cols_m=ncol(xrf_m),xrf_m=xrf_m,NAO_m=NAO_m,time_m=time_m)

NAOmodel<-
model
{

## MODERN DATA. likelihood
for(j in 1:N.cols_m) {
for(i in 1:N.rows_m) {
xrf_m[i,j] ~ dgamma(alpha[i,j],delta[i,j])

alpha[i,j] <- pow(gamma_mean[i,j],2)/pow(gamma_sd[i,j],2)
delta[i,j] <- gamma_mean[i,j]/pow(gamma_sd[i,j],2)

gamma_mean[i,j] <- exp(beta0[j] + beta1[j]*NAO_m[i]+beta2[j]*pow(NAO_m[i],2))
gamma_sd[i,j] <- exp(mu0[j])

}#End i loop, rows
}#End j loop, columns

## Priors. One for each column (geochemical data)
for (j in 1:N.cols_m) {

beta0[j] ~ dnorm(0,0.01)
beta1[j] ~ dnorm(0,0.01)
beta2[j] ~ dnorm(0,0.01)
mu0[j] ~ dnorm(0,0.01)

}#End loop priors

## Random walk prior distribution for NAO modern
for(i in 2:N.rows_m) {
NAO_m[i]~ dnorm(NAO_m[i-1],prec_m[i])
prec_m[i] <- 1/((time_m[i]-time_m[i-1])*pow(sd_rw,2))
}

#Prior distribution for rw parameter
sd_rw ~ dunif(0,100)

}##End model
"
pars=c("beta0","beta1","beta2","mu0","sd_rw")

myinitial<-function()
{list("beta0"=rnorm(1,0,3),"beta1"=rnorm(1,0,1),"beta2"=rnorm(1,0,1),"mu0"=rnorm(1,0,1))}
```

```
## RUN THE MODEL
run.mcmc <- jags(data=data, parameters.to.save=pars,
model.file=textConnection(NAOmodel),n.chains=4, n.iter=3000,
n.burnin=2000,n.thin=4,DIC=FALSE)

results.jags<-as.mcmc(run.mcmc)
plot(results.jags)

# Fit a log normal distribution to the sd_rw parameter
# Plan is to use this as a prior in the later fossil model

## Fit a log-normal distribution to the 50 random data set
results = run.mcmc$BUGSoutput$sims.list
lnorm_pars = fitdist(as.vector(results$sd_rw),'lnorm')
plot(lnorm_pars)

#####
#####
##Step2
##CREATING Marginal Data Posteriors(MDPs). Create MDPs of NAO_f from NAO_grid
#####
#####

# Now run importance sampling on a grid of NAO_f values to get MDPs of NAO_f,
#one for each layer

# Store these as just the mean and prec for use in the next jags model
NAO_grid = seq(-3,3,length=50)
beta0 = apply(results$beta0,2,'median')
beta1 = apply(results$beta1,2,'median')
beta2 = apply(results$beta2,2,'median')
mu0 = apply(results$mu0,2,'median')
N.rows_f = nrow(xrf_f)
MDP_raw = MDP = matrix(0,nrow=N.rows_f,ncol=length(NAO_grid))

# Create MDPs
for(i in 1:N.rows_f) {
  print(i)
  for(k in 1:length(NAO_grid)) {
    for(j in 1:nrow(results$beta0)) {
      beta0 = results$beta0[j,]
      beta1 = results$beta1[j,]
      beta2 = results$beta2[j,]
      mu0 = results$mu0[j,]
      gamma_mean = exp(beta0 + beta1*NAO_grid[k]+beta2*pow(NAO_grid[k],2))
      gamma_sd = exp(mu0)
      alpha = pow(gamma_mean,2)/pow(gamma_sd,2)
      delta = gamma_mean/pow(gamma_sd,2)
      MDP_raw[i,k] = MDP_raw[i,k] +
        sum(dgamma(xrf_f[i,],alpha,rate=delta,log=TRUE))
    }
    MDP[i,k] = exp(MDP_raw[i,k]/nrow(results$beta0))
  }
}

MDP_final = sweep(MDP,1,apply(MDP,1,'sum'),'/')
```

```
MDP_mean = round(MDP_final,5)%*%NAO_grid # Rounding required otherwise
numerical errors
MDP_sd = sqrt(round(MDP_final,5)%*%(NAO_grid^2)-MDP_mean^2)
MDP_prec = 1/(MDP_sd^2)
MDP_high = MDP_mean+2*MDP_sd
MDP_low = MDP_mean-2*MDP_sd

# If any of the MDP_prec values are infinite make them something finite
MDP_prec[is.infinite(MDP_prec)] = 1e10

# Plot MDPs
plot(time_f,MDP_mean,xlim=range(c(time_f,time_m)),ylim=range(c(MDP_low,MDP_hi
gh,NAO_m)),col='red',pch=19,cex=0.5)
points(time_m,NAO_m,pch=19,cex=0.5)
for(i in 1:N.rows_f) {
  lines(c(time_f[i],time_f[i]),c(MDP_low[i],MDP_high[i]),col='red')
}

#####
#####
##Step3
##MODEL FITTING. Now run a final jags model using the MDP means and precision
to obtain the ancient NAO (NAO_f)
#####
#####

fossil_model="

model {
# Likelihood for MDP
for(i in 1:N.rows_f) {
  MDP_mean[i] ~ dnorm(NAO_f[i],MDP_prec[i])
}

# Random walk prior for NAO_f
for(i in 2:N.rows_f) {
  NAO_f[i] ~ dnorm(NAO_f[i-1],prec_f[i])
  prec_f[i] <- 1/((time_f[i]-time_f[i-1])*pow(sd_rw,2))
}

# First fossil NAO should have vague prior
NAO_f[1] ~ dnorm(0,0.01)

# Also include first NAO_m value as this depends on last NAO_f value
NAO_m_1 ~ dnorm(NAO_f[N.rows_f],prec_m_f)
prec_m_f <- 1/((time_m_1-time_f[N.rows_f])*pow(sd_rw,2))

# Use a log normal prior on sd_rw, taken from the posterior from the modern
# data run
sd_rw ~ dlnorm(a_rw,b_rw) # a_rw and b_rw should be specified in the data
}
```

```
data=list(N.rows_f=nrow(xrf_f),MDP_mean=MDP_mean[,1],MDP_prec=MDP_prec[,1],ti  
me_f=time_f,NAO_m_1=NAO_m[1],time_m_1=time_m[1],a_rw=lnorm_pars$estimate[1],b  
_rw=1/pow(lnorm_pars$estimate[2],2))  
  
pars=c("NAO_f","sd_rw")  
myinitial<-function()  
{list('NAO_f'=rep(0,N.rows_f), 'sd_rw'=mean(results$sd_rw))}  
  
## RUN THE MODEL  
fossil_model_run = jags(data=data, parameters.to.save=pars, inits=myinitial,  
model.file=textConnection(fossil_model),n.chains=3, n.iter=3000,  
n.burnin=2000,n.thin=1,DIC=FALSE)  
  
# Plot NAO reconstruction  
par(mfrow=c(1,1))  
mcmc.jags<-fossil_model_run$BUGSoutput$sims.list  
NAO_fmed<-apply(mcmc.jags$NAO_f,2,median)  
NAO_flow<-apply(mcmc.jags$NAO_f,2,quantile,0.05)  
NAO_fhigh<-apply(mcmc.jags$NAO_f,2,quantile,0.95)  
time_all = c(data$time_f,time_m)  
NAO_all_med = c(NAO_fmed,NAO_m)  
NAO_all_low = c(NAO_flow,NAO_m)  
NAO_all_high = c(NAO_fhigh,NAO_m)  
  
plot(time_all,NAO_all_med,type="l",xaxt='n',ylim=c(-3,2))  
axis(1,at=seq(-200,2000,by=50))  
lines(time_all,NAO_all_low,col='red',lwd=1.5)  
lines(time_all,NAO_all_high,col='red',lwd=1.5)  
abline(h=0,col='red')  
  
# Save your reconstructed NAO  
write.table(NAO_fossil,file='NAO_fossil.csv',sep=',',col.names =  
TRUE,row.names=FALSE)  
  
##### REFERENCES #####  
  
#Plummer, M. 2003. JAGS: a program for analysis of Bayesian graphical models  
#using Gibbs sampling. In Proceedings of the 3rd International Workshop on  
#Distributed Statistical Computing.
```

Chemical and mineralogical data

Table B.1. Geochemical proxies analysed from PE12-01-01 core: TC, TN, (in percentages), $\delta^{13}\text{C}$ and $\delta^{15}\text{N}$ (in ‰).

Depth (cm)	TC (%)	$\delta^{13}\text{C}$ (‰)	TN (%)	$\delta^{15}\text{N}$ (‰)
0.2	4.93	-25.946	0.424	3.34
0.4	3.94	-25.984	0.338	3.73
0.6	4.14	-25.898	0.376	2.80
0.8	4.52	-26.118	0.388	3.42
1	5.02	-26.030	0.460	3.62
1.2	4.17	-26.019	0.381	2.91
1.4	4.27	-25.833	0.382	3.62
1.6	4.39	-26.070	0.379	2.98
1.8	4.51	-25.996	0.410	3.68
2	4.48	-25.899	0.395	3.00
2.2	5.05	-25.810	0.473	3.39
2.4	0.04	-25.860	0.004	3.61
2.6	4.69	-26.002	0.417	3.55
2.8	4.04	-25.734	0.376	3.58
3	4.75	-25.940	0.425	3.35
3.2	3.90	-25.928	0.348	2.96
3.4	3.76	-25.889	0.337	3.46
3.6	4.50	-25.918	0.414	3.57
3.8	3.88	-25.885	0.352	3.14
4	3.41	-26.023	0.300	2.75
4.2	3.63	-25.925	0.323	3.32
4.4	5.07	-25.881	0.436	3.76
4.6	4.88	-25.847	0.444	3.68

Depth (cm)	TC (%)	$\delta^{13}\text{C}$ (‰)	TN (%)	$\delta^{15}\text{N}$ (‰)
4.8	4.71	-26.047	0.393	3.35
5	5.08	-26.017	0.446	3.42
5.2	3.19	-25.253	0.309	3.31
5.4	4.24	-25.813	0.414	3.78
5.6	3.49	-25.879	0.345	3.29
5.8	4.42	-25.726	0.445	3.21
6	4.72	-25.919	0.440	3.83
6.2	3.46	-25.737	0.321	3.40
6.4	4.92	-26.072	0.445	3.36
6.6	4.54	-25.982	0.413	3.65
6.8	1.83	-25.783	0.203	1.83
7	5.14	-25.893	0.475	3.44
7.2	4.12	-25.910	0.391	3.37
7.4	5.11	-26.116	0.472	4.01
7.6	5.01	-25.941	0.470	3.22
7.8	4.83	-25.910	0.450	3.32
8	3.78	-25.720	0.378	3.49
8.2	3.85	-25.790	0.355	3.19
8.4	3.56	-25.923	0.333	3.54
8.6	4.77	-25.866	0.443	3.84
8.8	4.18	-25.881	0.385	3.25
9	5.30	-25.908	0.489	4.04
9.2	5.23	-25.965	0.475	3.95
9.4	4.37	-25.966	0.374	3.70
9.6	5.24	-26.006	0.469	3.78
9.8	4.87	-25.941	0.463	3.92
10	4.99	-25.878	0.475	3.40
10.2	4.66	-25.948	0.449	3.76
10.4	5.41	-25.957	0.492	3.68
10.6	4.87	-25.880	0.452	3.76

Chemical and mineralogical data

Depth (cm)	TC (%)	$\delta^{13}\text{C}$ (‰)	TN (%)	$\delta^{15}\text{N}$ (‰)
10.8	5.20	-25.943	0.474	3.55
11	4.81	-25.954	0.439	3.33
11.2	5.06	-25.937	0.466	3.85
11.4	4.91	-25.979	0.469	3.26
11.6	3.26	-25.567	0.346	3.64
11.8	5.10	-26.011	0.475	3.47
12	5.13	-25.805	0.482	4.00
12.2	5.33	-26.163	0.461	4.02
12.4	5.30	-26.163	0.500	4.00
12.6	4.96	-25.932	0.458	3.53
12.8	5.52	-26.988	0.496	3.75
13	4.32	-25.895	0.411	3.50
13.2	4.55	-26.024	0.419	3.88
13.4	4.50	-26.055	0.403	3.44
13.6	4.73	-25.933	0.440	3.23
13.8	4.58	-25.994	0.424	4.06
14	5.13	-26.047	0.466	3.80
14.2	5.02	-25.935	0.469	3.96
14.4	4.86	-26.011	0.449	3.70
14.6	5.63	-26.038	0.527	3.45
14.8	5.34	-26.010	0.497	3.46
15	5.29	-26.061	0.475	4.24
15.2	5.52	-25.962	0.485	3.52
15.4	5.86	-25.958	0.534	3.57
15.6	5.79	-25.958	0.523	4.63
15.8	5.83	-25.875	0.527	3.81
16	5.89	-25.867	0.537	3.84
16.2	5.63	-25.940	0.511	4.11
16.4	5.84	-25.882	0.531	3.89
16.6	5.84	-25.966	0.519	3.78

Depth (cm)	TC (%)	$\delta^{13}\text{C}$ (‰)	TN (%)	$\delta^{15}\text{N}$ (‰)
16.8	5.96	-25.821	0.531	4.06
17	5.35	-25.949	0.481	4.46
17.2	6.16	-25.954	0.559	3.84
17.4	5.45	-25.912	0.511	4.11
17.6	5.86	-25.911	0.531	3.52
17.8	5.72	-25.881	0.514	3.77
18	6.22	-27.667	0.524	4.59
18.2	5.72	-25.875	0.513	3.72
18.4	5.68	-25.918	0.514	3.88
18.6	5.04	-25.941	0.456	3.62
18.8	5.69	-25.858	0.528	3.78
19	5.59	-25.968	0.509	4.06
19.2	5.91	-25.955	0.547	3.92
19.4	6.10	-25.847	0.546	3.99
19.6	5.85	-25.891	0.529	3.44
19.8	5.86	-25.884	0.543	3.93
20	6.21	-25.902	0.530	3.56
20.2	5.17	-25.980	0.447	3.74
20.4	5.24	-25.956	0.478	4.05
20.6	5.03	-26.026	0.461	3.74
20.8	4.82	-25.838	0.437	4.54
21	4.74	-25.996	0.449	3.93
21.2	5.24	-25.950	0.473	4.02
21.4	5.03	-25.872	0.473	3.61
21.6	6.20	-25.938	0.563	3.82
21.8	5.21	-25.787	0.476	4.16
22	5.29	-26.092	0.469	4.00
22.2	4.87	-26.112	0.446	3.53
22.4	5.26	-25.831	0.491	4.07
22.6	1.96	-25.876	0.214	2.61

Chemical and mineralogical data

Depth (cm)	TC (%)	$\delta^{13}\text{C}$ (‰)	TN (%)	$\delta^{15}\text{N}$ (‰)
22.8	4.07	-25.974	0.366	3.27
23	2.31	-25.691	0.227	3.62
23.2	3.57	-25.887	0.328	3.60
23.4	3.79	-25.973	0.354	3.83
23.6	5.35	-25.886	0.489	4.27
23.8	5.55	-26.030	0.510	4.12
24	5.21	-26.020	0.467	3.91
24.2	5.60	-25.945	0.499	3.83
24.4	5.50	-25.984	0.491	4.03
24.6	5.29	-26.011	0.478	4.30
24.8	5.44	-25.840	0.495	4.00
25	5.19	-25.917	0.479	3.84
25.2	5.09	-25.908	0.454	3.72
25.4	5.10	-25.846	0.443	4.28
25.6	5.53	-25.814	0.488	4.33
25.8	5.59	-25.945	0.495	3.96
26	5.29	-25.855	0.447	4.05
26.2	5.00	-25.941	0.435	3.70
26.4	5.00	-25.988	0.407	3.80
26.6	5.02	-25.928	0.444	3.41
26.8	4.56	-25.803	0.383	3.78
27	4.98	-25.816	0.412	3.89
27.2	4.44	-25.865	0.380	3.34
27.4	4.86	-26.006	0.415	4.06
27.6	3.86	-25.836	0.319	3.26
27.8	2.62	-25.529	0.229	4.16
28	3.53	-25.633	0.293	3.76
28.2	2.94	-25.619	0.238	3.83
28.4	2.64	-25.711	0.218	3.04
28.6	2.64	-25.389	0.216	3.49

Depth (cm)	TC (%)	$\delta^{13}\text{C}$ (‰)	TN (%)	$\delta^{15}\text{N}$ (‰)
28.8	2.11	-25.490	0.177	3.13
29	2.97	-25.601	0.249	3.52
29.2	4.18	-25.854	0.356	3.87
29.4	3.54	-25.742	0.302	4.02
29.6	4.31	-25.804	0.374	3.83
29.8	3.92	-25.805	0.343	3.27
30	4.27	-25.559	0.362	3.87
30.2	3.42	-25.711	0.286	3.71
30.4	5.08	-26.752	0.352	3.79
30.6	4.20	-25.665	0.356	3.93
30.8	4.31	-25.764	0.362	4.18
31	3.87	-25.694	0.330	3.24
31.2	4.20	-25.647	0.355	3.78
31.4	4.08	-25.600	0.344	3.83
31.6	3.60	-25.634	0.305	3.42
31.8	3.65	-25.589	0.307	3.44
32	3.75	-25.618	0.328	3.93
32.2	3.60	-25.764	0.310	3.47
32.4	3.53	-25.736	0.293	3.91
32.6	3.26	-25.740	0.286	3.93
32.8	4.04	-25.297	0.268	3.23
33	2.98	-25.750	0.259	3.89
33.2	3.03	-25.416	0.272	3.85
33.4	3.39	-25.637	0.296	3.68
33.6	3.46	-25.625	0.275	3.97
33.8	3.62	-25.616	0.308	3.70
34	3.59	-25.650	0.299	3.40
34.2	3.54	-25.602	0.296	3.40
34.4	2.78	-25.566	0.236	3.03
34.6	3.49	-25.675	0.288	4.16

Chemical and mineralogical data

Depth (cm)	TC (%)	$\delta^{13}\text{C}$ (‰)	TN (%)	$\delta^{15}\text{N}$ (‰)
34.8	3.61	-25.680	0.301	3.49
35	4.37	-25.773	0.391	4.03
35.2	3.76	-25.560	0.335	3.68
35.4	4.10	-25.855	0.355	3.95
35.6	4.49	-25.690	0.400	4.04
35.8	4.20	-25.642	0.377	4.43
36	5.31	-25.846	0.459	4.26
36.2	5.47	-25.768	0.484	4.21
36.4	5.10	-25.737	0.450	4.19
36.6	5.13	-25.692	0.451	4.14
36.8	5.27	-25.623	0.453	4.35
37	5.18	-25.710	0.449	4.13
37.5	4.95	-25.665	0.437	3.69
38	4.93	-25.800	0.433	3.91
38.5	4.97	-25.762	0.436	3.97
39	4.69	-25.793	0.400	3.58
39.5	5.11	-25.672	0.444	3.89
40	5.04	-25.572	0.458	4.33
40.5	4.93	-25.632	0.437	4.00
41	5.18	-25.691	0.451	4.74
41.5	5.10	-25.785	0.434	3.88
42	4.85	-25.749	0.425	3.67
42.5	4.79	-25.765	0.421	4.11
43	4.95	-25.701	0.442	3.77
43.5	4.54	-25.611	0.388	3.79
44	4.59	-25.7	0.410	3.60
44.5	4.83	-25.733	0.428	3.62
45	4.99	-25.614	0.442	3.88
45.5	4.87	-25.648	0.454	4.42
46	5.05	-25.663	0.442	3.93

Depth (cm)	TC (%)	$\delta^{13}\text{C}$ (‰)	TN (%)	$\delta^{15}\text{N}$ (‰)
46.5	4.23	-25.619	0.376	3.49
47	4.44	-25.630	0.401	3.59
47.5	4.94	-25.798	0.433	3.16
48	4.25	-25.669	0.386	3.96
48.5	5.62	-25.701	0.503	4.20
49	5.20	-25.574	0.457	4.04
49.5	4.95	-25.713	0.439	3.99
50	5.08	-25.736	0.441	3.74
50.5	5.39	-25.756	0.456	4.01
51	4.74	-25.634	0.426	3.57
51.5	4.90	-25.682	0.449	3.71
52	5.20	-25.742	0.453	3.81
52.5	4.81	-25.691	0.429	3.66
53	4.82	-25.694	0.409	3.68
53.5	4.56	-25.664	0.403	4.29
54	4.58	-25.630	0.411	4.56
54.5	4.87	-25.700	0.430	3.63
55	4.81	-25.787	0.408	3.89
55.5	4.18	-25.692	0.384	3.20
56	3.82	-25.494	0.326	3.72
56.5	3.09	-25.482	0.277	3.24

Table B.2. Geochemical proxies analysed CIM12-04A core: TC, TN, (in percentages), $\delta^{13}\text{C}$ and $\delta^{15}\text{N}$ (in ‰).

Depth (cm)	TC (%)	$\delta^{13}\text{C}$ (‰)	TN (%)	$\delta^{15}\text{N}$ (‰)
0	5.67	-24.74	0.63	0.41
0.2	6.22	-25.35	0.57	0.51
0.4	7.72	-26.18	0.53	0.66

Chemical and mineralogical data

Depth (cm)	TC (%)	$\delta^{13}\text{C}$ (‰)	TN (%)	$\delta^{15}\text{N}$ (‰)
0.6	5.51	-24.41	0.59	0.44
0.8	5.36	-24.38	0.57	-0.20
1	5.26	-24.22	0.55	0.24
1.2	5.00	-24.41	0.52	0.02
1.4	4.94	-24.25	0.50	0.82
1.6	4.86	-24.43	0.51	0.34
1.8	4.62	-24.27	0.48	0.41
2	4.10	-24.10	0.40	1.30
2.2	4.43	-23.98	0.48	0.93
2.4	4.69	-24.07	0.50	0.74
2.6	4.62	-24.42	0.49	0.44
2.8	4.13	-24.29	0.44	0.27
3	5.32	-24.49	0.52	0.52
3.2	3.55	-24.38	0.35	0.76
3.4	3.63	-24.25	0.36	1.34
3.6	3.97	-24.22	0.41	0.90
3.8	4.03	-24.31	0.41	1.25
4	3.80	-24.24	0.38	1.30
4.2	3.82	-24.31	0.40	1.83
4.4	3.80	-24.33	0.38	1.46
4.6	3.24	-24.26	0.31	1.42
4.8	3.24	-24.17	0.32	0.91
5	3.16	-24.03	0.31	1.59
5.2	2.96	-24.29	0.29	1.14
5.4	2.96	-24.27	0.28	2.27
5.6	3.14	-24.03	0.30	2.30
5.8	3.46	-24.22	0.34	2.05
6	3.57	-24.29	0.34	2.18
6.2	3.64	-24.29	0.35	1.67
6.4	3.40	-24.27	0.34	1.58

Depth (cm)	TC (%)	$\delta^{13}\text{C}$ (‰)	TN (%)	$\delta^{15}\text{N}$ (‰)
6.6	3.57	-24.47	0.31	2.13
6.8	3.50	-24.52	0.31	1.84
7	3.66	-24.50	0.32	2.49
7.2	3.52	-24.31	0.31	2.18
7.4	3.38	-24.16	0.29	2.09
7.6	3.34	-24.31	0.30	2.12
7.8	2.58	-24.20	0.21	1.11
8	2.36	-24.32	0.19	1.39
8.2	2.97	-24.03	0.23	1.84
8.4	3.40	-24.24	0.29	1.38
8.6	3.27	-24.41	0.27	2.13
8.8	3.39	-24.35	0.28	2.08
9	3.39	-24.11	0.29	2.41
9.2	2.99	-24.60	0.26	1.54
9.4	3.13	-24.53	0.26	1.86
9.6	3.14	-24.55	0.27	2.35
9.8	3.16	-24.52	0.27	1.45
10	3.21	-24.59	0.27	2.24
10.2	2.89	-24.19	0.26	2.57
10.4	3.24	-24.18	0.28	2.27
10.6	3.36	-24.32	0.29	2.19
10.8	3.06	-24.63	0.26	1.74
11	3.16	-24.71	0.27	1.67
11.2	3.09	-24.54	0.25	1.58
11.4	3.34	-24.59	0.28	2.50
11.6	3.50	-24.53	0.29	1.82
11.8	3.46	-24.57	0.30	2.30
12	3.41	-24.47	0.29	1.98
12.2	3.48	-24.63	0.30	2.01
12.4	3.46	-24.73	0.29	2.23

Chemical and mineralogical data

Depth (cm)	TC (%)	$\delta^{13}\text{C}$ (‰)	TN (%)	$\delta^{15}\text{N}$ (‰)
12.6	3.42	-24.39	0.29	1.96
12.8	3.34	-24.40	0.28	1.93
13	3.25	-24.56	0.31	3.02
13.2	3.26	-24.42	0.31	2.23
13.4	3.23	-24.47	0.31	2.40
13.6	2.93	-24.43	0.28	2.18
13.8	2.44	-24.39	0.24	2.26
14	2.25	-24.37	0.24	1.86
14.2	2.55	-24.74	0.27	1.77
14.4	2.47	-24.61	0.24	1.83
14.6	2.60	-24.61	0.26	3.04
14.8	2.55	-24.60	0.26	2.30
15	2.59	-24.60	0.26	2.11
15.2	2.72	-24.51	0.26	2.64
15.4	2.73	-24.64	0.27	2.20
15.6	2.83	-24.52	0.27	2.55
15.8	2.94	-24.53	0.29	3.10
16	2.90	-24.43	0.28	2.84
16.2	2.89	-24.45	0.28	2.99
16.4	3.00	-24.30	0.29	2.71
16.6	3.15	-24.38	0.31	2.05
16.8	2.71	-24.40	0.27	2.26
17	2.81	-24.42	0.28	2.18
17.2	2.88	-24.36	0.29	3.19
17.4	2.77	-24.42	0.28	2.24
17.6	2.60	-24.59	0.26	2.29
17.8	2.63	-24.40	0.27	2.86
18	2.61	-24.42	0.26	2.46
18.2	2.55	-24.51	0.26	1.96
18.4	2.37	-24.49	0.24	2.05

Depth (cm)	TC (%)	$\delta^{13}\text{C}$ (‰)	TN (%)	$\delta^{15}\text{N}$ (‰)
18.6	2.81	-24.54	0.28	2.37
18.8	2.78	-24.51	0.29	2.48
19	2.54	-24.56	0.27	1.26
19.2	2.59	-24.63	0.26	2.85
19.4	2.56	-24.67	0.27	2.46
19.6	2.70	-24.68	0.29	2.58
19.8	2.61	-24.50	0.28	2.33
20	2.56	-24.54	0.27	2.67
20.2	2.19	-24.56	0.23	2.13
20.4	1.85	-24.72	0.20	1.12
20.6	1.65	-24.62	0.18	2.29
20.8	1.85	-24.55	0.20	2.37
21	2.45	-24.60	0.26	2.35
21.2	2.30	-24.67	0.24	1.41
21.4	2.06	-24.58	0.22	1.83
21.6	2.43	-24.64	0.26	1.99
21.8	2.52	-24.65	0.26	2.13
22	2.92	-24.77	0.30	2.37
22.2	2.96	-24.77	0.30	2.57
22.4	3.05	-24.72	0.31	2.33
22.6	3.22	-24.67	0.29	3.18
22.8	3.22	-24.65	0.36	1.72
23	3.07	-24.77	0.32	2.37
23.2	3.26	-24.83	0.33	2.28
23.4	3.26	-24.86	0.33	2.19
23.6	3.25	-24.95	0.34	1.58
23.8	3.33	-24.81	0.33	2.69
24	3.47	-24.76	0.34	2.49
24.2	3.40	-24.94	0.33	2.79
24.4	3.30	-24.84	0.33	2.60

Chemical and mineralogical data

Depth (cm)	TC (%)	$\delta^{13}\text{C}$ (‰)	TN (%)	$\delta^{15}\text{N}$ (‰)
24.6	3.34	-24.81	0.32	2.87
24.8	3.32	-24.81	0.32	2.61
25	3.30	-24.88	0.32	2.37
25.2	3.48	-24.90	0.35	2.85
25.4	3.12	-24.92	0.31	2.55
25.6	3.37	-25.01	0.34	2.44
25.8	3.20	-24.83	0.32	2.70
26	3.39	-24.83	0.34	2.35
26.2	3.49	-24.76	0.35	2.34
26.4	3.42	-24.71	0.34	2.55
26.6	3.50	-24.79	0.34	2.69
26.8	3.62	-24.82	0.36	2.89
27	3.39	-24.77	0.33	2.92
27.2	3.53	-25.03	0.33	2.94
27.4	3.39	-24.93	0.34	3.00
27.6	3.49	-24.90	0.34	2.85
27.8	3.27	-24.90	0.32	2.70
28	3.19	-24.89	0.32	2.79
28.2	3.27	-24.83	0.32	2.80
28.4	3.30	-24.70	0.33	2.96
28.6	3.32	-24.90	0.33	2.84
28.8	3.46	-24.79	0.34	2.80
29	3.30	-25.08	0.33	3.37
29.2	3.00	-24.90	0.31	2.52
29.4	3.14	-24.89	0.31	2.59
29.6	3.24	-24.84	0.32	2.56
29.8	4.06	-25.15	0.36	3.02
30	3.40	-24.89	0.34	2.90
30.2	3.92	-25.15	0.37	2.52
30.4	3.41	-24.84	0.34	2.50

Depth (cm)	TC (%)	$\delta^{13}\text{C}$ (‰)	TN (%)	$\delta^{15}\text{N}$ (‰)
30.6	3.53	-25.00	0.34	2.77
30.8	3.51	-25.02	0.34	2.84
31	3.21	-24.86	0.32	2.44
31.2	3.29	-24.94	0.33	2.55
31.4	3.26	-24.98	0.33	2.10
31.6	3.57	-24.80	0.36	2.32
31.8	3.05	-24.74	0.31	2.38
32	3.09	-24.81	0.30	2.98
32.2	3.22	-24.88	0.32	3.05
32.4	3.48	-25.17	0.32	2.38
32.6	3.27	-24.85	0.33	3.01
32.8	3.27	-24.87	0.32	2.41
33	3.30	-24.93	0.33	3.07
33.2	3.16	-24.88	0.31	2.86
33.4	3.73	-25.11	0.35	2.56
33.6	3.51	-25.13	0.34	3.04
33.8	3.48	-25.25	0.32	2.95
34	3.64	-25.03	0.33	2.97
34.2	3.51	-25.00	0.33	2.96
34.4	3.32	-25.01	0.30	3.17
34.6	3.23	-25.12	0.32	2.62
34.8	3.80	-25.11	0.37	2.96
35	3.59	-25.32	0.33	3.61
35.2	3.97	-25.21	0.37	3.31
35.4	3.34	-25.36	0.32	3.69
35.6	3.22	-25.35	0.31	3.46
35.8	2.82	-25.46	0.27	2.51
36	2.79	-25.46	0.27	3.23
36.5	3.28	-25.35	0.31	2.74
37	3.63	-25.42	0.36	3.31

Chemical and mineralogical data

Depth (cm)	TC (%)	$\delta^{13}\text{C}$ (‰)	TN (%)	$\delta^{15}\text{N}$ (‰)
37.5	3.90	-25.34	0.38	2.90
38	4.39	-25.44	0.40	2.93
38.5	4.42	-25.36	0.42	3.22
39	4.13	-25.25	0.39	3.00
39.5	3.71	-25.26	0.36	3.12
40	3.72	-25.17	0.36	2.66
40.5	3.93	-25.26	0.37	2.30
41	3.88	-25.19	0.38	2.44
41.5	3.60	-25.28	0.35	2.52
42	4.19	-25.37	0.40	2.46
42.5	3.75	-25.41	0.37	3.15
43	3.18	-25.37	0.32	2.77
43.5	3.00	-25.26	0.30	2.81
44	3.52	-25.34	0.34	3.21
44.5	3.53	-25.17	0.34	3.02
45	2.76	-25.14	0.28	2.82
45.5	1.85	-25.03	0.18	2.59
46	3.80	-25.26	0.37	2.71
46.5	4.06	-25.33	0.39	2.99
47	4.09	-25.23	0.38	2.42
47.5	3.71	-25.10	0.36	2.97
48	2.88	-25.04	0.29	2.32
48.5	3.70	-25.05	0.37	2.16
49	3.89	-25.06	0.40	2.51
49.5	3.67	-24.94	0.36	2.62
50	3.61	-24.96	0.37	2.52
50.5	3.80	-24.95	0.38	2.11
51	3.58	-25.12	0.35	1.91
51.5	3.54	-24.99	0.36	2.44
52	2.94	-24.81	0.29	2.19

Depth (cm)	TC (%)	$\delta^{13}\text{C}$ (‰)	TN (%)	$\delta^{15}\text{N}$ (‰)
52.5	3.30	-25.02	0.31	1.80
53	3.70	-24.83	0.37	2.28
53.5	3.56	-24.85	0.36	2.50
54	4.01	-24.78	0.42	2.23
54.5	3.73	-24.69	0.38	2.66
55	3.98	-24.92	0.40	2.56
55.5	3.90	-24.74	0.39	2.83
56	4.23	-25.03	0.42	3.00
56.5	4.20	-25.44	0.40	2.44
57	4.04	-25.11	0.41	2.11
57.5	4.92	-25.70	0.48	2.82
58	4.69	-25.58	0.45	2.80
58.5	4.78	-25.53	0.46	2.84
59	4.46	-25.16	0.43	2.96
59.5	4.17	-25.17	0.40	2.70
60	3.67	-25.01	0.37	2.87
60.5	3.14	-25.07	0.31	2.08
61	3.42	-25.12	0.35	2.14
61.5	3.83	-25.14	0.39	2.44
62	3.88	-25.06	0.38	2.16
62.5	3.10	-25.12	0.30	2.27
63	4.04	-25.06	0.38	2.61
63.5	4.44	-24.97	0.41	2.57
64	4.24	-25.04	0.41	2.91
64.5	4.13	-24.96	0.40	2.81
65	4.15	-25.02	0.39	2.95
65.5	3.23	-24.96	0.31	2.82
66	3.68	-24.79	0.34	2.49
66.5	3.92	-24.94	0.42	2.94
67	3.96	-25.03	0.38	2.46

Chemical and mineralogical data

Depth (cm)	TC (%)	$\delta^{13}\text{C}$ (‰)	TN (%)	$\delta^{15}\text{N}$ (‰)
67.5	4.25	-25.02	0.40	2.44
68	4.38	-25.10	0.42	2.33
68.5	3.73	-24.97	0.35	2.62
69	4.47	-24.97	0.42	2.40
69.5	4.57	-25.08	0.43	2.16
70	4.23	-25.02	0.39	1.97
70.5	3.75	-24.78	0.37	2.41
71	3.65	-24.86	0.34	2.19
71.5	3.38	-24.62	0.33	2.26
72	3.41	-24.63	0.34	1.93
72.5	2.69	-24.57	0.27	2.08
73	1.17	-24.99	0.13	1.44
73.5	1.67	-24.93	0.18	1.73
74	3.85	-25.02	0.38	1.90
74.5	3.23	-25.03	0.31	2.56
75	3.06	-25.04	0.31	2.19
75.5	3.37	-24.86	0.33	2.29
76	3.01	-24.77	0.29	2.50
76.5	3.09	-24.69	0.31	2.47
77	3.07	-24.82	0.29	2.10
77.5	1.93	-25.04	0.20	2.18
78	2.31	-24.80	0.22	2.19
78.5	3.32	-24.87	0.32	2.74
79	3.18	-24.72	0.35	2.11
79.5	2.67	-24.68	0.28	1.97
80	2.77	-24.79	0.28	2.60
80.5	3.76	-24.85	0.38	3.01
81	3.61	-24.74	0.36	2.09
81.5	3.65	-24.85	0.36	2.40
82	3.85	-24.71	0.37	2.60

Depth (cm)	TC (%)	$\delta^{13}\text{C}$ (‰)	TN (%)	$\delta^{15}\text{N}$ (‰)
82.5	3.83	-24.64	0.37	2.64
83	4.07	-24.75	0.40	2.31
83.5	4.01	-24.65	0.43	1.99
84	4.20	-24.67	0.42	2.07
84.5	4.23	-24.65	0.43	1.82
85	4.31	-24.51	0.44	2.42
85.5	3.28	-24.69	0.33	2.27
86	2.62	-24.75	0.27	1.71
86.5	3.08	-25.13	0.32	2.51
87	3.58	-25.13	0.35	2.53
87.5	3.67	-25.01	0.36	2.42
88	3.82	-25.18	0.36	2.60
88.5	3.83	-25.06	0.37	3.00
89	3.95	-25.04	0.39	2.88
89.5	3.87	-24.91	0.37	2.58
90	3.42	-24.79	0.35	2.55
90.5	4.22	-24.87	0.42	2.48
91	4.55	-24.96	0.45	2.55
91.5	4.43	-24.81	0.43	2.53
92	4.31	-24.85	0.41	2.88
92.5	3.72	-24.78	0.37	2.51
93	3.09	-24.84	0.30	2.40
93.5	3.73	-24.99	0.37	2.49
94	3.84	-24.87	0.38	2.56
94.5	4.13	-24.75	0.41	3.00
95	2.81	-24.76	0.28	2.91
95.5	3.46	-25.02	0.35	2.40
96	3.62	-24.90	0.35	2.73
96.5	3.33	-24.96	0.32	2.81
97	3.34	-25.02	0.31	2.67

Chemical and mineralogical data

Depth (cm)	TC (%)	$\delta^{13}\text{C}$ (‰)	TN (%)	$\delta^{15}\text{N}$ (‰)
97.5	3.53	-24.79	0.33	2.62
98	3.10	-24.96	0.30	3.01
98.5	3.39	-25.07	0.34	2.99
99	4.22	-25.34	0.40	3.10
99.5	4.49	-25.24	0.43	3.27
100	4.45	-25.14	0.43	3.03
100.5	4.04	-25.14	0.39	2.94
101	—	—	—	—
101.5	—	—	—	—
102	—	—	—	—
102.5	—	—	—	—
103	—	—	—	—
103.5	—	—	—	—
104	—	—	—	—
104.5	—	—	—	—
105	—	—	—	—
105.5	4.44	-25.66	0.40	2.88
106	5.05	-25.78	0.45	3.16
106.5	4.73	-25.63	0.44	2.97
107	4.88	-25.58	0.46	2.87
107.5	4.65	-25.26	0.43	2.60
108	4.16	-25.19	0.40	2.40
108.5	4.56	-25.31	0.42	2.67
109	4.73	-25.32	0.44	2.60
109.5	3.82	-25.08	0.37	2.48
110	4.15	-25.34	0.39	2.79
110.5	5.25	-25.36	0.49	2.54
111	4.95	-25.17	0.47	2.90
111.5	3.33	-25.14	0.33	1.87

Depth (cm)	TC (%)	$\delta^{13}\text{C}$ (‰)	TN (%)	$\delta^{15}\text{N}$ (‰)
112	3.04	-25.01	0.28	2.91
112.5	6.59	-25.29	0.97	-8.77
113	4.32	-24.95	0.42	2.44
113.5	4.20	-25.06	0.40	2.65
114	4.32	-25.18	0.41	2.55
114.5	3.70	-25.12	0.36	2.29
115	3.22	-25.24	0.31	2.70
115.5	4.20	-25.29	0.41	2.41
116	4.05	-25.21	0.39	2.34
116.5	3.90	-25.21	0.37	2.58
117	3.84	-25.12	0.37	2.65
117.5	1.79	-25.35	0.18	2.07
118	3.41	-25.27	0.32	2.04
118.5	2.90	-25.22	0.27	1.82
119	3.17	-25.34	0.31	2.42
119.5	3.79	-25.31	0.36	2.54
120	3.91	-25.24	0.37	2.76
120.5	3.78	-25.09	0.36	2.52
121	3.68	-25.02	0.35	2.67
121.5	4.00	-25.32	0.36	2.90
122	4.23	-25.16	0.38	2.37
122.5	3.78	-24.92	0.36	2.72
123	4.06	-24.92	0.38	2.52
123.5	3.71	-24.85	0.38	2.06
124	4.23	-24.82	0.41	2.65
124.5	4.85	-24.93	0.47	2.46
125	3.06	-25.23	0.30	2.04

Table B.3. Chemical elements XRF core-scanner measurements from PE12-01-01 core (in cps).

Depth (mm)	Al	Si	K	Ca	Ti	V	Cr	Mn	Fe	Zn	Rb	Sr	Zr
25	977	33309	20773	9023	10844	1632	1350	2120	132416	939	4764	2740	7374
26	1037	33250	21083	9367	10516	1385	1030	2567	132692	977	4752	3012	7756
28	759	31456	22747	9767	13511	1414	1454	2358	156390	979	5172	3212	9899
30	751	31829	27055	10769	15257	1669	1081	1953	163673	997	5198	3166	11496
32	1371	39020	30380	11585	16810	1504	1003	2367	174093	1124	5681	3523	8019
34	1690	43868	35197	12957	18090	1708	1275	2274	178984	1092	5703	3555	9445
36	1919	47674	40699	13559	20882	1748	1591	2485	201596	1146	5727	3592	9078
38	1749	46190	36428	12730	18300	1905	1254	2023	185695	1105	5737	3295	8080
40	1462	44221	35574	12085	17902	1966	1348	2353	181137	1068	5714	3479	8674
42	1493	43837	33887	12237	17849	1813	2045	2621	176769	1165	5364	3695	9902
44	1550	46204	35698	13038	17666	1517	1312	1876	178231	1011	5648	3824	9344
46	1630	43803	36544	12964	19183	1977	963	2097	181274	1098	5868	3729	10830
48	1395	41297	33681	13623	18084	1801	1792	2746	177558	1102	5662	3541	9065
50	1323	40796	33934	12157	16942	1966	1390	2019	173454	1178	5455	3161	9908
52	1266	37951	28874	11170	15460	1907	1291	2224	167462	1068	5157	3356	9022
54	1648	41372	28477	10837	14405	2096	1520	1933	151886	1001	5024	3002	8930
56	1348	38206	23974	9611	12044	1378	1577	1623	137718	1023	5028	3077	7067
58	1389	39797	29886	11250	15579	1482	1499	2241	167009	1030	5060	3288	9093
60	1889	46458	37684	13016	19514	1555	1367	2267	193402	1105	5529	3219	9520
62	1459	42131	35864	12097	17581	1758	1116	2025	182401	1030	5161	2942	9168
64	1711	44464	32902	11865	16862	1690	1733	2283	171862	1002	4922	3060	8504
66	1805	47026	37644	13490	17542	1586	1251	2366	175962	1109	5195	3092	7945
68	1663	44511	38029	13384	18288	1993	1118	2695	182561	1208	5189	3026	10465
70	1819	46463	36875	13452	18893	1677	1525	2055	188344	1174	5455	3169	9194
72	1583	42743	30839	12311	17076	1903	1065	2053	173450	1092	5204	3135	9946
74	877	34301	22809	9579	12605	1054	395	1811	153404	1078	5221	3121	8800
76	1366	40764	30394	11213	15316	1841	1606	2343	166103	1035	5158	3047	9211
78	1311	41427	32221	12137	16086	1852	1675	1850	171145	1069	5102	3214	10085
80	1457	42246	33892	12307	16771	2139	1660	1926	178958	1139	5455	3226	11395
82	1550	42421	33107	12184	17210	1721	1574	2159	180224	1098	5317	3242	9198
84	1251	40152	31896	11550	16566	1774	1213	1946	176261	1113	5387	3005	10208
86	1786	44962	35976	13183	18540	1573	1784	2450	192087	1085	5463	3131	10566
88	1772	42856	33936	12924	18559	1800	1303	2285	192081	1088	5516	3336	10958
90	1712	44088	34010	12213	17799	1469	1237	2035	185143	1104	5256	2943	9624

Depth (mm)	Al	Si	K	Ca	Ti	V	Cr	Mn	Fe	Zn	Rb	Sr	Zr
92	1658	45378	34166	13051	18767	2003	1217	2174	188883	1106	5499	3208	10344
94	1799	46474	37147	12572	18402	1504	2068	1965	185121	1081	5369	3012	9875
96	1396	39666	32814	12189	17627	2034	1710	1985	182623	1184	5587	3147	10340
98	1886	44711	31625	11996	18104	2152	1234	1932	181083	1120	5341	3096	11465
100	2434	52697	35480	12139	19410	1990	1631	1615	184686	1084	5529	3242	9302
102	2096	47149	33143	12248	18634	1809	1386	2297	179725	1090	5578	3165	9314
104	1614	44205	34749	12273	18529	1932	1343	2036	184808	1167	5669	3054	11266
106	1624	42897	33281	11291	17843	1842	1255	2176	184816	1190	5408	3179	9782
108	1995	48155	36795	12574	17437	1518	1014	2737	179966	1064	5487	3533	10619
110	1864	48132	37285	12215	19254	1360	1216	2316	185076	1079	5808	3578	10418
112	2128	48430	38193	12796	19305	1699	1605	2434	194793	1128	5599	3246	10699
114	2084	50353	38399	13476	18430	1564	1708	2340	192614	1120	5659	3349	11065
116	2323	52289	39506	13857	19855	1837	1194	1967	197051	1135	5618	3274	11514
118	2598	56773	43280	14358	19856	1823	1593	2358	198585	1190	5566	3294	10979
120	2762	54756	42758	14004	20407	1811	1037	2452	201291	1214	5889	3268	12886
122	1608	45018	36469	12982	18942	2100	1269	2153	194556	1148	5711	3273	11533
124	1882	48024	37404	13204	19088	2026	1278	1951	200671	1188	5558	3199	10675
126	2139	51063	39042	13520	18887	2308	1753	2313	194951	1245	5758	3185	9105
128	2129	50941	40512	13669	19664	1771	1840	2361	204868	1234	5669	3221	9548
130	2012	48402	36737	12149	18460	1670	1685	1747	191347	1109	5577	3173	10402
132	1978	48664	36374	12961	18374	2134	1324	2077	190608	1110	5491	3126	10405
134	2397	54613	43387	14231	20476	2584	1522	1948	200299	1222	5590	3316	9794
136	2382	53413	41923	14834	19426	1646	1111	2212	201585	1147	5540	3228	9259
138	1992	49668	38338	12644	18038	2053	1760	2338	190331	1189	5546	3280	8077
140	1908	48611	36134	12623	18659	1871	1606	1876	184281	1204	5605	3191	9953
142	1595	45083	33587	11960	17899	1917	1664	2013	181120	1117	5372	3089	10019
144	2391	52975	41241	13746	19342	1837	1236	2154	193371	1139	5225	3049	9453
146	1603	44159	35089	12407	18791	2295	1831	2325	194048	1169	5571	3182	10411
148	1361	39058	26012	9559	14488	1707	1745	1979	162460	1086	5342	3086	8982
150	1738	46412	35484	12295	18060	1776	1729	2034	185371	1083	5375	3079	8747
152	1755	46992	37447	13406	18797	2178	1776	2121	192194	1125	5519	3291	9576
154	1526	41807	33677	12369	16667	1507	1637	2576	183461	1166	5456	3018	9456
156	1935	46342	34315	12779	18912	1660	1221	2005	188559	1155	5459	3270	10405
158	2349	51580	41971	14401	20028	1725	1718	2252	197420	929	5366	3262	9624
160	2157	51568	42085	14147	21227	1776	1607	2267	199100	1028	5162	3312	10932

Chemical and mineralogical data

Depth (mm)	Al	Si	K	Ca	Ti	V	Cr	Mn	Fe	Zn	Rb	Sr	Zr
162	2094	49944	38516	14203	20132	1655	1439	2263	195025	1064	5456	3261	11749
164	2026	48896	40476	14118	19546	1938	1922	2514	195280	1057	5306	3151	9537
166	1752	44707	36906	12962	17925	1803	990	1710	186232	1015	5443	3091	9678
168	1735	44985	36505	12646	18213	2059	1387	2144	190702	1094	5289	3099	9464
170	1522	43745	35988	13846	19571	1647	834	2060	194636	1079	5349	3223	9454
172	1596	42022	35998	12801	19321	1733	1655	2492	195014	1111	5635	3360	11034
174	1405	39536	32761	12298	17340	1949	1597	2370	183989	1082	5611	3091	10830
176	1414	40892	33751	12056	16914	1513	1488	2094	171193	1070	5526	3380	9694
178	1513	41369	34815	12189	16308	1533	1476	2210	171732	993	5045	2857	10611
180	1247	39166	30422	11568	16403	1637	1387	2006	176738	1126	5448	3162	12021
182	1152	36112	29161	10679	16466	2212	1507	1771	175745	1092	5525	3171	10968
184	1248	40125	31742	12185	17579	1948	1198	2748	176840	1113	5319	3363	10017
186	1467	40672	33222	11952	17359	1457	839	2219	185205	1156	5626	3514	11022
188	1275	39652	31165	12462	18468	1803	1583	2070	186008	1246	5563	3316	9990
190	1536	41935	34475	12513	17794	1955	1431	1726	186957	1288	5292	3024	12264
192	1267	39232	31676	12245	16869	2320	1152	2151	177892	1150	5519	3396	10893
194	1311	40839	34758	12153	18617	1572	1484	2035	193699	1049	5544	3161	9297
196	1394	41870	32717	12548	17494	1728	1204	1895	183478	1170	5511	3266	9546
198	1333	41147	33278	13063	17728	1960	1273	2413	183578	1137	5426	3289	8774
200	1167	37452	31610	12161	17087	1745	1324	1923	184214	1126	5468	3406	9338
202	1117	35545	28321	10836	15880	1546	1447	1773	169045	1154	5376	3103	10288
204	1290	38357	27964	11236	15178	1572	1686	1788	165587	1128	5582	3421	10019
206	1428	40354	30354	11248	16157	1672	1803	2529	173101	1086	5661	3244	10155
208	1290	40466	31139	11551	15692	1397	1714	2174	168576	1075	5151	3191	9920
210	1179	38264	30639	11257	16238	1538	1272	1967	171755	1035	5590	3398	9831
212	1491	40613	32567	11590	17642	1912	1355	1918	183935	1151	5290	3144	13550
214	1329	39311	33941	13272	17128	2141	1670	2140	191780	1123	5611	3579	11936
216	1663	45246	41852	14605	20061	1679	1503	2115	202482	1012	6720	4692	11371
218	1707	45189	35808	13793	17738	1404	1147	2453	185686	1163	5878	3419	12348
220	2530	51831	41639	15895	19945	1733	1363	2209	195583	1092	5662	3668	11229
222	2029	50420	43427	14825	22112	1982	1543	2589	197661	1173	5747	3695	11076
224	1481	42195	36795	14260	18767	1878	1321	2156	182366	1123	5662	3283	11814
226	1043	37734	30869	11945	16807	1577	1484	2375	173706	1189	5528	3368	11739
228	729	30695	22721	10733	14661	1649	1314	2003	155747	1226	5409	3280	9830
230	458	27733	18479	8198	12528	1921	1144	1917	149850	1122	5282	3123	9197

Depth (mm)	Al	Si	K	Ca	Ti	V	Cr	Mn	Fe	Zn	Rb	Sr	Zr
232	1255	40655	27255	11014	13762	1383	894	1720	156716	1176	5356	3197	9805
234	1752	43407	33003	11829	15884	1860	1633	2121	168322	1025	5292	3146	9353
236	1526	40506	29072	10582	14824	2128	1100	1819	158999	1101	5296	3189	8671
238	1190	36392	28401	11284	16107	1910	921	1936	173110	1027	5137	3342	9349
240	1567	41800	34455	13321	17597	1757	917	2432	184526	1187	5569	3443	9023
242	1929	44707	36359	13202	17991	2128	1627	1982	183661	1103	5611	3410	10654
244	1555	44816	36454	12782	18213	2238	1524	2359	187499	1140	5393	3453	13181
246	1859	45301	35860	13031	18865	1842	1111	2211	187440	1096	5728	3105	10793
248	1889	47197	38719	13410	18849	1640	1190	2086	187466	1110	5496	3383	11485
250	1896	48348	38818	13513	19136	1636	1525	2354	191160	1232	5562	3466	10090
252	1958	48631	38850	15700	19171	1394	1558	2151	189910	1126	5634	3366	10757
254	1959	46448	36469	13966	19663	1365	1234	2171	184697	1073	5735	3611	10957
256	1523	41060	33830	12875	17917	1473	1091	1985	177705	1078	5705	3651	9522
258	617	28861	18955	8731	12315	1649	1078	1924	145957	1146	5274	3371	9666
260	693	29602	19011	8212	11543	1627	832	1395	132772	1087	5507	3625	8880
262	978	31616	18414	7882	11168	1659	1024	1830	128639	1065	5129	3199	9709
264	897	31792	16862	7574	9645	1460	572	1735	116375	853	5238	3559	10519
266	915	32858	21284	9283	10524	1297	1029	1928	128632	934	5225	3684	9306
268	1056	34696	21242	9907	11370	1353	961	1321	128345	897	4915	3547	9436
270	1786	43296	33805	12958	16993	1521	2042	1553	169487	936	4992	3469	9703
272	1561	41544	35022	12495	19267	2204	1801	2335	185618	957	6031	4101	9741
274	1594	42598	37149	14550	18627	1737	1537	2234	169962	880	5938	4817	9072
276	1800	46236	40976	15343	18707	2047	1489	2545	185754	959	6323	5345	12067
278	1206	39201	37196	13837	18988	1522	1255	1434	190306	1148	6763	5333	11648
280	1204	36417	34977	13125	18839	2122	1505	2228	184694	1188	6584	5132	8938
282	878	33547	29655	11950	15914	1840	1947	1995	164992	1017	6324	5637	10593
284	1339	39006	30742	11924	16047	1857	1877	2400	155955	929	6079	5674	12056
286	1535	41531	33731	12833	17937	1677	1020	2309	171673	919	5638	4991	9741
288	1565	40477	35536	15676	17927	2011	1144	2150	172522	1020	6752	4707	9139
290	1944	46060	40507	16125	19079	1803	1143	1926	190387	1140	5998	4605	9327
292	1526	39616	31587	12239	15732	1739	1002	1444	163472	1128	6432	4665	10549
294	1797	44402	36343	13764	20098	1985	1577	2198	175952	1028	6064	4985	10291
296	2476	52395	44868	14804	21419	1491	1710	2437	194338	1074	6121	4081	11167
298	2312	52625	45819	15700	21099	1742	1025	2019	193799	1090	6129	4293	11105
300	2305	50128	42100	15133	20389	1638	1763	2012	194441	1195	6187	4013	10001

Chemical and mineralogical data

Depth (mm)	Al	Si	K	Ca	Ti	V	Cr	Mn	Fe	Zn	Rb	Sr	Zr
302	2276	50589	45833	15380	22243	1720	1252	2918	209895	1057	6601	3936	10534
304	1997	47549	43984	14428	18908	1608	1443	2975	186644	1089	6160	4543	11284
306	1445	40522	38819	13963	17358	1676	1166	2261	168334	946	6361	4419	10453
308	1819	44579	40396	14215	20380	1844	1481	2446	190788	1018	6694	4472	9629
310	1798	46337	42665	14774	19370	2036	1655	2230	184296	955	6420	5053	10708
312	1620	44824	40780	15876	19634	1877	1220	1896	186473	1044	6341	4564	13899
314	1768	43202	38983	15768	18517	1908	1184	2454	175584	1008	6289	4603	11799
316	1597	41672	35838	13640	18949	1384	1060	2273	184388	952	6200	4101	10217
318	1333	37006	27865	11676	16006	1595	1390	2040	162019	1017	5950	3964	10864
320	1266	37168	26057	10443	12807	1481	1050	1742	129279	1043	6193	4256	10746
322	1606	37989	24669	9907	11651	1168	1691	1265	121343	877	5559	4018	12610
324	1404	37484	28512	10834	13378	1461	1305	1363	135810	890	5483	4052	13004
326	1062	32695	23192	11066	13094	1413	1006	1504	138801	817	5144	4048	11881
328	884	31510	23328	9426	12315	1429	208	1794	134747	902	5390	4428	10047
330	1979	46697	38987	14048	17864	2492	1511	1853	166498	852	6021	4687	9724
332	1606	43132	38853	13296	20195	1433	1554	1894	188093	852	6180	4643	11255
334	1727	43893	37341	14007	18533	1761	1197	2000	181817	1063	6251	4661	12870
336	2238	51996	41925	14056	21351	2374	1660	2345	189154	1045	6425	4837	13551
338	1662	42526	40966	13398	18680	2155	1271	1289	175082	983	6182	4436	13771
340	1565	41342	37181	13160	18204	1453	1276	2101	178833	1035	6606	4839	11147
342	1908	46528	41301	14863	18997	1945	1880	2108	172951	911	6509	4717	10420
344	1960	48621	41696	13885	18805	1579	1700	2157	181012	943	6130	4517	11619
346	1893	46512	40764	13333	19498	1626	1025	1949	188999	969	6292	4217	11913
348	1877	42829	36325	12357	17148	1740	1331	1624	169135	912	6055	3723	10639
350	1866	46656	38638	13100	19805	2328	1275	2518	184028	1009	6272	3714	8445
352	1976	47048	39429	14332	19139	1711	1088	2231	188791	1097	5953	3512	9361
354	1573	42670	38391	13508	19548	2043	1508	2428	193965	1111	6015	3517	11174
356	1581	41128	37061	14751	18569	2261	1155	2304	187902	1169	6247	3621	11750
358	3001	56999	40979	14646	19869	1732	1789	2617	191735	1014	6027	3574	11827
360	1898	45758	38977	14426	19848	2023	1637	2337	196397	1054	6022	3417	11056
362	1649	43015	38215	14155	19467	1616	1895	1682	191735	1206	6289	3681	10642
364	2005	47801	41985	14657	20411	1458	1364	1889	191644	1190	6104	3709	10641
366	1919	45945	37024	13718	19801	2100	1811	2680	194477	1160	6395	3523	11015
368	1995	48548	40911	15008	21349	1902	1681	1752	199087	1172	6331	3861	10193
370	1728	44646	38570	13076	20049	2031	1000	2519	195761	1093	6498	3715	10715

Depth (mm)	Al	Si	K	Ca	Ti	V	Cr	Mn	Fe	Zn	Rb	Sr	Zr
372	2125	50297	42628	15510	20731	1651	1523	2017	201886	1154	6277	3765	12063
374	2525	52628	44007	15550	20644	1676	1420	2311	201595	1025	6314	3761	12311
376	2722	56007	48534	16502	21583	1423	1711	2270	207470	1182	6372	3855	11689
378	1968	48286	42446	15360	20077	2008	2430	2142	198142	1075	6353	3752	13378
380	2027	45952	37020	13718	19348	2201	1232	2209	188196	1090	6431	3904	14540
382	1828	43340	35020	13379	19609	2252	1277	1799	189658	1155	6251	3620	10466
384	1304	35678	28728	10676	16297	1995	1052	1961	174718	1088	6304	3476	11201
386	1640	42773	35833	13610	18838	1642	1315	2019	181501	1143	6240	3838	13063
388	1801	44994	37354	13472	18426	1149	1540	2279	187175	1039	6412	3595	11420
390	2149	48506	41158	13877	19754	1893	1500	2540	192285	1082	6240	3792	11920
392	2068	49570	42450	14815	21263	1748	2109	1960	204425	979	6387	3968	12943
394	2254	49292	44146	15056	20934	1888	1265	2019	198016	1128	6561	3861	12453
396	2310	49828	41923	14424	19857	1807	2128	2436	197379	1108	6468	3873	12484
398	2190	49084	41884	15727	20052	2327	1566	1914	194534	1172	6524	3752	12506
400	1699	42463	36079	13533	17516	2057	1227	2036	183266	1052	6263	3836	12622
402	1699	44923	36813	13731	19425	1326	1625	2214	189213	1040	6446	3651	12626
404	2087	47354	37940	13440	18458	1704	1185	2429	189944	1218	6293	3832	11465
406	2188	48951	40050	14032	20045	1459	1284	1540	186651	1079	6413	3778	12031
408	1514	40924	31663	12134	16178	1883	1224	1992	157233	1023	6206	3625	11727
410	1196	34891	21791	8660	10181	1483	1142	1837	120495	1042	5788	3449	11533
412	955	33714	18692	8604	9717	1586	1249	1432	112795	875	5015	3200	10947
414	552	29474	13148	7478	6949	1473	393	1303	87422	804	4633	2764	9494
416	621	29729	13739	6817	6887	1584	950	1536	85924	804	4294	2635	7366
418	622	28680	13153	6641	6201	1178	998	1244	90532	818	4400	2712	7878
420	620	29105	14630	6851	6944	1589	1038	753	89647	827	4563	2788	8437
422	730	28352	14733	7369	8225	1650	1332	1289	100557	823	4580	2865	9896
424	1185	34178	18645	7938	8567	1904	818	896	99083	825	4703	2962	7913
426	1078	33017	20309	8536	10904	1601	1136	1478	109612	873	5128	2870	8533
428	1514	39518	28230	11061	16120	1941	966	1762	158911	938	5611	3380	10035
430	2613	53181	42787	15038	20469	1693	2163	2407	194098	1099	6354	3789	11994
432	2852	57323	47990	17046	21713	1286	949	2708	207313	1071	6641	4096	11303
434	2767	58054	48046	16905	23104	1921	1464	2605	208755	1091	6771	4063	13261
436	2665	55898	47271	16238	22168	2061	1419	2376	201258	1182	6761	4422	12886
438	2212	50947	41258	16196	20211	1993	1529	2302	192638	1060	6827	4299	13311
440	2044	49800	40427	14358	19137	1666	1389	2710	181658	1039	6415	3874	10216

Chemical and mineralogical data

Depth (mm)	Al	Si	K	Ca	Ti	V	Cr	Mn	Fe	Zn	Rb	Sr	Zr
442	2175	52766	41615	15904	20213	1530	1509	2446	187848	1046	6099	3707	12683
444	2934	59209	46889	16353	21932	1881	1364	1996	207943	1093	6600	3850	12771
446	2878	60175	48396	16689	21606	1882	1306	2118	206835	1125	6652	3886	12445
448	2929	58441	47455	17020	21622	2188	1758	2223	197065	1072	6428	3882	11557
450	2667	54731	44649	15190	20586	1982	1382	3077	200221	1014	6592	3942	11136
452	3073	61053	49353	16264	21534	2010	1960	2578	201514	1045	6546	3851	11489
454	2861	57063	46196	16337	20768	1928	1783	2159	197667	1124	6490	3912	12804
456	2841	56819	45831	16495	21119	1681	1447	2123	203417	1085	6484	3764	12057
458	3109	59462	48571	17751	22028	2308	1311	2372	202142	1144	6399	3812	12358
460	2569	56619	48045	16593	21900	1824	1672	2513	204417	1170	6536	3749	12085
462	2868	57193	45759	16692	21603	1946	1413	2059	196453	1143	6531	3725	11373
464	3019	62381	50812	17435	22344	2121	1594	2656	207321	1155	6359	3825	12747
466	3029	60980	47434	17331	22399	1727	1363	2963	205421	1111	6443	3831	11654
468	3301	61619	49551	17901	22128	1888	2125	2388	203649	1187	6281	3716	10957
470	2919	57537	46397	17425	22484	1906	1905	2145	203592	1123	6320	3738	12379
472	3356	63158	51083	17426	22523	1372	1714	2005	208157	1191	6547	3642	10861
474	2538	55199	46977	16481	22243	1601	1311	2584	206947	1160	6342	3911	12787
476	3080	59101	49201	17640	22718	1704	1520	2588	211459	1180	6543	3725	12129
478	3375	64589	51831	18159	23373	1881	1813	3012	212114	1221	6615	3714	10128
480	2744	56793	47140	16866	22261	1533	1826	2152	206083	1104	6623	3672	11758
482	2443	52886	44466	15100	21685	2132	1720	1983	202429	1166	6407	3713	10757
484	3089	57214	47725	16023	22835	1946	1663	2522	205135	1203	6485	3750	10482
486	2913	57752	47075	15867	23120	2231	2097	2200	203993	1183	6512	4021	10539
488	2531	53809	46346	16383	22000	1648	2031	2765	204541	1161	6588	3850	12782
490	2442	52231	42602	15839	22181	2221	1841	2452	200963	1218	6457	3957	11543
492	2484	51847	42277	15414	21262	2094	1620	2978	204373	1132	6516	3786	11863
494	2386	49704	38338	14604	18987	1623	1404	2723	196059	1189	6446	3850	11173
496	1942	45837	36985	14536	19572	1941	1481	2222	190917	1158	6273	3924	11834
498	1186	36665	29272	12024	17724	2033	1150	1882	182840	1067	6455	3820	11122
500	1926	45749	35486	13930	18450	1780	1552	1852	183311	1107	6255	3814	11483
502	2033	46365	34449	12797	18086	1861	1511	2110	177382	1106	6465	3888	11349
504	1791	44396	35933	13976	18355	1901	1247	2704	188575	1071	6355	3760	11831
506	1983	47129	38265	14295	19462	1996	1685	2514	190754	1185	6399	3890	10763
508	1977	47299	39280	14490	19994	1929	1600	2294	195771	1145	6576	3903	12516
510	2177	51948	44497	16367	21756	1796	1673	2639	202060	1187	6756	4026	11890

Depth (mm)	Al	Si	K	Ca	Ti	V	Cr	Mn	Fe	Zn	Rb	Sr	Zr
512	2826	57337	49078	17072	21968	1902	1659	2494	208860	1212	6481	4230	12601
514	2544	54518	47650	16356	21694	1925	1557	2825	209779	1180	6665	4083	10273
516	2137	48028	42354	15636	22087	1842	1897	2317	208213	1270	6642	3922	12100
518	2010	48080	41590	15663	20526	2329	1072	2369	205983	1222	6735	4059	10759
520	2459	51423	45259	16798	21838	2027	1532	2575	208903	1227	6627	4080	12342
522	1532	40906	35950	13980	19607	1738	1336	2514	193893	1051	6743	4127	13023
524	1110	37150	31481	13135	18094	1555	1353	1841	190076	1114	6714	3958	10855
526	1406	39362	31974	13524	18441	2038	1756	2376	191243	1160	6720	4111	10996
528	2199	51626	44810	16478	21146	1755	1683	2860	205338	1139	6658	3988	10347
530	1810	45034	40890	15558	19576	1492	1282	1931	195610	1199	6761	4121	10150
532	2186	48486	43949	16679	21379	1762	1316	2135	205459	1202	6916	4188	10373
534	2356	55417	53084	18271	23187	1859	1720	2501	215353	1221	6801	4060	10818
536	2948	55944	54970	18839	23460	1649	1817	2302	217794	1240	6732	4253	10372
538	2640	55808	49716	18229	22530	1585	1480	2816	211138	1161	6447	3639	11395
540	2804	54521	49238	17828	21836	1580	1633	2854	205156	1020	6259	4235	9210
542	1896	43870	42857	16056	19837	1766	1521	2007	179095	910	6432	4552	6901
544	2218	48532	47795	17660	18993	1250	2424	2061	182719	949	6030	4722	7255
546	1926	43371	42526	17564	20035	1406	1547	2456	177942	844	5766	4695	8423
548	1908	45302	42589	15926	17443	1531	1365	2815	164590	758	5453	3975	8756
550	1718	44201	40874	15584	17638	1096	1318	2078	160801	721	5190	3655	7407
552	1720	41766	31923	12828	13212	1417	1814	2116	128299	793	4552	3466	7363
554	2211	46058	27186	10234	10855	1449	1489	1340	103822	645	3933	3040	6575
556	1779	40808	29295	10694	11540	1023	2324	933	103735	622	4224	3062	5579
558	1591	39217	28811	12541	13142	1228	1660	1210	118472	590	4534	3911	5288
560	1582	41267	30769	12126	13722	1641	1287	1684	130410	718	4389	3172	5650
562	2209	46827	37035	14025	15107	1876	1505	1743	142399	624	3969	3570	5329
564	2432	49910	41592	15569	17285	1767	1730	2012	166976	706	4381	4172	6287
566	2256	47153	38558	14125	17777	2044	1602	2332	172371	695	4431	3971	6236

Table B.4. Chemical elements XRF core-scanner measurements from CIM12-04A core (in cps)

Depth (mm)	Al	Si	K	Ca	Ti	V	Cr	Mn	Fe	Zn	Rb	Sr	Zr
0	955	30561	17416	8324	7974	1624	607	1210	130191	916	6079	2815	9011
1	965	31240	19631	8314	9120	1266	1063	1616	144219	951	6425	2705	9255

Chemical and mineralogical data

Depth (mm)	Al	Si	K	Ca	Ti	V	Cr	Mn	Fe	Zn	Rb	Sr	Zr
3	788	30304	20528	9240	9833	1170	722	1940	148490	1063	6617	2800	9942
5	767	31268	18933	7674	8682	1311	1273	1323	136680	988	6577	2834	9429
7	1340	38152	27017	9829	10660	1612	1585	1686	145515	1055	6414	2827	9473
9	1692	39477	29283	10148	11520	1494	1263	1515	148465	1030	6576	2760	8956
11	1469	37523	27885	9328	11576	1633	1070	1218	145763	967	6543	2828	10698
13	1580	41139	31785	10464	12420	1196	1271	1638	159511	1094	6824	2821	8811
15	1879	42172	29406	10167	11734	1275	1252	1033	151077	974	6738	2995	9526
17	1396	37633	26162	9576	9586	1184	902	1738	127035	895	5781	2452	8292
19	949	29417	14365	6201	5997	1198	965	1550	100936	846	5534	2355	7244
21	914	30600	15181	7350	5867	1415	976	1245	87066	838	5796	2315	7253
23	1044	32154	16368	7004	5456	1041	972	1817	84896	868	5587	2481	7501
25	1553	37040	23920	8976	8978	1336	1117	1505	114546	1095	6122	2652	8284
27	1622	38536	27525	10401	10780	770	1243	1949	139096	1129	7040	3067	10493
29	1985	41733	31927	11403	12017	1290	1712	1438	149572	1203	7260	3172	10938
31	2425	44941	36143	13467	13446	1404	1355	1831	156319	1333	7359	3158	10749
33	1897	38577	25250	11082	9334	1153	1608	1631	125325	1166	6764	2982	10280
35	1347	33977	16907	7938	5898	1023	592	1338	95235	1008	6219	2677	7981
37	1516	35143	16324	7060	4872	1052	916	1364	70018	988	6186	2728	8963
39	2194	42030	30971	12069	10200	1144	1774	1597	127110	1091	7098	3215	11073
41	2561	47718	44630	15501	15636	1071	1913	2701	173909	1268	7977	3506	12256
43	2014	43691	42780	14818	16048	1717	1176	1646	180770	1333	8126	3518	12284
45	2374	44441	43001	14240	15310	1767	1606	1666	180939	1394	8198	3424	11234
47	2296	45472	41927	15911	16196	1415	1803	2350	178739	1273	8271	3234	10573
49	1898	40764	36589	12751	14611	1698	1252	1017	168932	1173	8243	3354	10124
51	1725	38264	38002	13739	14410	1501	1328	1885	169588	1082	8705	3551	10407
53	1436	37123	32340	11499	12829	1617	1393	1862	156888	1119	8772	3583	10430
55	1677	36898	34788	13717	14479	1628	1738	1993	162701	1205	9318	3885	10017
57	1474	37366	33862	13356	13622	1503	991	2497	162031	1198	8720	3696	9602
59	1458	36151	34956	13087	13711	1374	1253	1839	167709	1236	8053	3492	11422
61	1609	39209	38707	13726	15094	1642	1726	1958	173539	1289	8210	3340	11318
63	2003	41450	40229	15256	16281	1792	1834	1540	181020	1200	8237	3431	11545
65	2139	45421	44182	15206	16660	1723	1300	1914	188155	1266	8420	3421	10594
67	2516	47710	48060	16037	16947	1530	1619	2052	193847	1150	8516	3518	12311
69	2099	44674	43928	16795	17609	1841	1100	2076	191800	1211	8471	3458	11438
71	1514	37435	38320	15000	15830	1626	833	1756	182546	1234	8324	3479	11030

Depth (mm)	Al	Si	K	Ca	Ti	V	Cr	Mn	Fe	Zn	Rb	Sr	Zr
73	1145	33982	34777	13879	15105	1201	661	1660	179131	1206	8415	3527	10821
75	1100	32241	28514	12081	13143	1512	1425	2206	169465	1222	8305	3609	9900
77	782	30896	25151	11443	11350	1417	1355	1503	149439	1159	8588	3600	10828
79	522	27653	20234	9815	10246	1211	907	2022	146049	1122	9412	3555	10513
81	689	30301	28142	13324	11239	789	889	1010	140199	1283	11924	4231	10660
83	890	30152	25214	13059	11577	1590	1116	1416	140924	1203	12078	4285	9787
85	850	29439	24415	10388	10424	1479	1029	828	136168	1138	9974	3891	8935
87	858	30302	28143	12723	13064	1889	1020	1813	154518	1162	9229	4144	9285
89	725	30723	26419	11196	11171	1850	1133	1327	147875	1184	8690	3923	10042
91	811	31437	27862	14390	13235	1414	1080	1162	157693	1231	8095	3291	10801
93	887	31929	32025	15900	13836	1793	1528	1799	169578	1197	8513	3283	11874
95	976	31409	31769	16078	13882	1737	1247	1752	171562	1333	8934	3466	11026
97	981	31599	32696	15564	13792	1627	1202	1891	164757	1172	8829	3422	10705
99	821	31363	31269	15393	13592	1385	1275	1960	170787	1194	8812	3602	10483
101	944	31816	32724	16402	13986	1769	1361	1839	170881	1102	8398	3718	10269
103	1016	31184	33271	16547	13682	1724	843	1958	168788	1226	8507	3703	10941
105	837	30642	33418	17459	13918	1639	1185	1375	172253	1200	8834	3607	11765
107	916	30243	32035	16925	14678	1654	1723	2058	179017	1279	8318	3445	12231
109	635	29657	32717	16256	13974	1370	1848	1525	175890	1232	8373	3365	11564
111	786	30647	32755	15588	14506	1747	1255	2182	176689	1355	8517	3458	11726
113	991	31871	34511	15512	14707	1646	1055	1781	178687	1261	8289	3400	12240
115	631	29006	29441	15018	14411	1426	1481	1833	175488	1263	8296	3395	11788
117	525	28691	30075	14824	13682	1951	1254	1466	167776	1212	8303	3400	12283
119	930	29860	28324	13514	13699	1726	1361	1667	171495	1209	8417	3377	12122
121	910	32318	30667	13977	13899	1517	1204	2008	170112	1299	8322	3553	12936
123	661	28692	26493	12868	12861	1400	1157	1912	162903	1184	8249	3207	10476
125	843	29464	25290	12682	12080	1647	1319	1621	154662	1243	8375	3639	12293
127	792	28114	22769	12296	11380	1259	1485	1255	145991	1153	9209	3698	10820
129	829	30548	23944	12877	10967	1431	1090	1483	150675	1128	9862	3971	10040
131	919	30855	26842	14476	11561	1197	1235	1577	146318	1102	9449	4117	10214
133	794	29371	26787	15221	12045	1604	914	1925	158678	1097	9667	4249	10103
135	697	28747	30362	15020	14967	1344	1309	1812	168946	1115	9846	4071	10558
137	850	29025	30572	16140	13687	1557	1082	1577	171938	1112	9881	3926	12043
139	777	31172	32916	16167	14738	1267	1445	1747	180422	1242	9710	3721	11790
141	861	30962	29894	14539	13178	1660	737	1571	167841	1229	9093	3846	11502

Chemical and mineralogical data

Depth (mm)	Al	Si	K	Ca	Ti	V	Cr	Mn	Fe	Zn	Rb	Sr	Zr
143	886	29582	26311	14897	12107	1293	849	1649	164607	1189	9286	3705	11070
145	1007	31721	32687	16284	13746	1360	710	1801	178472	1215	9234	3748	13091
147	846	31250	31306	16174	13614	1537	583	1842	178868	1227	9205	3860	11895
149	1011	33406	36790	18343	15605	1725	1507	1662	187420	1301	9078	3774	11313
151	1047	32625	39274	19494	16163	1862	1352	2115	193288	1228	9017	3784	11729
153	1118	34832	44603	18636	17157	2002	1219	1850	196557	1299	8830	3551	12038
155	978	33629	43350	19619	17431	2028	1172	1811	193186	1296	8947	3610	12992
157	1182	33915	41048	20523	17187	1766	1582	2283	191180	1230	9152	3708	10883
159	962	33236	42708	19995	17385	1607	1149	1732	191340	1291	9514	3917	12651
161	979	32866	42378	19174	17766	1997	1717	1763	205376	1292	8889	3584	12306
163	778	31866	39338	17843	16379	1455	846	1695	196778	1246	8992	3493	13562
165	918	31145	36137	16543	15722	1844	1245	1788	187104	1264	8909	3636	11801
167	838	30288	34179	16651	15581	1584	1248	1670	189463	1207	9147	3581	12290
169	1171	33658	38704	17694	15463	1506	721	1628	186447	1219	9233	3555	11199
171	1288	34238	36691	16583	15462	1523	1127	1821	183311	1171	9344	3734	11856
173	1180	34803	39430	14901	14983	1358	709	1605	177318	1195	9487	3723	11849
175	1336	36438	40836	17453	15593	1527	996	1643	185050	1110	9387	3758	11544
177	1390	38675	45815	17368	16476	1749	1749	1918	185050	1173	9935	3990	10915
179	1533	39641	46406	16978	16682	1559	1628	1655	188741	1127	9689	4063	12103
181	1718	40235	47227	15965	17446	2029	1338	1783	195505	1136	9324	3562	11026
183	1423	39317	46432	16622	17232	1732	991	1417	191475	1145	9249	3658	10856
185	1678	41496	47238	15725	17173	1638	1455	1599	190391	1071	9045	3519	11450
187	1979	44949	49840	15968	17535	2174	1376	1105	192778	1144	9344	3565	12070
189	1815	43156	46896	13948	16592	1629	1830	1787	191131	1159	9318	3577	10936
191	1618	40964	45708	14081	17553	1987	1474	1682	191136	1130	9409	3615	11292
193	1914	42909	47495	15633	17026	1857	1050	1648	190476	1144	9263	3712	11714
195	1115	33243	30160	10912	12347	1496	1097	1268	155026	1047	9301	3765	11917
197	1175	33648	21364	9877	8753	1477	1085	1709	118322	1178	9461	3486	9295
199	867	29854	23909	9072	10398	1036	1214	1736	118857	913	10556	3912	11610
201	1640	38625	37342	13799	12745	1381	1802	1976	148338	876	10140	4144	10046
203	1943	44215	44150	14949	15914	1797	1614	1655	184703	1009	9039	3777	9444
205	2914	52114	54961	19435	19561	1901	1397	2034	207593	1182	8889	3686	10623
207	3670	57972	56219	18156	18146	1464	1490	1435	202963	1157	9146	3610	11590
209	3950	64059	64004	20219	19571	1809	2425	2374	198266	1158	9313	3871	11792
211	3477	59631	59605	21092	20830	1578	1403	1713	199845	1130	9369	4123	11725

Depth (mm)	Al	Si	K	Ca	Ti	V	Cr	Mn	Fe	Zn	Rb	Sr	Zr
213	3060	54448	53076	18730	19292	2047	2092	2192	209899	1160	9953	4317	9968
215	2710	50362	50429	18598	17619	1417	1358	2421	181962	1079	9410	3692	11466
217	1801	42445	40471	14402	17179	1415	1622	1500	158665	845	9238	3532	12597
219	1501	37742	30650	10619	10153	1258	1699	1429	123562	1053	8360	3333	10658
221	824	29020	15938	6650	6062	782	1417	1327	85268	988	7771	3207	10242
223	901	29417	12604	5086	4125	1266	767	1161	59756	850	6850	2986	9087
225	651	26191	6594	4771	3358	1066	582	1708	50487	820	6920	2554	11137
227	402	24057	5624	5600	4760	1439	1191	1519	79406	879	7410	2993	10832
229	1105	33752	31184	11088	12191	1023	945	1371	148381	927	7873	3154	10173
231	2447	49359	49598	15757	17384	1232	1226	1924	191091	1133	8841	3340	10487
233	2788	52400	53359	14563	17536	1512	1690	1251	198724	1173	9177	3645	12411
235	2989	52623	52542	16501	17816	1595	1901	1853	193333	1255	9292	3659	11366
237	2965	53411	50582	13921	18343	1963	2061	1944	194881	1183	9184	3604	11879
239	3207	55561	53749	14740	19461	1863	2058	1622	196270	1100	9341	3669	10695
241	2886	52328	50548	14158	18390	1485	1960	1854	199817	1138	9085	3725	13063
243	2641	48092	45886	14225	16451	1844	1680	1632	195986	1190	9235	3578	11178
245	2757	49744	49661	13154	17449	2122	1576	1491	195311	1123	8975	3565	12144
247	2631	50928	49522	13785	17975	1428	1680	1727	196742	1074	9159	3498	12236
249	2591	47924	44349	12790	17590	1924	1792	1586	188259	1285	9293	3345	12367
251	2551	47179	43688	12138	16358	1599	1421	1484	188522	1185	9058	3574	11366
253	2745	49369	49528	12614	17674	1687	1834	1702	197332	1135	9048	3669	11804
255	2291	44944	45642	12404	16608	1852	1797	1744	197017	1162	8830	3571	11012
257	2465	48090	44509	12204	15588	1733	1634	1685	190230	1182	9510	3585	10929
259	2190	44766	43905	14034	16214	1615	1555	1479	192284	1197	9397	3379	11228
261	2392	43896	43536	12491	15432	1724	1461	1482	189070	1152	9024	3790	11144
263	1995	43663	46498	13364	17267	1737	1042	2208	191658	1234	8956	3557	12497
265	2499	46854	48157	13756	18027	1811	1428	1565	196756	1207	9138	3498	14263
267	2281	46669	47720	13014	18484	1964	1489	2035	196092	1107	9271	3489	12231
269	2112	43514	43408	13785	17582	1531	1065	1532	193253	1160	9021	3491	11513
271	2596	46197	46647	13014	16910	1800	1564	1260	190164	1273	9030	3488	11486
273	2276	46678	49582	14510	17892	1842	1834	1835	197653	1237	9483	3609	10772
275	2064	44237	46643	13344	17607	1432	1591	1853	189110	1167	8821	3431	12378
277	2123	43444	44277	12864	15948	1501	1410	1754	185704	1199	9068	3397	12585
279	1555	38798	41205	12005	14288	1192	379	1269	178036	1127	9408	3595	11757
281	1579	39705	41854	14844	15517	1372	1283	1813	180893	1126	9066	3449	11335

Chemical and mineralogical data

Depth (mm)	Al	Si	K	Ca	Ti	V	Cr	Mn	Fe	Zn	Rb	Sr	Zr
283	1824	40643	45383	13608	16614	1295	1404	1594	184111	1183	9092	3335	10843
285	1311	37092	43857	13402	16345	1115	1034	1499	179780	1113	9315	3592	12252
287	1593	40894	45753	13748	16279	1702	1802	1959	181573	1069	9225	3478	11302
289	2049	45434	47757	14989	17237	1461	1467	2035	190580	1132	9167	3527	10986
291	2246	46974	50059	13715	15465	1457	1883	1574	185345	1155	9297	3515	11089
293	2740	50199	52233	14335	16723	1840	1238	1535	192337	1068	9407	3472	10922
295	1782	40424	41721	14414	15272	1871	1230	1715	179409	1160	9405	3440	12725
297	1759	41070	47002	13030	15450	1599	1772	1639	183356	1127	9567	3342	11104
299	2324	44091	48720	13286	15823	1739	1245	1811	186629	1129	9521	3552	11180
301	1639	40904	44598	13080	15791	1522	1238	2351	181266	1206	9494	3500	12711
303	1240	37553	40350	11920	15274	1668	1472	1311	180909	1127	9292	3580	13159
305	1970	42537	46841	14487	16784	1732	1403	1778	192602	1194	9143	3478	12769
307	2041	44288	47679	14599	16696	1523	1846	2264	194523	1305	8794	3608	11811
309	2408	47280	50713	15199	18318	1457	1954	2194	196298	1236	9362	3662	11833
311	2673	49766	53957	15773	17784	2023	1669	1721	191204	1067	9642	3683	13696
313	2703	50772	51892	15602	17276	1556	1755	1815	192607	1034	9119	3370	11912
315	2000	43374	47282	12979	16532	1605	1340	1981	196090	1131	8746	3458	10614
317	2069	44461	47451	14767	18157	1518	2170	1913	189966	1202	8749	3504	11063
319	2297	45994	45297	14307	16442	1650	891	1735	189805	1140	9263	3512	11130
321	2132	43964	50216	13917	16745	1133	1061	1567	196590	1142	9629	3607	11014
323	2170	45413	47316	14155	19254	1601	1186	1440	194067	1245	9266	3369	12151
325	1757	41245	46970	12627	16257	1602	1195	1451	181965	1282	9444	3619	10030
327	2222	46477	52805	13797	17496	1645	1156	1576	182956	1021	9489	3599	10191
329	2628	48101	50963	13723	18830	1899	1941	1704	196073	1141	9827	3345	11306
331	2993	53048	54819	15156	17008	1445	1675	1927	192113	1200	9264	3451	11606
333	2437	48742	50998	14598	16292	1504	1531	1546	182914	1122	9365	3693	10257
335	2061	41981	40551	12719	13941	1428	989	1251	155772	1130	9162	3384	11192
337	2441	45413	43787	11842	15033	1700	1319	1129	165303	1040	9357	3481	12030
339	2680	49161	49172	11917	17032	1623	1856	1498	192742	1205	9804	3680	11154
341	2416	46520	48587	12046	17314	1869	1466	1499	190474	1007	10251	3532	10991
343	2271	44783	47416	12111	15913	1363	1147	1783	175824	1098	10647	3799	10407
345	2066	44013	48949	12237	17127	1574	1135	1682	186246	993	10198	3539	11318
347	2310	44831	49347	12593	18009	1666	1526	1656	191814	1160	9764	3684	12835
349	2291	45088	48146	12575	17054	1201	1269	1577	184005	1113	9913	3705	12018
351	2200	45773	50945	12289	17730	1524	1223	1508	190148	1096	10564	3494	12086

Depth (mm)	Al	Si	K	Ca	Ti	V	Cr	Mn	Fe	Zn	Rb	Sr	Zr
353	2316	45305	50368	12256	16650	1562	620	1711	185945	1052	10273	3500	11459
355	2069	44632	50594	13431	17322	1507	1179	1835	181775	1149	10355	3520	13191
357	1468	36118	43630	12039	13928	1756	858	1601	168253	1002	10425	3749	12348
359	2007	40615	43788	11337	14657	1133	692	1326	164891	1001	10946	3766	12251
361	1852	38853	43333	10429	14162	1437	1028	1024	160088	1017	11791	3843	11697
363	1851	40331	45949	11572	15712	1692	1018	1558	172604	896	10940	3511	11190
365	1783	39708	37566	10592	12335	1617	712	2184	153833	1003	10281	3856	11795
367	1339	34908	32913	10141	12002	1317	1133	1398	151246	897	9875	3637	8778
369	1442	38236	38941	13439	15159	2002	1486	1472	183659	993	9350	3636	9756
371	1374	36204	35040	10228	15234	1465	809	1575	185979	1026	8690	3601	12049
373	1304	34712	36657	10785	15620	1691	1374	1716	184410	1037	8090	3530	12991
375	1355	34945	36872	9776	16850	1618	1472	2019	196157	1002	8454	3395	11662
377	1537	38586	41828	11098	16126	1941	1143	1693	194833	999	8301	3382	11996
379	1584	37464	39189	11258	15748	1999	1265	1920	192518	1160	8200	3434	11509
381	1088	33936	33909	10636	15832	1588	1303	1671	186272	1135	8426	3437	10063
383	964	28711	22543	7885	12265	1052	1567	1480	154122	1045	8212	3469	11070
385	1117	34326	33051	9715	14296	1881	1266	1453	177797	1088	7904	3113	11702
387	1141	32730	36309	10341	15591	1468	925	1414	190466	1087	7957	3428	11471
389	1198	34743	37729	11163	15034	1378	1226	1210	187856	1022	8087	3378	12084
391	999	32853	35936	10942	14437	1449	1344	1561	185795	1100	8116	3171	11687
393	1405	37561	40926	10705	15912	1709	1560	1181	193977	1081	8606	3310	10240
395	1181	32947	35166	10745	15421	1706	809	1791	186112	1150	8720	3632	10931
397	1089	31588	33103	10703	15700	1612	760	1811	186097	1061	8914	3552	12649
399	1092	34775	36749	11776	15475	1725	1168	1475	189201	1086	8508	3348	11406
401	1411	35501	36744	11263	15628	1706	1613	996	184053	1082	8438	3517	11109
403	1243	35513	35741	10487	14503	1750	985	1325	182231	1017	8607	3474	11116
405	1240	33825	34589	11284	14493	1466	1490	2230	182593	1064	9339	3628	11983
407	1374	35846	35855	11208	14801	1566	1553	1285	189509	1007	8507	3728	12341
409	1148	32647	33482	9576	14125	1428	1564	1512	184287	1140	8467	3290	10989
411	1090	32527	31476	9224	14931	1759	1044	1556	186880	1013	8560	3450	10830
413	902	31487	33434	9662	14829	1190	1451	1701	177873	1020	8894	3651	10241
415	1263	34013	35370	9285	14719	1949	1130	1130	173796	969	9154	3725	9875
417	1034	34090	35989	11180	15185	1606	1449	1073	186952	1041	9008	3589	11819
419	775	27757	28558	10318	13139	1673	1494	1141	173750	1055	8512	3415	11772
421	688	26851	24767	8054	13375	1846	1297	1187	170270	1016	8304	3453	10684

Chemical and mineralogical data

Depth (mm)	Al	Si	K	Ca	Ti	V	Cr	Mn	Fe	Zn	Rb	Sr	Zr
423	630	26044	20319	7905	11014	1442	1456	1342	160489	1028	8777	3545	10860
425	459	25307	20866	7213	11189	1287	1393	1391	158524	1012	9320	3783	11630
427	662	25629	23439	8398	12696	1417	1218	1424	172125	1092	9080	3662	11878
429	370	24201	18114	7676	10599	1216	1043	1015	158805	1069	8780	3548	11530
431	484	25537	18730	7864	10292	1369	1069	1166	147138	1002	8395	3587	11121
433	306	22324	4972	4956	4809	1374	290	1458	105243	954	7736	3176	10657
435	359	23279	5221	4473	5101	998	456	1577	101517	880	7671	3051	10670
437	425	24462	14757	6471	10000	1309	895	1641	145757	980	7812	3271	10694
439	493	25643	17640	8161	9945	1809	1147	1551	152088	1191	8326	3589	10562
441	429	26948	19651	6733	10225	1058	925	1416	145814	1008	9156	3815	9784
443	471	26205	15904	6114	6687	1350	791	1111	122415	875	10055	5302	7751
445	675	26771	17075	7741	8037	1284	346	1426	116717	916	10285	4554	10677
447	991	28866	15984	6422	7453	1023	863	1436	122908	788	8718	3330	10646
449	565	25502	17335	6652	9594	869	697	1703	136125	889	9065	3547	11022
451	626	26668	20829	7818	11127	1291	800	1596	148025	941	8665	3476	10954
453	745	26049	18367	7418	10483	1548	1013	1560	148781	986	8285	3193	10263
455	607	27504	24748	8451	11439	834	941	1457	161014	1029	8132	3348	10444
457	1290	34343	26862	8513	11195	1145	864	1153	157381	1042	7604	3456	10193
459	976	30149	12268	5613	4659	1070	657	964	81888	872	7338	2917	9821
461	796	27238	3222	4300	2087	1155	526	1666	51152	803	7050	3022	10392
463	938	28277	3021	3952	1878	1083	552	1298	44009	645	6962	2654	9370
465	668	26652	5845	4779	3058	1203	392	1218	67741	632	6922	2807	7953
467	805	26629	9904	5544	3452	1345	755	1491	76182	719	7093	2474	6641
469	633	25330	8196	5136	3640	1094	1387	1288	63422	618	7423	3111	5450
471	627	26644	13696	5972	6345	1100	229	1294	109775	646	8746	4166	8844
473	645	26640	14106	5448	5573	1528	304	1666	102639	777	8422	3691	9532
475	830	26522	18120	6345	8173	1302	623	1345	128047	699	8968	3207	10347
477	796	26767	12723	6066	7142	975	1148	1298	114325	877	8319	2942	9319
479	681	26220	14037	6284	7796	1354	1059	1901	137618	977	7638	2931	9888
481	813	25763	8950	5795	5906	831	179	1072	119936	930	7034	2905	9393
483	833	27847	14649	6728	7292	1129	884	1132	138202	956	7353	2841	9271
485	707	27690	18627	7498	8739	1098	403	1446	149906	947	7969	3062	10078
487	1153	34005	29970	10207	11923	1541	1287	1549	172353	1001	7791	3281	9595
489	1343	33577	32890	11096	13379	1593	794	1836	183699	1076	7565	3186	9472
491	1319	31299	23772	8364	10459	983	1076	1636	167663	1140	7794	3310	9998

Depth (mm)	Al	Si	K	Ca	Ti	V	Cr	Mn	Fe	Zn	Rb	Sr	Zr
493	1518	35359	32323	10795	12744	1335	857	1580	181169	1158	7536	3053	10563
495	1109	30370	22672	8097	11826	1245	1399	1786	165647	1051	7483	3148	9608
497	1449	35953	27715	8804	11097	1488	1205	1538	167932	1046	7508	3192	9646
499	1016	29550	24468	9595	11101	1366	925	1689	167129	1136	7943	3424	10727
501	1047	32148	30668	10814	12041	1351	1348	1634	178233	1098	7878	3184	10702
503	1252	33795	34649	10430	13185	917	1055	1516	179598	1191	8290	3323	10820
505	994	30098	27739	8101	10794	1329	947	1665	166778	1055	8425	3444	11352
507	1095	31388	29690	9925	12625	1469	1291	1332	177123	1140	8083	3383	10613
509	1614	38958	42852	11911	14287	1412	1486	1843	195013	1182	8800	3558	10881
511	1990	41595	41648	12338	14867	1704	1597	1937	172823	1082	9190	3506	11278
513	2337	47482	48111	13053	16341	1527	1809	1877	189487	1044	9277	3359	8494
515	2333	47227	51744	14031	16422	1350	1453	1923	193255	1163	8855	3962	9236
517	1226	34572	31129	10579	12895	1380	1121	1643	173680	1222	8338	3443	9555
519	1866	42911	42601	12237	15587	1583	1417	1689	188421	1132	8082	3292	9853
521	2358	47416	46089	12655	16964	1816	1804	1615	199253	1180	8175	3411	11846
523	1938	46194	44048	11960	16089	1443	1610	1570	187191	1154	8430	3163	10087
525	2527	52405	46771	12629	16670	1503	1351	2123	191634	1176	8369	3306	11622
527	2192	46833	46707	12231	15988	1813	1784	1693	196664	1171	8311	3424	10039
529	2164	48287	44109	11777	16110	1607	1383	1595	192451	1090	7922	3311	10435
531	2549	51285	50168	13805	16936	1396	1906	1599	197636	1195	8133	3195	9390
533	2122	47206	46913	13454	18044	2059	1447	2035	193991	1061	8272	3499	10429
535	1653	40491	45436	13061	16075	1524	1322	1803	190127	1048	8581	3396	11005
537	923	30623	30157	10829	13040	1330	1155	1389	175577	1051	8700	3445	9715
539	758	31846	39169	11169	14383	1407	858	1615	174531	967	8770	3338	9451
541	596	25406	15972	6731	7973	1309	521	1302	145594	1006	7931	3170	10334
543	369	24790	13481	6774	8654	1212	227	1777	145520	851	7696	3190	9871
545	720	26452	20603	7540	10779	1440	1154	1831	156247	1020	7540	2991	10142
547	667	27299	19444	8207	10269	1252	888	1248	151722	833	7274	2868	9971
549	822	28173	18236	7681	8357	1623	1319	2184	140312	893	7315	2793	9150
551	571	25054	10279	5675	7160	1311	599	1245	125971	897	7139	2898	9119
553	699	27120	14157	6890	7694	1206	1213	1582	129135	953	7440	2960	9887
555	675	25180	13022	5916	7197	1073	1126	1142	124930	1018	7305	3152	10373
557	336	22547	9789	6295	8803	1265	702	1605	131089	862	7210	3119	10557
559	282	23456	11034	6272	7858	1485	1059	1511	130223	906	7288	3092	9798
561	389	23876	12703	6692	7815	1255	1055	1308	136009	864	7079	2891	9245

Chemical and mineralogical data

Depth (mm)	Al	Si	K	Ca	Ti	V	Cr	Mn	Fe	Zn	Rb	Sr	Zr
563	446	23902	13662	6599	8744	1046	1179	1395	143384	975	7119	2809	9710
565	369	25091	15312	6803	7852	1090	1202	1419	128001	906	7539	3034	9302
567	747	29579	27614	8703	11725	1524	1066	970	150877	968	7635	3043	9377
569	817	30298	29495	9867	12357	1570	1094	1203	159499	968	7619	3123	8661
571	749	29753	25165	8684	10657	1240	1541	1408	150926	948	7380	2947	8540
573	851	29126	20672	7411	8878	1051	885	1538	135127	859	7082	2750	8424
575	890	29417	19200	7423	7836	1127	1008	1249	123066	823	6633	2634	9910
577	744	27194	18316	6823	7912	1184	211	1085	122575	871	6741	2713	9459
579	713	27102	20645	8843	9852	1064	720	2156	146024	1031	7059	2925	9024
581	982	30584	28418	9848	11047	1879	1152	1140	151428	971	7238	3071	10604
583	888	29745	24751	9242	10020	1127	870	1080	150527	917	7316	2895	9023
585	847	30404	19745	7914	8341	1417	716	1394	127123	987	7786	3197	9420
587	465	23714	4498	4617	2382	887	422	1260	65973	876	7190	3033	9118
589	701	27171	14088	7075	5701	892	435	1347	113551	858	6997	2624	8308
591	1276	32046	23760	8009	9777	1264	1285	1212	142723	1043	7667	3122	10443
593	1129	28800	14725	6177	6814	1173	462	1549	115762	1084	8067	3224	9112
595	630	26411	14542	6234	5585	1062	490	1239	100204	912	9189	3768	8645
597	1152	30920	23367	7516	11108	1806	740	1944	135525	1006	8992	3462	10521
599	1306	36256	32034	10128	11803	1414	1320	1213	161683	1174	8229	3257	9639
601	1208	34305	33847	10068	11975	1765	1334	1975	166100	1057	8211	3263	9108
603	1453	36422	33276	9947	12755	1905	1187	1917	173215	1138	8364	3138	10127
605	1340	36448	39605	11106	13523	1562	1466	1996	174615	1087	8596	3333	9954
607	1151	34015	31928	9749	13559	1449	1784	1656	174622	1146	8840	3365	10175
609	1658	38181	34805	9820	12992	1331	1298	1388	171795	1092	8007	3310	11534
611	1278	35850	31275	9026	12262	1407	1394	1522	173032	1122	8365	3129	9687
613	1465	35998	31786	9735	11702	1266	1122	1682	156646	1031	8454	3263	10369
615	2108	42715	37202	11123	13330	1386	976	1882	167493	1048	8649	3325	9502
617	2451	48562	43624	11963	15372	1661	997	1740	175285	1037	8094	3285	10500
619	2592	50758	46470	12837	15438	1544	1865	1615	182998	1029	8433	3229	9532
621	2579	50899	44741	11952	15799	1549	1370	1574	193091	1117	8159	3380	9080
623	1751	40962	38715	11774	15466	1598	1597	1762	189660	1171	8122	3550	10140
625	2350	48150	46376	11635	17187	1226	1528	1786	204599	1193	7974	3372	11308
627	2038	46715	46159	12966	15927	1888	1627	1764	200943	1138	8145	3202	10221
629	2109	43538	40749	12006	15206	1615	1601	849	194705	1172	8361	3031	9543
631	1672	39062	35706	10352	13907	1490	1298	1294	185395	1127	8507	3263	10272

Depth (mm)	Al	Si	K	Ca	Ti	V	Cr	Mn	Fe	Zn	Rb	Sr	Zr
633	1853	42550	41585	10451	15092	1522	1489	2051	190638	1073	8179	3458	9667
635	2244	45721	43830	11214	15716	1584	1105	1816	197012	1068	7915	3313	9840
637	1479	35650	32214	9937	12117	1358	1287	1556	176143	1184	8312	3339	9770
639	2211	45811	44616	11518	15246	1145	2004	1765	191348	1180	8244	3179	9341
641	2254	46197	45138	12937	15557	1335	985	1827	198426	1194	8723	3453	10813
643	1639	38559	35799	11202	13445	1395	1514	1855	177560	1089	8733	3331	10368
645	2122	45862	44396	12122	14795	1807	1541	1891	190237	1204	9126	3385	11020
647	1350	35673	35046	9729	13257	1481	1099	1664	171650	1155	9148	3617	9712
649	2235	44562	46403	12280	15685	1890	1522	1180	180763	1013	9569	3670	12784
651	2936	53026	51579	13196	16227	1719	1410	1792	196485	1103	8534	3314	11508
653	2205	44372	45658	11947	15517	1791	1720	1668	196768	1206	8395	3253	10398
655	1903	40842	38000	11515	11933	1360	834	1351	174719	1064	8717	3320	9539
657	2406	47484	43961	11126	15573	1104	1286	1664	188305	1127	9221	3639	9693
659	2293	47071	44620	11831	15257	1001	1328	1507	181596	1046	9216	3929	11556
661	2057	42954	40360	11019	13875	1433	807	1329	180086	1142	8531	3300	10052
663	2991	54852	53244	13433	16799	1175	1443	1352	199400	1104	8555	3186	9704
665	3116	54499	52245	12709	17289	1377	1493	1705	206520	1150	8178	3131	10407
667	2697	51637	49713	12533	17601	1874	1217	1877	196012	1146	8329	3087	10581
669	3060	52825	52958	13216	16597	1625	1475	1838	200442	1152	8305	3254	11154
671	2846	52002	50656	12952	16746	1442	1665	1951	200282	1122	8336	3250	10863
673	2659	49393	46556	12549	14842	1632	1416	1855	191648	1150	8600	3052	11458
675	2732	51271	51555	13874	16887	1791	1486	2027	197797	1038	9280	3441	12109
677	3335	56048	56212	13893	19666	1299	1340	1945	204449	1136	9360	3646	11962
679	2821	52061	49428	13574	15870	1892	2177	1667	191952	1089	9378	3562	11164
681	2809	52346	50955	13413	15949	1143	1316	1507	177488	1122	9154	3434	10074
683	3281	57689	55239	13514	17039	1532	2044	1634	185958	1132	8384	3206	9797
685	3196	57255	51337	13000	15334	1957	1271	2122	187003	1090	8335	3140	9526
687	2820	55135	50769	13227	15801	1827	1502	1858	195393	1088	8400	3227	10572
689	3105	55690	52053	13009	16469	1414	1453	1879	200840	1160	8376	3166	10332
691	3143	56785	52644	13942	16239	1571	1683	1780	199221	1148	8474	3218	10095
693	3199	56111	53096	12653	16310	1798	1779	1715	198211	1133	8683	3183	10484
695	3067	53634	50736	12644	17188	1692	1599	1612	198841	1218	8264	3166	9866
697	3217	55198	52556	12899	16514	1492	1382	2417	200721	1168	8553	3255	10386
699	2395	48187	52197	12582	17056	1831	1615	1809	198557	1089	8712	3390	10722
701	3191	56438	54509	13891	17367	1924	1586	1760	202300	1106	8847	3492	11824

Chemical and mineralogical data

Depth (mm)	Al	Si	K	Ca	Ti	V	Cr	Mn	Fe	Zn	Rb	Sr	Zr
703	2965	56229	55568	13658	17392	1556	1255	1579	204540	1203	8804	3529	11963
705	2644	49234	50645	13781	15323	1492	1217	1547	197318	1092	8861	3407	11445
707	2497	48264	51594	13233	18689	1475	1538	1735	201174	1011	8939	3409	12009
709	1978	44001	48369	12722	15647	1694	1311	2061	195046	1031	9113	3497	11937
711	1727	41712	48317	13224	16341	1897	891	1753	192562	1092	8934	3256	11835
713	1915	44143	49674	13723	16252	1654	1748	1876	195499	1125	8842	3414	10163
715	1416	37618	40443	11946	13452	1171	1102	1523	185179	1101	8937	3260	11362
717	1095	32492	33018	10782	12298	1312	1728	1357	170559	1073	8979	3827	11575
719	1213	31298	29703	10133	11181	1252	1407	2173	149127	1006	10217	3921	8795
721	891	28356	18366	6596	5847	987	688	798	96686	861	10993	4335	8150
723	776	29787	22641	7876	7494	1034	1641	1422	112040	775	10590	4228	8708
725	1570	40449	45425	11663	14380	1083	1875	2215	174845	830	10247	3814	9173
727	2097	46375	49233	11668	13541	1279	1407	1726	169336	1015	12222	3859	9519
729	2233	49099	51582	12737	15853	1328	1530	1714	184084	1004	11317	3359	11905
731	2042	43984	45457	11230	14435	1426	916	1829	184323	1060	8919	3242	10448
733	1675	39830	42354	12001	14390	1446	925	1303	177456	1043	8730	3126	10855
735	1223	35662	38064	10850	12987	1808	797	1910	179520	1125	8685	3235	10320
737	1454	37962	42835	11106	14092	1863	1450	1982	176198	1005	8511	3589	11415
739	1864	42321	44952	12291	15295	1211	1173	1180	194605	1065	8378	3273	12278
741	2045	44208	47961	12460	16181	1338	1515	1308	195571	1104	8530	3265	11509
743	2091	46105	52142	13926	16887	1622	1903	1505	207406	1176	8752	3200	11773
745	1717	42358	49904	13973	16115	1241	1470	1869	203369	1094	9170	3493	12142
747	2052	41925	47899	12544	16811	1396	1435	1668	206341	1286	9319	3484	10690
749	1610	38398	46273	12460	15944	1603	1368	1860	198071	1089	8981	3231	10544
751	1337	38184	46570	12915	15853	1476	1070	1537	200440	1149	9083	3210	11625
753	1598	37734	42820	11520	15308	1347	1020	1140	190952	1109	9388	3483	11213
755	1616	39068	47151	13447	15699	1647	966	1462	192381	1200	10259	3716	11526
757	1033	33819	39624	12064	15016	1269	1045	1053	177771	1047	10780	3647	10746
759	2317	41862	37126	11317	14264	1616	1851	2076	175565	1008	9980	3722	10649
761	1241	34253	35393	9501	13276	1492	1438	1600	185366	1103	10057	3842	11338
763	1567	36426	41139	10813	14539	1411	1084	1539	174138	1087	10539	3802	9887
765	1108	31727	34867	10376	14215	2029	1089	1708	181297	1026	10167	3821	9304
767	1244	33777	33853	10743	12796	1319	1293	1775	175492	1105	10496	3724	9913
769	939	32074	36152	9989	13545	2137	1418	1470	175647	1113	9851	3564	10372
771	1194	30422	20240	7831	10482	1281	346	1492	156453	1088	8462	3087	9786

Depth (mm)	Al	Si	K	Ca	Ti	V	Cr	Mn	Fe	Zn	Rb	Sr	Zr
773	1323	34175	31245	9664	10612	1230	1458	1850	160440	1099	8006	3229	10281
775	1907	42563	45465	12211	15891	1279	1063	1064	190472	1114	8405	3065	8469
777	2553	49398	49738	14380	16352	1552	1482	1767	191175	1126	8775	3430	9699
779	2325	48074	46902	12667	15645	1338	1341	1814	175453	1037	10049	4157	9722
781	1658	40475	41930	11200	12122	1621	1102	2096	145586	798	11193	3759	10712
783	1498	37096	34650	10415	10867	1565	707	1283	147460	893	9634	3554	8650
785	1645	38403	38289	9768	13523	1247	1731	1616	161345	937	13092	3770	8968
787	1455	38034	38209	10323	13474	1513	1381	1751	167531	991	11471	3299	10352
789	1403	37753	38577	11252	13082	1253	1528	1532	173119	998	9637	3625	9606
791	1518	37900	36567	13695	12826	1668	1101	1897	171262	915	9270	3234	9263
793	845	30576	29720	9759	12358	1282	1062	1136	172688	1043	8859	3444	10059
795	1161	35147	36753	10961	14418	1026	761	1475	188393	1108	8867	3140	10421
797	1006	34140	39332	11450	13263	1795	1056	1524	175488	1033	9182	3430	12418
799	1127	31612	32556	9927	12867	1449	772	1070	171957	1060	8935	3330	10963
801	983	32148	33004	10143	13263	1345	1013	1887	177354	1098	8901	3507	10639
803	1094	31226	32163	9542	14281	1890	1181	1454	189102	1214	8956	3460	10478
805	1109	32747	35104	9979	12817	1707	1203	1618	182928	1022	9005	3326	10137
807	1433	35418	32146	9106	12025	1599	1215	1528	163564	1004	8339	3130	9193
809	1161	30242	14051	6437	6603	1577	730	1473	117014	1041	8003	3207	9876
811	1092	31236	23782	8100	9532	1408	1227	2008	146364	948	7738	2859	10245
813	769	26656	17769	6785	8521	1399	1037	1492	141819	1016	8412	3082	9276
815	584	24412	4787	4285	4147	1313	1262	1548	100696	972	7625	2939	9973
817	590	24040	3995	4099	3704	963	423	1908	94560	948	7456	2992	8550
819	1251	31178	17748	6795	7417	1547	956	1603	125896	954	7319	2826	9223
821	1270	31116	21067	7763	8564	1390	807	1315	142911	1006	7495	2967	9120
823	1049	30054	19262	7100	7745	1263	1267	1807	135032	943	7659	2830	9444
825	1263	32455	20089	7517	7971	1363	716	1518	131490	969	7570	3033	9413
827	1063	32917	21333	7376	8336	1383	827	1590	136522	996	7518	2873	8268
829	1357	35584	28615	9355	10631	969	1169	1434	152374	966	7749	3145	9576
831	1317	33320	27346	8745	10949	1010	982	1443	153275	1037	7459	2933	9433
833	705	29149	22017	7600	9552	1036	1148	1447	147551	1014	7623	2906	8603
835	454	25406	16133	6608	8358	1240	1386	1599	141387	1065	8269	2807	9055
837	1136	33065	28347	9128	11339	1516	1005	1204	157411	1046	7626	2737	8991
839	1555	38371	33740	9576	12230	1241	1527	1833	162188	1045	7368	2900	9563
841	1403	37264	32219	9458	11503	1560	781	1724	155885	972	7313	2831	8489

Chemical and mineralogical data

Depth (mm)	Al	Si	K	Ca	Ti	V	Cr	Mn	Fe	Zn	Rb	Sr	Zr
843	1447	36420	31346	9730	11359	1160	772	1346	156729	1037	7766	2903	9292
845	1329	34850	29523	9613	10941	1446	1614	1631	148801	913	7959	3067	8614
847	1387	35254	34283	9906	11654	1938	1135	1105	145456	932	10874	4479	8465
849	1319	35106	34204	10128	12361	1248	1089	992	144040	835	10323	4265	9123
851	1046	33816	31544	9154	12320	1125	756	1062	150221	992	9130	3241	11255
853	1372	36971	35188	11038	13922	1147	1477	1407	148056	972	9932	3763	10368
855	1606	38535	40226	11720	14815	931	1379	1210	170357	902	10090	3513	8749
857	1183	33470	37149	10686	12974	1641	715	1713	171900	1027	8778	3350	9759
859	1211	34684	36731	10644	13783	1573	1503	1675	179674	1131	7984	3146	10374
861	1184	34768	38169	10173	13716	1342	1077	1226	183796	1143	8605	3334	9903
863	1195	34909	39170	10927	14011	1218	1529	1869	181756	1158	8737	3217	10380
865	1347	37200	41557	11612	14440	1472	1118	1337	185893	1090	8661	3379	10848
867	1530	39380	42470	11650	15324	1651	1180	1661	188573	1158	8184	3303	12628
869	1432	37304	37137	10673	14400	1261	1612	1611	185252	1124	8700	3218	11287
871	1533	37751	34093	10240	13093	1583	1375	1229	176048	1107	8415	3352	11477
873	785	29210	24486	8311	10698	1593	1292	2116	162907	1071	8440	2979	10481
875	1069	32373	37271	10318	13681	1048	1910	1598	184711	1080	8562	3127	11521
877	1250	33048	39294	11017	15201	1349	1612	1587	185140	1090	8798	3179	11102
879	1655	39222	45556	11895	14991	1559	1073	1657	189341	1213	8481	3136	10057
881	1220	33578	40248	10752	14109	1492	1555	1543	187679	1092	8261	3462	10855
883	1631	40008	43931	12177	15450	1521	937	973	193620	1144	8378	3402	11232
885	1894	40223	39680	11096	13935	1341	1052	1530	183216	1061	8547	3231	10209
887	1612	39046	43371	11413	15083	1392	1415	1731	186600	1099	8465	3100	10048
889	2433	47342	48905	11731	15992	1200	1400	1758	193940	1094	8620	3267	9928
891	2424	46491	49634	12935	16601	1687	1037	1573	176715	972	9294	3553	10969
893	2352	46666	48829	14162	15987	1604	1434	1938	182847	1055	8533	3246	9952
895	2265	47400	46112	13450	15053	1453	1133	1969	178577	1023	8415	3297	9519
897	2416	46366	45924	11359	14667	1416	1114	2027	182637	996	8459	3243	10140
899	2399	44472	43164	11493	14906	1506	1469	1144	184660	1096	8227	3339	10330
901	2578	47595	43616	11620	15060	1596	1492	1517	191328	1092	7902	3150	10867
903	3285	54944	51413	13117	17066	1589	1859	2342	195581	1132	7806	2936	9945
905	3069	52583	47841	12221	15948	1216	1489	1738	189206	1054	8024	3034	9585
907	2873	53313	47830	13341	16162	1519	1802	1479	187579	1076	7991	3136	9910
909	2942	54806	47875	12815	16307	1246	1523	1801	191535	1035	7825	3097	10521
911	2985	54104	49937	14169	17339	1896	2159	2227	193978	1026	8352	3255	10669

Depth (mm)	Al	Si	K	Ca	Ti	V	Cr	Mn	Fe	Zn	Rb	Sr	Zr
913	2894	53901	48251	12374	16438	1311	1546	1792	191361	1060	8054	2940	10347
915	3150	55166	48563	12543	16780	1828	1675	2020	195433	1048	8071	3131	9453
917	2962	53744	49317	13121	15591	1554	1450	1730	186978	1031	8467	3315	9542
919	3094	53581	49581	13767	15277	1280	1191	1802	181391	1036	8328	3227	9415
921	2540	47931	46541	11992	15344	1626	1482	1571	177398	1064	8728	3384	8917
923	2350	45765	45009	11983	16138	1288	987	2287	181214	1090	9565	3752	9844
925	2191	45302	46897	12658	17046	1282	1922	2274	187424	1069	8256	3247	11008
927	2746	51272	53394	14162	18243	1273	1710	2245	195507	1170	9183	3465	10239
929	3276	55800	56729	15212	16291	1454	1865	1693	184269	1057	9485	3680	11922
931	3241	54016	51894	14003	16671	1825	1301	1613	186885	1100	8748	3668	9940
933	2662	50874	49593	13804	16309	1072	927	1662	196045	1185	8308	3360	11203
935	2713	49212	49778	12983	16415	1461	1471	2091	193431	1159	8352	3166	10988
937	2646	50586	50720	15054	16970	1448	1338	2149	194409	1110	8783	3384	11185
939	2485	48750	50215	13445	15745	1555	1997	2318	184293	1102	9305	3535	10424
941	3354	54587	52903	15655	17613	1741	1814	2214	195758	1165	9243	3670	10791
943	2755	52152	51933	13645	15774	1434	1535	2016	184861	940	11255	3943	8945
945	2566	50237	46737	13155	16283	1900	956	1818	182704	966	10378	3828	8240
947	2469	47836	47036	13513	15705	1442	1492	2124	183040	1100	8757	3465	11265
949	2118	45198	45080	11398	16205	1419	816	1578	171550	1006	9902	3394	10841
951	3155	55715	54113	13778	16260	962	2029	1513	185549	996	11409	3746	9114
953	3045	55289	54999	14691	16119	1460	1730	1862	187583	1088	9787	3534	10891
955	2076	43136	43304	12388	14757	1581	1649	1780	178816	1233	8613	3354	11355
957	1602	39948	40258	11952	14640	1655	1296	1697	178624	1262	8844	3408	10296
959	1612	37973	37542	11164	14711	1632	1717	1290	169546	1127	9573	4231	9136
961	1399	34858	29526	9586	12161	1381	1194	1241	152126	1055	9362	3631	9318
963	963	28983	23005	8568	11116	1735	1128	2059	152225	1136	9369	3326	10753
965	944	29589	22422	8801	10794	1400	702	2175	160613	1191	9152	3481	11767
967	1324	33849	28981	10112	12353	1317	1657	1530	165661	1202	9303	3728	12386
969	1575	37424	32933	10642	13303	1684	822	2314	168866	1235	9619	3669	10804
971	2229	43915	43108	13137	15633	1784	1218	2364	185557	1116	9575	3660	12447
973	3306	57970	58628	14844	19016	1700	1891	2127	195625	1245	9637	3816	12499
975	3155	56611	60172	15721	19458	1720	2007	1966	201517	1218	9659	3723	11591
977	3071	54489	59281	14611	17665	1404	1915	1204	187513	1113	10615	3731	9739
979	2721	50897	55742	14617	17466	1793	1333	2068	181406	970	10680	3644	10106
981	2940	51733	53800	15968	17521	2087	1644	2222	182896	1086	9313	3432	10215

Chemical and mineralogical data

Depth (mm)	Al	Si	K	Ca	Ti	V	Cr	Mn	Fe	Zn	Rb	Sr	Zr
983	3102	54219	53498	13840	17958	1307	1503	2571	180468	1166	9269	3455	11167
985	4268	65152	59635	15565	18719	1536	1850	2427	182818	1376	8829	3390	10445
987	4421	67092	59036	17167	18295	1284	1571	2047	186066	1174	9158	3262	10609
989	4626	68368	59886	15786	17931	1613	1845	2029	184042	1225	9239	3261	10712
991	4748	69046	60380	16109	19117	1403	1596	2008	183896	1224	8622	3344	10004
993	4257	66572	58308	15944	16906	1264	1927	2035	177819	1227	8817	3340	10820
995	4512	68097	58272	15796	18237	1786	1586	2530	183619	1261	8699	3228	10587
997	5007	70998	64314	17276	19149	1626	2046	2212	183225	1275	8781	3492	11818
999	4389	64603	60511	17083	18333	1398	1800	2693	183395	1242	9467	3508	10853
1001	3286	56747	57629	14868	19562	1388	1397	2423	188387	1229	9663	3694	10988
1003	2903	51389	49744	14446	16860	1540	1223	1712	182403	1165	8729	3270	10866
1005	2957	53003	48441	13479	17863	1749	1154	2059	194008	1220	8907	3333	9874
1007	2049	43709	41896	11435	15132	1432	1510	1666	187131	1102	8784	3386	9289
1009	2295	45351	41573	11073	12876	1692	1228	1805	171224	959	9811	3822	8772
1011	1495	38520	31082	8426	7360	1082	1159	932	115347	698	11193	4206	5758
1013	1486	35214	25010	7369	7755	1060	1312	771	105960	642	11234	3335	7982
1015	1671	39415	38433	12252	12507	1597	1002	999	151895	912	9888	4012	8460
1017	1743	38856	30128	10047	11801	1193	528	1773	135283	807	11384	4298	8887
1019	1863	41522	37724	11710	11221	1802	794	1522	126415	719	11860	5979	8385
1021	1737	39733	38976	11127	12258	1174	992	1381	131854	681	11696	4780	6690
1023	1289	34438	28715	10028	9394	1440	958	1532	116360	663	11002	4463	6378
1025	2641	47419	42532	14121	11430	1398	1303	1135	139948	1008	10301	4088	7991
1027	2500	47631	44693	12429	15811	1680	812	2605	157476	1117	10199	3726	9150
1029	1507	34337	26405	7855	10632	1053	753	2371	120679	869	10533	4562	7770
1031	1963	41661	38715	13089	14206	1403	1514	1936	142527	896	9099	3452	8680
1033	1858	41714	37406	11628	13291	1180	874	1737	152478	1150	8906	3201	10180
1035	1756	39056	37206	9395	12993	1694	1168	1827	167453	1041	8540	3131	9152
1037	1540	37223	41263	10518	9625	1514	840	1207	132443	746	10840	4080	7934
1039	1784	37402	26506	17069	7316	1113	299	1315	101974	665	11347	4120	6887
1041	1628	39210	30020	11410	18877	1683	1555	1315	142289	768	9499	3771	8438
1043	1511	37830	38620	11731	14058	1383	1662	1823	173972	996	9218	4860	9660
1045	1479	36222	32695	11095	14518	1541	901	1587	164374	1071	8983	3542	11339
1047	2838	49815	48608	14947	16773	2191	1709	1803	171071	1114	9317	3991	10155
1049	3637	58406	52979	14791	16636	1430	1617	1612	173487	1260	8664	3226	11703
1051	2709	51335	47371	13368	16907	1452	1998	1931	185655	1312	8384	3181	10286

Depth (mm)	Al	Si	K	Ca	Ti	V	Cr	Mn	Fe	Zn	Rb	Sr	Zr
1053	2706	48956	47045	13212	16093	1502	1319	2336	184411	1261	8386	3293	11183
1055	2998	53869	47426	13049	16215	1310	1571	2362	188453	1171	8328	3198	10670
1057	2091	42101	38934	10885	14179	1455	1371	2122	169077	1132	8381	3336	8517
1059	2220	45240	44840	12457	16236	543	687	2349	163160	1214	8432	3188	10349
1061	1817	41582	35844	11176	13205	1439	605	2326	151220	1155	7706	3130	10155
1063	1509	38460	36158	12211	12942	1086	818	1916	144118	1236	7937	3180	10057
1065	1059	30962	26945	9925	11191	1389	1135	2443	137429	1335	7847	3011	9973
1067	738	28764	22447	9238	10426	1132	856	1714	128245	1210	8151	3156	10544
1069	885	27921	20567	8477	9939	997	1048	2200	123369	1168	8225	3375	9050
1071	1120	29413	14314	6882	7234	1345	1075	1731	112643	1140	7790	3073	10243
1073	1019	27794	15743	7647	7409	1073	746	1835	114894	1193	8036	3102	9034
1075	1437	35437	32362	12057	13547	1420	541	2195	138725	1139	8087	3053	10381
1077	1155	31560	21086	9276	10294	1368	771	2015	127592	1167	7635	2999	10434
1079	808	26967	18572	8624	8286	1037	764	2299	121610	1104	7192	2849	10423
1081	849	28584	17691	8433	8866	984	1109	1821	119594	1157	7541	3181	10416
1083	966	29287	17493	8116	8224	1213	791	1909	121416	1086	7341	2909	10746
1085	1089	30150	20805	9009	9327	1653	875	1932	125406	1142	7560	2919	9093
1087	1136	32608	28624	10162	11290	1490	1437	2129	132024	1091	7878	3248	8376
1089	958	29369	22646	9408	9964	1380	793	1413	123151	1019	7964	3136	9063
1091	1146	32408	26174	9698	9131	1123	858	1943	121440	985	7972	3242	9731
1093	1525	36279	27620	10364	11091	1114	1074	2197	128845	1097	7346	3040	9835
1095	1355	35048	24538	9737	10106	1445	1115	2248	125142	1118	7334	3106	8769
1097	1000	31953	24145	11190	10869	1434	869	2503	132354	1052	7312	2956	9119
1099	1045	29923	21302	9478	9533	1107	694	1913	130184	1129	7218	3012	9923
1101	864	29688	19155	8564	9440	777	912	2138	126054	1187	7391	3011	10009
1103	1523	36586	25558	9448	10242	1517	1126	2212	134284	1107	7213	3013	9522
1105	1974	39835	33053	11242	11828	1570	1159	2464	133846	1178	8092	3368	9771
1107	1324	33102	23290	9199	10499	1315	577	1732	128540	1180	7872	3330	9226
1109	1353	34600	25524	9783	10573	1651	1170	1672	134066	1217	7732	3291	11197
1111	1609	37781	30460	10530	11745	1517	1220	2220	139539	1167	8158	3296	10903
1113	1656	36400	31147	11619	11379	1791	784	2091	136696	1149	8499	3173	10192
1115	2025	41508	39110	12441	13550	1428	1155	2271	140455	1028	10028	3792	10562
1117	2103	44728	42289	12902	14276	1238	1242	1333	139918	1043	10758	4044	8811
1119	1858	43351	38550	12482	13707	1329	920	1850	150893	1167	8971	3447	9375
1121	2152	44443	40138	12690	14947	1442	1347	2229	150885	1275	8519	3427	9800

Chemical and mineralogical data

Depth (mm)	Al	Si	K	Ca	Ti	V	Cr	Mn	Fe	Zn	Rb	Sr	Zr
1123	2148	45317	40104	13127	14238	1693	1010	1953	154832	1346	7876	3319	8681
1125	2420	45461	40286	12587	14930	1513	1478	2147	156923	1201	7804	3118	8922
1127	1016	33287	27203	10111	10417	1379	820	1715	128227	1252	7486	2955	9280
1129	1039	30831	21269	8970	8894	1085	1042	1660	118146	1031	8295	3294	9685
1131	1384	33750	19883	8176	8234	1046	789	1819	117673	1147	7741	3429	11977
1133	1621	34764	20680	8397	8710	1540	976	1540	113982	1081	7927	3248	8693
1135	1392	34577	26092	9411	10083	954	1121	2033	122247	1121	7924	3119	9680
1137	1096	33433	25034	10290	10585	1473	1419	2587	133011	1104	7876	3203	9998
1139	1302	33477	24686	10102	10337	940	1357	2364	130381	1063	8355	3329	9713
1141	1310	34079	27674	9779	10653	1176	1504	1801	130189	1030	8470	3448	9440
1143	1222	33410	26385	10072	10420	1763	876	1776	129017	1095	8956	3839	9614
1145	1054	32347	25392	10317	9427	1162	1228	1858	118443	1050	8775	3743	9021
1147	1386	34557	28119	10693	9846	1298	1233	1888	119359	1156	8332	3387	9662
1149	1304	34023	26599	9995	10290	1438	915	1858	129132	1107	8044	3262	9698
1151	1761	39230	28558	10431	11392	1490	1667	2306	139829	1150	8223	3401	10362
1153	1660	36732	26106	9750	10084	1440	1184	1974	131048	1258	8642	3181	10701
1155	1876	41321	36600	11961	12599	1221	1282	2152	147083	1197	9295	3676	11108
1157	2117	44631	44723	13161	14685	1407	1285	2537	160810	1104	9432	3663	11451
1159	2216	44361	43798	14382	15439	1525	1499	2323	161286	1087	9410	3756	12035
1161	2725	48655	46650	13449	15960	1809	1285	2200	178440	1185	9347	3582	11584
1163	2634	48867	44229	13810	17075	1293	1067	2053	166354	1122	9520	3901	11701
1165	2275	47639	46572	14012	16919	1283	1058	2027	161915	1231	9914	3701	10360
1167	2754	50953	47591	14653	15956	1600	1524	2075	161324	1267	10187	3886	9786
1169	1399	31361	20722	7593	8145	1361	681	1419	104578	753	10879	3999	9571
1171	1367	36349	34330	12268	11185	940	1177	1021	133184	901	10046	3731	11957
1173	1849	40193	34621	13234	11781	1834	854	1829	143531	1026	8891	3529	10530
1175	1847	39302	31061	9739	11433	1269	1082	1794	143934	1077	8611	3477	10088
1177	1854	39536	32965	10922	11454	1380	858	1885	141342	1041	8984	3622	11664
1179	1877	39941	32716	10706	11372	1087	1056	2126	142717	1021	9053	3629	11651
1181	1801	38903	35653	10163	13277	1512	1324	1800	151169	1038	10650	4049	10132
1183	1561	35702	33279	10732	12814	1163	1074	1812	146220	953	9737	3546	10868
1185	1648	36191	31392	10648	11452	1550	1094	1771	143600	1065	8908	3478	11347
1187	1619	39045	36437	11688	12794	1491	1687	1796	153159	1104	8548	3308	10690
1189	1717	38582	35162	11374	12334	1277	880	1649	148556	1138	8710	3385	10780
1191	1624	37196	31640	11686	12300	1544	1101	2479	140615	1095	8903	3215	9980

Depth (mm)	Al	Si	K	Ca	Ti	V	Cr	Mn	Fe	Zn	Rb	Sr	Zr
1193	1427	34734	30719	9600	11507	1107	1164	2129	134722	1258	7963	3469	10025
1195	1238	35110	33368	10930	12434	1671	1757	2153	138692	1184	7963	3439	10574
1197	1561	37247	31597	9994	12446	1281	1360	2001	161071	1183	7916	3111	9664
1199	1909	40402	34206	9924	12503	1421	1777	1802	167212	1079	7791	2978	9917
1201	1829	40809	33561	9706	11998	1040	1336	1879	137274	1107	9297	3638	10754
1203	3231	58449	55657	13950	16959	1394	1801	1854	159542	1093	10196	3639	9391
1205	4127	67647	57541	14453	18036	1439	2036	2086	165214	1246	9030	3549	10424
1207	4023	66502	56697	14586	17647	1714	2035	2104	164341	1238	9002	3567	11261
1209	4342	65369	55195	14441	17269	1784	1624	2141	166586	1132	8951	3670	11490
1211	3840	60241	53406	14318	17033	1622	1951	2029	170637	1297	8756	3438	11770
1213	3673	59298	51788	13711	16924	1505	1533	1700	173034	1198	8783	3463	10594
1215	1910	44524	40967	11745	13991	1697	1190	1584	159284	1058	9035	4056	9622
1217	2006	42459	40169	10818	13854	1432	1120	1590	158807	980	9234	3686	10782
1219	1496	38819	35560	11372	14100	1320	1783	1893	162201	1166	8775	3414	10445
1221	1894	41953	41616	11774	15499	1607	1274	1879	167751	1122	8527	3298	12174
1223	1640	37476	32267	10667	12884	1001	1119	1908	153944	1044	8666	3427	11185
1225	1729	37026	28059	9014	11880	1246	1185	1784	143565	1083	8751	3487	10021
1227	2633	45677	35360	9845	12273	1476	1612	1522	141473	974	8818	3600	8928
1229	1735	37877	28160	8468	10088	1440	1481	1117	126167	940	8110	3886	7800
1231	1300	32145	21046	7508	8721	1330	953	1742	110106	887	7051	3258	8195
1233	2733	49841	36701	10286	12181	1584	1103	1569	134095	987	7098	2734	8594
1235	2263	44693	35243	9885	12710	1130	1398	2173	146416	1011	7293	2751	8397
1237	1575	39353	26904	8931	10396	1283	1472	1583	141896	914	7198	2534	7842
1239	1864	41939	33616	8768	11264	1230	1575	1562	164452	789	8112	2538	6444

Table B.5. XRD intensity measurements of bulk mineralogical composition from PE12-01-01 core (in cps).

Depth (cm)	Muscovite	Kaolinite	Clinochlore	Quartz	Microcline	Albite
0.2	62.49	20.41	20.41	147.8	18.25	41.75
0.4	58.83	19.54	19.54	131.6	9.44	43.61
0.6	31.61	22.22	22.22	100.2	12.66	29.48

Chemical and mineralogical data

Depth (cm)	Muscovite	Kaolinite	Clinochlore	Quartz	Microcline	Albite
0.8	50.81	21.33	21.33	72.58	9.64	18.47
1.0	36.32	10.14	10.14	75.66	11.83	23.09
1.2	38.51	19.25	19.25	87.61	9.28	32.6
1.4	41.23	19.57	19.57	82.19	40.9	28.53
1.6	57.63	14.84	14.84	134.5	23.85	40.47
1.8	46.78	14.58	14.58	103.3	17.63	21.38
2.0	37.54	14.45	14.45	60.82	29.9	18.28
2.2	33.67	14.71	14.71	62.1	3.72	22.31
2.4	52.65	21.61	21.61	125.3	11.12	42.43
2.6	29.22	15.21	15.21	58.99	8.54	22.63
2.8	53.76	22.81	22.81	134.1	15.73	56.23
3.0	58.68	18.75	18.75	124.7	20.83	34.56
3.2	79	24.87	24.87	139.2	8.7	51.42
3.4	38.56	25.28	25.28	64.51	7.96	23.59
3.6	39.25	17.74	17.74	85.37	7.18	23.3
3.8	36.1	16.39	16.39	115.9	8.67	30.26
4.0	16.72	7.48	7.48	31.27	7.11	6.3
4.2	51.15	15.2	15.2	144	11.91	46.37
4.4	35.54	8.28	8.28	69.58	4.69	28.47
4.6	32.09	12.31	12.31	57.7	8.66	22.61
4.8	54.13	22.58	22.58	79.32	13.24	34.9
5.0	30.02	17.33	17.33	57.11	7.92	22.32
5.2	31.28	30.23	30.23	99.28	14.75	39.24
5.4	45.21	14.3	14.3	102.6	5.5	28.17
5.6	54.41	17.85	17.85	96.23	10.48	41.13
5.8	35.54	13.23	13.23	80.69	10.52	31.96
6.0	31.97	12.43	12.43	57.68	11.15	27.39
6.2	49.12	17.49	17.49	96	11.1	27.13
6.4	25.87	8.8	8.8	63.54	2.1	4.29
6.6	38.72	20.23	20.23	77.13	11.26	17.63

Depth (cm)	Muscovite	Kaolinite	Clinochlore	Quartz	Microcline	Albite
6.8	51.71	15.18	15.18	138.4	13.15	34.76
7.0	27.41	19.97	19.97	65.93	4.17	21.35
7.2	41.6	18.39	18.39	125	14.02	43.72
7.4	52.47	9.48	9.48	64.2	12.11	20.48
7.6	43.58	12.86	12.86	136.3	12.45	41.59
7.8	35.14	14.97	14.97	68.1	9.62	22.49
8.0	40.09	20.43	20.43	132.3	17.42	48.33
8.2	20.84	6.64	6.64	81.72	16.08	32.7
8.4	54.33	18.11	18.11	101.7	10.46	27.76
8.6	38.38	15.91	15.91	134.9	8.1	49.03
8.8	19	5.66	5.66	87.82	13.06	35.78
9.0	20.09	12	12	75.73	7.65	20.07
9.2	20.82	11.76	11.76	45.66	7.09	19.68
9.4	30.44	14.44	14.44	52.03	2.81	3.7
9.6	31.2	11.29	11.29	141.1	28.8	24.8
9.8	20.92	9.39	9.39	57.21	6.3	14.58
10.0	23.05	23.05	23.05	108.9	19.69	30.48
10.2	37.34	20.34	20.34	97.67	13.57	31.36
10.4	27.01	14.79	14.79	61.98	12.68	10.25
10.6	28.38	12.41	12.41	104.9	10.48	36.48
10.8	24.82	26.41	26.41	126.5	11.78	62.89
11.0	21.89	11.45	11.45	75.32	11.77	28.59
11.2	32.33	7.36	7.36	76.79	8.3	22.37
11.4	25.17	12.6	12.6	66.35	9.45	22.53
11.6	32.22	14.83	14.83	66.73	4.83	16.83
11.8	13.52	8.83	8.83	96.94	10.88	24.39
12.0	35.78	12.51	12.51	61.84	6.75	22.48
12.3	20.27	14.37	14.37	47.11	4.54	12.86
12.6	35.29	10.15	10.15	82.32	6.71	66.94
12.8	37.28	19.84	19.84	131.1	8.54	25.77

Chemical and mineralogical data

Depth (cm)	Muscovite	Kaolinite	Clinochlore	Quartz	Microcline	Albite
13.0	41.88	22.84	22.84	182.9	21.14	36.76
13.2	29.09	13.13	13.13	86.54	13.48	33.55
13.4	36.58	14.69	14.69	138.8	11.45	48.54
13.6	23.81	12.58	12.58	67.46	6.5	32.95
13.8	37.51	17.53	17.53	114.9	8.36	32.14
14.0	32.23	12.62	12.62	121	12.33	26.47
14.2	20.68	12.24	12.24	63.03	8.62	27.71
14.4	21.21	4.92	4.92	73.51	4.9	17.25
14.6	47.04	15.54	15.54	118.9	8.54	49.9
14.8	41.29	10.04	10.04	66.69	11.52	22.66
15.0	22.74	9.65	9.65	91.95	4.88	28.78
15.2	44.28	22.6	22.6	107.6	12.68	46.07
15.4	30.43	6.99	6.99	44.75	4.1	8.46
15.6	22.86	12.2	12.2	81.43	9.47	23.53
15.8	24.9	5.86	5.86	91.26	12.79	33.17
16.0	39.78	16.95	16.95	92.98	12.92	44.41
16.2	40.79	15.41	15.41	86.53	5.12	30.59
16.4	44.31	12.63	12.63	94.18	9.51	29.81
16.6	20.51	8.56	8.56	98.78	14.57	33.49
16.8	19.93	9.58	9.58	85.81	10.25	38.7
16.8	23.27	10.82	10.82	101.5	15.29	25.32
17.0	33.85	12.79	12.79	68.86	14.53	23.38
17.2	24.52	9.51	9.51	63.05	12.03	22.88
17.4	53.79	10.28	10.28	137.1	12.63	33.72
17.6	27.42	16.53	16.53	51.31	13.52	20.1
17.8	35.8	12.68	12.68	58.72	11.21	51.17
18.0	22.27	13.97	13.97	72.47	11.17	17.48
18.2	24.97	11.81	11.81	41.27	6.23	37.02
18.4	25.27	9.79	9.79	71.1	13.37	19.43
18.6	29.48	13.02	13.02	113	0.01	39.25

Depth (cm)	Muscovite	Kaolinite	Clinochlore	Quartz	Microcline	Albite
18.8	44.93	12.99	12.99	102.7	3.65	21.88
19.0	17.19	9.94	9.94	94.26	15.4	28.52
19.2	20.7	13.42	13.42	67.69	9.18	24.37
19.4	17.7	5.43	5.43	103.3	10.93	12.38
19.6	35.14	10.23	10.23	81.89	21.89	22.92
19.8	30.53	12.45	12.45	58.17	8.61	22.46
20.0	40.62	21.84	21.84	132.3	17.85	50.07
20.2	27.47	16.96	16.96	64.9	8.37	20.94
20.4	28.71	9.71	9.71	81.96	12.63	22.37
20.6	26.51	11.51	11.51	91.72	13.84	19.06
20.8	53.19	12.24	12.24	119.4	9.84	17.58
21.0	40.35	17.3	17.3	104.4	16.56	36.35
21.2	28.27	10.16	10.16	68.9	11.68	16.4
21.4	42.29	12.96	12.96	136.8	15.31	47.88
21.6	34.89	11.61	11.61	82.84	14.38	32.99
21.8	35.76	14.67	14.67	62.32	3.53	38.42
22.0	44.29	14.58	14.58	154	14	49.79
22.2	39	8.2	8.2	80.01	11.24	26.67
22.4	48.75	11.99	11.99	112.6	9.14	27.48
22.6	50.3	16.75	16.75	194.3	9.11	150.3
22.8	50.94	13.85	13.85	191.6	20.3	49.78
23.0	51.09	10.28	10.28	155	14.93	39.03
23.2	23.17	9.83	9.83	108.1	16.52	21.45
23.4	30.62	12.95	12.95	125.9	16.98	52
23.6	38.04	16.26	16.26	168.2	14.73	43.72
23.8	39.94	23.44	23.44	172	18.03	58.39
24.0	11.69	12.01	12.01	80.9	16.22	18.24
24.2	36.28	10.02	10.02	129.6	78.68	35.53
24.4	44.56	17.29	17.29	116.7	12.95	36.58
24.6	25.57	14.77	14.77	74.49	10.48	25.7

Chemical and mineralogical data

Depth (cm)	Muscovite	Kaolinite	Clinochlore	Quartz	Microcline	Albite
24.8	40.88	17.84	17.84	126.4	4.92	46.06
25.0	44.31	14.93	14.93	73.83	8.93	21.1
25.2	43.78	17.95	17.95	95.54	16.04	26.42
25.4	33.83	9.32	9.32	96.12	15.49	27.79
25.6	40.47	13.13	13.13	103.8	15.6	35.09
25.8	33.99	19.96	19.96	107.9	4.06	25.68
26.0	46.94	21.42	21.42	123.1	12.61	28.63
26.2	40.22	25.49	25.49	150.4	13.29	77.79
26.4	31.54	12.3	12.3	116.7	12.84	27.2
26.6	43.84	15.1	15.1	131.2	12.16	36.13
26.8	33.63	23.59	23.59	130.2	12.55	25.13
27.0	40.17	17.7	17.7	141.6	17.24	40.36
27.2	27.41	15.6	15.6	134.1	17.02	41.82
27.4	28.8	16.08	16.08	107.8	15.32	31.48
27.6	37.22	14.29	14.29	150.7	12.68	64.84
27.8	46.17	26.51	26.51	302.4	35.92	64.76
28.0	49.62	24.69	24.69	215.6	29	57.9
28.2	44.23	12	12	153.1	13.38	57.87
28.4	54.57	24.67	24.67	238.7	29.74	105.3
28.6	50.7	22.76	22.76	223.4	35.3	67.38
28.8	44.44	24.4	24.4	226.7	33.79	53.49
29.0	32.09	9.65	9.65	186.2	24.6	49.63
29.2	36.89	16.96	16.96	163.4	17.76	41.77
29.4	29.26	19.62	19.62	196.6	19.48	59.28
29.6	33.1	21.54	21.54	177.7	11.98	39.22
29.8	48.99	23.74	23.74	122.1	16.86	39.58
30.0	42.83	13.81	13.81	178.5	29.77	50.18
30.2	36.7	16.4	16.4	74.7	14.95	55.52
30.4	—	—	—	—	—	—
30.6	53.64	16.44	16.44	166.8	23.93	70.68

Depth (cm)	Muscovite	Kaolinite	Clinochlore	Quartz	Microcline	Albite
30.8	38.13	24.26	24.26	158.4	14.9	48.11
31.0	50.71	23.14	23.14	162.2	23.66	42.57
31.2	74.42	22.53	22.53	206.8	27	49.01
31.4	69.88	27.86	27.86	208.8	37.46	51.28
31.6	60.1	20.18	20.18	217.6	34.02	63.38
31.8	67.41	27.81	27.81	204.9	22.08	61.88
32.0	47	28.64	28.64	196	23.96	36.88
32.2	43.05	12.68	12.68	155.4	15.72	37.42
32.4	43.48	12.52	12.52	96.43	16.67	29.38
32.6	57.55	13.99	13.99	193	23.13	57.19
32.8	35.02	12.91	12.91	151	9.6	40.67
33.0	53.8	19.65	19.65	223	26.73	83.5
33.2	35.39	16.76	16.76	229.9	134.9	96.67
33.4	85.52	20.34	20.34	251.1	38.14	68.85
33.6	39.83	12.95	12.95	164.2	17.32	36.25
33.8	60.81	15.7	15.7	225.6	37.55	74.83
34.0	41.31	25.14	25.14	214.5	30.91	103.7
34.2	69.9	21.33	21.33	301.5	24.38	114.7
34.4	52.75	27.83	27.83	204.4	23.71	46.63
34.6	48.12	20.81	20.81	145.1	18.23	37.99
34.8	32.58	30.31	30.31	202.6	18.49	40.9
35.0	43.53	22.01	22.01	160.3	24.77	40.44
35.2	62.96	23.84	23.84	179.4	16.08	58
35.4	47.66	5.3	5.3	128	17.39	34.04
35.6	34.79	15.78	15.78	148.5	23.86	70.42
35.8	40.65	13.08	13.08	163.4	15.15	37.88
36.0	33.88	9.33	9.33	85.22	3.37	15.98
36.2	23.18	8.91	8.91	129.1	12.68	39.29
36.4	49.66	23.92	23.92	153.1	16.19	30.66
36.6	26.73	7.63	7.63	106.1	13.96	29.97

Chemical and mineralogical data

Depth (cm)	Muscovite	Kaolinite	Clinochlore	Quartz	Microcline	Albite
36.8	27.54	12.2	12.2	99.13	18.87	48.47
37.0	60.05	19.91	19.91	188.8	22.98	44.05
37.5	77.19	28.07	28.07	202.9	31.45	47.74
38.0	99.44	23.32	23.32	213.2	32.62	62.08
38.5	63.54	19.2	19.2	159.7	29.58	40.98
39.0	98.45	6.25	6.25	211.2	26.81	65.03
39.5	64.29	24.51	24.51	174.5	22.14	50.62
40.0	41.49	17.34	17.34	152.1	21.33	50.97
40.5	58.35	25.24	25.24	161	27.3	46.55
41.0	56.64	18.4	18.4	180	27.65	89
41.5	42.89	19.86	19.86	145.6	13.27	42.79
42.0	75.42	31.16	31.16	181.6	22.24	59.57
42.5	60.4	18.78	18.78	178	17.92	53.46
43.0	82.82	24.15	24.15	191.6	34.91	56.11
43.5	78.49	25.27	25.27	181	16.23	52.57
44.0	78.76	29.17	29.17	219.3	35.43	69.28
44.5	90.16	28.01	28.01	217.3	33.21	63.88
45.0	82.94	18.8	18.8	165	26.94	53.71
45.5	76.44	22.31	22.31	206.1	47.22	68.78
46.0	59.97	27.45	27.45	172.7	32.9	41.59
46.5	64.18	19.55	19.55	218.4	32.43	64.98
47.0	47.86	23.28	23.28	173.6	16.7	16.53
47.5	32.92	27.66	27.66	122	21.13	52.42
48.0	70.75	19.83	19.83	189.6	27.2	71.35
48.5	41.23	19.27	19.27	92.32	3.89	19.25
49.0	49.99	10.33	10.33	145.8	35.64	55.61
49.5	69.01	23.04	23.04	157.5	20.82	33.38
50.0	74.98	19.84	19.84	171.1	20.33	70.45
50.5	60.38	21.91	21.91	193.1	19.19	57.15
51.0	77.28	26.79	26.79	213.8	28.7	58.72

Depth (cm)	Muscovite	Kaolinite	Clinochlore	Quartz	Microcline	Albite
51.5	54.98	18.01	18.01	172.2	14.57	47.22
52.0	50.07	15.46	15.46	161.8	26.23	57.48
52.5	59.68	19.71	19.71	166.8	65.86	51.71
53.0	34.67	12.49	12.49	162.1	26.9	35.53
53.5	46.64	21.74	21.74	151.9	19.17	44.77
54.0	42.07	10.16	10.16	149.3	13.24	52.2
54.5	58.72	18.36	18.36	168.8	20.99	54.7
55.0	54	23.08	23.08	152	14.57	74.31
55.5	58.17	17.68	17.68	190.8	31.37	58.09
56.0	71.94	24.02	24.02	214.8	27.14	68.22
56.5	53.57	19.97	19.97	193.8	32.22	34.02

Table B.6. XRD intensity measurements of bulk mineralogical composition from CIM12-04A core (in cps).

Depth (cm)	Muscovite	Kaolinite	Clinochlore	Quartz	Microcline	Albite
0	13.24	13.82	13.82	89.28	17.83	23.49
0.2	18.01	13.3	13.3	96.44	16.58	36.38
0.4	20.5	9.63	9.63	57.44	9.92	16.42
0.6	28.52	10.13	10.13	65.02	12.34	4.72
0.8	16.75	11.67	11.67	42.22	11.32	6.49
1.0	20.4	13.88	13.88	45.26	5.99	6.64
1.2	15.93	16.27	16.27	30.88	8.57	9.33
1.4	20	8.58	8.58	26.33	3.22	4.11
1.6	21.45	13.12	13.12	82.99	16.42	17.58
1.8	28.89	13.14	13.14	97.87	22.14	41.03
2.0	26.4	12.16	12.16	88.68	10.32	33.47
2.2	20.62	11.78	11.78	39.91	7.6	6.83
2.4	26.38	17.36	17.36	187.5	14.39	11.02
2.6	28.78	17.21	17.21	71.97	7.82	23.88

Chemical and mineralogical data

Depth (cm)	Muscovite	Kaolinite	Clinochlore	Quartz	Microcline	Albite
2.8	31.71	13.32	13.32	78.88	35.02	128.9
3.0	26.26	23.1	23.1	81.75	11.82	23.61
3.2	22.81	19.02	19.02	109.5	21.75	28.88
3.4	27.5	14.49	14.49	77.18	12.46	20.18
3.6	21.73	18.77	18.77	93.73	48.86	89.08
3.8	13.37	14.76	14.76	47.12	5.75	19.88
4.0	21.1	12.29	12.29	77.43	10.23	22.54
4.2	26.64	21.24	21.24	95.46	17.89	23.11
4.4	31.08	13.38	13.38	114.4	10.42	15.82
4.6	16.45	9.65	9.65	81.78	14.79	14.63
4.8	25.79	14.91	14.91	65.8	18.34	15.84
5.0	21.46	12.28	12.28	71.74	11.71	23.62
5.2	18.69	15.63	15.63	118.3	23.31	37.81
5.4	21.52	18.45	18.45	60.84	11.82	15.38
5.6	24.06	21.5	21.5	59.16	48.54	16.47
5.8	12.06	19.11	19.11	36.52	14.71	3.43
6.0	17.09	14.8	14.8	62.38	9.54	13.65
6.2	26.39	16.49	16.49	95.45	14.29	15.02
6.4	28.04	14.9	14.9	105.3	13.48	30.54
6.6	17.17	14.09	14.09	36.35	10.92	6.68
6.8	8.19	14.07	14.07	60.85	13.73	22.54
7.0	22.45	15.5	15.5	119.9	11.52	12.88
7.2	31.67	15.96	15.96	115.7	24.8	25.88
7.4	23.78	18.48	18.48	103	17.85	33.06
7.6	16.31	11.98	11.98	63.21	6.3	10.34
7.8	12.38	16.86	16.86	72.38	10.41	19.88
8.0	20.92	19.07	19.07	105.8	20.35	43.97
8.2	20.19	11.76	11.76	82.78	10.96	14.83
8.4	12.23	12.03	12.03	70.16	11.56	28.48
8.6	13.78	20.72	20.72	65.33	6.9	22.36

Depth (cm)	Muscovite	Kaolinite	Clinochlore	Quartz	Microcline	Albite
8.8	23.48	14.75	14.75	104.5	15.04	21.07
9.0	27.96	18.5	18.5	157.4	16.19	21.62
9.2	24.98	15.79	15.79	97.21	23.75	35.03
9.4	7.48	11.53	11.53	61.95	12.88	30.43
9.6	17.5	13.41	13.41	77.95	19.35	24.7
9.8	26.48	13.85	13.85	52.29	9.95	17.87
10.0	11.49	16.49	16.49	70.05	10.81	16.13
10.2	21.58	14.89	14.89	113.4	29.6	40.1
10.4	21.96	12.59	12.59	94.11	17.79	35.27
10.6	35.9	17.92	17.92	111.9	35.03	24.89
10.8	29.07	14.54	14.54	156.7	15.99	35.73
11.0	35.31	29.03	29.03	136.1	25.52	39.8
11.2	32.67	21.91	21.91	99.69	18.35	39.63
11.4	39.48	20.82	20.82	110.4	20.08	33.53
11.6	17.44	15.82	15.82	127	14.27	37.2
11.8	31.47	16.37	16.37	177	14.64	35.91
12.0	27.96	23.74	23.74	144.6	46.47	62.76
12.2	13.27	19.99	19.99	95.03	15.13	25.25
12.4	34.03	18.39	18.39	98.49	17.61	24.27
12.6	25.86	21.81	21.81	93.9	12.57	39.39
12.8	28.54	20.84	20.84	130.4	15.73	24.81
13.0	26.52	20.47	20.47	66.44	10.61	26.04
13.2	16.48	15.49	15.49	121.2	16.64	30.34
13.4	27.43	16.33	16.33	109.6	27.05	44.97
13.6	18.39	20.79	20.79	116.4	33.39	25.38
13.8	41.39	20.39	20.39	137.8	25.63	149.3
14.0	22.88	19.68	19.68	157.2	30.72	29.94
14.2	31.31	18.74	18.74	123.3	26.12	40.47
14.4	44	23.32	23.32	143.2	66.15	35.87
14.6	24	16.08	16.08	48.34	5.15	12.13

Chemical and mineralogical data

Depth (cm)	Muscovite	Kaolinite	Clinochlore	Quartz	Microcline	Albite
14.8	26.11	21.89	21.89	113.6	32.72	63.67
15.0	36.72	25.2	25.2	148	25.64	52.82
15.2	31.91	28.33	28.33	121.8	53.1	29.51
15.4	21.06	18.52	18.52	119.7	21.46	42.98
15.6	27.88	23.72	23.72	94.14	25.61	28.84
15.8	30.26	25.07	25.07	191.9	27.08	59.14
16.0	38.42	23.02	23.02	141.6	24.88	55.51
16.2	36.07	21.11	21.11	146.7	24.57	60.86
16.4	28.74	26.58	26.58	108.3	15.61	40.83
16.6	32.23	20.61	20.61	119.7	41.37	35.76
16.8	25.92	27.04	27.04	122.4	15.05	37.22
17.0	34.42	22.87	22.87	169.4	29.59	39.18
17.2	29.88	22.59	22.59	119.2	14.38	43.08
17.4	32.54	18.27	18.27	119.1	18.58	69.23
17.6	26.29	21.06	21.06	122	14.6	31.07
17.8	29.57	24.11	24.11	110.9	17.45	130
18.0	64.94	21.74	21.74	191.6	51.35	66.79
18.2	32.78	20.55	20.55	133.4	23.77	42.66
18.4	35.48	25.46	25.46	163.6	24.77	103.5
18.6	42.57	22.88	22.88	160.7	107.8	178.4
18.8	59.62	25.15	25.15	193.2	36.43	48.47
19.0	35.76	28.64	28.64	195.3	70.38	58.44
19.2	28.22	19.04	19.04	141.6	21.58	29.82
19.4	32.75	21.46	21.46	151.4	60.49	92.41
19.6	44.22	24.84	24.84	228.5	21.48	45.06
19.8	55.17	22.22	22.22	193.8	45.52	54.27
20.0	46.03	26.34	26.34	166.7	31.75	64.81
20.2	48.21	26.46	26.46	210.6	60.47	51.96
20.4	34.16	24.45	24.45	150.6	43.15	67.68
20.6	86.29	24.92	24.92	286.8	137	83.76

Depth (cm)	Muscovite	Kaolinite	Clinochlore	Quartz	Microcline	Albite
20.8	43.78	20.18	20.18	213.7	100.1	43.48
21.0	38.24	21.23	21.23	139.1	16.5	46.02
21.2	25.71	18.9	18.9	144.5	31.7	56.51
21.4	34.88	24.37	24.37	197	25.65	108.6
21.6	28.97	18.46	18.46	118.1	27.38	33.37
21.8	33.97	25.58	25.58	165.2	34.55	82.28
22.0	34.35	20.46	20.46	124.7	18.48	44.22
22.2	29.3	21.11	21.11	158.2	16.74	31.33
22.4	45.33	31.11	31.11	162.1	21.95	44.83
22.6	29.59	21.25	21.25	110	33.44	38.17
22.8	36.91	28.51	28.51	131.2	28.33	59.68
23.0	30.69	19.84	19.84	99.73	17.54	31.58
23.2	28.5	27.29	27.29	116.5	23.2	40.58
23.4	30.77	26.27	26.27	198.1	25.3	37.64
23.6	37.15	21.99	21.99	100.1	18.98	39.5
23.8	52.81	28.59	28.59	166.4	20.77	51.72
24.0	30.14	23.05	23.05	86	10.02	23.77
24.2	31.06	25.02	25.02	115	14.84	41.58
24.4	31.38	19.87	19.87	124	26.05	23.99
24.6	35.43	20.69	20.69	139.2	17.99	48.93
24.8	41.09	19.14	19.14	172.3	27.48	41.8
25.0	22.81	18.57	18.57	94.74	19.98	19.98
25.2	22.75	17.59	17.59	86.09	9.62	31.43
25.4	24.43	19.69	19.69	101.3	17.43	35.93
25.6	30.73	25.61	25.61	139.3	17.99	48.93
25.8	36.22	19.58	19.58	112.6	22.06	40.58
26.0	24.42	13.49	13.49	92.46	17.23	24.4
26.2	23.63	20.07	20.07	100.6	23.68	29.3
26.4	32.19	19.12	19.12	134.5	27.99	41.85
26.6	19.91	17.27	17.27	118.2	15.89	62.22

Chemical and mineralogical data

Depth (cm)	Muscovite	Kaolinite	Clinochlore	Quartz	Microcline	Albite
26.8	29.44	17.61	17.61	105.3	19.19	34.62
27.0	22.71	18.65	18.65	100	28.91	38.94
27.2	25.52	19.57	19.57	83.48	11.07	31.72
27.4	36.67	14.42	14.42	110.1	19.27	35.89
27.6	21.14	17.12	17.12	89.27	65.59	33.96
27.8	29.12	20.83	20.83	124.4	12.35	71.52
28.0	29.11	25.74	25.74	126.1	16.62	29.98
28.2	17.92	26.54	26.54	114.4	20.17	34.7
28.4	23.42	22.61	22.61	138.3	30.84	42.33
28.6	28.83	30.15	30.15	119.2	24.02	47.55
28.8	33.18	21.57	21.57	96.71	15.94	20.92
29.0	33.98	18.42	18.42	166.3	28.03	31.51
29.2	23.77	21.39	21.39	92.43	20.68	31.44
29.4	81.25	25.74	25.74	179.9	51.58	73.71
29.6	26.31	19.47	19.47	112.8	17.01	32.2
29.8	35.67	26.59	26.59	135.8	32.75	36.92
30.0	37.15	28.98	28.98	134.4	23.97	39.2
30.2	18.48	16.34	16.34	75	18.29	25.72
30.4	31.22	19.12	19.12	116.5	21.12	33.48
30.6	32.61	19.85	19.85	108.7	31.63	39.48
30.8	10.94	18.57	18.57	108.1	11.53	25.93
31.0	35.03	23.07	23.07	119.7	26.19	36.33
31.2	34.66	21.49	21.49	133.4	16.64	38.21
31.4	39.57	19.13	19.13	131.3	29.48	36.7
31.6	37.35	18.97	18.97	124.6	52.44	52.7
31.8	34.41	21.35	21.35	117.2	15.55	34.06
32.0	32.72	20.27	20.27	110.8	41.88	27.47
32.2	28.23	16.69	16.69	120.9	18.46	35.81
32.4	25.17	15.52	15.52	112.2	24.29	36.44
32.6	27.72	16.71	16.71	113.2	17.1	32.06

Depth (cm)	Muscovite	Kaolinite	Clinochlore	Quartz	Microcline	Albite
32.8	28.36	18.8	18.8	130.1	23.22	28.7
33.0	32.03	20.13	20.13	113.4	22.53	41.14
33.2	31.17	16.15	16.15	96.54	16.48	68.32
33.4	34.51	22.69	22.69	121.4	45.09	34.97
33.6	26.52	26.35	26.35	103.3	22.74	25.73
33.8	22.38	23.44	23.44	135.1	17.98	31.79
34.0	29.84	23.76	23.76	97.43	28.36	27.23
34.2	38.44	24.7	24.7	146.9	21.38	50.38
34.4	38.74	16.79	16.79	154.8	24.98	49.63
34.6	35.47	17.89	17.89	172.7	36.12	31.92
34.8	46.21	19.94	19.94	184.3	52.17	140.1
35.0	28.84	10.29	10.29	131.4	54.36	42.57
35.2	23.12	19.04	19.04	117.9	17.39	27.31
35.4	32.06	24.75	24.75	131.3	87.95	39.07
35.6	39.14	17.4	17.4	151.4	32.76	51.03
35.8	32.51	22.5	22.5	129.6	52.52	42.33
36.0	65.08	16.91	16.91	255.1	101.5	92.06
36.5	32.72	16.36	16.36	160.9	26.83	48.92
37.0	38.58	19.27	19.27	155.1	33.43	49.63
37.5	41.63	18.93	18.93	160.6	77.61	49.92
38.0	34.43	17.05	17.05	125.3	24.96	33.3
38.5	30.14	16.59	16.59	120.3	18.45	32.59
39.0	35.41	18.23	18.23	131.9	26.58	35.22
39.5	51.66	19.64	19.64	138.1	27.38	30.7
40.0	33.67	19.01	19.01	156.9	94.31	32.88
40.5	31.57	19.43	19.43	130.5	20.56	43.67
41.0	35.08	17.13	17.13	131.1	35.92	30.13
41.5	36.49	16.36	16.36	146.4	43.94	39.75
42.0	35.68	18.91	18.91	129.1	21.12	31.19
42.5	35.38	16.88	16.88	140.3	32.25	31.09

Chemical and mineralogical data

Depth (cm)	Muscovite	Kaolinite	Clinochlore	Quartz	Microcline	Albite
43.0	32.95	19.93	19.93	138.9	26.88	34.99
43.5	38.45	19.76	19.76	190.1	62.24	47.33
44.0	29.99	17.86	17.86	140.7	26.25	80.41
44.5	34.67	21.76	21.76	153.3	40.73	73.94
45.0	43.52	17.49	17.49	178.5	46.53	70.06
45.5	66.18	24.92	24.92	299	81.93	64.03
46.0	33.8	16.7	16.7	136.9	23.46	51.1
46.5	38.48	19.07	19.07	138.7	36.81	31.99
47.0	35.27	15.17	15.17	153.3	19.01	30.53
47.5	41.78	19.51	19.51	169.1	53.42	38.67
48.0	41.22	16.47	16.47	182.2	60.12	34.83
48.5	32.56	18.62	18.62	151.1	22.91	34.72
49.0	36	18.39	18.39	163.8	28.75	44.74
49.5	39.11	19.63	19.63	153.9	43.17	43
50.0	38.42	20.27	20.27	164.3	36.88	39.89
50.5	34.13	18.2	18.2	140.5	29.92	39.17
51.0	37.67	19.7	19.7	133.4	31.88	44.97
51.5	50.17	24.42	24.42	142.1	28.63	44.97
52.0	55.58	25.07	25.07	210.9	65.41	46.33
52.5	35.15	18.94	18.94	135.7	32.62	44.16
53.0	33.47	19.19	19.19	142.4	30.06	30.59
53.5	36.64	17.14	17.14	148.1	26.87	45.51
54.0	39.83	25.16	25.16	117.6	24.77	31.05
54.5	48.6	19.92	19.92	142.2	21.23	54.91
55.0	35.35	21.62	21.62	123.8	18.23	42.31
55.5	43.17	21.39	21.39	128	95.32	52.12
56.0	37.35	25.34	25.34	132.8	24.52	28.17
56.5	27.67	20.86	20.86	119.6	20.21	32.63
57.0	52.58	24.15	24.15	155.8	37.28	44.2
57.5	36.97	21.67	21.67	154.2	44.63	37.46

Depth (cm)	Muscovite	Kaolinite	Clinochlore	Quartz	Microcline	Albite
58.0	54.13	22.78	22.78	154.7	25.31	51.18
58.5	44.33	21.92	21.92	143.5	31.53	36.86
59.0	53.18	23.99	23.99	167.8	36.87	46.47
59.5	63.32	28.08	28.08	195.6	46.56	42.33
60.0	54.24	22.95	22.95	183.6	46.63	72.96
60.5	64.52	26.16	26.16	203.7	63.92	48.86
61.0	48.19	22.35	22.35	214.5	46.26	55.62
61.5	34.79	21.19	21.19	162.9	23.13	37.65
62.0	32.98	15.51	18.51	127.9	32.7	38.08
62.5	56.96	25.94	25.94	197.5	83.93	48
63.0	32.69	18.4	18.4	154.5	86.22	36.52
63.5	30.62	17.72	17.72	139	27.9	48.45
64.0	44.66	21.55	21.55	141	34.85	47.98
64.5	38.49	21.06	21.06	129.5	26.88	42.11
65.0	49.61	21.15	21.15	161.4	33.48	50.42
65.5	32.53	20.17	20.17	150.6	38.7	53.05
66.0	39.89	16.76	16.76	186.3	23.53	52.11
66.5	32.53	20.17	20.17	150.6	38.7	53.05
67.0	37.17	18.75	18.75	182.5	22.94	38.52
67.5	34.83	20.67	20.67	133.8	52.3	28.36
68.0	44.86	21.38	21.38	155.2	30.55	38.91
68.5	46.88	22.95	22.95	149.3	31.89	41.65
69.0	42.37	19.54	19.54	150	28.21	41.63
69.5	36.51	21.55	21.55	128.3	27.54	37.09
70.0	50.97	22.03	22.03	149.1	33.42	48.03
70.5	49.17	19.99	19.99	144.2	35.46	52.84
71.0	43.69	24.43	24.43	153.3	28.47	50
71.5	29.7	18.02	18.02	118.1	21.63	34.26
72.0	50.63	23.9	23.9	171.3	46.77	38.53
72.5	34.55	17.93	17.93	175.4	54.83	47.53

Chemical and mineralogical data

Depth (cm)	Muscovite	Kaolinite	Clinochlore	Quartz	Microcline	Albite
73.0	77.07	26.34	26.34	319.5	172.7	75.07
73.5	42.68	19.69	19.69	213.9	71.84	59.3
74.0	25.46	15.98	15.98	114.7	18.33	28.44
74.5	36.79	17.02	17.02	142.4	30.67	41.08
75.0	47.06	19.98	19.98	140.2	74.2	55.52
75.5	38.47	19.39	19.39	121	26.33	40.97
76.0	38.8	25.04	25.04	161.3	47.72	57.87
76.5	66.63	24.34	24.34	184.3	45.76	56.68
77.0	54.17	24.041	24.04	204.5	60.75	70.46
77.5	43.4	19.35	19.35	222.5	76.49	64.74
78.0	34.6	18.6	18.6	185.1	50.08	82.03
78.5	44.25	20.24	20.24	182.9	44.13	47.26
79.0	35.42	17.82	17.82	172.3	45.83	52.72
79.5	40.13	21.81	21.81	190.2	63.46	59.23
80.0	29.12	16.92	16.92	136.1	37.3	37.87
80.5	35.84	19.54	19.54	125.2	27.57	40.72
81.0	58.44	22.96	22.96	166.1	47.21	56.73
81.5	37.08	25.19	25.19	127.7	36.54	37.97
82.0	47.53	21.57	21.57	137	39.91	53.78
82.5	41.67	21.04	21.04	117.3	23.93	54.14
83.0	30.27	19.5	19.5	139.8	18.15	64.22
83.5	34.3	18.99	18.99	125.2	20.67	33.56
84.0	44.24	20.27	20.27	123.6	33.13	36.52
84.5	34.3	18.99	18.99	125.2	20.67	33.56
85.0	30.66	17.72	17.72	124.5	16.21	34.81
85.5	52.13	21.29	21.29	140.2	22.42	52.33
86.0	53.55	21.4	21.4	210.6	81.91	45.91
86.5	52.28	27.73	27.73	153.6	38.27	53.18
87.0	33.42	19.26	19.26	127.1	22.02	52.13
87.5	41.81	20.75	20.75	133.2	28.67	38.58

Depth (cm)	Muscovite	Kaolinite	Clinochlore	Quartz	Microcline	Albite
88.0	42.07	20.99	20.99	152.5	31.74	51.13
88.5	39.24	21.1	21.1	131.7	22.98	44.28
89.0	39.24	20.22	20.22	142.3	21.42	38.03
89.5	37.72	19.36	19.36	139.7	26.53	34.47
90.0	46.47	25.93	25.93	164.4	59.07	42.68
90.5	45.28	21.44	21.44	128.9	31.15	37.14
91.0	34.59	19.1	19.1	138.7	39.18	45.01
91.5	56.04	21.02	21.02	154	36.81	48.74
92.0	42.36	21.17	21.17	134	29.21	48.99
92.5	32.29	20.45	20.45	141.7	40.63	43.72
93.0	45.68	21.66	21.66	147.9	50.99	33.28
93.5	30.12	18.56	18.56	123.5	20.21	35.42
94.0	40.66	17.93	17.93	124.6	32.37	37.57
94.5	43.88	17.43	17.43	138.8	40.88	49.78
95.0	43.77	18.45	18.45	165.4	50.92	43.31
95.5	48.74	24.11	24.11	165.8	51.97	61.41
96.0	38.9	20.1	20.1	135.2	31.54	56.14
96.5	51.43	22.1	22.1	156.9	36.9	44.54
97.0	37.55	19.02	19.02	163	31.95	38.92
97.5	39.22	21.11	21.11	125.1	35.95	43.06
98.0	62.49	21.92	21.92	257.8	32.64	50.74
98.5	36.69	18.18	18.18	149.8	28.03	40.34
99.0	39.98	23.16	23.16	130.8	41.69	74.25
99.5	46.83	24.84	24.84	152	39.49	55.78
100.0	30.57	20.61	20.61	157.6	22.27	37.98
100.5	26.77	16.92	16.92	130.7	23.7	33.25
101.0	43.72	22.92	22.92	178.6	69.67	58.28
101.5	48.42	18.77	18.77	239.1	97.03	75.94
102.0	52.05	19.6	19.6	268.5	161.4	92.57
102.5	65.94	19.88	19.88	286.6	120	83.59

Chemical and mineralogical data

Depth (cm)	Muscovite	Kaolinite	Clinochlore	Quartz	Microcline	Albite
103.0	53.98	20.94	20.94	186	78.19	54.95
103.5	44.38	17.89	17.89	220.2	70.84	67.97
104.0	32.71	18.6	18.6	195.8	42.07	70.67
104.5	44.08	18.5	18.5	218.3	102.9	58.66
105.0	38.71	17.66	17.66	234	71.22	46.88
105.5	31.13	17.21	17.21	139.9	21.4	47.43
106.0	28.88	19.07	19.07	116.2	26.45	37.53
106.5	35.95	19.41	19.41	151.8	25.15	34.64
107.0	34.09	17.19	17.19	120.2	19.46	40.63
107.5	38.62	19.24	19.24	118	30.4	40.1
108.0	46.65	23.59	23.59	134.8	27.19	89.31
108.5	29.11	18.85	18.85	126.9	20.71	49.57
109.0	33.99	20.43	20.43	118.5	27.34	40.92
109.5	44	20.83	20.83	164.9	54.87	32.86
110.0	37.95	14.78	14.78	140	47.98	73.99
110.5	34.96	18.32	18.32	127.2	21.84	30.92
111.0	40.27	18.87	18.87	142.9	33.22	35.12
111.5	35.48	18.25	18.25	120.4	22.02	31.63
112.0	48.23	22.95	22.95	210.6	60.6	42.47
112.5	48.5	19.19	19.19	187.9	65.39	58.11
113.0	35.72	21.93	21.93	133.1	42.72	45.11
113.5	37.97	24.76	24.76	143	26.24	49.58
114.0	31.33	18.61	18.61	125.6	25.95	36.68
114.5	38.67	19.38	19.38	133.4	29.78	41.98
115.0	40.89	19.89	19.89	153.7	23.67	55.05
115.5	30.88	20.59	20.59	127.4	26.15	48.94
116.0	30.21	20.73	20.73	111.6	21.33	46.23
116.5	41.81	22.63	22.63	128.1	43.76	30.06
117.0	52.88	22.25	22.25	164.4	22.52	44.35
117.5	47.18	20.31	20.31	221.2	53.17	72.58

Depth (cm)	Muscovite	Kaolinite	Clinochlore	Quartz	Microcline	Albite
118.0	37.34	18.96	18.96	143.7	34.68	51.66
118.5	57.69	24.53	24.53	183.2	101.2	158
119.0	62.83	27.48	27.48	181.3	35.22	37.65
119.5	46.17	21.52	21.52	133.7	28.15	33.42
120.0	42.33	20.36	20.36	147.1	20.57	41.05
120.5	66.15	26.79	26.79	165.5	38.72	50.53
121.0	31.88	18.79	18.79	135.8	28.55	66.11
121.5	55.13	24.76	24.76	168.8	66.23	49.24
122.0	40.67	22.28	22.28	127.3	26.21	37.58
122.5	39.66	18.63	18.63	158.4	29.82	36.35
123.0	56.03	23.49	23.49	167.2	24.52	34.81
123.5	41.79	16.79	16.79	173.9	48.74	40.03
124.0	26.77	16.11	16.11	136.1	34.61	41.66
124.5	34.25	18.86	18.86	132	42.53	40.01
125.0	50.9	23.37	23.37	194.1	75.13	50.21

Table B.7. XRD intensity measurements of bulk clay minerals composition from PE12-01-01 core (in cps); Sap=saponite, Clc=clinochlore, Pkg=palygorskite, Ms=muscovite, Kln=kaolinite.

Depth (mm)	Sample	Sap glycolated	Clc dried	Pkg heated	Ms dried	Kln dried	Pkg dried
2	AO-1	3.13	7.17	33.57	22.06	9.6	3.08
10	AO-2	–	6.86	29.42	19.4	9.09	3.76
18	AO-3	2.12	8.05	29.1	23.41	8.71	2.88
34	AO-4	–	6.51	25.12	18.37	8.3	1.21
48	AO-5	–	7.13	21.43	12.89	6.97	1.7
68	AO-6	–	8.68	29.16	22.21	9.35	2.54
80	AO-7	1.36	11.03	22.88	15.82	8.64	2.66
98	AO-8	–	9.15	20.92	14.01	6.92	2.89
114	AO-9	0.69	6.59	16.43	10.77	6.49	2.78
130	AO-10	–	5.83	12.65	6.89	7.29	2.81

Chemical and mineralogical data

146	AO-11	1.53	5.61	14.76	8.38	12.62	3.05
162	AO-12	1.95	5.62	11.87	7.9	6.67	1.83
178	AO-13	–	7.34	15.69	10.71	6.63	2.46
192	AO-14	2.02	4.39	14.3	9.6	6.92	2.98
210	AO-15	–	6.8	14.56	9.04	7.14	3.67
226	AO-16	–	5.97	18.8	13	7.4	3.01
242	AO-17	–	7.76	13.94	7.27	6.04	2.63
258	AO-18	–	5.86	11.22	7.75	5.62	3.11
276	AO-19	–	7.09	11.82	6.94	6.6	3.71
290	AO-20	2.93	5.19	12.68	8.28	6.43	3.31
298	AO-21	–	9.51	12.02	8.36	5.37	3.14
330	AO-22	2.85	7.36	10.68	7.74	5.98	2.91
346	AO-23	–	6.76	12.84	9.07	6.56	3.41
370	AO-24	–	4.95	13.09	7.84	6.59	2.59
380	AO-25	–	4.14	8.53	5.95	5.98	4.12
395	AO-26	2.99	7.08	15.9	8.43	6.46	2.35
415	AO-27	–	4.15	11.89	7	6.44	2.09
435	AO-28	–	7.53	18.62	9.33	7.29	3.8
455	AO-29	–	8.71	18.1	11.23	7.84	3.6
475	AO-30	–	9.31	14.63	10.26	8.33	3.15
495	AO-31	–	8.07	15.94	9.33	6.9	3.59
515	AO-32	–	7.83	15.85	9.6	6.67	3.07
535	AO-33	2.73	7.48	16.12	10.21	7.99	2.98
555	AO-34	–	9.74	16.67	10.33	6.93	3.39
560	AO-35	5.15	15.18	28.16	17.87	10.29	3.21

Table B.8. XRD intensity measurements of bulk clay minerals composition from CIM12-04A core (in cps); Sap=saponite, Clc=clinochlore, Pkg=palygorskite, Ms=muscovite, Kln=kaolinite.

Depth (mm)	Sample	Sap glycolated	Clc dried	Pkg heated	Ms dried	Kln dried	Pkg dried
2	AO-36	–	9.73	8.37	7.96	8.95	3.32

16	AO-37	2.4	7.66	8.64	6.87	8.14	3.58
30	AO-38	1.73	8.54	11.16	8.53	9.02	3.23
42	AO-39	1.75	10.17	14.69	9.9	10.26	3.81
54	AO-40	2.25	11.81	14.51	10.45	10.49	3.04
72	AO-41	—	6.85	12.88	9.67	9.3	3.12
86	AO-42	—	7.95	12.42	9.53	8.89	2.55
96	AO-43	1.63	9.56	13.09	8.06	9.29	3.64
110	AO-44	—	10.47	14.18	10	9.41	3.25
128	AO-45	—	13.31	15.81	9.84	10.25	3.76
138	AO-46	3.17	10.29	14.97	9.8	9.06	2.97
152	AO-47	—	10.66	13.07	7.38	9.65	4.08
168	AO-48	1.88	10.22	19.55	11.72	12.84	4.21
180	AO-49	1.99	14.94	20.5	12.45	15.42	6.99
198	AO-50	—	9.28	18.36	11.12	12.39	4.52
214	AO-51	2.9	11.34	14.73	12.71	11.87	3.99
224	AO-52	—	8.7	17.15	10.94	9.5	2.92
238	AO-53	2.79	9.82	14.54	11.17	10.35	3.24
254	AO-54	—	9.79	13.38	10.24	9.37	2.31
264	AO-55	—	10.97	12.9	9.11	9.71	3.14
278	AO-56	—	8.63	12.4	9.08	10.01	4.3
294	AO-57	—	8.96	15.44	10.2	9.67	3.51
310	AO-58	—	7.12	11.81	8.65	9.23	4.51
324	AO-59	1.67	5.91	10.46	7.92	8.44	3.92
334	AO-60	2.63	8.06	11.37	7.44	9.87	3.81
352	AO-61	—	8.4	11.98	8.04	9.57	4.2
365	AO-62	—	11.79	14.43	10	10.76	4.93
390	AO-63	1.76	9.69	14.46	9.5	11.48	4.67
415	AO-64	—	9.23	16.94	9.38	4.31	4.31
440	AO-65	—	5.14	14.52	8.61	10.66	4.29
465	AO-66	—	9.66	14.73	9.29	11.82	4.31
490	AO-67	1.6	7.1	14.7	9.56	10.94	4.28

Chemical and mineralogical data

515	AO-68	—	9.31	15.94	11.57	13.62	3.93
540	AO-69	2.65	8.84	13.24	10.43	11.11	3.13
565	AO-70	—	6.74	11.78	8.9	9.7	2.83
590	AO-71	—	7.32	18.64	12.11	14.45	3.89
615	AO-72	—	8.6	16.54	10.73	14.26	4.09
640	AO-73	—	5.31	16.3	14.56	13.2	3.6
665	AO-74	—	11.74	16.82	13.43	12.71	4.14
690	AO-75	—	6.6	11.18	10.11	10.71	4.39
715	AO-76	2.38	1.53	16.14	7.29	11.73	4.84
740	AO-77	—	5.79	11.79	10.52	11.13	3.54
765	AO-78	—	10.62	15.96	12.84	15.32	4.22
790	AO-79	—	7.91	15.4	14.43	14.06	4.35
815	AO-80	—	7.29	18.01	12.94	14.11	3.37
840	AO-81	—	8.01	15.78	14.22	12.33	6.75
865	AO-82	1.71	9.32	14.52	11.79	12.13	4.36
890	AO-83	—	10.54	16.12	11.32	13.12	4.47
915	AO-84	—	6.44	16.26	10.69	11.6	4.78
940	AO-85	2.3	6.44	11.05	9.81	10.555	3.71
965	AO-86	—	7.23	15.76	13.1	12.71	4.2
990	AO-87	—	10.07	15.31	12.17	12.55	5.3
1015	AO-88	—	8.63	14.74	9.98	12	5.46
1040	AO-89	2.37	4.18	14.76	12.35	10.79	4.13
1065	AO-90	—	4.17	10.21	8.54	10.21	4.17
1090	AO-91	1.73	2.99	12.55	8.36	9.15	4.69
1115	AO-92	—	4.87	12.89	10.44	10.55	4.63
1140	AO-93	—	5.68	14.76	9.19	11.04	4.18
1165	AO-94	—	8.35	14.22	11.92	13.56	4.18
1190	AO-95	—	7.13	18.73	12.87	14.37	4.58
1215	AO-96	—	5.99	19.28	11.98	13.19	5.19
1240	AO-97	—	8.18	14.38	12.71	14.96	5.19
1250	AO-98	—	9.86	17.52	16.37	14.54	4.53